Non-planar thin film structures for spintronics

Dissertation zur Erlangung des akademischen Grades
Doctor rerum naturalium
(Dr. rer. nat.)

vorgelegt von

Sebastian Sailler

an der

Universität Konstanz
Mathematisch-Naturwissenschaftliche Sektion
Fachbereich Physik

Konstanz, 2025

Tag der mündlichen Prüfung	24.10.2025
Erstgutachter (Betreuer)	Prof. Dr. Sebastian T. B. Goennenwein
Zweitgutachter	Prof. Dr. Lukas Schmidt-Mende

Eidesstattliche Versicherung gem. §6 der Promotionsordnung der Universität Konstanz

1. Bei der eingereichten Dissertation zum Thema "*Non-planar thin film structures for spintronics*" handelt es sich um meine eigenständig erbrachte Leistung.

2. Ich habe nur die angegebenen Quellen und Hilfsmittel benutzt und mich keiner unzulässigen Hilfe Dritter bedient. Insbesondere habe ich wörtlich oder sinngemäß aus anderen Werken übernommene Inhalte als solche kenntlich gemacht.

3. Falls ich textgenerierende KI-Tools als Hilfsmittel verwendet habe, ist mir bewusst, dass ich allein für die inhaltliche Richtigkeit von KI generierten Textpassagen und die Kennzeichnung von Formulierungen und Ideen anderer Personen gemäß den Grundsätzen der guten wissenschatlichen Praxis verantwortlich bin. Die Arbeit oder Teile davon habe ich bislang nicht an einer Hochschule des In- oder Auslands als Bestandteil einer Prüfungs- oder Qualifikationsleistung vorgelegt.

4. Die Richtigkeit der vorstehenden Erklärungen bestätige ich.

5. Die Bedeutung der eidesstattlichen Versicherung und die strafrechtlichen Folgen einer unrichtigen oder unvollständigen eidesstattlichen Versicherung sind mir bekannt.

Ich versichere an Eides statt, dass ich nach bestem Wissen die reine Wahrheit erklärt und nichts verschwiegen habe.

Konstanz, 30.07.2025

Ort, Datum

Unterschrift

ABSTRACT

Progress in materials science is one of the main enabling forces for the technological advance, especially in electronic based devices. In the light of this evolvement, the field of spin-orbitronics has become a prominent research field, aiming to exploit not only the charge of an electron but also its angular moment for increased functionality. A promising route is the utilisation of pure spin or orbital currents, which can be generated in spin or orbital Hall active materials, like Pt or Ti. In combination with a magnetically ordered material, the resulting structures allow to generate spin-waves in the adjacent magnetic layer or exert spin-orbit torques on its magnetisation. The most commonly used material to study the transport of spin information on a fundamental level is crystalline yttrium iron garnet (YIG). However, the majority of studies focuses on planar layers, as these are readily available from standard deposition methods. While non-planar geometries pose a challenge in deposition, they are predicted to host interesting physical phenomena, like curvature or topology induced effects. In order to probe such samples, magnetotransport experiments could be envisioned. This commonly applied technique enables the injection and detection of spin-waves at both levels of non-planar samples in Pt strips. Therefore, magnetotransport constitutes one pathway to study non-planar geometries.

This thesis aims to provide a platform for the investigation of non-planar YIG geometries using transport experiments. To that end, the first part of the thesis details the sample fabrication of non-planar YIG films. In the second part fundamental magnetotransport experiments in prototypical materials and bilayers are described.

Part I presents the sputter deposition and subsequent annealing of amorphous YIG, which yields single crystalline, non-planar structures. YIG is the material of choice due to its excellent properties, like its low magnetic damping and electrically insulating nature. However, to obtain these properties crystalline YIG is necessary. To achieve single crystalline YIG out of the amorphous phase, specific substrates and high annealing temperatures need to be employed. To characterise the dependence of the crystallisation process on the annealing temperature, the crystallisation dynamics of YIG on different, planar substrates are initially investigated. The results lead to an all-encompassing description of the crystallisation process of YIG with concrete crystallisation velocities depending on the temperature. This knowledge enables the development of single crystalline, non-planar YIG on top of an artificial $\mathrm{SiO_x}$ mesa. With these devices at hand, the first aim of the thesis is achieved.

Non-planar spin transport experiments in YIG can now be conceived. To that end, spin or orbital currents need to be generated. Here, prototypical materials are Pt and Ti. These materials are characterised by a large interconversion efficiency of a charge current to a pure flow of spin or orbital angular momentum. In combination, i.e., bilayers of YIG/Pt, the angular moments in Pt can be injected into the YIG layer. For an adequate interaction of the spin current with the adjacent magnetisation in YIG, a well defined and consistent interface is essential.

In part II ground laying magnetotransport experiments are conducted, first, to study the charge to spin (orbital) current conversion in metal layers and second, to thoroughly characterise the interface quality and influences of the underlying crystal structure. To that end, in the beginning the spin- and orbitronic properties of typical materials are investigated. A similar scaling with resistivity and crystallinity is observed in single layers of Pt and Ti, implying a close connection of the subfields of spintronics and orbitronics. In conjunction, spin and orbital Hall active films could drastically increase the spin current injection into a magnetic film, like YIG. Knowing the optimal parameters to maximise the generation of pure spin and orbital currents, the transfer of the angular momentum into the magnetic layer needs to be optimized. Hence, a process of obtaining an optimal interface is developed. This process is confirmed by a statistical analysis of the spin transfer across the interface. These statistical measurements not only confirm the interface quality, but also showcase an influence of the crystal direction on the magnetotransport response. A dependency of angular moment injection and transport on the crystal orientation needs to be carefully considered in non-planar studies, as the crystal direction naturally changes in these geometries. Therefore, both the statistical distribution and the influence of the underlying crystal structure affect the observed transport response and are of fundamental importance for non-planar experiments. Hence, the groundwork for magnetotransport experiments in non-planar structures is laid in the second part of the thesis.

The results presented in this work, not only demonstrate a fabrication pathway for non-planar magnetic structures out of crystalline YIG, but also lay the experimental foundation for magnetotransport experiments in these structures. Taken together, the results of this thesis pave the way for investigating spintronic devices in non-planar geometries using magnetotransport.

Kurzfassung

Materialwissenschaftliche Entwicklungen sind eine der wichtigsten Triebkräfte für den technologischen Fortschritt, welcher in elektronischen Geräten besonders stark bemerkbar ist. Angesichts des rasant ansteigenden Bedarfs hat sich das Feld der Spin- und Orbitronik entwickelt, in dem nicht nur die Ladung des Elektrons, sondern auch sein Drehimpuls ausgenutzt wird, um eine erhöhte Funktionalität zu erreichen. Ein vielversprechender Ansatz ist das Ausnutzen von reinen Spin- oder Orbitalströmen, die in Materialien wie Pt und Ti durch den Spin- beziehungsweise Orbital-Hall-Effekt erzeugt werden können. Durch Kombination mit einem magnetisch geordneten Material, wie zum Beispiel Yttrium-Eisen-Granat (YIG, Englisch: yttrium iron garnet), können in diesem Spinwellen erzeugt oder ein Drehmoment auf die Magnetisierung ausgeübt werden. Jedoch konzentriert sich die Forschung überwiegend auf planare Schichten, da solche in Standardprozessen hergestellt werden können. Nichtplanare Schichten stellen zwar eine Herausforderung an die Herstellung, aber in diesen sind interessante physikalische Phänomene theoretisch vorhergesagt, die durch die Krümmung oder Topologie der nichtplanaren Strukturen hervorgerufen werden. Eine geeignete Methode um solche Effekte zu vermessen sind Transportexperimente. Diese häufig verwendete Technik erlaubt eine Injektion und Detektion von Spinwellen durch Pt-Streifen auf beiden Niveaus der nichtplanaren Struktur. Magnetotransportmessungen stellen daher eine geeignete Möglichkeit dar, um nichtplanare Strukturen zu untersuchen.

Ziel der Arbeit ist es, eine Plattform für die Untersuchung von nichtplanaren YIG-Strukturen mittels Transportexperimenten zu etablieren. Dazu wird zuerst die Herstellung von nichtplanaren YIG Dünnfilmen beschrieben und daraufhin die an prototypischen Materialien durchgeführten Magnetotransportmessungen.

Teil I befasst sich mit der Sputterdeposition und anschließender Auslagerung von amorphem YIG, woraus nichtplanare, einkristalline Strukturen hergestellt werden. YIG ist das Material der Wahl auf Grund seiner herausragenden Eigenschaften, wie zum Beispiel einer geringen magnetischen Dämpfung. Um diese Eigenschaften zu erreichen, ist

jedoch kristallines YIG erforderlich. Dieses kann in einkristalliner Form aus der amorphen Phase mittels geeigneter Substrate sowie hohen Auslagerungstemperaturen hergestellt werden. Um die Temperaturabhängigkeit des Kristallisationsprozesses zu untersuchen, wird anfänglich die Dynamik der Kristallisation von YIG auf verschiedenen, planaren Substraten untersucht. Die Ergebnisse resultieren in einer allumfassenden Beschreibung des Kristallisationsverhalten von YIG. Dieses Wissen ermöglicht die Entwicklung und Herstellung von einkristallinen, nichtplanaren YIG-Strukturen auf künstlich definierten SiO_x Stufen.

Die hergestellten Strukturen eröffnen die Möglichkeit, nichtplanare Spin-Transportexperimente zu konzipieren. Hierfür müssen Spin- oder Orbitalströme erzeugt werden. Zwei prototypische Materialien sind Pt und Ti, die sich durch ihre hohe Umwandlungseffizienz von Ladungsstrom zu Spin- bzw. Orbitalstrom auszeichnen. Eine Kombination von YIG und Pt Bilagen ermöglicht den Übertrag von Drehimpuls an der Grenzfläche. Für eine gute Ankopplung der Spinakkumulation in Pt mit der Magnetisierung des YIG ist eine wohl definierte, saubere Grenzfläche essenziell.

Teil II der Arbeit beschreibt grundlegende Magnetotransportmessungen, wobei zuerst die Umwandlung von Ladungsstrom in Spin- oder Orbitalstrom in metallischen Dünnfilmen untersucht und anschließend die Qualität der Grenzfläche, sowie der Einfluss der Kristallstruktur an YIG/Pt-Bilagen charakterisiert wird. Anfänglich werden dafür die charakteristischen Eigenschaften von Spin- oder Orbital-Hall-aktivem Material untersucht. Hierbei weisen Pt und Ti eine vergleichbare Abhängigkeit zum spezifischen Widerstand und der Kristallinität auf, was auf eine enge Überschneidung der Teilbereiche Spintronik und Orbitronik deutet. Eine Kombination von solch Spin- und Orbital-Hall-aktiven Materialien könnte eine drastische Steigerung der injizierten magnetischen Momente in ein angrenzendes, magnetisch geordnetes Material, wie YIG, ermöglichen. Da jetzt die optimalen Parameter zur Maximierung der Erzeugung reiner Spin- und Orbitalströme bekannt sind, muss nun die Einkopplung des Drehimpulses in die magnetische Schicht optimiert werden. Dafür wird zunächst ein Prozess für eine optimale Grenzfläche entwickelt. Dieser Prozess wird durch eine statistische Analyse des Spintransfers über die Grenzfläche verifiziert. Die Messergebnisse bestätigen nicht nur die Qualität der Grenzfläche sondern zeigen zudem einen Einfluss der unterliegenden YIG Kristallstruktur auf die Transporteigenschaften des Pt auf. Eine Abhängigkeit der Einbringung und des Transports von Spinmomenten von der Kristallorientierung muss vor allem in nichtplanaren Experimenten berücksichtigt werden, da sich die Kristallrichtung in diesen Geometrien unvermeidlich ändert. Daher sind sowohl die statistische Verteilung sowie der Einfluss der Kristallstruktur von grundlegender Bedeutung für Magnetotransportexperimente in nichtplanaren Strukturen. Damit legen die hier durchgeführten Versuche den Grundstein für Transportexperimente in komplexen YIG-Geometrien.

Die in dieser Arbeit vorgestellten Ergebnisse zeigen nicht nur einen Herstellungsweg für nichtplanare Strukturen aus einkristallinem YIG auf, sondern legen zusätzlich die Grundlagen für Magnetotransportexperimente in solchen Strukturen. Insgesamt gesehen ebnen die Ergebnisse dieser Arbeit den Weg für die Untersuchung von nichtplanaren spintronischen Proben mittels Magnetotransport.

CONTENTS

Chapter 1

INTRODUCTION

Modern materials science has been crucial in paving the way for the technological progress in the last century in virtually every area in our lives [9]. This technological advance is especially noticeable in electronic devices, where new processing techniques and material optimisation have resulted in smartphones, computers and smart devices. At the heart of this lies the semiconductor industry with its capability to manufacture silicon based chips at nanometre precision. The advancement in semiconductor technology has been historically guided by Moore's Law, which predicts the doubling of transistor density approximately every two years [10]. In order to enable this self fulfilling law, precise deposition techniques and optical lithography to define nanoscale features are required. The most recent technology nodes — with feature sizes reaching below 7 nm — demand rigorous control over material deposition, the patterning process as well as the etching [11].

The focus of this thesis lies in thin film deposition, which is one of the key steps facilitating today's semiconductor devices. Not only does the deposition have to come with atomic precision, but it also needs to be conformal over the complete wafer, scalable and yield high purity films. To that end, different physical as well as chemical vapour deposition techniques, like sputtering [12], atomic layer deposition [13] or molecular beam epitaxy [14] have found their way into the manufacturing process. Deposited materials range from semiconductors over metals, dielectrics and oxides [15].

While high precision deposition techniques and the introduction of extreme ultraviolet lithography [16] made a downscaling towards several nanometres possible, fundamental physical limits are reached [17, 18]. These limitations stem from the finite size of the individual atoms and the need for continuos nodes. Further, an increasing power dissipation stemming, e.g. from leakage currents by tunnelling are expected to develop at single digit nanometre structural sizes. With the semiconductor miniaturisation reaching a fundamental limit, one concept being firmly pursued is the 3D integration [19], which improves the lateral downscaling of MOSFET structures.

A different approach to improve scaling, power consumption, and data processing speed is attempted to be reached via spintronics. While the conventional semiconductor industry focuses on controlling the flow of electrons, spintronics aims to additionally interconvert electrical and magnetic signals [20]. The roots of spintronics can be traced back to the observation of the giant magnetoresistance (GMR), an effect resulting from spin orientation dependent electron scattering [21]. Magnetoresistive effects, like the GMR, found application in magnetic storage devices, i.e. in hard disk drives (HDD's) [22]. While nowadays HDD's are mostly replaced by the faster solid state drives (SSD) in computers and laptops, they still play a crucial role in data storage of clouds and servers due to their long term stability [23]. Advancing magnetic storage [24] led to the recent commercialisation of a spintronics based spin transfer torque random access memory (STT-MRAM), further highlighting the potential of the field [25]. More efficient and faster performance is expected to be reached via spin orbit torques (SOT), a concept where the torque is provided from a non-ferromagnetic material [26, 27].

Both the spin transfer (STT) and the spin orbit torque (SOT) can be used to control the magnetisation in a magnetic layer. The STT arises, e.g. in Co/Cu or Fe/Cr multilayers [28] and is utilised in spin valves [29, 30] or in magnetic tunnel junctions (MTJ), where the prototypical tunnel barrier consists of insulating single crystalline MgO [31]. In contrast, SOTs originate from materials with large spin-orbit coupling like Pt, W and Ta [32] and do not require a magnetic layer for their generation. Instead spin currents emerge from the spin Hall effect [33, 34] or the Rashba-Edelstein effect [35], which in turn can cause a torque on the magnetisation and subsequently, a switching of an adjacent magnetic layer [26]. The SOT is expected to be more energy efficient and not limited in the amount of angular momentum which can be transferred per electron [32].

Next to the spin degree of freedom utilised in spintronics, the orbital degree of freedom has recently gained significant interest with the respective field dubbed as orbitronics. The microscopic description is similar and orbital effects are predicted to be large and prevalent in a multitude of materials [36, 37]. Several nanometres of comparably cheap materials like CuO_x have already been shown to significantly improve the torque or injection efficiency of existing spintronic devices [38–40]. Implementing the ideas from orbitronics successfully would lead to an increased efficiency of future devices aiming to utilise more than just the charge of the electron at low costs.

Improving these existing and finding new promising concepts has always been the scope of fundamental research. The basis of research, progress and technological advance are suitable materials and samples. In spintronics research, two materials are prominently employed due to their remarkable properties: Pt and yttrium iron garnet (YIG). Pt is known for its large intrinsic [41] charge to spin conversion [42] of up to 10 % [43, 44], depending on its electrical properties [45]. These spin currents can be injected into an underlying magnetic material. Here, YIG, a synthetic ferrimagnet, is the material of choice, as it has a large bandgap of roughly 2 eV [46], making it electrically insulating, which allows for the investigation of pure spin currents [42, 47]. Furthermore, YIG exhibits an exceptionally low ferromagnetic damping in the order of 10^{-5} [48–50], which allows for long distance spin transport [51–53] as well as investigations into magnetisation dynamics [50, 54]. In orbitronics different materials are currently being investigated with examples being Ti [37], Mn [55] or Cr [56].

Due to the exceptional properties, YIG is considered for applications in spin wave computing [57, 58]. Similarly, non-planar structures of YIG would allow for an increased lateral downscaling and could further host interesting new physics, stemming from curvature or topology induced effects [59, 60]. Hence, non-planar YIG is of fundamental interest and continued advancements in materials science will be essential for realising the full potential of next-generation electronics.

Content of this thesis and personal contributions

The thesis follows the overarching goal of elevating spintronic research from planar thin films to non-planar geometries. The first part of the thesis details thin film deposition, crystallisation and the successful fabrication of single crystalline, non-planar YIG. To that end, the crystallisation behaviour of YIG films on various substrates and at different temperatures are extensively studied (cp. Fig. 1.1(a)(1) and chapter 3). From these experiments, distinct crystallisation windows depending on the substrate material can be defined and the results described in a general crystallographic model for the (vertical) crystallisation of YIG. The insights gained from the vertical crystallisation are the key to obtain single crystalline YIG on an artificial mesa. This lateral crystallisation (cp. Fig. 1.1(a)(2)), its temperature windows and velocities are then detailed in chapter 4.

The second part of the thesis delves into magnetotransport experiments, representatively depicted as a Hall bar in Fig. 1.1(b). Here, a detailed investigation into the prototypical spin and orbital Hall active materials of Pt [61] and Ti [37] is conducted. The results in chapter 6 highlight a generic scaling of the occurring magnetoresistances in both materials, suggesting a close relation between the subfields. Afterwards, bilayers of YIG/Pt are considered (see Fig. 1.1(c)), and the first statistical investigation of the magnetotransport in YIG/Pt is conducted in chapter 7. A narrowly distributed magnetoresistance effect is observed, which sensitively depends on the interface. Furthermore, a previously unrecognised dependency on the underlying crystal structure is described.

Lastly, the thesis is summarised and concluded. With this thesis, the tools and samples available for spin transport experiments on non-planar YIG structures were significantly advanced. The research I conducted during the course of the PhD so far resulted in 3 first author manuscripts and 1 in preparation. The individual contributions are stated at the start of each chapter, which details the work in my own words.

Beyond the scientific contributions, I established the structural characterisation and the sputtering processes of several materials, including YIG, Pt and Ti, in our group. I was further in charge of several cryogenic systems. Lastly, I advised the Bachelor's theses of Rony Werner and Denise Reustlen, the student internships of Anna Schwarz, Robin Swoboda, Denise Reustlen, Davina Schmidt, Rony Werner and Thorben Bielewski, as well as the Master's thesis of Gregor Skobjin, Akis Rachoutis and Denise Reustlen. While I

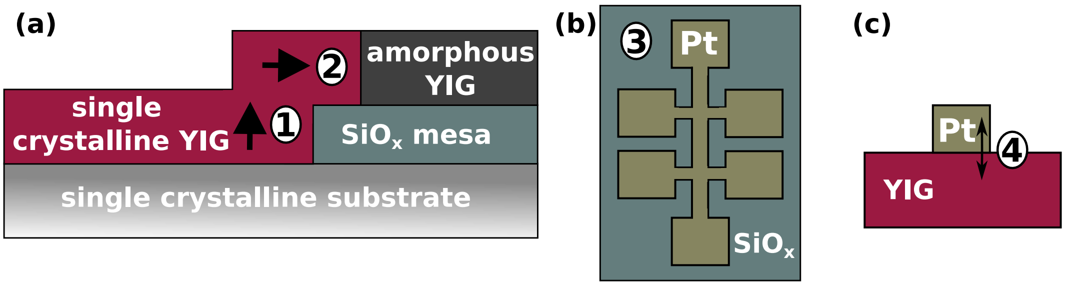

Figure 1.1: Content overview of this thesis: (a) Non-planar yttrium iron garnet (YIG) structure fabricated and discussed throughout the thesis. To achieve these step like structures, first a vertical crystallisation of YIG starting from the interface with the single crystalline substrate needs to take place (1). Afterwards, the YIG continues to crystallise laterally over the SiO_x mesa, yielding a single crystalline, non-planar YIG thin film structure (2). (b) Transporting information in the YIG thin film is then usually achieved by injecting spin currents from a Pt strip (3). Knowledge about the transport properties of Pt is therefore crucial. From the Pt strip the spin current needs to interact with the underlying YIG (c). Therefore, the interface is a crucial parameter determining how well spin information can be transferred from the Pt into the YIG (4).

instructed the students in acquiring the data, the final evaluation, analysis and visualisation of all data presented in this thesis was performed by myself. The interpretation of the data was conducted together with all co-authors.

PART I: CRYSTALLISATION DYNAMICS

One main objective of the thesis is to fabricate non-planar structures for spintronic devices. Therefore, the first part of the thesis focuses on the deposition of yttrium iron garnet (YIG) thin films. Despite YIG being the prototypical material for spintronic research, experiments rely almost exclusively on planar thin films [48–50, 62]. While other magnetic compounds have been manufactured in 3D geometries [63] and pose promising effects, e.g. in curved geometries [59], they are typically based on polymer matrices which support the magnetic compound [60]. This approach can be used for example for Ni or Co, which exhibit magnetic properties when deposited at room temperature. However, the concept cannot be easily applied to YIG as its complex crystal structure only forms at elevated temperatures [64–66] and the crystalline phase is required for YIG's magnetic properties [67]. Furthermore, high quality YIG films are only obtained on specific, lattice matched substrates, as they enable the formation of single crystalline YIG [50]. Hence, in order to crystallise YIG in non-planar geometries, precise knowledge about the crystallisation behaviour as well as a temperature stable template is needed [68, 69].

In the next chapter, YIG is firstly introduced followed by suitable deposition techniques yielding high quality YIG thin films. Afterwards, the material and methods used in this part of the thesis are detailed. Chapter 3 then describes the crystallisation behaviour of YIG on different substrates. The results are the enabling step for the newly established method of the lateral crystallisation of YIG, described in chapter 4.

Chapter 2

FUNDAMENTALS OF THIN FILM DEPOSITION AND CRYSTALLISATION

In this chapter, firstly YIG is introduced, as it is the material of choice throughout the first part of the thesis. Afterwards, a brief introduction into deposition techniques is given, with the focus on sputter deposition. Subsequently (lateral) solid phase epitaxy is described and the materials and methods utilised in this part are presented.

2.1 Yttrium iron garnet (YIG)

The material of choice in spintronics research is yttrium iron garnet ($Y_3Fe_5O_{12}$, YIG), an electrically insulating ferrimagnet, which crystallises in a cubic lattice with $Ia\bar{3}d$ symmetry [70]. Its unit cell with the position of the atoms are given in Fig. 2.1. The ferrimagnetism arises from the differently coordinated Fe^{3+} atoms, as three of five Fe^{3+} atoms occupy tetrahedral sites, while the remaining two are situated on octahedrally coordinated sites [71]. The two Fe sublattices then are aligned antiparallel to each other, resulting in an effective magnetic moment of $S = 5/2$ in the direction of the tetragonally coordinated Fe atoms [72]. The dodecahedrally coordinated Y^{3+} atoms do not carry any magnetic moment. This configuration leads to the ferrimagnetic properties of YIG, with a Curie temperature of $T_C = 559\,K$ and a room temperature saturation magnetisation of $M_{sat} = 143\,kA/m$ [64, 73].

YIGs combination of electric and magnetic properties render it a prototypical candidate for fundamental research. The insulating nature accompanied by a long spin diffusion length, make YIG an ideal material for studies revolving around pure spin currents [43, 47, 51]. Moreover, YIG exhibits an exceptionally low Gilbert damping and a small coercive field, which allows investigations of magnon dynamics through techniques such as ferromagnetic

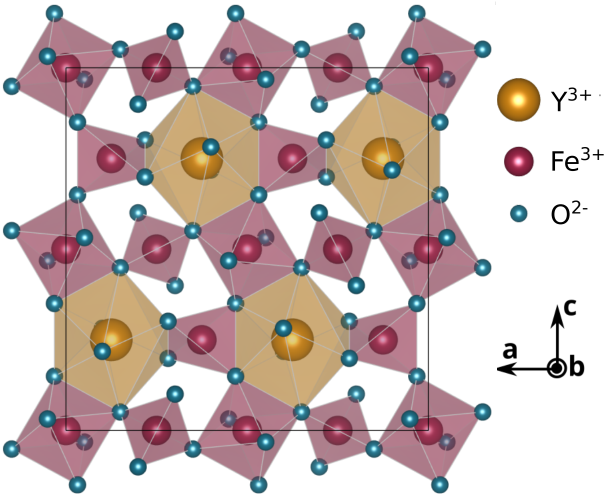

Figure 2.1: Unit cell of yttrium iron garnet.

resonance [50, 54, 74–76]. These remarkable properties have led to extensive research on and with YIG establishing it as a model system in spintronics. Here, the majority of samples utilised are planar thin films grown on suitable substrates, which is detailed in the following section.

2.2 Deposition techniques and crystallisation of YIG thin films

For over half a century, numerous studies employing various deposition techniques have demonstrated that single crystalline YIG thin films with excellent quality can be obtained on lattice matched substrates, like gadolinium gallium garnet (GGG) [48–50, 62, 65, 77, 78]. The most commonly used mechanism resulting in single crystals is called epitaxy. Here, the (thin film) crystal grows in an ordered manner starting from the substrate with a well defined relation to it [79, 80]. When material is epitaxially grown on a substrate of the same material, the process is referred to as homoepitaxy. If substrate and thin film differ the respective process is called heteroepitaxy. As epitaxial thin films take on the orientation and crystalline structure of the underlying substrate, it is essential that film and substrate are compatible in that regard. This condition is inherently satisfied for homoepitaxy, whereas for heteroepitaxy a careful selection of the substrate material is required to ensure compatibility. The matching degree between thin film and substrate is characterised by the lattice mismatch ϵ of the respective lattice parameter a_{film} and $a_{\text{substrate}}$ as given by Eq. (2.1) [81]:

$$\epsilon = \frac{a_{\text{film}} - a_{\text{substrate}}}{a_{\text{substrate}}} \cdot 100\% \tag{2.1}$$

The driving force of an epitaxial process is the lower free energy of the system, i.e., the interfacial energy of a nearly continuous interface at the boundary between film and substrate. Even if the interfacial energy increases with the lattice mismatch, it is often small compared to the energy needed for dislocations or for nucleation [82]. Different growth modes exist depending on the free energy of the system and can be characterised in island growth, layer by layer growth or a mixture of both [83]. For very large lattice mismatches or if no lattice is given at all, a thermodynamically stable nucleus needs to form for a crystallisation process to start. As nucleation is thermally activated, elevated temperatures result in many different nuclei and, by that, the formation of a polycrystalline thin film.

Depending on the deposition technique, different forms of epitaxy are possible. The oldest technique for obtaining single crystalline YIG is called liquid phase epitaxy (LPE) [50, 72, 77, 84–86]. Here, a YIG crystal forms onto a single crystalline substrate out of a fluxed solution of precursors via an epitaxial process as described above. Due to the direct formation out of the liquid phase only closely lattice matched substrates are utilised and the resulting YIG films typically exhibit excellent crystal quality and magnetic properties [50]. More recently developed deposition techniques utilising a solid, stoichiometric YIG target are pulsed laser deposition (PLD), [49, 62, 87–92] and radio-frequency (RF) magnetron sputtering [48, 65, 67, 93–107]. PLD uses a laser to ablate material from the YIG target, while sputtering utilises a plasma to accelerate ions of a process gas onto the target, which forces atoms out of it. In both processes, a layer forms on a given substrate. Depending on the temperature and substrate, direct epitaxial growth, crystallisation via solid phase epitaxy (SPE), as well as nucleation plus crystallisation can be observed [65, 67, 95]. SPE describes the phase transition in the solid state from an amorphous film to a single crystalline one (cp. chapter 3). Lastly, methods using gaseous precursors like atomic layer deposition (ALD) or metal organic deposition have emerged in the last years [78, 108, 109]. Here, the combined precursors consist of the nominal composition of YIG, with the YIG crystal only forming in a subsequent annealing process.

While each technique has their advantages and limitations, the resulting film quality is comparable between the deposition methods [48–50, 78]. Here, sputter deposition is used and the solid phase heteroepitaxy of YIG studied in chapter 3.

2.3 Lateral solid phase epitaxy

Solid phase epitaxy (SPE) has been investigated in many different materials and material combinations [110, 111]. Here, the prototypical elements are Si and Ge, stemming from their similarity and technological relevance for the semiconductor industry [112]. Their (homo)epitaxy is therefore extensively studied, e.g. by amorphisation due to ion implantation and subsequent crystallisation [113–116]. Using transmission electron microscopy (TEM) with an in-situ heating stage, the propagation of a moving crystallisation front at the interface of crystalline to amorphous material can be monitored [117]. In these experiments, the crystal orientation, different dopants, implanted atoms as well as the ion-dose and even hydrostatic pressure are reported to influence the velocity of the propagating crystal front [111, 116, 118, 119].

Lateral solid phase epitaxy (LSPE) describes a variation of SPE, where the propagation of the crystallising front is perpendicular to the seed surface provided by the substrate [120, 121]. Much like for SPE, the prototypical material investigated is Si, crystallised over SiO_2, so called silicon on insulator (SOI) structures. These SOI based devices are more robust, allow for an increased performance and reduce short circuit effects in comparison to bulk Si structures [122]. Their technological relevance is highlighted by their commercial use in large scale wafer manufacturing starting from 1998 and consistent appearance in the international technology roadmap for semiconductors (ITRS) [112, 122]. The basis for the technological application is the materials research and engineering that went into the LSPE of Si with the aim of controlling and enhancing the crystallisation over insulator structures, while maintaining highly crystalline Si [120, 121, 123].

Therefore, lateral solid phase epitaxy enables the formation of single crystalline material in non-planar structures and is utilised in chapter 4.

2.4 Experimental techniques and substrate materials

The deposition technique used throughout this thesis is magnetron sputtering, a commonly applied physical vapour deposition technique. Here, the sputtering targets, i.e. the materials to be deposited, are placed in an (ultra) high vacuum chamber, as depicted in Fig. 2.2. During the sputter deposition, an inert gas (typically Ar) is introduced into the sputtering chamber with 10^{-3} to 1×10^{-2} mbar and a plasma is generated by applying a high voltage between cathode and the anode. Here, the sputter target acts as the cathode (cp. Fig. 2.2(c)). Due to the electrical field Ar^+ ions are accelerated towards the target, where they eject (sputter) atoms from the surface by momentum transfer. At the same time, due to the bombardment of the target with Ar^+ ions, electrons are generated and accelerated away from the target, colliding on the way with the inert gas. Inelastic collisions of both ions and electrons cause further ionisation of the gas and by that give rise to a self sustaining plasma. By applying a magnetic field near the target surface, the efficiency of the sputtering process can be enhanced, hence named magnetron sputtering. This magnetic field confines electrons close to the target in a cycloidal path giving rise to higher deposition rates.

When sputtering, two different methods can be distinguished: direct current (DC) and radio-frequency (RF) magnetron sputtering. DC sputtering works with conducting target materials and typically yields high deposition rates, however, falls short of sputtering oxides due to the accumulation of positively charged ions at the surface. One possibility to counteract this is to use RF sputtering, where an alternating electric field accelerates electrons in the negative cycle and positively charged ions in the positive cycle. This alternation prevents a charging of the target and allows electrical insulators like YIG to be sputtered.

Regardless of RF or DC sputtering, the ejected atoms condense onto a provided substrate, forming a film made out of the atoms from the sputter target. As detailed before a suitable substrate for the target material - in this case YIG - needs to be chosen.

The substrates investigated in this part of the thesis include yttrium aluminum garnet (YAG, $Y_3Al_5O_{12}$, *CrysTec*) and gadolinium gallium garnet (GGG, $Gd_3Ga_5O_{12}$, *SurfaceNet*),

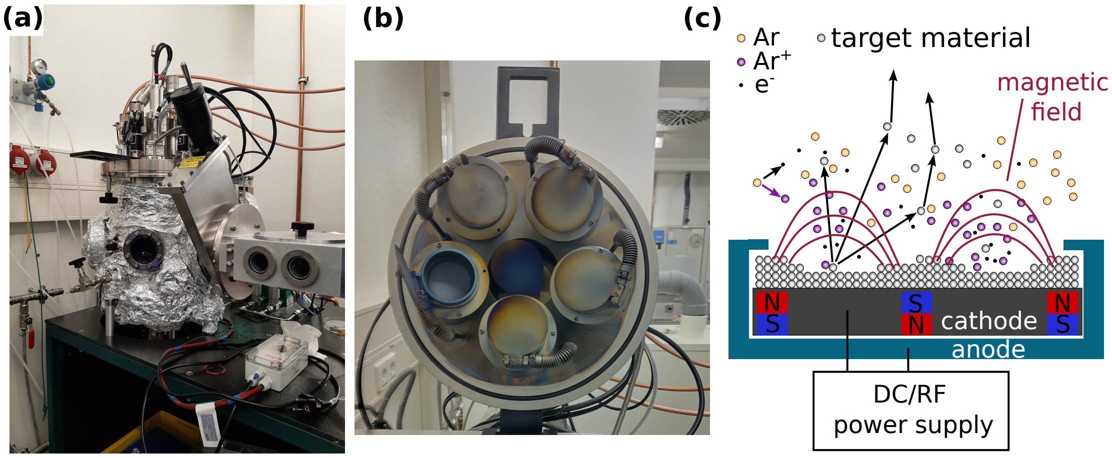

Figure 2.2: (a) AJA International Orion sputtering system used throughout this thesis. (b) Open lid with the five sputtering guns of which one is opened and the built in target visible. (c) Schematic depiction of magnetron sputtering, adapted from Ref. [124].

as well as thermally oxidized silicon wafers (SiO_x, *MicroChemicals*). If not noted otherwise, the crystallographic $\langle 111 \rangle$ direction is perpendicular to the surface of GGG and YAG substrates. The oxide layer thickness of the SiO_x was 500 nm, the crystal orientation of the Si below the oxide being $\langle 100 \rangle$. Both GGG and YAG crystallise in the same cubic space group ($Ia\bar{3}d$) as YIG, and exhibit similar lattice constants a_{GGG} of 1.2376 nm [125] and a_{YAG} of 1.2009 nm [126], respectively, compared to a_{YIG} of 1.2380 nm [127]. The lattice mismatch ϵ to YIG, calculated according to Eq. (2.1), is 0.03 % for GGG and 3.09 % for YAG, meaning that both substrates can be considered as lattice matched. In contrast, the amorphous nature of the thermally oxidized SiO_x means that no template is given for an epitaxial crystallisation. Furthermore, due to the fundamentally different space group ($Fd\bar{3}m$) and lattice parameter (0.543 nm) of the Si crystal, no influence on the crystallisation of the YIG film is anticipated. Therefore, the SiO_x substrates are considered and treated as an arbitrary, non lattice matched substrate.

Prior to deposition, all substrates were subjected to ultrasonic cleaning for five minutes in both acetone and isopropanol, followed by one minute in de-ionized water. The deposition was then performed in a sputtering chamber (Orion, *AJA International*) with a base pressure better than 1.3×10^{-7} mbar. All YIG thin films were deposited at room temperature onto various substrates using magnetron sputtering from a YIG sinter target at 2.7×10^{-3} mbar argon pressure with 80 W RF power. The rate of the deposition was 0.0135 nm/s and the nominal thickness of YIG films investigated in chapter 3 33 nm. The subsequent annealing was carried out under ambient air in a single zone furnace.

The SiO_x layer required in chapter 4 was deposited at 2.7×10^{-3} mbar process pressure, either from a SiO_2 sinter target in Ar atmosphere using 17 sccm flow, at 150 W with a rate of 0.0208 nm/s or reactively from a Si target with 13 sccm Ar and 4 sccm O_2 flow, 100 W and a rate of 0.0172 nm/s.

In this part of the thesis, structural characterisation by X-rays is conducted in a Rigaku Smart Lab diffractometer using Cu K_α radiation. Here, both X-ray diffraction measurements (XRD) as well as X-ray reflectivity (XRR) measurements were performed. XRD yields information about the crystal structure and quality of the thin film [128], whereas XRR can be utilised to investigate the thickness, roughness and density of the YIG thin films [129]. Surface morphology and microstructure were further analysed via a scanning electron microscope (SEM) (*Zeiss*, Gemini SEM) and inbuilt energy-dispersive X-ray spectroscopy (EDX) and electron backscatter diffraction (EBSD) detectors. To that end, the insulating garnet samples were coated with 5 nm carbon and contacted with silver paste, to ensure some conductivity and reduce the drift during imaging and mapping.

The in-situ XRD measurements shown in section 3.5 were performed by Michaela Lammel during a visit at the Université de Bretagne Occidentale in Brest (France). The XRD utilised for this study is an Empyrean XRD from Panalytical with a DHS1100 heating stage from Anton Paar, both provided by F. Michaud and J. Ben Youssef from Brest. As the XRD has no monochromator, the Cu-$K_{\alpha,1}$ and Cu-$K_{\alpha,2}$ peaks appear in the diffraction data (cp. Fig. 3.19(a)).

The magnetic characterisation of the YIG films were studied using the magneto-optical Kerr effect in longitudinal geometry (L-MOKE) in a commercial Kerr microscope (*Evico Magnetics*. With L-MOKE a quick, spatially resolved, magnetic characterisation of the YIG thin films is possible. However, as L-MOKE only qualitatively probes the magnetic hysteresis, superconducting quantum interference device (SQUID) magnetometry was conducted in a Quantum Design MPMS-XL5 SQUID at room temperature to complement the L-MOKE data. To further extend the magnetic characterisation by the linewidth of the Kittel mode as well as the Gilbert damping, broadband ferromagnetic resonance (bb-FMR) experiments were performed via a Keysight N5225B vector network analyser (VNA). To that end YIG films were placed onto a co-planar wave-guide with a 180 µm thick centre line in an electromagnet and measured at room temperature.

To monitor the lateral crystallisation in chapter 4 each sample was investigated using the SEM, where the crystalline region was analysed via EBSD. To complement this data, transmission electron microscopy (TEM) investigations were conducted by Darius Pohl and Alexander Tahn using a JEOL JEM F200 at 200 kV acceleration voltage, equipped with a GATAN OneView CMOS camera for fast imaging. Here, a conducting Au/Pd/Pt layer was deposited on top of the sample, which strives to mitigate charging effects and prevent amorphisation of the YIG during the ion beam processing.

The listed materials and techniques are used for depositing and characterising the planar and non-planar YIG thin films throughout part 1.

Chapter 3

CRYSTALLISATION DYNAMICS OF AMORPHOUS YTTRIUM IRON GARNET THIN FILMS

This chapter details the deposition, characterisation and crystallisation of yttrium iron garnet (YIG) on different planar substrate materials as a first prerequisite for the fabrication of non-planar YIG. All YIG films are obtained by magnetron sputtering at room temperature, which requires a subsequent annealing step to induce crystallisation. The formation of crystalline YIG thin films out of the amorphous phase is monitored and the typical structural and magnetic properties of the so deposited and crystallised YIG thin films characterised.

With this information at hand an extended picture of the crystallisation dynamics of YIG at different temperatures and annealing times will be presented. The results provide a general crystallographic description of the crystallisation process out of the solid phase for YIG thin films and summarize the crystallisation parameters found in the literature. The insights on the crystallisation dynamics allow to define different crystallisation windows depending on the substrate material. The knowledge of these dynamics is crucial for obtaining single crystalline YIG on a mesa structure and lay the foundation for the fabrication of non-planar yttrium iron garnet (YIG).

This chapter is partially reproduced from S. Sailler et al. [6] *"Crystallization dynamics of amorphous yttrium iron garnet thin films", Phys. Rev. Mater.* **8***, 043402 (2024) with the permission of APS Publishing. For this publication I deposited the YIG thin film samples and characterised them structurally and magnetically or advised students in the deposition and characterisation. I then evaluated the data, refined the individual crystallisation windows for YIG on all substrates and modelled the crystallisation behaviour of YIG on each substrate. Lastly, I illustrated the data and wrote the first draft of the manuscript. All authors contributed to the scientific discussion and helped to improve the manuscript.*

3.1 Room temperature sputtering and subsequent annealing

Magnetron sputtering allows to deposit both, amorphous and crystalline YIG thin films, depending on the substrate and its temperature during the sputtering process [65, 66]. Sputter depositing YIG at room temperature results in amorphous films independent on the underlying substrate [48, 65–67, 93–99, 101–107]. In contrast, for the deposition of YIG onto gadolinium gallium garnet (GGG, cp. section 2.4) substrates - a material with a lattice mismatch of $\epsilon = 0.03\,\%$ with respect to the YIG - direct epitaxial growth can be observed for process temperatures of 700 °C and above [65, 66, 130]. This distinct behaviour can be traced back to the thermal energy the system needs to arrange in a crystalline order. However, as the composition of the deposited film is not expected to change with the deposition temperature, obtaining single crystalline YIG from the amorphous material gained via room temperature deposition, is also possible.

The process describing the phase transition of an amorphous solid to its crystalline form while in contact with a crystalline substrate of a similar or identical lattice parameter is called solid phase epitaxy (SPE) [111]. SPE is a subset of epitaxy (cp. chapter 2.4) and describes a crystallisation starting from the interface of a thin film with a matching substrate. As the film is already in a solid form, diffusion and energy minimization are the two driving forces, while the requirements for epitaxy remain the same. To induce a crystallisation via SPE, thermal energy needs to be introduced into the system, which is commonly achieved by a subsequent annealing process of the amorphous film [67, 106]. The SPE process is schematically illustrated in Fig. 3.1(a) and (b). Here, the lattice matched substrates enable the formation of single crystalline YIG via SPE causing a crystallisation front to propagate through the amorphous material [111, 113, 131]. Despite the large lattice mismatch in Fig. 3.1(b), the SPE is still favoured in comparison to nucleation.

In contrast, for substrates with substantial lattice mismatch ($> 3\,\%$) or substrates lacking crystalline order, SPE is not possible due to the lack of a seed. Here, the subsequent annealing process is always necessary, due to the absence of a matching interface [132]. Further, the crystallisation is initiated through the formation of nuclei from which crystallisation proceeds. The initial nucleation typically leads to randomly oriented grains, which continue to crystallise until they encounter either another grain or the physical boundary of the sample. Regardless of whether crystallisation proceeds via SPE or nucleation, the process requires thermal activation at a temperature characteristic of the specific thin film/substrate combination [133].

The annealing process itself is commonly conducted in air [67, 102] or reduced oxygen atmosphere [95, 106, 108, 134] to compensate for potential oxygen vacancies in the YIG lattice. In the case of amorphous YIG thin films deposited via PLD, the subsequent annealing in inert argon atmosphere did not have any deteriorating effects [89]. However, annealing crystalline YIG thin films obtained from sputter deposition in vacuum could be associated with a degradation of typical material characteristic properties like the spin Hall magnetoresistance in YIG/Pt heterostructures [134]. Moreover, the annealing process itself can induce an interdiffusion of the constituent ions of YIG and the respective substrate at the interface [102, 135]. This inter-diffusion can give rise to a magnetic dead layer [86, 102,

Figure 3.1: Influence of the underlying substrate on the crystallisation of amorphous YIG thin films obtained via room temperature magnetron sputtering. The as-deposited (a.d.) films crystallise via solid phase epitaxy (SPE) on lattice matched GGG ($Gd_3Ga_5O_{12}$) (a) and YAG ($Y_3Al_5O_{12}$) (b) (cp. section 2.4). Here, a homogeneous crystallisation front is initiated at the interface between substrate and film and propagates towards the upper thin film border. For non lattice matched substrates as in (c), the formation of nuclei is necessary for a crystal to form, which is thermally activated with the nuclei being randomly oriented. Depending on the substrate either a single crystalline (sc) thin film (a) and (b) or a polycrystalline (pc) YIG film is obtained.

135], as well as an increase of the ferromagnetic resonance linewidth, particularly at low temperatures [88, 136], meaning a deterioration of the YIG quality.

Among the different deposition methods for YIG thin films, each comes with its advantages and limitations. The direct epitaxial growth of YIG films on GGG via LPE requires no post annealing and by that suppresses a Gd interdiffusion, yielding an atomically sharp interface [86]. However, LPE faces challenges in terms of scalability and flexibility. In contrast, vapour based methods like room temperature sputter deposition [48] and atomic layer deposition [78] support wafer-scale fabrication, but require a subsequent annealing step. For efficient processing and minimal interdiffusion of Y and Gd, this annealing step must be carefully optimized towards a minimal time which still yields a fully crystalline film. Naturally, the substrate drastically influences the crystallisation behaviour and the resulting microstructure of the YIG thin film.

However, the concrete dynamics of YIG thin films crystallising during the subsequent annealing step remain insufficiently characterized in the literature. Most reports only provide the annealing temperature and duration which result in a fully crystallised thin film without detailing intermediate stages or the exact mechanism. In the following, the structural and magnetic properties of YIG on three different substrates - GGG, YAG and SiO_x - are characterised. Afterwards, the crystallisation dynamics of YIG on the respective substrates are explored.

3.2 Structural characterisation

The quality of any YIG thin film is inherently dictated by its structural properties. A careful characterisation is critical to ensure that high quality YIG thin films are obtained by deposition plus annealing.

X-ray reflectivity (XRR) measurements were continuously conducted to determine the thickness of the YIG thin films. Each sample was analysed after deposition (as dep) and after the annealing step with the corresponding results for typical YIG films on GGG, YAG and SiO_x being depicted in Fig. 3.2 (a)-(c), respectively. The annealing temperature for YIG films on GGG and YAG were 600 °C and for YIG SiO_x 800 °C, while the annealing time for all films was 48 h. This combination will be used as typical samples for the following evaluations. As confirmed in the following, this annealing time plus temperature are enough to yield fully crystalline YIG films. To access the thickness, a fast Fourier transform (FFT) approach was used as described in Lammel et al. [137]. Here, the oscillatory patterns observed at angles beyond the critical angle θ_c are evaluated by the FFT after the subtraction of a θ^4 background. The resulting, respective FFT amplitudes as a function of film thickness are shown in Fig. 3.2 (d-f). A Lorentzian fit given in Eq. (3.1) is then applied to the FFT data:

$$L(p) = \frac{a}{1 + ((p_{\max} - p)/(w/2))^2} \tag{3.1}$$

Here, p is the position of the variable, i.e., in this case the film thickness, $p_{\max}$ the position of the maximum, a the amplitude and w the full width at half maximum (FWHM).

The fit (solid line) to the FFT data (dotted) with the extracted YIG thickness is shown in Figure 3.2(d-f). Minor variations in the film thickness between the samples can be traced back to deposition in different sputtering processes (cp. Fig. 3.2(d-f)). After the annealing step a reduction in thickness is observed, which is attributed to a compacting of the YIG during crystallisation, resulting in a lower volume. The extracted thickness values are used to monitor the sputtering process throughout the chapter and will be needed for the quantification of the amount of crystalline YIG particularly on GGG substrates as described in section 3.4.

X-ray diffraction (XRD) was further employed to access the structural properties of YIG films using a symmetric $\theta - 2\theta$ scan. The results for again nominally identical samples are depicted in Fig. 3.3(a)-(c). The as deposited YIG films only exhibit a peak from the respective substrate, as indicated by the grey dashed lines. After annealing, additional peaks emerge in the spectra: On GGG so called Laue oscillations appear, signalizing high structural quality (cp. Fig. 3.3 (a)). On YAG a distinct diffraction peak becomes visible (cp. Fig. 3.3 (b)), whereas on SiO_x, no peaks attributable to YIG can be observed. As no epitaxial growth is expected (see section 3.1), a section including the nominally highest intensity YIG peak of (420) is plotted. Here, the only peak in Fig. 3.3(c) at 32.96° is visible both in the as deposited and the annealed film and further is too sharp to stem from the film. This peak corresponds to the forbidden Si (200) peak due to detour excitation in the substrate [138]. This observation is in contrast to literature reports, where polycrystalline

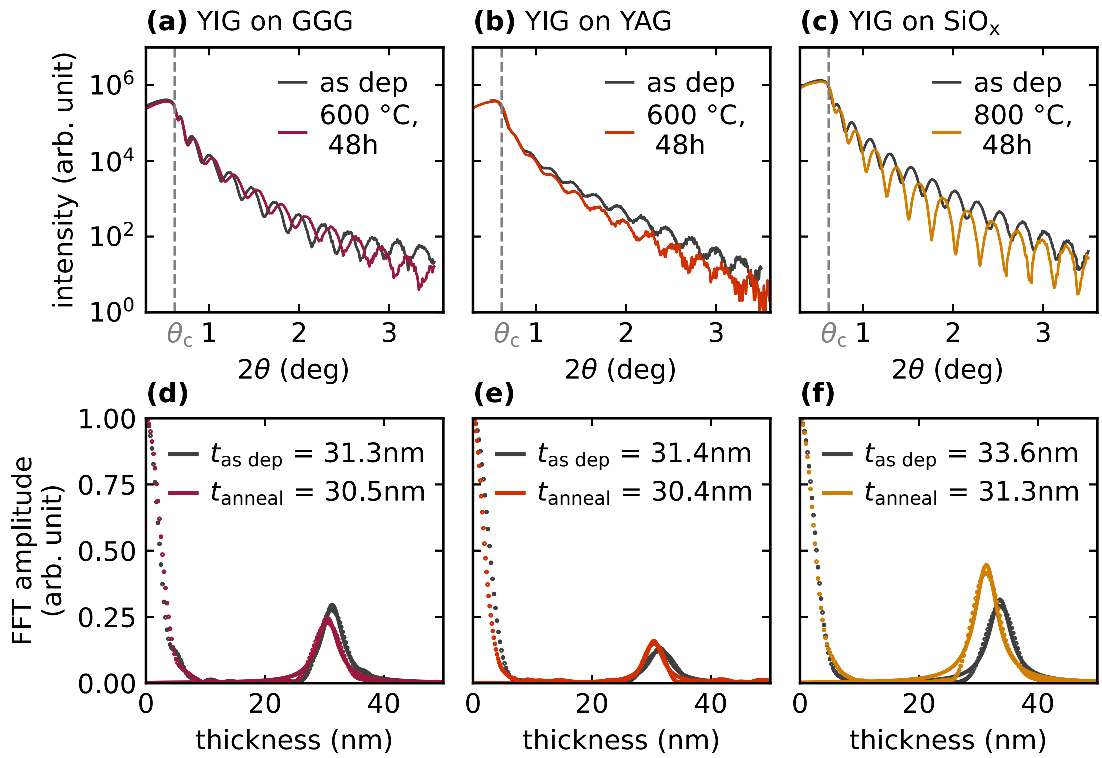

Figure 3.2: X-ray reflectivity (XRR) data of YIG thin films on GGG (a),(d), YAG (b),(e) and SiO_x(c),(f). The as deposited films are depicted in black, whereas the annealed films are coloured. The annealing temperature of YIG on GGG and YAG was 600 °C and on SiO_x 800 °C and the annealing time for all 48 h. (a)-(c) depicts the measured intensity versus the 2θ angle, while (d-f) show the result of the fast Fourier transform (FFT) analysis. A Lorentzian fit (solid line) to the FFT data (dotted) then yields the film thickness. A decrease in YIG film thickness is observed after the annealing step, which can be understood as a compacting due to ordering as well as crystallisation.

YIG was reported on SiO_x using lower annealing temperatures than the 800 °C for 48 h in Fig. 3.3(c) [67, 95, 132]. However, these films were significantly thicker as the ones investigated here. Furthermore, no peaks could be resolved for any annealing time and temperature pair for 30 nm thick YIG films. Thus, the YIG layer on SiO_x is not expected to remain amorphous, as confirmed in the subsequent analysis and later via the magnetic properties in chapter 3.3.

To obtain structural information from YIG on SiO_x the complementary structural technique of electron back scatter diffraction (EBSD) was carried out. With this technique Kikuchi patterns are detected and later evaluated. The Kikuchi patterns form from electrons whose last scattering process was Bragg diffraction, with a typical Kikuchi pattern being depicted in Fig. 3.4(a). Each of the observed lines corresponds to a lattice plane with the spacing between the lines being correlated to the diffraction angle, i.e., the crystal structure. Intersecting lines form points which represent a crystal orientation. A measured

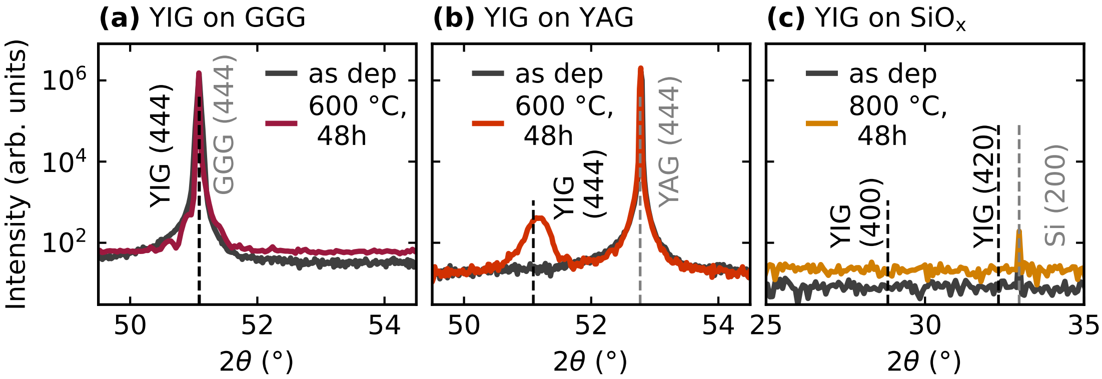

Figure 3.3: (a)-(c) XRD investigation of YIG on the three exemplary substrates as before. The literature positions of substrate and YIG are indicated by the grey and black dashed lines [125–127, 139]. For the as deposited YIG only the substrate appears in the diffraction data. Upon annealing, crystalline YIG becomes visible on GGG as Laue oscillations (a) and a peak on YAG (b). No feature stemming from YIG can be observed on SiO$_x$, where the additional peak marked with Si(200) comes from a detour excitation from the substrate.

Kikuchi pattern is indexed as seen in Fig. 3.4(b), which yields the orientation of the crystal. This structural information comes from lattice planes close to the surface with the reported signal depth being 10 to 40 nm [140]. A major advantage of this technique is the nanometre resolution, which will become important in the next chapter 4. Note, that instead of EBSD an analysis via grazing incidence XRD in theory would also be possible to investigate YIG on SiO$_x$, but was omitted due to the advantageous local resolution of EBSD.

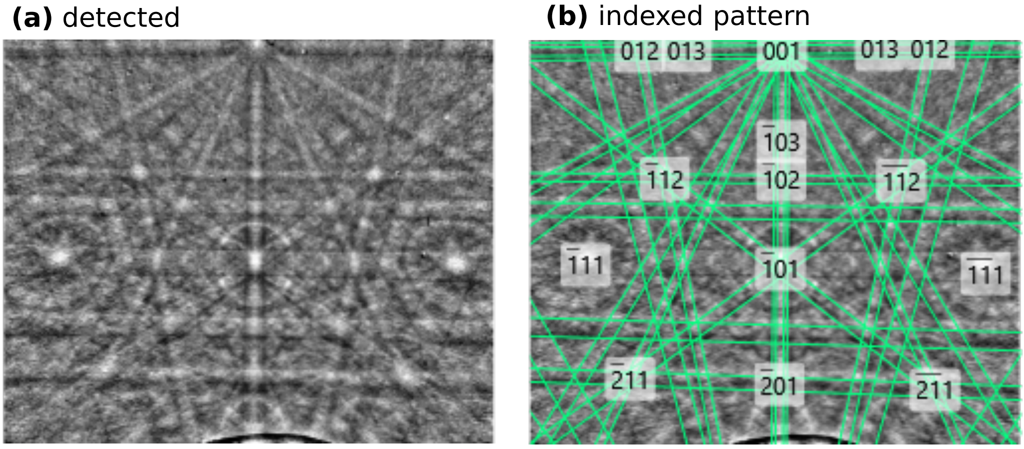

Figure 3.4: (a) Detected and (b) indexed Kikuchi pattern of a YIG ⟨001⟩ crystal measured via electron backscatter diffraction (EBSD).

Investigating the as deposited YIG films via EBSD did not yield any Kikuchi patterns

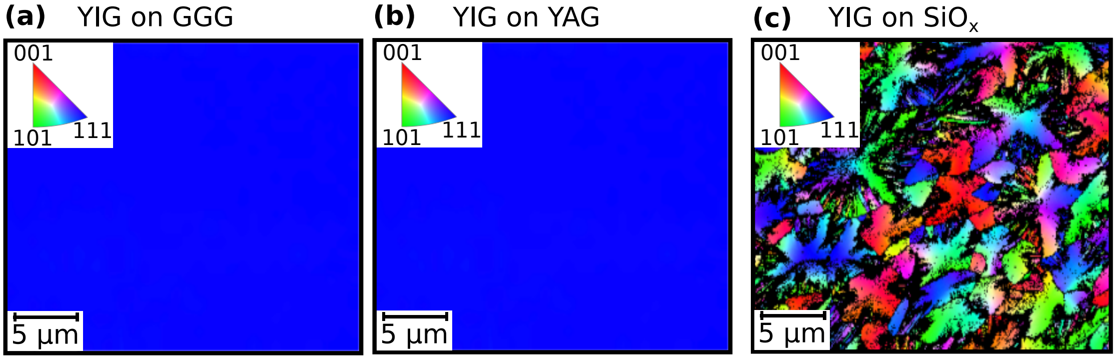

Figure 3.5: (a)-(c) EBSD investigation of the annealed YIG thin films already investigated via XRD in Fig. 3.3. Depicted is the inverse pole figure along the surface normal direction extracted from the Kikuchi patterns for a direct comparison with XRD.

on any of the three substrates. This observation means that the as deposited films are indeed amorphous upon deposition. Furthermore, this confirms the information depth of several nanometres and that any patterns observed from annealed samples originate from the YIG film and not the lattice matched substrates of GGG and YAG.

Figure 3.5(a)-(c) then depicts the EBSD results for the annealed YIG on GGG, YAG and SiO_x, respectively. The analysed samples are those already investigated via XRD in Fig. 3.3. For a direct comparison, the inverse pole figure depicts the crystallographic orientation along the surface normal direction. For YIG on GGG (cp. Fig. 3.5(a)) and YAG (cp. Fig. 3.5(b)) a single colour is extracted over the whole area, which confirms a crystallisation along the $\langle 111 \rangle$ direction, consistent with the findings from XRD (cp. Fig. 3.3). The results corroborate a crystallisation via SPE from the substrate and further confirm EBSD as a suitable method.

In contrast, YIG films on SiO_x exhibit a variety of colours corresponding to a variety of orientations (cp. Fig. 3.5(c)). The random nucleation observed yields a polycrystalline microstructure which is accompanied by distinct cross shaped areas, indicating anisotropic crystallisation velocities. This preferential crystallisation along $\langle 110 \rangle$ or higher indexed orientations like $\langle 112 \rangle$, aligns with earlier findings for YIG and other rare-earth garnets [93, 141–143] as well as PLD grown bismuth iron garnet [87].

Lastly, the absence of YIG peaks in the XRD is now discussed, which presumably stems from a limited coherent scattering volume, as discussed before [100, 103, 109]. A typical cross shaped grain contributing to the diffraction intensity of YIG on SiO_x has an estimated volume of $0.5\,\mu m^3$, derived from a lateral size of about $15\,\mu m^2$ (as obtained from SEM and EBSD, Fig 3.5(c)) and a YIG thickness of 32 nm (as extracted via XRR, Fig. 3.2). In contrast, in a single crystalline YIG thin film, the whole area contributes to one peak with a six orders of magnitude larger volume, in comparison to one grain on SiO_x, of $7 \times 10^5\,\mu m^3$. Another effect influencing the intensity of the data, is X-ray fluorescence (XRF), which the Cu-K_α induces in iron and its oxides. The XRF of Fe causes a larger background in the diffracted data with a reduced intensity in the peaks, which is why typically Co tubes are used for the investigation of Fe based compounds [144, 145]. In consequence, the diffraction intensity of the polycrystalline YIG on SiO_x is insufficient to generate a discernible peak for 30 nm thick films. This interpretation is corroborated by the observation of a YIG (420) peak in films with a thickness of 40 nm or greater using Co-radiation in Dresden.[1]

In conclusion, the structural properties of YIG on GGG and YAG can be probed and analysed via XRD and XRR, where a high crystalline quality was found for YIG on GGG. With EBSD, a method for the quantitative assessment of the crystalline fraction for YIG on SiO_x with high spatial resolution has been established. These methods lay the basis for the extraction of the crystallisation window in section 3.4. Before coming to that, the magnetic properties of the YIG thin films are now presented.

3.3 Magnetic characterisation

The structural quality, as introduced beforehand, closely influences the magnetic properties of the YIG thin films. As the magnetic properties are important for the technological relevancy [57, 146], a profound magnetic characterisation is also necessary, to confirm the excellent properties known from YIG, as introduced in section 2.1.

A first magnetic characterisation of the YIG thin films was carried via the longitudinal magneto-optical Kerr effect (L-MOKE) as seen in Fig. 3.6(a)-(c). The same samples as in the XRD and EBSD in the previous section were investigated here, allowing for a direct comparison. Similar to the structural characterisation the L-MOKE measurements enable a clear distinction between as deposited (amorphous) and annealed (crystalline) YIG films. In the as deposited state, the amorphous YIG exhibits a linear L-MOKE response, which is

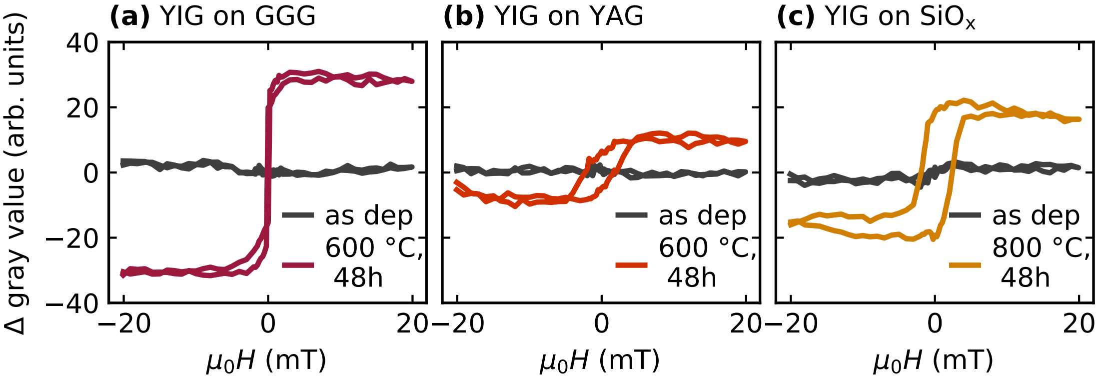

Figure 3.6: Kerr microscopy data taken via L-MOKE on a central spot of the thin film for YIG on (a) GGG, (b) YAG and (c) SiO_x. Similar to the structural properties, no signal attributed to the YIG can be observed in the as deposited films, whereas a hysteresis opens when probing an annealed film. The change in gray value corresponds to the magnetisation of the YIG thin film, which differs significantly between the three substrates.

---

[1] *These measurements were performed by H. Schlörb.*

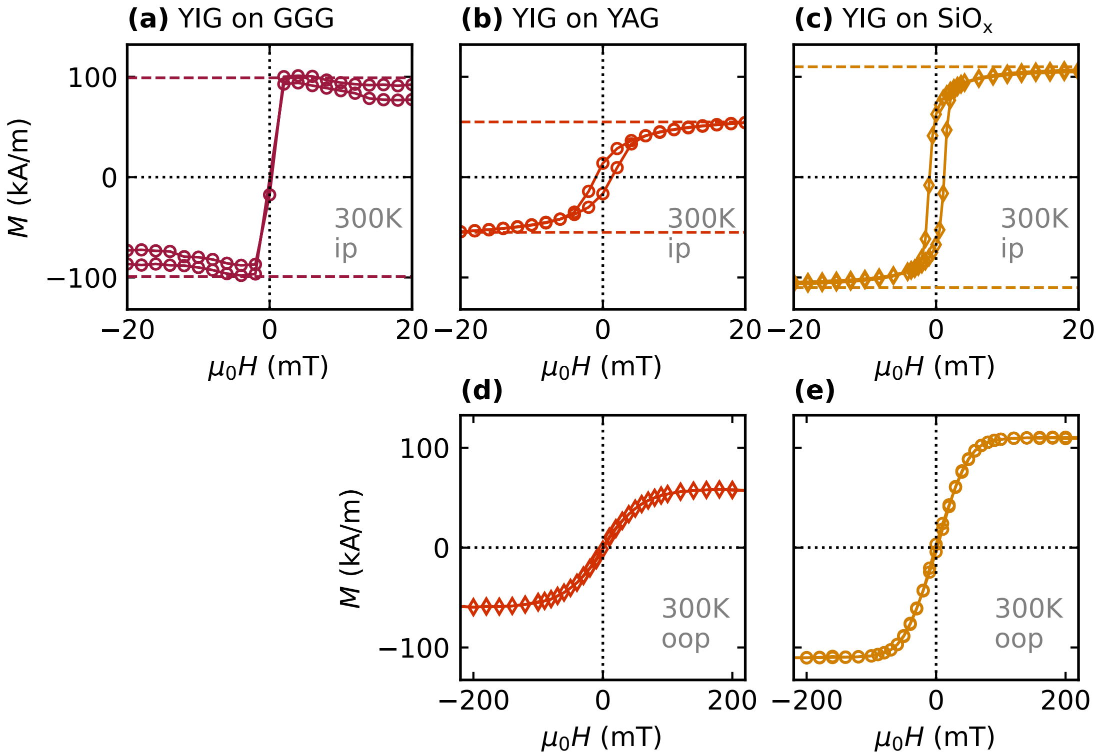

Figure 3.7: Superconducting quantum interference device (SQUID) magnetometry data of YIG films annealed for 48 h at 600 °C on GGG (a) and at 800 °C for YIG on YAG (b,d) and SiO$_x$ (c,e). All data is taken at 300 K and a linear background caused by the substrate removed. (a)-(c) depicts the response of YIG on each substrate for the external field applied in plane (ip), whereas (d,e) depicts the respective out of plane (oop) values. YIG on GGG could not be resolved in the oop configuration due to the large paramagnetic background caused by the GGG. The gray lines act as a guide to the eye, whereas the coloured lines indicate the respective, extracted saturation magnetisation.

subtracted in the following. After annealing the now crystalline YIG develops a magnetic hysteresis on all substrates, indicating the onset of long ranging magnetic order. Among the substrates, the sharpest hysteresis loop is observed for YIG on GGG and the broadest for YIG on SiO$_x$(cp. Fig. 3.6(a)-(c)). The polycrystalline nature of YIG on SiO$_x$ naïvely suggests that domains with differently oriented easy axes exist, resulting in an increased coercive field. This behaviour is reflected in our data and consistent with literature reports [49, 95, 101, 147]. Specifically, YIG films on GGG typically exhibit coercive fields below 0.1 mT [49, 101] whereas YIG on SiO$_x$ is reported to show significantly larger values of 2.2-3 mT [95, 147]. The emergence of an hysteresis upon annealing confirms the formation of a magnetic phase, regardless of the substrate.

However, L-MOKE falls short in providing absolute magnetisation values, as only a change in gray value is measured. Hence, SQUID magnetometry data is included in Fig. 3.7. Measured were YIG films on all three substrates both in out of plane (oop) and in

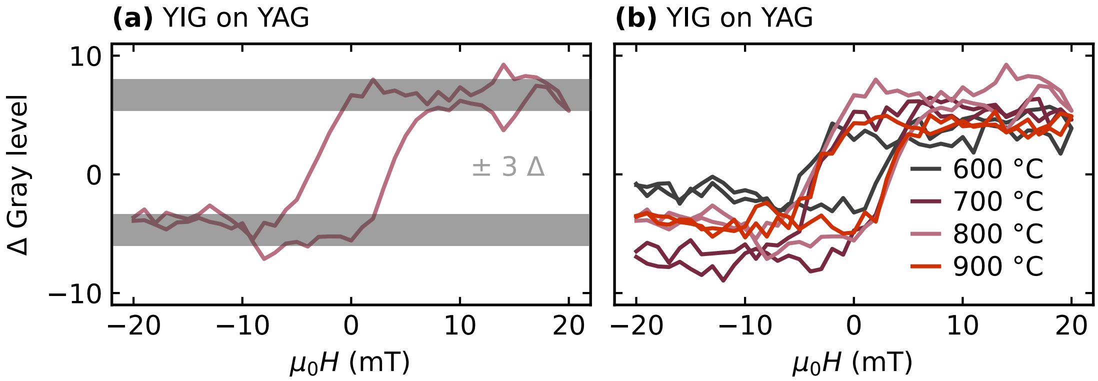

Figure 3.8: (a) L-MOKE data for a YIG film on YAG annealed at 800 °C for 4 h. Next to the open hysteresis a change in gray value of ± 3 can be seen as a noise level (shaded in gray). (b) Comparing the hysteresis loops of four nominally identical samples annealed at different temperatures shows no significant changes in absolute gray level or coercive field. All samples are expected to be fully crystalline, as later discussed, see section 3.5

plane (ip) geometry, with ip and oop referring to the orientation of the external magnetic field relative to the film plane. The oop magnetisation of YIG on GGG could not be resolved due to the strong paramagnetic background of the substrate. From the ip measurements saturation magnetisations of 99 kA/m, 55 kA/m and 110 kA/m for YIG on GGG, YAG and SiO_x, respectively, can be extracted (cp. Fig. 3.7(a)-(c)). All samples show an in plane magnetisation with curve shapes similar to those observed via L-MOKE (cp. Fig. 3.6).

Notably, the saturation magnetisations of all films fall below the theoretical bulk value of 143 kA/m at room temperature [73]. Generally, films with thicknesses below 100 nm are often reported to exhibit a lower saturation magnetisation compared to the bulk value [148, 149]. One reason can be a so called magnetic dead layer, which effectively lowers the magnetisation. This layer can form during the annealing step by interdiffusion at the interface and occupy 4-6 nm of the film [86, 102, 135]. Therefore, a 6 nm magnetic dead layer in a 30 nm film reduces the saturation magnetisation by 20 %. Lastly, changes in the composition could also significantly alter the magnetic properties and could stem from anisotropic sputter yield during the deposition. Here, no changes in composition could be resolved using XRD when sputtering under identical conditions. This observation is corroborated by the reproducible results obtained in the following.

The saturation magnetisation and the coercive fields could be reproduced in multiple samples and for different annealing temperatures. This observation is also independent on the substrate and measuring technique, i.e., MOKE and SQUID magnetometry. Exemplarily shown in Fig. 3.8 is the L-MOKE response of YIG films on YAG annealed at different temperatures for 4 h. The 800 °C curve is present in Fig. 3.8(a) and (b) for an easier comparison. Deducted from the measurements is a noise level of ±3 in gray value. Within this noise, no significant changes in the absolute gray level in Fig. 3.8(b) can be observed. This observation suggests, that the magnetic properties of the YIG thin films on one particular substrate are - once fully crystallised - mostly independent on the annealing

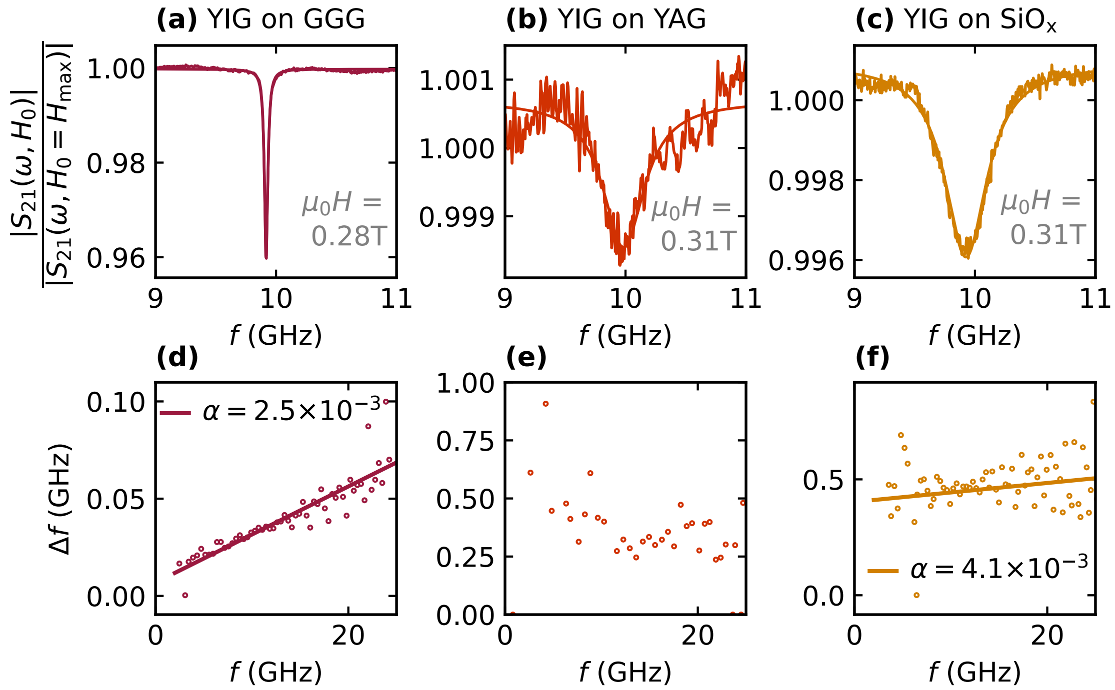

Figure 3.9: Broadband ferromagnetic resonance (bb-FMR) data for the typical YIG films annealed for 48 h at 600 °C for GGG (a,d) and 800 °C for YAG (b,e) as well as SiO_x (c,f). Panel (a-c) exemplary show the characteristic FMR response for YIG on each substrate. Here, the transmission parameter S_{21} is plotted over the frequency of the microwave field f. Each measurement is conducted at a fixed external magnetic field B_{ext}, which was chosen to show resonance frequencies around 10 GHz. For visibility, S_{21} is normalised with respect to the value measured at the highest B_{ext}. Each resonance curve is then fit by a Lorentzian function (see Eq. (3.1)) to extract the full width at half maximum (FWHM) which is taken as the linewidth Δf. Panels (d-f) depict the extracted behaviour of the linewidth as a function of the frequency of the resonance f. A linear fit was applied to the data to extract the Gilbert damping α from the slope. Reasonable values can be extracted for YIG on GGG and SiO_x [97, 134, 136], whereas on YAG no meaningful Gilbert damping could be obtained. The latter is due to the pronounced inhomogeneous broadening of the linewidth at low frequencies, stemming from the lower crystalline quality of YIG film on YAG (e) [150].

temperature. This holds true for the here tested temperatures of up to 900 °C and will be further investigated in the following.

The dynamic magnetic properties of YIG thin films are of utmost importance for technological application [57, 146]. These properties can be probed using broadband ferromagnetic resonance (bb-FMR), which is therefore conducted for the sputtered YIG films. Figure 3.9 displays the results for YIG on the three exemplary substrates at the typical annealing temperature and time combinations used previously (GGG, YAG: 600 °C, 48 h and SiO_x: 800 °C, 48 h). In the experiment, the transmission (scattering) parameter S_{21} is measured as a function of external magnetic field B_{ext} and frequency f of the applied microwave field. As the resolution in f exceeds that of B_{ext} the consecutive analysis of the linewidth Δf and the Gilbert damping α is conducted in the frequency domain.

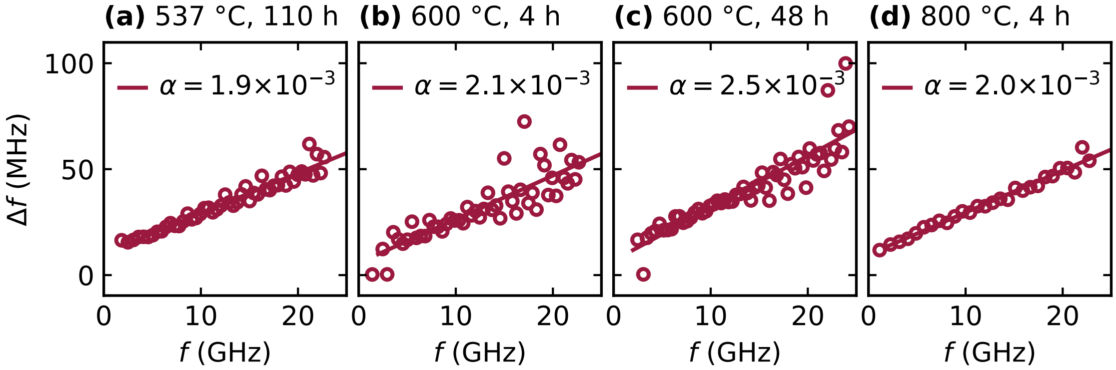

Figure 3.10: (a)-(d) Extracted linewidth Δf versus resonance frequency of YIG films on GGG with different annealing parameters as indicated above each figure. A linear fit is applied to the data to extract the Gilbert damping α. Here, no significant dependence on the annealing time nor on the annealing temperature can be observed.

The top row of Fig. 3.9(a)-(c) depicts the normalised S_{21} parameter for YIG on all substrates versus f, with an applied external magnetic field B_{ext} of roughly 0.3 T. By choosing this magnetic field, the data is comparable to typical X-Band resonators. To enhance the visualisation, the S_{21} parameter is normalized with respect to the data at the highest B_{ext}. Widely different curve shapes can be observed for YIG on the different substrates, with a distinct dip appearing at the resonance frequency on all substrates, as seen in Fig. 3.9(a)-(c). To evaluate the dip, a Lorentzian function, as introduced earlier with Eq. (3.1), is fitted to the data where the linewidth Δf is then extracted as the full width at half maximum (FWHM). The linewidth for YIG on GGG is the narrowest with $\Delta f_{\mathrm{GGG}} = 32.7\,\mathrm{MHz}$ ($\Delta\mu_0 H_{\mathrm{GGG}} = 1.2\,\mathrm{mT}$), while the amplitude $a_{\mathrm{GGG}} = 0.041$ is the highest (Fig. 3.9(a)). In contrast, YIG films on YAG (Fig. 3.9(b)) and $\mathrm{SiO_x}$ (Fig. 3.9(b)), show significantly broader resonance dips with the linewidths being $\Delta f_{\mathrm{YAG}} = 414.7\,\mathrm{MHz}$ ($\Delta\mu_0 H_{\mathrm{YAG}} = 14.8\,\mathrm{mT}$) and $\Delta f_{\mathrm{SiOx}} = 424.9\,\mathrm{MHz}$ ($\Delta\mu_0 H_{\mathrm{SiOx}} = 15.2\,\mathrm{mT}$) and respective amplitudes in the resonance of $a_{\mathrm{YAG}} = 0.002$ and $a_{\mathrm{SiOx}} = 0.005$. The here obtained linewidths align well with the previous structural properties (see section 3.2) and with the existing literature, where YIG films on GGG show the highest crystal qualities and narrowest linewidths [88, 100, 103, 107, 150]. The broader values observed for YIG on YAG and YIG on $\mathrm{SiO_x}$ have previously been attributed to a lower film quality [103, 150]. Here, the connection to the structural properties becomes evident: as the crystallisation of YIG via SPE on GGG results in an almost perfectly single crystalline film, the radio frequency response is uniform over the hole film, resulting in the narrow linewidth. Due to the large lattice mismatch with YAG, large strain and defects were reported to be the cause of the broadening of the linewidth for YIG films on YAG [150]. Later, rocking curves for YIG films on YAG showing a large mosaicity of the crystal will be discussed, see section 3.4, Fig. 3.12. Similarly, for YIG on $\mathrm{SiO_x}$ the different crystal orientations of the polycrystalline film contribute differently to a broader dip.

The Gilbert damping parameter α can be extracted out of the evolution of the linewidth Δf over multiple frequencies, as depicted in Fig. 3.9(d-f). The slope of a linear fit to the data yields the α with the respective values detailed in the plot. For YIG on GGG a value for α of 2.5×10^{-3} is extracted (cp. Fig. 3.9(d)), which is in good agreement with literature values for sputtered YIG films [97, 134, 136]. For YIG on YAG on the other hand no Gilbert α could be extracted (cp. Fig. 3.9(e)). Especially at low frequencies a large inhomogeneous broadening of the linewidth can be observed, which was previously reported and traced back to strain stemming from the large lattice mismatch [150]. Lastly, on SiO_x, YIG exhibits a larger Gilbert damping of 4.6×10^{-3} (cp. Fig. 3.9(f)). The lowest damping combined with the narrow linewidth make GGG the preferred substrate for YIG thin films in the literature [48–50, 86, 88, 97, 106, 136].

Similar to the L-MOKE (Fig. 3.8), the influence of the annealing temperature onto the FMR properties is discussed below. Due to the significantly better properties, this analysis is conducted on YIG films on GGG, where all films are confirmed to be fully crystalline via XRD. Fig. 3.10 depicts the evaluated bb-FMR data for YIG on GGG. Across different annealing conditions ranging from 537 °C to 800 °C and 4 h to 110 h no significant change in Δf or α can be observed. These findings suggest that an ideal stoichiometry of the YIG is a crucial parameter for films with low damping, while annealing time and temperature are of secondary importance. As demonstrated recently in Ref. [130], the optimisation of YIG films towards a wanted magnetic property lies in the deposition process itself and by that the composition.

Optimising the deposition process itself, however, is not straight forward. Due to the manifold of different parameters, larger series would be needed which could not be performed in the shared sputtering system. Varying the parameters given in section 3.1 only yielded samples with a worse Gilbert damping. The only parameter exhibiting a clear trend within these series was the sample position on the sample holder. Changing the position while keeping the sample holder static, i.e., no rotation, led to an improvement of α, which was, however, not pursued further due to the inhomogeneity of the thickness over one sample.

Importantly, however, the magnetic properties do not change with the annealing parameters. This observation opens the path to analyse the crystallisation behaviour while maintaining the magnetic properties of the individual films.

3.4 Onset of crystallisation and extraction of the crystalline percentage

The previously described structural and magnetic characterisation is the foundation to investigate and describe the crystallisation behaviour. With these methods YIG films can be distinguished as amorphous, partly and fully crystalline and the evolution of the crystallinity monitored over time. The most suited methods for tracking the crystallisation are the diffraction based techniques or the L-MOKE due to their ability for a quick quantification of the amount of crystalline material.

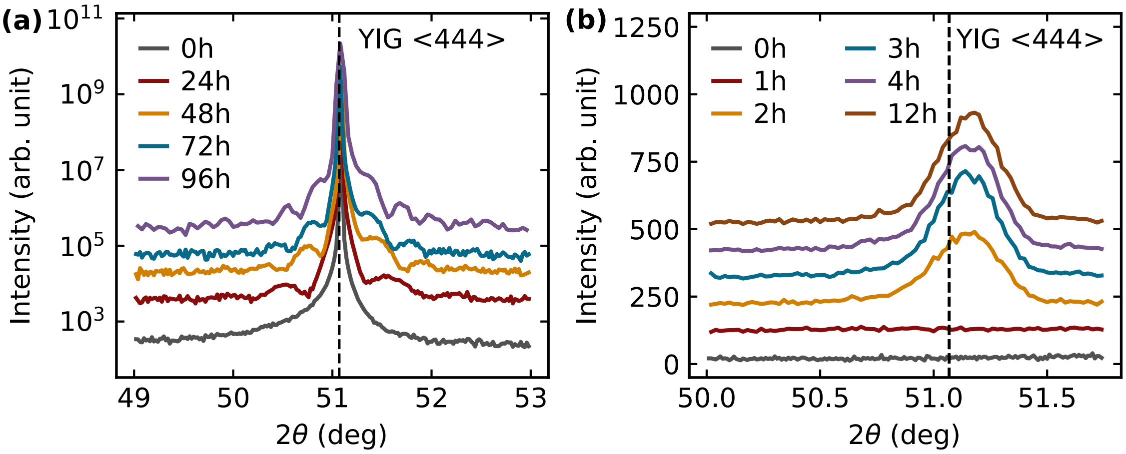

Figure 3.11: Observation the crystallisation of YIG on (a) GGG at 537 °C and (b) YAG at 600 °C. (a) After deposition (0 h) no intensity of the YIG can be observed. For YIG on GGG, Laue oscillations start to appear with an increasingly tighter spacing, signalizing more diffracting planes. The spacing of the diffracting planes can be utilised to extract the thickness of the YIG. By comparing the thickness of contributing diffraction planes with the thickness of the whole film as extracted by XRR (cp. Chapter 3.2), the percentage of crystalline YIG can be extracted. (b) For YIG on YAG, the area under the peak increases until the film is fully crystalline. Then even further temperature treatment does not cause a difference in the peak (further confirmed with Fig. 3.16). By extracting the area of the peak via Eq. (3.3) and normalising it with the saturated area, the percentage is extracted.

Initially, the quantification of crystalline YIG will be described using structural characterisation methods. Due to the different behaviour of the YIG, see section 3.2, the percentage of crystalline YIG is extracted differently for each substrate:

On GGG, the Laue oscillations (cp. Fig 3.11(a)) are evaluated to calculate the degree of crystallinity. With increasing annealing temperature, the spacing of the secondary maxima becomes narrower, which in turn represents an increase of crystallised material. Since the Laue oscillation frequency is directly correlated to the number of coherently diffracting lattice planes, the amount of crystalline YIG can be extracted, which is described via Eq. (3.2) [151]:

$$I(Q) \propto \frac{\sin(\frac{N}{2}Qa)^2}{\sin(\frac{1}{2}Qa)^2} \tag{3.2}$$

Here, I is the intensity, Q the scattering vector and N the number of coherently diffracting planes with a lattice plane spacing a. The scattering vector is connected to the 2θ angle of the XRD measurements via $Q = 2\pi/d$, where d is the lattice spacing. Using Bragg's law, Q can then be calculated as $(4\pi/\lambda) \times \sin(\theta/2)$. λ describes the wavelength of the X-rays, which for $\mathrm{Cu}_{\mathrm{K},\alpha}$ equals 0.154 056 nm. The periodicity of the Laue oscillations then follows $\Delta Q = \frac{2\pi}{Na}$. By evaluating the 2θ angles of the secondary maxima, the thickness of the interfering lattice planes can be calculated [151]. Together with the absolute film thickness

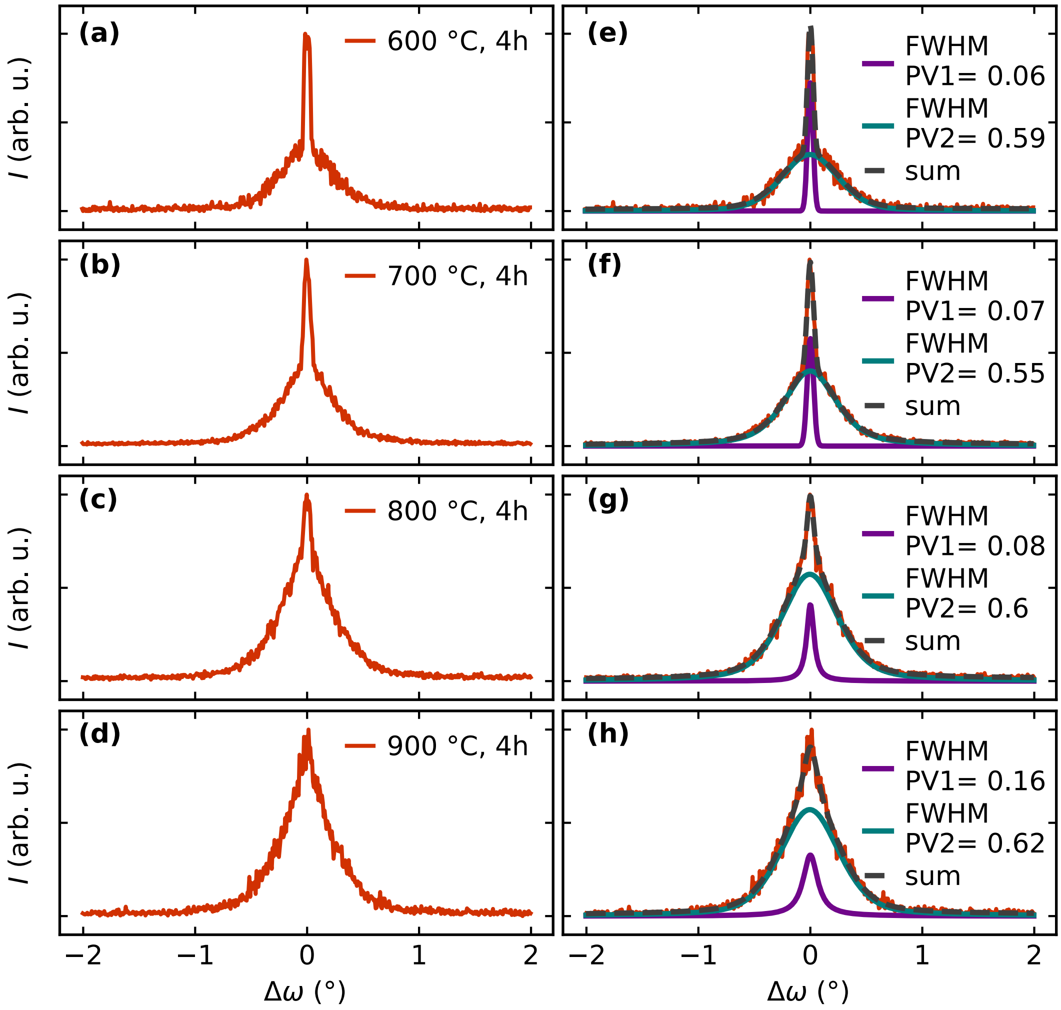

Figure 3.12: (a-d) Rocking curves of YIG thin films on YAG annealed for 4 h at increasing temperatures. The intensity I is depicted versus the change of the incident angle $\Delta\omega$. The left column shows the raw data, which exhibits a sharp peak as well as a broader one. To fit the data, two pseudo-Voigt (PV) functions were utilised. The first sharp peak modeled by PV1 corresponds to high quality YIG, which grew epitaxially from the substrate. The broader peak (PV2) is attributed to a region of high mosaicity. The sum of both pseudo Voigts exactly resembles the measured curve in (e)-(h).

obtained via XRR (section 3.2, Fig. 3.2) the progress of the crystallisation of YIG on GGG can be monitored.

On YAG, the amount of crystalline YIG is obtained from the Bragg peak, as depicted in Fig. 3.11(b). To access the area under the peak, a pseudo Voigt function is fit to the data, as given by Eq. (3.3):

$$PV(p) = v \times \left[\frac{a}{1+x^2}\right] + (1-v) \times \left[a \times \mathrm{e}^{-(\ln(2))x^2}\right] \tag{3.3}$$

The pseudo Voigt is a weighted sum of a Lorentzian and Gaussian curve shape, with x being $x = \frac{p - p_{\max}}{w/2}$, a being the amplitude, p the position, $p_{\max}$ the position of the maximum, w the full width at half maximum (FWHM) and v a weighing factor $\in [0,1]$. By integrating the fit, the area under the peak is extracted. With each annealing step the area under the peak, i.e., the amount of crystalline YIG increases until reaching a maximum, where the area saturates as the film has become fully crystalline, see Fig. 3.11(b). This saturated value is then taken to normalise the area, giving the percentage of crystalline YIG after each annealing step.

However, by integrating the area under the peak of the symmetric θ-2θ scan, not all crystalline YIG is captured, as this scan is only sensitive to the out of plane lattice constant. This is illustrated nicely by the rocking curves in Fig 3.12. Here, the 2θ value is kept fix and only the ω value changed, with $\Delta\omega = 0°$ being the value seen in the symmetric θ-2θ scan. All samples in Fig 3.12 stem from the same sputtering process, exhibit the same thickness of 30 nm and were annealed for 4 h at different temperatures, ranging from (a) 600 °C to (d) 900 °C. Especially in Fig 3.12(a) and (b) two peaks can be seen in the rocking curves. The sharper peak corresponds to a highly crystalline area with low mosaicity, whereas the broader peak stems from an area of high mosaicity, i.e., slightly titled crystals with respect to the $\langle 444 \rangle$ direction. With increasing annealing temperature, the rocking curves broaden continuously, indicating an increase in mosaic spread [128].

Using the sum of two pseudo-Voigt (PV1 + PV2) functions allows to fit and model the two areas in the YIG film. Especially the FWHM values support the hypothesis of increasing mosaicity as these values increase in both PV functions: At 600 °C the FWHM value is 0.06° for PV1 (sharp peak) and 0.59° for PV2 (broad peak), which increases to 0.16° for PV1 and 0.62° for PV2 at 900 °C. This mosaic spread is not captured in the extraction of the crystalline percentage, likely resulting in an underestimated value of crystalline YIG. Only for the fully amorphous and crystalline films this poses no problem. Hence, for the extraction of the crystalline percentage for YIG on YAG, especially towards higher temperatures, the mosaic spread needs to be kept in mind, as discussed later within this section.

On SiO_x, acting as an arbitrary substrate, EBSD mappings were taken and evaluated to extract the percentage of (poly)crystalline YIG. Exemplarily, a SEM analysis of a YIG film annealed for 8 h at 700 °C is depicted in Fig 3.13, with (a) showing the SEM image of the Inlens detector and (b) the EBSD mapping of the same region. In Fig 3.13(a), circular regions exhibiting a darker contrast are visible across the image along with a few rectangular regions. The latter arise from adjusting the focal plane at that spot. The subsequent EBSD mapping in Fig 3.13(b) confirms that the circular regions correspond to (poly)crystalline YIG with small individual crystallites, while the surrounding area remain amorphous. This observation suggests a nucleation driven crystallisation (cp. section 3.1, Fig. 3.1), starting from a nucleation centre in the middle of a circle. The crystallisation then proceeds outward radially until the crystalline areas reach a boundary, i.e., another crystal or the sample boundary, eventually forming a fully crystalline film. The uniformity of the circular regions implies that the temperature allows stable nuclei to form and that the crystallisation velocity is similar along all directions.

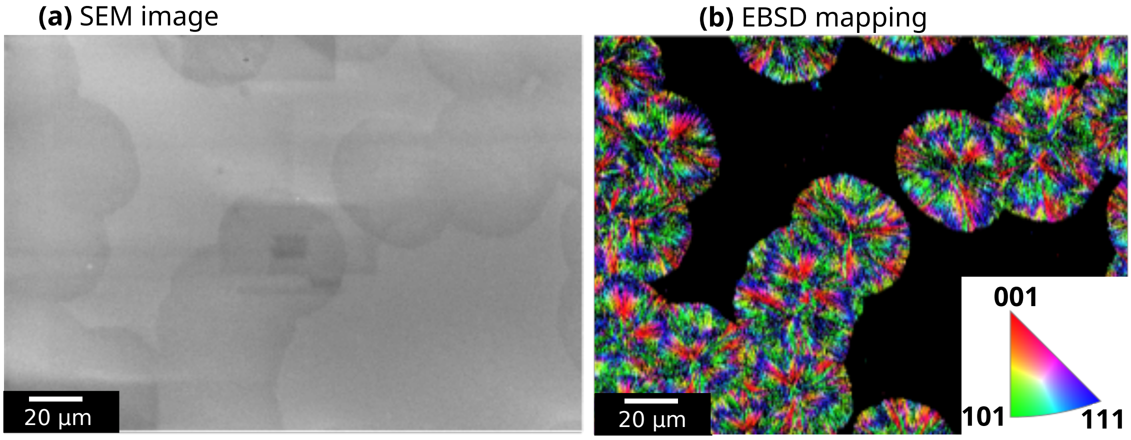

Figure 3.13: (a) SEM image as captured by an In-lens detector and (b) processed EBSD mapping of a YIG film annealed at 700 °C for 8 h. The rectangular shapes in (a) stem from adjusting the focus planes, whereas the circular regions indicate the crystalline phase. The EBSD mapping in (b) confirms the partly (poly)crystalline YIG in the circular regions and non-crystalline YIG around. The typical EBSD colour code represents the orientation of the individual crystallites parallel to the surface normal direction.

The EBSD mapping now provides a means to quantify the amount of (poly)crystalline YIG on SiO_x. Evidently, the YIG film in Fig. 3.13(b) is only partly crystalline, whereas the YIG film annealed at 800 °C for 48 h in Fig. 3.5(c) appears to be fully crystalline. By monitoring the amount of crystallites, as quantified by the percentage of detected Kikuchi patterns, the percentage of crystalline YIG is extracted. Importantly, the magnification and step size of the SEM rasterising needs to be identical for each sample or annealing step.

Comparing the two YIG films on SiO_x reveals that while the individual crystallites of YIG are of comparable size the microstructure differs. The sample annealed at 800 °C (Fig. 3.5(c)), has much smaller grains due to the elevated temperatures and the consequently easier nucleation in comparison to 700 °C (Fig. 3.13(b)).

With Fig. 3.11 and Fig. 3.13(b) a means to quantify the percentage of YIG on each substrate has been found. This will be the preferred method, as it allows for an unambiguous determination of the amount of crystallised YIG. However, knowing that the crystalline, ferrimagnetic phase is indeed YIG, similar results to the structural methods can be obtained via L-MOKE, as presented now.

Fig. 3.14(a) depicts a Kerr-microscopy image of a partly crystallised YIG on SiO_x sample with an external magnetic field of 20 mT applied. Similar to the previous SEM image (cp. Fig. 3.13(a)), a circular gray shaded contrast arises. In order to analyse the areas with respect to the contrast, different regions of interest (ROI) as indicated by the rectangles were defined within the image. The hysteresis loops measured locally in these rectangles show that darker regions (orange rectangles) exhibit a magnetic hysteresis while lighter (gray rectangle) do not (cp. Fig. 3.14(b)). Correlating the hysteresis loop shapes to the ones in section 3.3 and the EBSD in Fig. 3.13(b), reveals that the lighter areas consist of an amorphous, magnetically inactive YIG, whereas the darker, circular areas consist of

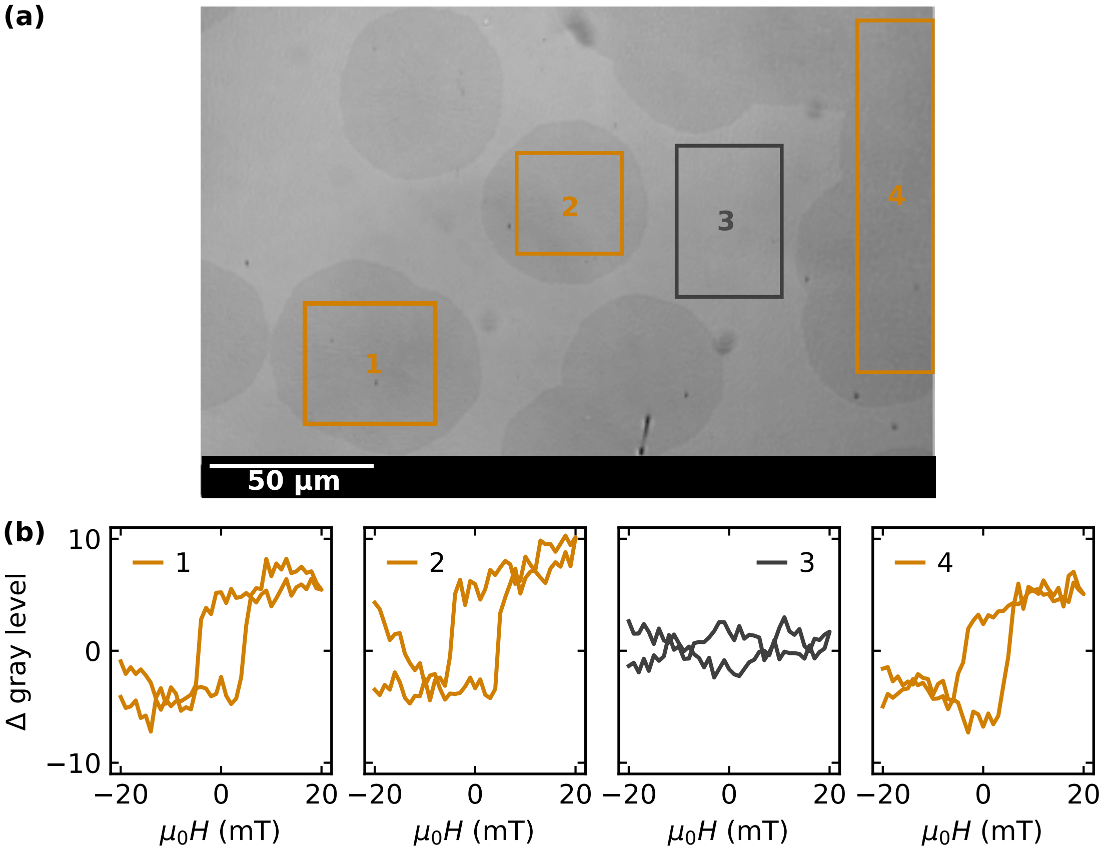

Figure 3.14: (a) Kerr-microscopy image of the YIG film on SiO_x annealed at 700 °C for 8 h. Similar to the SEM (cp. Fig. 3.13), circular regions are visible which correspond to polycrystalline YIG and which appear darker than the non-crystalline areas around them. For defined areas, given by the rectangles labelled 1 to 4, local L-MOKE measurements were conducted. (b) shows the obtained hysteresis loops for the four defined regions. Each loop recorded in a dark circular area in (a) exhibits a hysteresis whereas the third in the brighter area (rectangle 3) does not. Local L-MOKE measurements therefore allow to distinguish between crystalline and non-crystalline YIG on SiO_x.

(poly)crystalline YIG with a magnetic hysteresis. This observation indicates that L-MOKE allows to reliably differentiate between amorphous and crystalline YIG via the contrasting magnetic properties of the two phases. Furthermore, these results highlight the spatial resolution gained by EBSD and MOKE.

It should be noted, that due to the fine grain sizes of the individual YIG crystals in the polycrystalline film (cp. Fig. 3.13(b)) the obtained L-MOKE signal integrates over all crystalline directions. Therefore, no significant differences in gray level or coercive field are observed between the areas. Attempts to define even smaller ROIs did no longer result in a magneto-optical response. Consequently, the L-MOKE data shown here and in 3.3 are always the result of an averaged magnetic response and qualitatively match the SQUID magnetometry data.

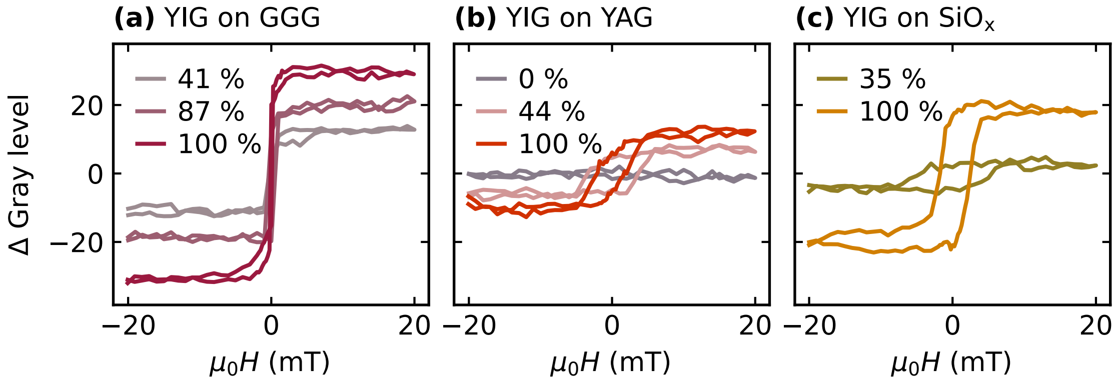

Figure 3.15: L-MOKE hysteresis loops obtained on partially crystalline YIG films on (a) GGG, (b) YAG and (c) SiO$_x$. The percentage in each figure corresponds to the value extracted from the structural analysis (cp. Fig. 3.11 and Fig. 3.13(b)). As described in section 3.3, the gray level is in first order correlated to the saturation magnetisation. One observes a clear correlation between the absolute gray level and the extracted amount of crystalline YIG on each substrate.

Next to the spatial resolution, L-MOKE further allows to extract a percentage value corresponding to the magnetically active material by comparing the absolute gray value (without ROIs). This correlation is possible on all substrates as depicted in Fig. 3.15. The percentages are displayed in Tab. 3.1 and stem from the structural analysis (cp. Fig. 3.11 and Fig. 3.13(b)), which corroborate the L-MOKE data. While the curve shape of each loop is comparable within each substrate, the absolute gray value changes. The differences in gray value qualitatively track the degree of crystallinity, as the gray level is correlated to the saturation magnetisation (cp. section 3.3), which in turn is only finite in the crystalline, ferrimagnetic phase. By normalising the absolute gray level with respect to the maximum observed contrast, i.e. the fully crystalline sample, the percentage of magnetically active YIG value is extracted on each substrate as summarised in Tab. 3.1.

The correlation between magnetic and structural properties is evident from Tab. 3.1. The magnetic properties arise once crystalline YIG has formed, which is captured in the extracted percentages. For example, a YIG film annealed for 1 h at 600 °C yields 41 % YIG on GGG and 0 % YIG on YAG via L-MOKE. These values are in excellent agreement with the percentages extracted via structural methods, suggesting a coherent extraction of the crystalline percentage. However, the values cannot always be perfectly correlated. For a YIG film on YAG annealed for 4 h at 587 °C 44 % crystalline YIG is obtained via XRD and 61 % via L-MOKE. Similar differences are obtained on YAG, when the film is partially crystalline. A possible reason is the previously mentioned underestimation of the crystalline percentage via XRD (section 3.2, Fig. 3.12). However, some difference might also arise from the calibration of the Kerr-microscope which is performed separately for each sample and cannot be completely ruled out as a source of error. While both structural and magnetic characterisation are valid options to monitor the crystallisation, the structural methods are utilised in the following.

To investigate the crystallisation behaviour, the onset temperature at which YIG starts

Table 3.1: Percentages of crystalline YIG obtained via structural methods (XRD cp. Fig. 3.11, EBSD cp. Fig. 3.13) and via magnetic characterization (L-MOKE cp. Fig. 3.15).

extracted % via	GGG	YAG	SiO_x
XRD + EBSD	41 % | 87 % | 100 %	0 % | 44 % | 100 %	35 % | 100 %
L-MOKE	42 % | 67 % | 100 %	0 % | 61 % | 100 %	24 % | 100 %

to crystallise needs to be determined. Since the crystallisation is thermally activated, it depends exponentially on the annealing temperature, resulting in a narrow window in which the onset of crystallisation can be observed, as depicted in Fig. 3.16. As the onset temperature is substrate dependent [133], the value differs between 550 °C for YIG on GGG (Fig. 3.16(a)), 575 °C for YIG on YAG (Fig. 3.16(b)) and 700 °C for YIG on SiO_x (Fig. 3.16(c)). At these temperatures, a sudden increase in the crystallinity of YIG is observed.

This observation suggests, that on YAG and GGG fully crystalline YIG films can be obtained at roughly 600 °C, whereas on SiO_x, temperatures of approximately 700 °C are necessary. The ΔT of 100 °C already indicates the additional thermal energy required to form a nucleus (cp. Fig.3.13 and Fig. 3.1).

Beyond these temperatures, the degree of crystallinity either saturates or slightly decreases, indicating the formation of a fully crystalline YIG film. Especially on YAG and GGG, this decrease in intensity is pronounced (cp. Fig. 3.16(a)+(b)). This observation can be understood via the emergence of another crystallisation mechanism next to the SPE. As nucleation gets more pronounced with higher annealing temperatures (cp. Fig. 3.16(c)), polycrystalline YIG could form and thereby degrade the crystalline quality. Furthermore, due to the high lattice mismatch between YIG and YAG lattice defects likely form at these elevated temperatures. This reduction in crystal quality was clearly visible in the rocking curves (cp. Fig. 3.12) and likely causes the underestimation of crystalline percentage extracted via XRD. As all films are from the same sputtering process and of the same thickness, a lower intensity due to thickness variations can be ruled out.

With the onset temperature of crystallisation found, the evolution of the crystallisation over time can now be studied. The lower panel in Fig. 3.16 depicts this exemplarily for the YIG thin films on all three substrates. Each of the samples was annealed repeatedly, for up to 48 h. Independent on the substrate, the extracted value saturates, confirming the onset temperatures on the respective substrate and further confirming that the reduced value in Fig. 3.16(a)+(b) does not originate from a partially crystallised film. With this at hand, the dynamics will be analysed and modeled in full detail in the next section.

3.5 Crystallisation behaviour of amorphous YIG thin films

In the following, the process of extracting a diagram of the phase transition from amorphous to crystalline for YIG on each substrate is described. To that end, a mathematical description of the crystallisation process at an arbitrary temperature is derived, starting

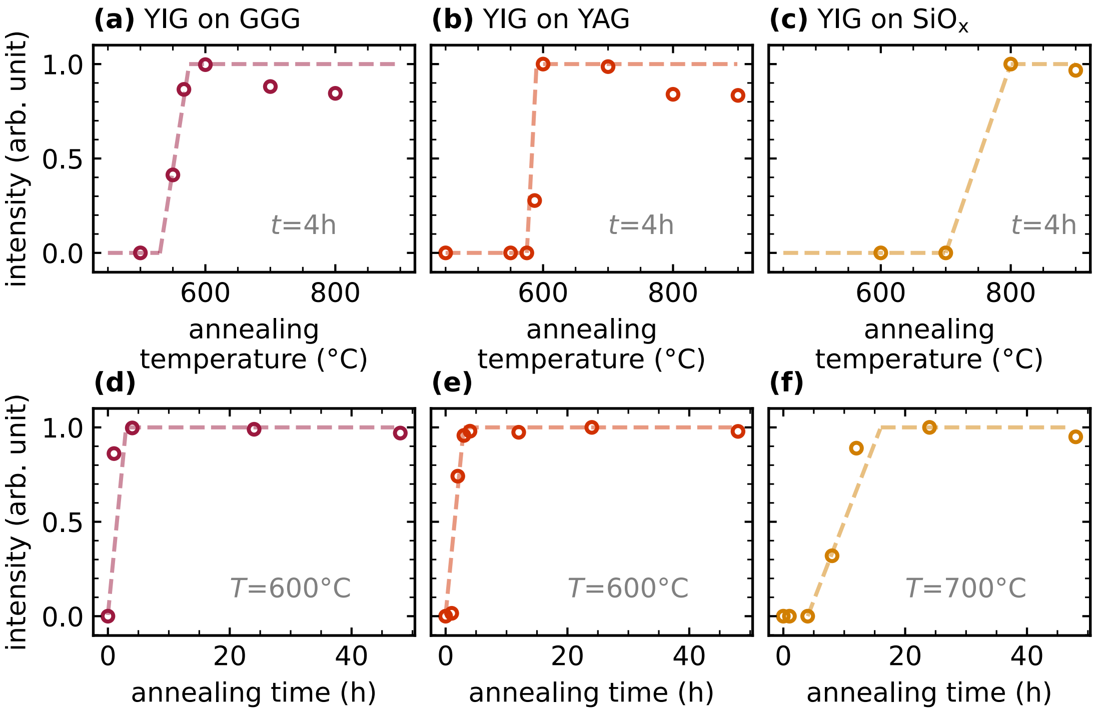

Figure 3.16: Evolution of the crystallinity as a function of the annealing temperature for a constant annealing time of 4 h (a,b,c) and for different times at a constant temperature of 600 °C on GGG, YAG (d,e) or 800 °C on SiO_x(f). The dotted lines act as a guide to the eye.

with the Avrami equation (sometimes also called JMAK-equation), which is derived from classical nucleation theory [152–155]:

$$\theta_c = 1 - e^{-k \cdot t^n} \tag{3.4}$$

Here, θ_c is the fraction of material transformed from amorphous to crystalline and t the annealing time. The k describes the rate constant, while n depends on the dimensionality of nucleation and growth, meaning both can be expressed as a sum $k = k_N + k_G$, $n = n_N + n_G$) [155]. For instantaneous, controlled nucleation n_N is 0, whereas for continuos or random nucleation n_N equals 1. For mixed nucleation, n_N can take on values between 0 and 1, accordingly. The growth part n_G depends on the growth mechanism (interface-controlled or diffusion controlled) and the dimensionality, i.e., can take on values between 1 and 3 [155]. Hence, values for n between 1 and 4 are expected and commonly observed in material science.

The rate constant k will be modelled using a standard Arrhenius dependency [156], as given in Eq. (3.5):

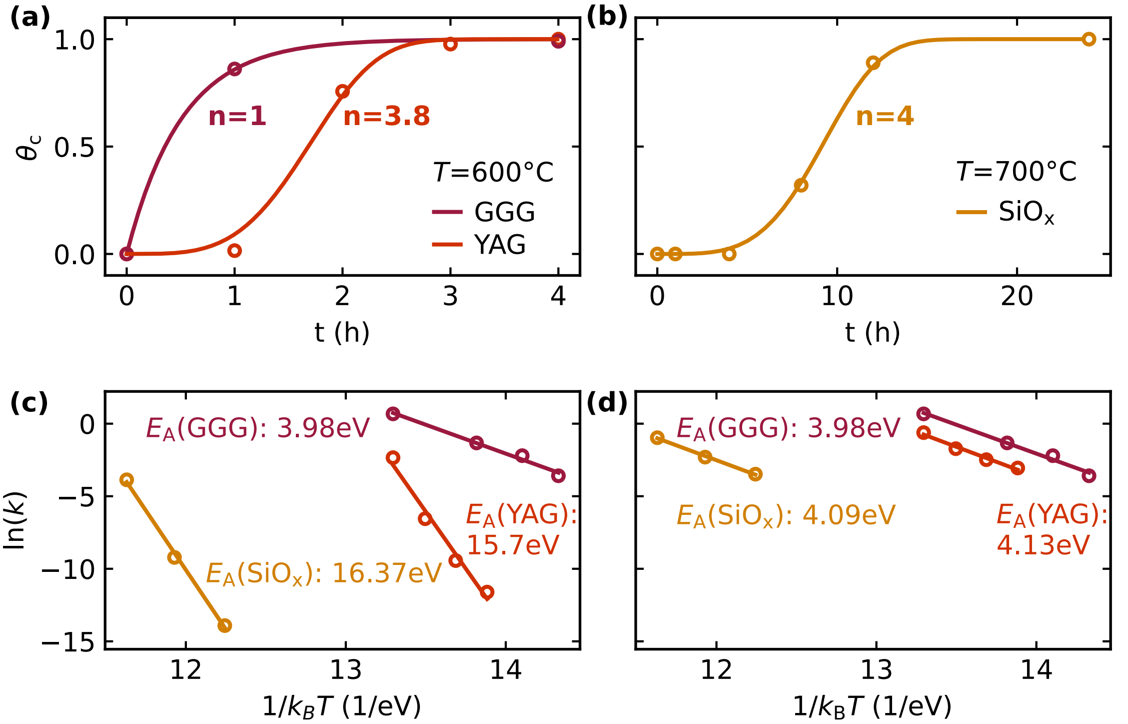

Figure 3.17: For all substrates, the crystalline fraction θ_c is normalised to 1 to allow a description via Eq. (3.4). (a) depicts the time evolution of the YIG crystallisation on GGG and YAG at 600 °C and (b) the same for YIG on SiO_x at 700 °C, where each data point was extracted from XRD or EBSD as detailed in section 3.4. A fit to the data of Eq. (3.4) is depicted as the solid line with the respective Avrami exponent n. As discussed in Fig. 3.1, nucleation and crystallisation is expected to differ between the substrates, which is represented by the different annealing time and temperature combinations as well as extracted n values. Performing the same experiment as in (a) and (b) for multiple temperatures allows to extract the respective rate constants $k(T)$ at that temperature, depicted by the symbols in (c). By plotting the logarithm of the rate constants over the inverse temperature, the pre-factor k_0 and activation energy E_A for YIG on each substrate can be extracted from a linear fit to the data according to Eq. (3.5). (d) Same as in (c), while taking a modified Avrami equation into account, where the rate constant also depends on the exponent, i.e., $(k)^n$.

$$k = k_0 e^{\frac{-E_A}{k_B \cdot T}} \tag{3.5}$$

Here, k_0 is the pre-factor and E_A the activation energy, whose values are characteristic for the investigated system [133]. The resulting rate constants k characterise the crystallisation velocity, or to be more precise, the nucleation and growth of the crystalline YIG phase, in units of $[t] = \mathrm{h}^{-1}$. Using both the Arrhenius (Eq. (3.5)) and the Avrami equation (Eq. (3.4)), the crystallisation of YIG on all substrates can now be described. For this analysis the fraction of crystalline YIG θ_c, as determined in Fig. 3.16, was normalised to 1 and then fit using Eq. (3.4). For the fitting routine, fixed boundaries for n between 1 and 4 were utilised.

Fig. 3.17(a) depicts the results for YIG on GGG (red) and YAG (orange) at 600 °C, where the symbols correspond to the extracted crystallinity and the solid lines represent the fit using Eq. (3.4).

YIG films on GGG being to show an immediate onset of crystallisation, where the fit to the data yields a k of $1.96\,\mathrm{h}^{-1}$ and a n of 1. The value of n means, that nucleation is instantaneous ($n_{\mathrm{N}} = 0$) and that the growth proceeds in one spatial direction ($n_{\mathrm{G}} = 1$), which corroborates the expected SPE behaviour. Moreover, this growth behaviour is comparable to the layer-by-layer growth in the classical epitaxial picture. For a 30 nm thick YIG film, the extracted rate constants corresponds to an initial growth velocity of 0.98 nm/min, which slows down as the film extends towards its physical boundaries.

In contrast, the crystallisation of YIG on YAG exhibits an initial temporal delay, before the onset of crystallisation (see Fig. 3.17(a)). This difference is reflected in the lowered k of $0.10\,\mathrm{h}^{-1}$ and the larger corresponding exponent of $n = 3.8$. Especially the high exponent suggests, that the crystallisation does not follow a standard SPE behaviour and that additional nucleation processes occur ($n_{\mathrm{N}} > 0$). However, the YIG films on YAG were single crystalline (cp. Fig. 3.3(b) and Fig. 3.5(b)), meaning that the nucleation suggested from n is needed to form a YIG nucleus on YAG. The broadening in the rocking curves also suggests a large mosaicity and competing nucleation processes (see Fig. 3.12). This crystallisation behaviour fits to the island growth, which, as a growth type, was reported for substituted YIG films on YAG [124], corroborating the results here. The difference in crystallisation behaviour between GGG and YAG most likely stems from the large lattice mismatch of 3 % (cp. section 2.4), which requires nucleation or the formation of energetically costly strains [157]. To translate the rate constant into a crystallisation velocity the n-th root is taken, yielding a velocity of 0.27 nm/min for a 30 nm film.

Fig. 3.17(b) represents the crystallisation data for YIG on $\mathrm{SiO_x}$ at 700 °C. In comparison to GGG and YAG (cp. Fig. 3.17(a)), a higher annealing temperature was needed on $\mathrm{SiO_x}$ to observe crystalline YIG, highlighting the different mechanism (cp. Fig. 3.1). Fitting the data points in Fig. 3.17(b) yields a k of $9.9 \times 10^{-5}\,\mathrm{h}^{-1}$ and n equal to 4. The exponent of 4 confirms the random nucleation ($n_{\mathrm{N}} = 1$) and subsequent 3D growth ($n_{\mathrm{G}} = 3$), which requires temperatures of 675 °C and above for the nucleation and crystallisation of polycrystalline YIG to be observable at reasonable time scales. The elevated annealing temperature highlights the additionally required energy for the nuclei to form.

Transferring the rate constant to an actual crystallisation velocity can be achieved by analysing the EBSD data. Assuming that the crystallisation of YIG on $\mathrm{SiO_x}$ originates from a nucleus in the middle of a cross shaped feature, as seen in cp. Fig. 3.5(c) and proceeds until encountering either an adjacent crystallite or the samples boundary, allows to extract a crystallisation distance. This distance is influenced by the number of nucleation sites and the crystallographic orientation. Different annealing temperatures hence influence the microstructure and the size of the individual crystallites, whereas the orientation needs to be taken into account for the comparison with YIG on GGG and YAG. Therefore, only YIG crystallites on $\mathrm{SiO_x}$ growing along $\langle 111 \rangle$ are evaluated here, reaching lengths of 10 µm after a minimum of 12 h at 700 °C. Translating this value into a crystallisation velocity yields 16.7 nm/min on an arbitrary substrate along the $\langle 111 \rangle$ direction. While a comparison at

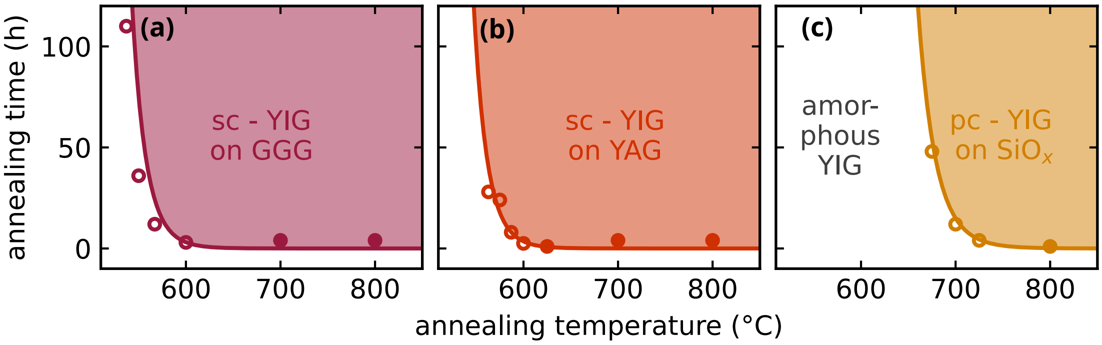

Figure 3.18: Annealing time vs temperature diagram showcasing the phase transition from amorphous to crystalline YIG for time and temperature combinations on (a) GGG, (b) YAG and (c) SiO_x. Each symbol corresponds to a fully crystalline sample as determined via XRD/EBSD. The open symbols are used in the fitting routine via Eq. (3.7), which determines the boundary separating single crystalline (sc) or polycrystalline (pc) YIG from amorphous or partially crystalline YIG (white region). For the fit, a crystalline fraction of 0.999 is utilised in combination with the substrate dependent parameters summarised in Tab. 3.2 as extracted from Fig. 3.17(c). The full symbols represent additionally investigated samples not included in the fit. Using any annealing time and temperature combination from the respective coloured areas is expected to yield a fully crystalline YIG.

600 °C would be preferred, no YIG crystallites could be obtained at that temperature. On the other hand, the larger crystallisation velocity extracted for YIG on SiO_x is due to the elevated temperatures compared to GGG and YAG.

To enable a direct comparison of the crystallisation velocities, the temperature dependence of k needs to be taken into account. Knowing the parameters of the Arrhenius dependency (cp. Eq. (3.5)) for YIG on each substrate, allows to calculate the crystallisation rate for an arbitrary temperature. To extract k_0 and E_A, the natural logarithm of each rate constant k is plotted over the inverse temperature. The resulting data is depicted in Fig. 3.17(c), to which a linear fit can now be applied, yielding the pre-factors and activation energies from Eq. (3.5) for YIG on each substrate, as summarised in Tab. 3.2. With this at hand, the crystallisation velocities of YIG on GGG and SiO_x can now be compared at the same temperature. Extracting the respective crystallisation rates for 700 °C indicates, that the crystallisation rate would be approximately 30 times greater on GGG in comparison to that on SiO_x.

The extracted value for E_A of 3.98 eV (cp. Tab. 3.2) for the crystallisation of YIG on GGG aligns well with previously reported literature values. For instance, the formation of bulk YIG with oxide powder precursors revealed an activation energy of 5.08 eV [158], while for polycrystalline YAG a value of 4.5 eV was reported [159]. The latter is expected to be comparable as YAG and YIG share the same crystal structure with similar elements and lattice parameters (cp. section 2.4). The lower E_A value of 3.98 eV extracted here reflects the reduced energy needed for crystallisation on the almost perfectly lattice matched GGG substrate, i.e., the provided seed layer.

In comparison, the activation energies determined for YIG on YAG and SiO_x are significantly higher than on GGG (cp. Tab. 3.2). Despite the largely different values, the annealing times and temperatures needed for a fully crystalline YIG film are comparable. Especially on YAG, only a slightly higher activation energy (or lower pre-factor) was expected as a single crystalline YIG film forms after aIn contrast to the Avrami equation described above (cp.Eq. xX)I khanna et al. proposed a modified Avrami equation, Where the rate constant short time delay. Despite this expectation, the E_A on YAG is comparable to the one on SiO_x instead of GGG. While in both cases, for YIG on YAG and YIG on SiO_x, a kinetic hindrance needs to be overcome, the activation energies appear unreasonably high, especially in comparison to the differences of 1-2 eV discussed in the previous paragraph and with the literature [133, 158, 159]. Plausible reasons for this are discussed in the following.

In contrast to the Avrami equation described above (cp. Eq. (3.5)) Khanna et al. proposed a modified Avrami equation, where the rate constant also depends on the Avrami exponent, see Eq. (3.6) [160]. As the Avrami exponent is not affected, the conclusions regarding nucleation and growth extracted there remain identical.

$$\theta_c = 1 - e^{-(kt)^n} \tag{3.6}$$

Khanna et al. [160] argue that the modification seen in Eq. (3.6), allows to compare the rate constants of systems with a different Avrami exponent. Intuitively, this was already done for the comparison of the crystallisation velocities in nm/min extracted from the constants, where the units needed to be matched. However, for the evaluation of the activation energies in Fig. 3.17(c), this modification was initially not considered. To compare the difference between these two Avrami equations, an analogous analysis as previously described for Fig. 3.17(c) is conducted, which now considers a weighted rate constant as obtained in via Eq. (3.6).

Fig. 3.17(d) depicts the resulting diagram and the extracted k_0 and E_A, when considering Eq. (3.6). For the crystallisation of YIG on GGG no difference is obtained, as the exponent equals to 1, i.e. the description is identical. The previous discussion for YIG on GGG is therefore unchanged. For YIG on YAG and SiO_x, the extracted value changes significantly, as effectively the 4-th root is taken of each k value. This way, activation energies of 4.13 eV and 4.09 eV are extracted on YAG and SiO_x, respectively. The YAG curve now always lies slightly below GGG, highlighting the crystallisation at similar temperatures with a lower rate, as previously described by the crystallisation velocity. The likeness of the E_A values now captures the energy required for the formation of YIG. The main difference in crystallisation velocity between SPE and nucleation lies in the rate constant. The slightly higher energy needed for random nucleation on YAG and SiO_x might be attributed to the additionally required nucleation, as indicated by $n > 1$. However, as the values are accompanied by a large uncertainty (cp. Tab. 3.2), further experiments would be needed to confirm, e.g. if the activation energy of YIG on YAG actually lies above the one of SiO_x.

The so extracted values appear to capture the behaviour better and yield activation energies comparable to literature [133, 158, 159]. However, the crystallisation diagram (cp. Fig. 3.18) and the following evaluation based on the values extracted from Eq. (3.6) would only qualitatively be affected, as the mathematical description differs. The message and the resulting boundaries remain the same.

Furthermore, some deviations are expected from the experimental procedure of the annealing adding to the uncertainty mentioned in Tab. 3.2. By annealing the sample step by step, the extracted data always includes the heating up and down cycles. These steps cause the crystallisation to begin before reaching the set temperature and also continuing for a while upon cooling the furnace down.

An elegant way of monitoring a continued crystallisation process can, e.g. be achieved via in-situ x-ray diffraction. An exemplary data set of a 100 nm thick YIG film is depicted in Fig. 3.19. *The measurements were performed by M. Lammel during a stay in Brest on a X-ray diffractometer without a monochromator, see section 2.4.*

Figure 3.19(a) depicts the temporal evolution of the ⟨444⟩ YIG peak over time at 650 °C. Initially, much like in Fig. 3.17(a), an initial delay is observed before the onset of crystallisation after roughly 3 h. To determine a crystalline fraction, two pseudo-Voigt functions (see Eq. (3.3)) are fit to the data and the area under the Cu-$K_{\alpha,1}$ peak extracted. The area is then normalised with respect to the value at 14 h, yielding the crystalline fraction θ_c.

In Fig. 3.19(b), θ_c is plotted versus the annealing time Δt. Here, the Avrami equation (Eq. (3.4)) can be applied to the data, resulting in a rate constant of $k = 1.38 \times 10^{-3}\,\mathrm{h}^{-4}$ with an Avrami exponent of $n = 4$.

The n and k from the in situ extracting corroborate the data from the annealing experiments in Fig. 3.17. The Avrami exponent of $n = 4 \pm 0.32$ corroborates the values extracted from the ex-situ annealing for YIG on YAG of 3.80 ± 0.36 and therefore the crystallisation behaviour described earlier. Therefore, the crystallisation behaviour is not influenced by the annealing method. To compare the rate constants, the n-th root is taken of k, translating into a crystallisation velocity of 0.32 nm/min by taking the thickness of 100 nm into account. Surprisingly, this value extracted at 650 °C is similar to the 0.27 nm/min extracted in Fig. 3.17 at 600 °C. Due to the exponential dependency of Eq. (3.4), this cannot be reconciled via the thickness difference of the samples and more likely comes from a temperature calibration error. As the in-situ XRD was not calibrated, the temperature at the

Table 3.2: Summary of the activation energies E_A and pre-factors k_0 for YIG on all substrates. The first two columns represent the values as determined via Eq. (3.5) from the data obtained via Eq. (3.4) in Fig. 3.17(c), whereas the following two columns describe the data extracted via Eq. (3.6) from Fig. 3.17(d). The last column gives the Avrami exponent, which is the same for the two variations.

	E_A via Eq. (3.4) (eV)	k_0 via Eq. (3.4) (1/h^n)	E_A via Eq. (3.6) (eV)	k_0 via Eq. (3.6) (1/h)	n
YIG on GGG	3.98 ± 0.32	$2.0 \cdot 10^{23}$	3.98 ± 0.32	$2.0 \cdot 10^{23}$	1
YIG on YAG	15.70 ± 1.59	$2.6 \cdot 10^{89}$	4.13 ± 0.42	$3.4 \cdot 10^{23}$	3.8
YIG on SiO_x	16.37 ± 0.85	$8.4 \cdot 10^{80}$	4.09 ± 0.21	$1.7 \cdot 10^{20}$	4

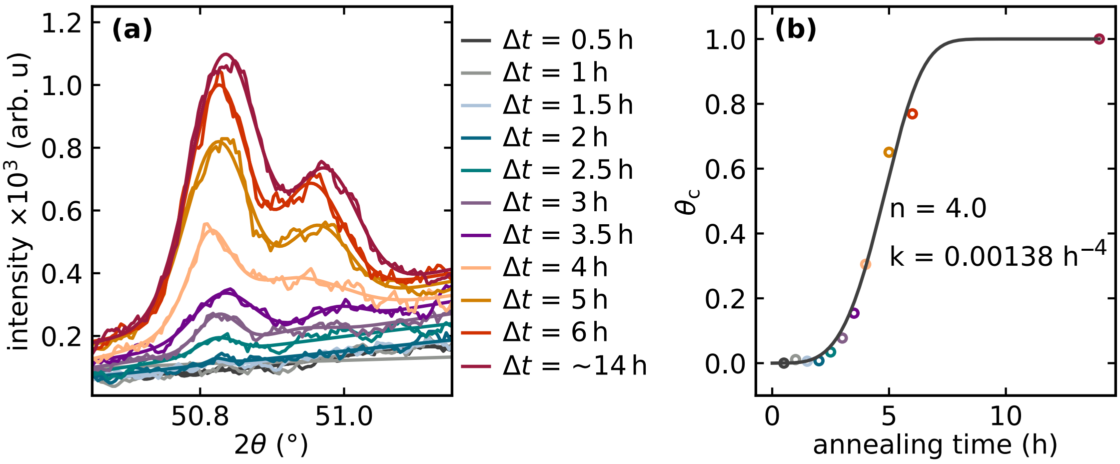

Figure 3.19: In-situ XRD study of a 100 nm thick YIG film on YAG at nominally 650 °C. The measurements were performed by Michaela Lammel. (a) Evolution of the ⟨444⟩ YIG peak over time, showing an inital delay and an onset of crystallisation after approx. 3 h. Due to the missing monochromator, both $K_{\alpha,1}$ and $K_{\alpha,2}$ are visible. By fitting two pseudo-Voigt functions (cp. Eq. (3.3)) to the data the area under the YIG peak can be extracted. The area is then normalised with respect to the last value extracted at 14 h yielding the crystalline fraction θ_c. (b) θ_c as a function of the annealing time, allowing a fit by Eq. (3.4). The extracted rate constant k and Avrami exponent n are given next to the fit.

sample likely differs, resulting in the temperature offset of almost 50 K. While this value appears large, similar temperature differences occur in the sputtering chamber, where the thermocouple is near the heater and not the sample.

The in-situ study demonstrates that the crystallisation behaviour, i.e., the Avrami exponent, is consistent over multiple methods. As the access to this device was limited and a large temperature difference suspected, no further experiments were conducted. The difference in k can only be reconciled via a large temperature offset, which needs to be carefully considered in similar measurements. A comparison of this value is therefore complicated, even after taking the n-th root. However, by using the in-situ XRD, the evolution of the YIG peak can be observed without the crystallisation starting early or continuing during the heating up and cooling down steps of the furnace. For the exact understanding of the activation energy and its separation into rate constants for nucleation and crystallisation, further experiments would be required, where further in-situ studies should be considered.

Based on the results of Fig. 3.17, a crystallisation diagram illustrating the annealing time and temperature combinations yielding a fully crystalline film can be constructed (cp. Fig. 3.18). For a quantitative description, Eq. (3.4) is combined with Eq. (3.5) enabling an expression of the crystallinity of YIG as a function of annealing time and temperature, as given by as given by Eq. (3.7) [6], where all symbols represent the previously defined variables.

$$t = \left(\left[- \frac{\ln(1-\theta_{\mathrm{c}})}{k_0} \right] \mathrm{e}^{\frac{E_{\mathrm{A}}}{k_B T}} \right)^{\frac{1}{n}} \tag{3.7}$$

Note, that a slightly different equation would be obtained when using the modified Avrami equation (cp. Eq. (3.6)) to derive the dependence on t, cp. Eq. (3.8):

$$t = \frac{-\left(\ln(1-\theta_{\mathrm{c}})\right)^{\frac{1}{n}}}{k_0} \mathrm{e}^{\frac{E_{\mathrm{A}}}{k_B T}} \tag{3.8}$$

However, when using the corresponding values extracted via Eq. (3.4) and Eq. (3.6) given by Tab. 3.2 and inserting these into respective equation, i.e., Eq. (3.7) or Eq. (3.8), the description and extracted curves are identical.

Figure 3.18(a)-(c) summarises the annealing time and temperature study on GGG, YAG and $\mathrm{SiO_x}$, respectively. Each symbol in Figure 3.18 represents a fully crystallised YIG film, as obtained from section 3.4. Of these, the open circles represent those samples utilised in the fitting routine in Fig. 3.16(c), whereas filled circles are samples, which were obtained with θ_{c} of 100 %. Hence, the rate constant and annealing time could not be unambiguously determined and the points are only used to corroborate the diagram. Equation (3.7), in combination with the values of n, k_0 and E_{A} from Tab. 3.2 and a crystalline fraction θ_{c} of 0.999, now allows to determine a region in the time- temperature space where the parameters yield fully crystalline YIG. It should be noted, that a value of $\theta_{\mathrm{c}} = 0.999$ is needed to avoid the divergence of the logarithm in Eq. (3.7). A lower θ_{c} value would exhibit a qualitatively similar curve shape of the boundary, which would be shifted to the left. The so determined crystalline regions depend on the substrate and are shaded in the respective colour (cp. Fig. 3.18(a)-(c)). As expected, the formation of polycrystalline (pc) YIG on $\mathrm{SiO_x}$ (cp. Fig. 3.18(c)), acting as a typical non-lattice matched substrate, requires significantly higher annealing temperatures compared to the SPE of single crystalline (sc) YIG on GGG or YAG (cp. Fig. 3.18(a)+(b)).

The differences in annealing time and temperature required for crystallisation arise from the substrates. For both GGG and YAG, the lattice of the substrates serves as a single crystalline seed which replaces the need of a nucleus. The deviation in crystallisation behaviour between the two substrates is, therefore, attributed to the different lattice mismatch with respect to the YIG. Due to the much larger lattice mismatch on YAG, higher strain is induced and nucleation is partly necessary for the crystallisation to start. As a result, slightly elevated annealing temperatures are needed on YAG in comparison to GGG. When comparing the lattice matched substrates to $\mathrm{SiO_x}$, one observes that notably higher annealing temperatures are required for the crystalline YIG to form. The additional thermal energy is need for the YIG crystals need to form by nucleation due to the absence of a crystallisation seed from the substrate. The thermally activated process of nucleation explains the higher temperatures as well as the formation of polycrystalline YIG on $\mathrm{SiO_x}$.

The extracted regions yielding fully crystalline YIG films align well with previous publications, see Fig. 3.20. This match does not only include sputtered YIG films [48, 65, 67, 93–99, 101–107], but also amorphous YIG films obtained by pulsed laser deposition

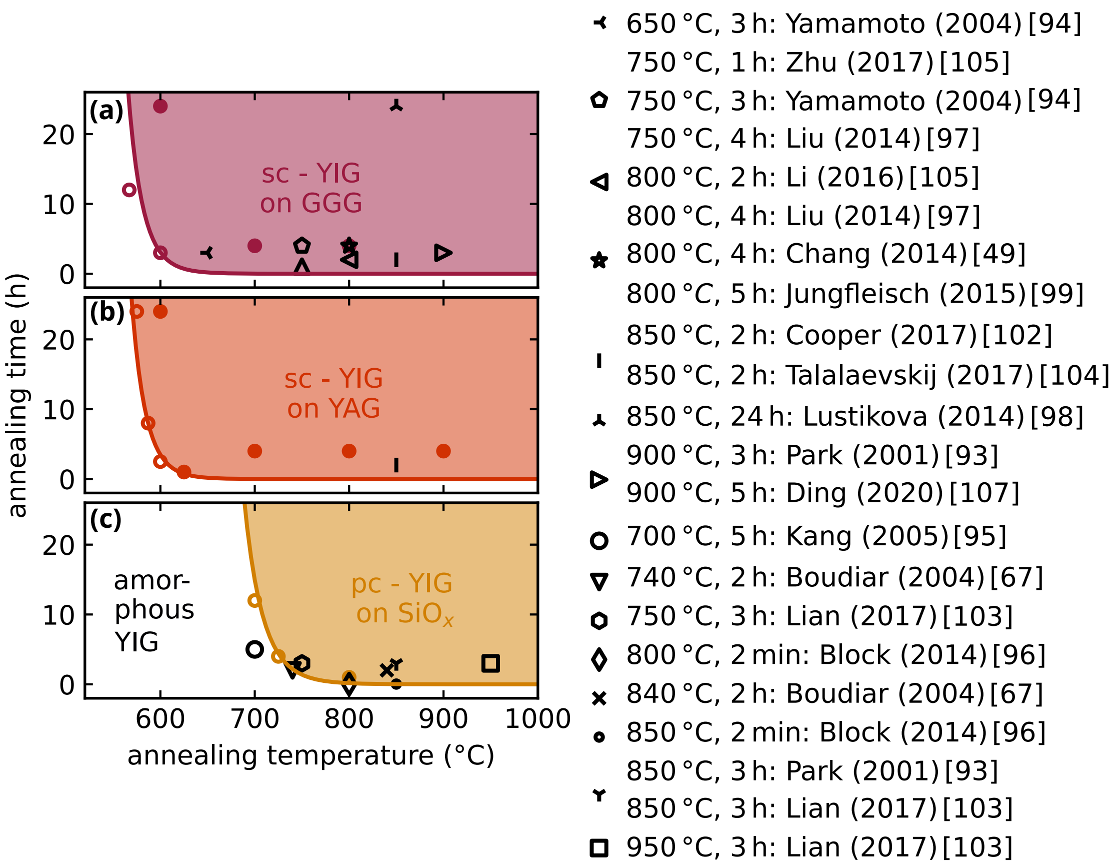

Figure 3.20: Crystallisation diagrams as in Fig. 3.18 with a reduced annealing time axis, to enhance the visibility. As indicated by the black symbols, the extracted crystallisation windows are compared to other studies on sputtered YIG films [48, 65, 67, 93–99, 101–107]. It should be noted, that, while not shown here, YIG films obtained by pulsed laser deposition (PLD) and subsequent annealing also fit into the shaded areas [49, 62, 87–91], indicating a generally valid description of the crystallisation of YIG thin films.

and subsequent annealing [49, 62, 87–91]. As such, the annealing time and temperature diagram in Fig. 3.18 serves as a general description of the phase transition from amorphous to crystalline YIG.

3.6 Summary: Crystallisation dynamics of YIG thin films

In conclusion, sputtered YIG thin films were thoroughly investigated using structural and magnetic characterisation methods. The as deposited films show no signs of a crystalline phase or magnetic order. Upon annealing at a suited temperature and time frame, crystalline YIG forms in a single crystalline manner on GGG and YAG, and polycrystalline on SiO$_x$, acting as an arbitrary substrate. The highest quality YIG films are obtained on GGG and are comparable to sputtered YIG films in the literature. Furthermore, no significant impact of the annealing parameters on the magnetic properties is observed for the times and temperatures tested here.

The evolution of the crystallisation of YIG thin films on the different substrates was then thoroughly monitored using structural methods. Here, YIG films on GGG films follow a typical SPE behaviour, i.e., layer by layer growth, whereas a more complicated behaviour involving nucleation is found on YAG. On SiO_x, the polycrystalline YIG always requires nucleation and forms at higher temperatures in comparison to GGG and YAG.

Extracting the activation energy and the pre-factor allows to establish an annealing time and temperature diagram indicating where crystalline YIG films are obtained. These values are summarised in Tab. 3.2 and allow to set boundaries after which fully crystalline YIG films form (cp. Fig. 3.18). Furthermore, with these parameters, the crystallisation velocity for YIG on each substrate at any temperature can be extrapolated. Within these boundaries, a fully crystalline YIG film could be obtained on GGG at a temperature of 537 °C after annealing for 110 h. On arbitrary, non-lattice matched substrates like SiO_x, nucleation is not expected to set in below 660 °C within a time scale of days.

With this chapter, a complete description of the phase transition of YIG from amorphous to crystalline on three different substrates has been obtained. Not only do these results allow to optimise the annealing process, e.g. in regard of speed [108] or reduction of interdiffusion [135], but it also lays the foundation for the investigation of the lateral crystallisation of YIG in the next chapter. There, the difference in annealing temperature depending on the substrate found here will be exploited to observe the lateral crystallisation of non-planar YIG thin films.

Chapter 4

LATERAL SOLID PHASE EPITAXY OF YTTRIUM IRON GARNET

In this chapter, the fabrication of non-planar YIG using sputter deposition will be described. Crucial for any further experiments on the non-planar structures is to maintain a single crystalline YIG film across the whole non-planar structure. Grain boundaries or other defects, which act as scattering centres, would significantly reduce the transport properties of the YIG. To achieve non-planar YIG, an artificial mesa structure is defined on a lattice matched substrate onto which amorphous YIG is deposited. The crystallisation dynamics of YIG on different substrates detailed in the previous chapter are the essential ingredient to obtain single crystalline YIG.

The process of obtaining single crystalline YIG over an artificial mesa is achieved via lateral solid phase epitaxy (LSPE), which is quantitatively described and analysed in the following. From systematic annealing experiments the activation energy as well as the crystallisation velocity are extracted allowing for a full description of the LSPE of YIG.

This chapter is partly reproduced from S. Sailler et al. [7] *"Lateral solid phase epitaxy of yttrium iron garnet", Phys. Rev. Mater.* ***8****, L020402 (2024) with the permission of APS Publishing. For this publication, I modified the lateral crystallisation experiments to the suited temperature range and then deposited, microstructured and annealed multiple samples for this purpose. Afterwards, I investigated each sample using SEM and EBSD obtaining the data sets for the publication. A transmission electron microscopy study was conducted by Alexander Tahn, Darius Pohl and Bernd Rellinghaus, which confirmed the results from Konstanz. I then created all figures and wrote the first draft of this paper. All authors contributed to the scientific discussion.*

4.1 Lateral crystallisation experiments

The fundamental experiments in Si and Ge led to a mathematical description of the SPE and LSPE (cp. section 2.3). As there procures fall into the category of homoepitaxy, the description slightly differs to the one used in chapter 3. At a given temperature T, the propagating front between crystalline and amorphous material is expected to move linearly in time with a constant (lateral) crystallisation velocity v. The dependency of v on the temperature follows a modified Arrhenius equation [111, 116, 131]:

$$v = v_0 e^{\frac{-E_A}{k_B \cdot T}} \tag{4.1}$$

Here, v_0 represents the maximal crystallisation velocity, k_B the Boltzmann constant and E_A the activation energy. In comparison to chapter 3.5, the rate constant is replaced by a velocity, effectively assuming that the sample's boundaries do not influence the velocity of the propagating crystal front. The resulting v therefore only depends on the system specific v_0 and E_A and then scales exponentially with temperature.

LSPE experiments have recently started to emerge in more complex compounds consisting of multiple elements. Examples include oxides of $Ba_{0.6}Sr_{0.4}TiO_3$ [161], Nb:TiO_2 [162] and $SrTiO_3$ [163]. This chapter now complements the list with the description of the LSPE of YIG by extracting the descriptive parameters introduced in Eq. (4.1). Previous knowledge about the crystallisation of non-planar YIG existed in the form of a bridge structure, fabricated by Heyroth et al. [90] using a coated resist template and pulsed laser deposition. In the subsequent annealing step at 800 °C for 3 h they obtained a single crystalline YIG bridge, showcasing the feasibility of the process. However, no investigation into the crystallisation dynamics, such as the crystallisation velocity was conducted. Furthermore, as detailed in the previous chapter, polycrystalline YIG begins to form at elevated temperatures of 660 °C and above, making the scaling and transferring of their process challenging.

In order to study the lateral crystallisation, a mesa structure is patterned onto a lattice matched substrate. Here, GGG substrates with $n \| \langle 001 \rangle$ and $n \| \langle 111 \rangle$ were utilised. All other experimental details of sample preparation and sputtering parameters are described in chapter 2.4. The complete processing is then depicted in Fig. 4.1. For LSPE experiments, a nominally 20 nm thick artificial mesa structure out of SiO_x is added on top of YAG or GGG (cp. Fig. 4.1(a)).

Initially, different paths yielding a SiO_x mesa structure were pursued. The simplest method consists of using Kapton tape on a cleaned garnet substrate, SiO_x deposition and subsequently ripping off the Kapton tape. However, the edges obtained this way are comparably rough and hard to characterise. By using optical lithography, the edge roughness can be improved significantly, which is utilised throughout the chapter. Here, the substrate is coated with a photoresist (maP-1205) (cp. Fig. 4.1(b)) into which the structures are then defined (cp. Fig. 4.1(c)) using a Smart Print system (*Smartforce Technologies*). Later use of the Nanowriter Advanced (*Polos*) led to even better edges due to sub μm resolution. The defined layout is then transferred by physical etching in an PlasmaPro 80 RIE (*Oxford*

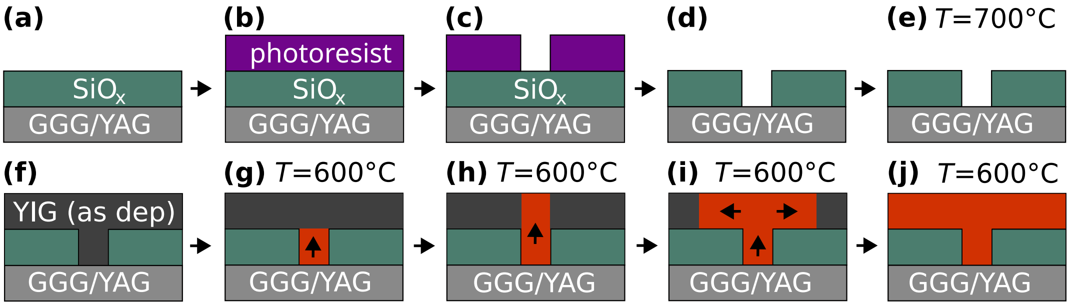

Figure 4.1: Sample processing for the LSPE experiments: (a) Initially, a lattice matched garnet substrate is coated by a roughly 20 nm thick SiO_x layer, (b) onto which a photoresist is spun, (c) into which a pattern is defined using optical lithography. (d) The layout is then transferred via etching and the varnish removed. (e) After baking the garnet/SiO_x stack at 700 °C, the YIG layer is then deposited in (f). (g) By annealing at a temperature between 600 °C - 650 °C, the vertical crystallisation process begins from the garnet substrate. After reaching the sample surface in (h), the single crystalline YIG acts as a seed for the LSPE indicated in (i), which could ideally continue until the YIG is fully crystalline (j).

Instrument) system (cp. Fig. 4.1(d)). For the etching, both a SF_6 plasma as well as an Ar plasma proved to be suitable, with the SF_6 yielding much faster etching rates. Here, the SiO_x layer needs to be completely etched away, since the garnet substrates act as the seed for the later crystallisation of YIG. As the YAG / GGG surface was bombarded with ions, the garnet/SiO_x stack was annealed at 700 °C for 4 h to negate any potential damage to the garnet crystal structure at the surface (cp. Fig. 4.1(e)). Furthermore, chemical etching using buffered HF was tested, when the RIE was out of order, yielding a comparable edge roughness. Here, the annealing step was omitted, as no damage was expected on the substrate. However, later analysis concluded that the SiO_x layer becomes more compact upon annealing, similarly to the thickness reduction described in Fig. 3.2, which can cause problems in later processing steps. The annealing steps should therefore always be performed, regardless of etching technique.

To observe lateral crystallisation of YIG on top of the mesa, the YIG layer needs to be continuos over the mesa edge. To that end, the nominal thickness of YIG was at least twice the height of the SiO_x mesa, here about 45 nm. It should be noted that in later experiments a stack consisting of a 90 nm SiO_x mesa layered with 105 nm YIG, i.e., a factor 1.16 did also show LSPE over the edge. Hence, the conditions for LSPE are, that the as deposited YIG in the defined trench must be in direct contact with the garnet substrate acting as a template for SPE and simultaneously to some extend continuous over the edge.

The crystallisation of YIG is then induced by annealing the complete stack at temperatures between 600 °C and 650 °C in a tube furnace under air. Initially, single crystalline YIG forms at the garnet substrate interface, crystallising vertically via SPE (cp. Fig. 4.1(h) and chapter 3.2). Upon reaching the top boundary, the single crystalline YIG now acts as the seed layer for lateral solid phase (homo)epitaxy of YIG on the SiO_x mesa (cp. Fig. 4.1(i). As described in chapter 4.1, a single crystalline front is expected to propagate through the amorphous YIG, until reaching the sample boundaries (cp. Fig. 4.1(j)).

4.2 Observation of the lateral solid phase epitaxy of YIG

For observing the LSPE of YIG, choosing the ideal annealing temperature is essential. To that end, the findings of the previous chapter will be exploited (cp. chapter 3.5), where the annealing time and temperature combinations for a fully crystalline film on different substrates were extracted (cp. Fig. 3.18). The SPE from lattice matched GGG and YAG was found to occur at lower temperatures in comparison to the nucleation driven crystallisation on SiO_x. This difference is crucial, as polycrystals would hinder the propagation of the single crystalline YIG from as depicted in Fig. 4.1(h), in the worst case making it unobservable. By annealing at temperatures lower than 660 °C, the nucleation of polycrystalline YIG should be significantly hindered, ideally suppressed. Yet, thermodynamically stable nuclei may still statistically form. These nuclei then continue crystallising with the velocity for that respective temperature. External nucleation sites like dirt particles cause nucleation to occur more often than expected from the description in chapter 3.5. Furthermore, when the SiO_x layer was not annealed as mentioned earlier, the compacting of the layer led to an increased nucleation of YIG.

As both nucleation and crystallisation exhibit an exponential dependency on the temperature (cp. Eq. (3.4), Eq. (3.5) and Eq. (4.1)), the optimisation process is inherently complex. While lowering the temperature reduces the nucleation probability, it also affects the SPE or LSPE. This dependency was evident from the SPE of a YIG film on GGG annealed at 537 °C, which took roughly 110 h to become fully crystalline. Note that after this time only 30 nm of single crystalline YIG had formed. For the LSPE, the crystallisation velocity exponentially shrinks as described by Eq. (4.1). However, for further experiments, several µm of single crystalline YIG on the mesa structure are needed to enable processing or contacting of the lateral YIG. Furthermore, the LSPE must be experimentally detectable, i.e. several 100 nm of single crystalline YIG would be desirable. Therefore, the study of the LSPE of YIG is confined to temperatures between 550 °C and 660 °C, reducing nucleation as much as possible while maintaining reasonable crystallisation velocities.

Initially, the LSPE of YIG is confirmed via SEM analysis and EBSD data, see Fig. 4.2. To that end, a YIG film on YAG was annealed at 600 °C multiple times and characterised each time. Fig. 4.2(a) depicts the crystallisation front after 96 h as seen via the secondary electron detector. Above the SEM image, the expected behaviour is schematically illustrated, as described in Fig. 4.1. After vertically crystallising via SPE from the YAG substrate, a laterally propagating YIG crystal front is expected on top of the mesa. The mesa edge is clearly visible in the centre of the SEM image (cp. Fig. 4.2). On the right side of the mesa, YIG crystallised on YAG, where a slight contrast is visible, most likely stemming from the physical etching during the processing. Towards the left of the mesa edge, the crystallisation front of the LSPE of YIG is expected moving from right to left. Here, a gray contrast can be observed in the SEM (cp. Fig. 4.2), which is attributed to the formation of single crystalline YIG and the consequential change in density and height of the material in the probed area.

To further corroborate this interpretation, the SEM image is superimposed with the corresponding colour of the inverse pole figure along the out of plane direction extracted by

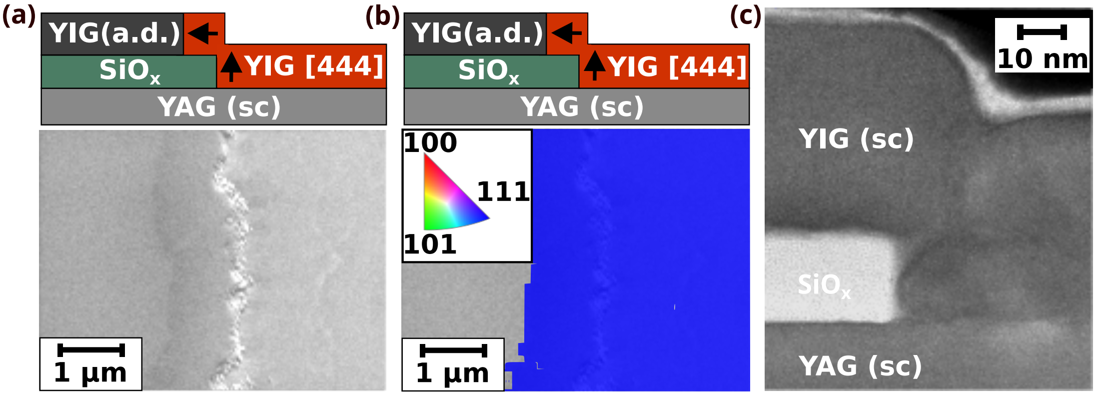

Figure 4.2: Observation of LSPE of YIG on YAG over a SiO$_x$ mesa structure after annealing at 600 °C for 96 h. (a) Schematic of the expected crystallisation behaviour (side view) and SEM image near the SiO$_x$ mesa edge as obtained via a secondary electron (SE) detector (top view). As described in Fig. 4.1, YIG begins to start crystallising vertically via SPE at the interface to YAG, which causes the as deposited (a.d.) YIG to become single crystalline (sc). The respective area is seen on the right side of the SEM image, where a slight contrast can be observed, which is attributed to the physical etching during the previous processing. After the vertical crystallisation is complete, the YIG crystallises laterally via LSPE over the elevated mesa edge in the centre of the image. Here, a clear gray contrast can be observed which is attributed to the change in density upon crystallisation. (b) Overlaying the SEM image from (a) with data from the EBSD mapping confirms the interpretation from (a). Here, the colour correlates to the out of plane direction of YIG as extracted from the inverse pole figure and corroborates the SPE of YIG on YAG and the LSPE over the SiO$_x$ mesa. (c) The TEM analysis was conducted by D. Pohl and A. Tahn and corroborates the data obtained from the SEM and gives insights into the crystallisation near the mesa edge.

EBSD (cp. Fig. 4.2(b)). The monochrome colour of the overlay confirms a single crystalline YIG starting from the YAG, which then acts as a seed for the lateral crystallisation over the mesa. The $\langle 111 \rangle$ out-of-plane orientation, as given by the blue colour, is taken on from the orientation of the YAG substrate. The in plane directions spanning the coordinate system are known from notches in the substrate as $\langle 1\bar{1}0 \rangle$ and $\langle 11\bar{2} \rangle$. The EBSD data further allows to exclude the formation of polycrystalline YIG on top of the mesa for this annealing time and temperature combination. The combined SEM plus EBSD analysis confirms the successful observation of LSPE over a 18 nm high mesa. After 96 h at 600 °C, the LSPE of YIG propagated roughly 1 µm, corroborating the slow dynamics expected for this temperature. Furthermore, at this annealing time and temperature pair no polycrystalline YIG was detected. However, for longer times and/or higher temperatures, nucleation started to become more prevalent, as expected from Si or other oxides [120, 121, 162, 163].

Moreover, the sample was then investigated via TEM, see Fig. 4.2(c), which further verifies the LSPE of YIG. Via TEM, a cross-sectional view of the mesa structure with YIG on top can be obtained, which resembles the schematics in Fig. 4.2(a + b). The TEM images reveal a sharp edge of the SiO$_x$ mesa structure and a more rounded edge of the overlying YIG. Furthermore, the atomic pillars observed via TEM corroborate the SPE of YIG on YAG and the continuing LSPE of YIG over the SiO$_x$ mesa as previously evaluated via SEM.

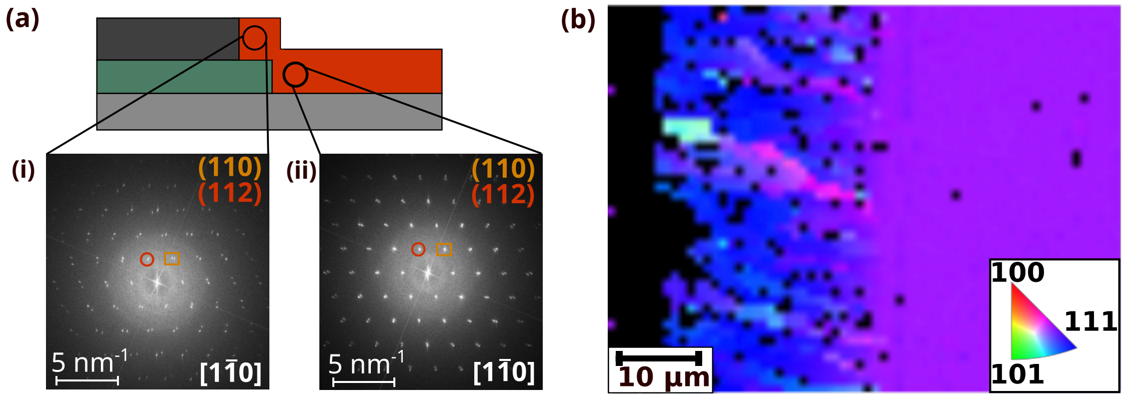

Figure 4.3: (a) Fast Fourier transforms (FFT) of two TEM images at the marked locations: (i) near the end of the lateral crystallisation front and (ii) near the mesa edge. The zone axis is along $[1\bar{1}0]$ and the peaks of two YIG planes along (110) and (112) are marked. A clear rotation of the YIG crystal with respect to the underlying YAG can be observed at the end of the laterally crystallised YIG in (i) in comparison to near the edge in (ii). The imperfections seen in Fig. 4.2(c) are expected to cause this rotation which then transfers into the YIG grown via LSPE. (b) EBSD mapping with an in plane pole figure along a $\langle 112 \rangle$ direction after annealing at 650 °C for 150 h.

Upon closer analysis of the TEM images, some imperfections and a rotation in the crystalline orientation of the LSPE of YIG can be resolved. Near the mesa edge the atomic pillars are not perfectly ordered, possibly influencing the LSPE (cp. Fig. 4.2(c)). The rotation of the YIG can be quantified by a fast Fourier transform (FFT) of two TEM images obtained near the mesa edge (cp. Fig. 4.3(a)(i)) and towards the end of the crystallisation front (cp. Fig. 4.3(a)(ii)). The zone axis of the respective FFT is along $[1\bar{1}0]$ and two reflections along (110) and (112) are marked for identification purposes. In both FFTs, a lateral distortion of the YIG peaks can be observed, stemming from the lattice mismatch of YIG and YAG. Additionally, near the mesa edge a rotation emerges in the FFT of the TEM image (cp. Fig. 4.3(a)). The imperfect crystallisation near the mesa may cause this rotation, which is then transferred and continued in the LSPE since the YIG at the mesa edge acts as its seed.

However, the rotation observed in TEM is too small to be prevalent in the colour code of the superimposed EBSD data in Fig. 4.2(b). Still, the rotation persists in further laterally crystallised YIG and then also becomes visible in the EBSD. Figure 4.3(b) depicts the inverse pole figure along a $[11\bar{2}]$ in plane direction of YIG as extracted via EBSD. The results corroborate the rotation detailed from the TEM and prove that it can be resolved via EBSD as well. Here, however, the rotation completely changed the direction of the crystal, so that on top of the mesa the crystal rotated by 90°. However, this sample was annealed at 650 °C for 150 h resulting in a lateral crystallisation of roughly 20 μm. The much larger extend of the crystallisation and higher temperature do not allow for a direct comparison to Fig. 4.2(b). In all evaluated cases, the crystal rotation could only be observed along the $[11\bar{2}]$ and [111] directions, not along the $[1\bar{1}0]$ direction of YIG. Furthermore, no rotation

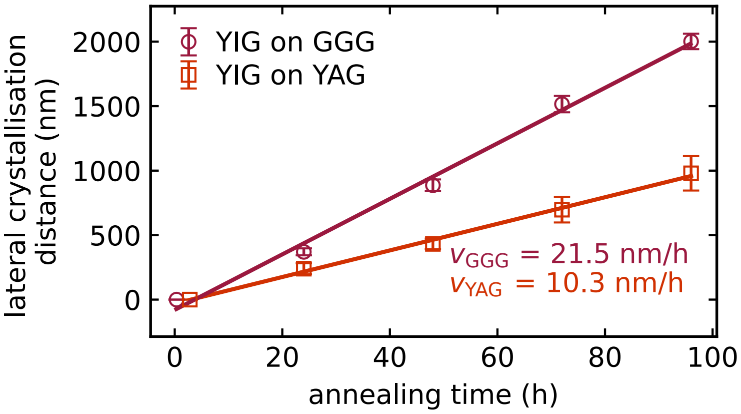

Figure 4.4: Extraction of the lateral crystallisation velocity for YIG on YAG and GGG at 600 °C. Each sample was annealed several times and the progression of the LSPE monitored. For each annealing time, multiple lateral crystallisation distances were extracted from SEM images at different points on the mesa and their mean values plus standard deviations plotted. For each temperature and substrate, a temporal offset was calculated based on the dynamics of the vertical crystallisation (cp. chapter 3.5). A linear fit was then applied to the data, yielding the lateral crystallisation velocity. A difference in LSPE velocity can be observed, where a value of 10.3 nm/h is obtained for YAG in comparison to the 21.5 nm/h on GGG.

could be observed on GGG substrates with the surface normal direction parallel to [100]. The exact reason for this rotation and its selective appearance in some crystal orientations remain subject to further studies.

In summary, both SEM and TEM allow to obtain the lateral crystallisation distance *l* of YIG on top of the mesa structure. Due to the significantly faster preparation and measurement via SEM, the following analysis of the LSPE and the extraction of *l* will be conducted with SEM and EBSD.

4.3 Description and dynamics of the lateral solid phase epitaxy in YIG

In the following, the dynamics of the LSPE of YIG will be analysed. To that end, a sample is annealed multiple times for a defined annealing time *t* at a given temperature *T*. The mean crystallisation distance *l* and its standard deviation for each annealing time and temperature combination is extracted from multiple SEM images across the mesa edge. As detailed in Fig. 4.1(g)-(i), the vertical crystallisation is required for the lateral to start. Here, the 20 nm height of the SiO_x mesa needs to be overcome before the LSPE can start. Therefore, the annealing time offset, after which 20 nm YIG have vertically crystallised, is calculated with the findings from chapter 3.5. At 600 °C, the SPE of YIG on GGG was determined to be roughly 1 nm/min and therefore a 20 min offset.

Figure 4.4 depicts the results of the LSPE study at 600 °C for YIG on YAG and GGG, where for both substrates the ⟨111⟩ orientation is along the surface normal direction. Each data point is extracted as described before and the lateral crystallisation velocity v_{lat} determined by a linear fit to the data. On YAG, this velocity is $v_{\mathrm{lat,YAG}} = 10.3\,\mathrm{nm/h}$, whereas on GGG a value of $v_{\mathrm{lat,GGG}} = 21.5\,\mathrm{nm/h}$ is obtained.

This extracted difference in v_{lat} stands in stark contrast to the expectation. As YIG crystallises via lateral homoepitaxy on both substrates, the velocity is expected to be identical or comparable. A possible explanation for the differences in v_{lat} stems from the substrates themselves. As detailed in chapter 3.1, the lattice mismatch of YIG to GGG is small and high quality films are obtained (cp. chapter 3.2). The higher quality of the vertically crystallised YIG on GGG in comparison to YAG then acts as the seed for the LSPE and could influence v_{lat}. Furthermore, imperfections in the SPE of YIG near the $\mathrm{SiO_x}$ mesa in Fig. 4.2(c) were observed, which could also influence the seed quality and resulting propagation velocity. Lastly, impurities in the sputtering target or slight changes in composition of the film might further affect quality and velocity of the LSPE. However, the exact cause could not be determined suggesting that further detailed experiments will be necessary.

Next to the deviation in v_{lat} between the substrates, a difference is also discovered between vertical and lateral crystallisation. To that end, the vertical crystallisation velocities v_{ver} reported in chapter 3.5 will be compared to the ones extracted from Fig. 4.4. For the SPE of YIG on GGG, v_{ver} was 58.8 nm/h, a value 3.6 times higher than the v_{lat} of 21.5 nm/h. Similarly, the extracted vertical velocity on YAG was 16.2 nm/h, 1.6 times faster than the lateral value of 10.3 nm/h. Despite the near perfect vertical crystallisation via SPE for YIG on GGG and thereby comparability to the LSPE, the latter is significantly slower. While this is unexpected, a similar behaviour was reported in the prototypical Si, where the LSPE was 4-8 times slower in comparison to the vertical value [120]. Here, the behaviour was traced back to the formation of facets and defects during the LSPE. A similar observation was made here, see Fig. 4.2(c) and Fig. 4.3, where defects or a rotation was visible. Therefore, the crystal quality of YIG appears to sensitively impact the crystallisation velocities.

Another possible influence not discussed thus far is the underlying crystal orientation. In Si large differences in v_{ver} depending on the direction of growth are reported [113, 114] and known to also transfer into v_{lat} [123]. Similarly, for v_{ver} of YIG, a crystal orientation dependence has also been reported [141, 142, 164] and briefly mentioned earlier (cp. Fig. 3.5(c)).

Here, the vertical crystallisation in chapter 3.5 was along [111], whereas the LSPE is perpendicular to it, in this case along the $[11\bar{2}]$. The third complementing direction is the $[1\bar{1}0]$. These directions can be inferred from the substrate, as these are specifically cut with notches indicating the $[1\bar{1}0]$ direction.

For a better comparison of vertical and lateral velocity, the values should be compared along the same crystal orientation. This approach allows to evaluate whether the direction dependence accounts for the factors of 1.6 or 3.6 on YAG and GGG, respectively. Furthermore, by annealing multiple samples at different temperatures, the dynamics of the crystallisation could further be compared and the exponential dependency, as described in Eq. (4.1), confirmed.

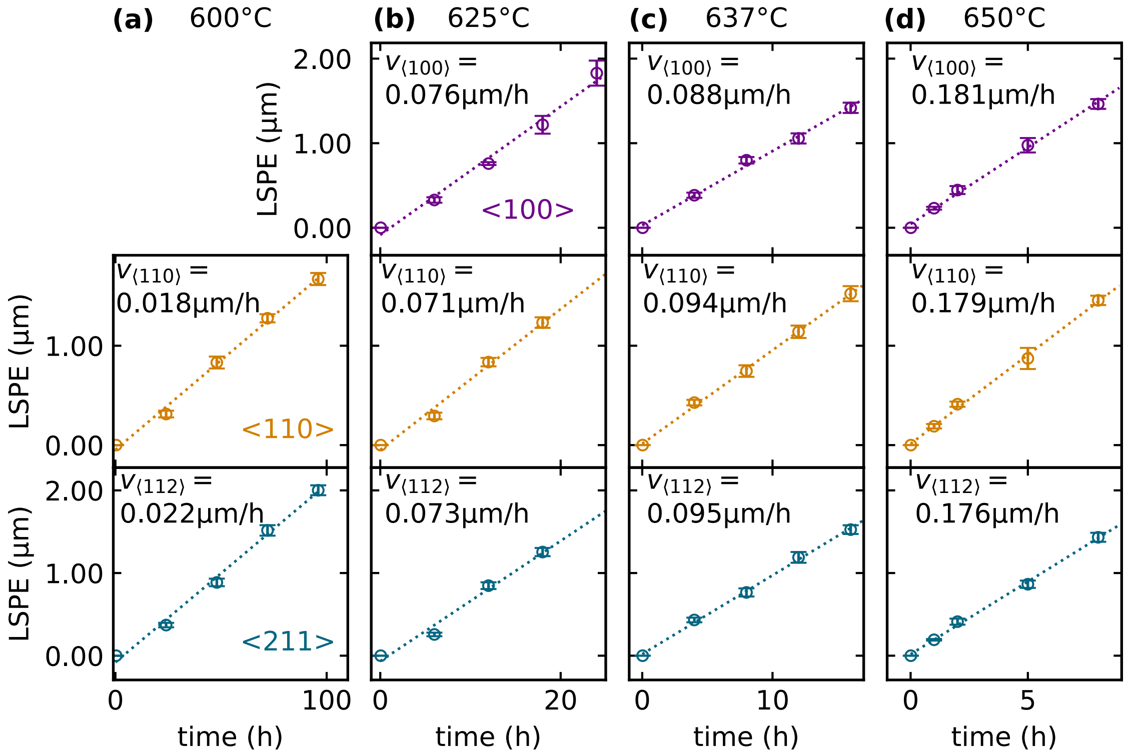

Figure 4.5: Mean lateral crystallisation distances for YIG on GGG as extracted by SEM and EBSD for different temperatures and crystal orientations. A linear fit is applied for each combination of temperature and orientation, yielding the respective crystallisation velocity.

To that end, multiple GGG samples with either the [001] or the [111] direction parallel to the surface normal were prepared, as described in Fig. 4.1. One in-plane crystal direction of the GGG is further known, allowing to calculate the third direction perpendicular to both. Therefore, the two substrates enable the investigation of the LSPE along four well defined directions, [100] and [010] $(\perp[001])$, as well as $[1\bar{1}0]$ and $[11\bar{2}]$ $(\perp[111])$. Due to the cubic crystal structure of YIG (cp. chapter 2.1), [100] and [010] are equivalent and will be referred to as $\langle 100\rangle$. While the other two directions differ, they will also be referred to as their equivalent $\langle 110\rangle$ and $\langle 112\rangle$ in the following. The dependence on the crystal orientation is then extended by extracting v_{lat} at several annealing temperatures of 600 °C, 625 °C, 637 °C and 650 °C.

Figure 4.5 depicts the results for these temperatures and the direction along which the LSPE front propagated. As before, multiple images were analysed and the mean lateral crystallisation distances with its error plotted at the respective temperature. The initial delay was calculated for each temperature and a linear fit applied to the data, yielding a v_{lat} for each temperature and crystal orientation. The lateral velocities range from 18 nm/h at 600 °C to 180 nm/h at 650 °C and exhibit similar values at each temperature. The data

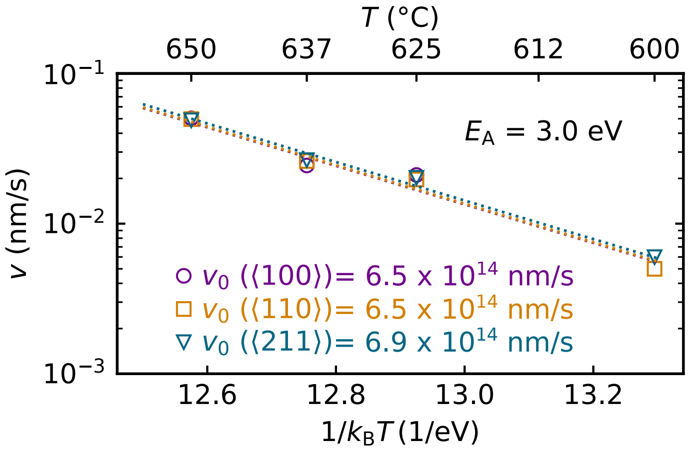

Figure 4.6: Semi-logarithmic plot of the crystallisation velocities of YIG on GGG along different crystalline directions versus the inverse temperature. By a linear fit to the data the activation energy E_A and the maximum velocity v_0 are obtained. An activation energy of $E_A = 3.0$ eV is extracted for YIG. The crystal orientation only exhibits a small influence on the respective maximal velocities with $v_0(<100>) = 6.5 \times 10^{14}$ nm/s, $v_0(<110>) = 6.5 \times 10^{14}$ nm/s and $v_0(<112>) = 6.9 \times 10^{14}$ nm/s.

clearly corroborates the linearly propagating crystal front as expected for LSPE.

As discussed before, a higher annealing temperature leads to an increased lateral crystallisation velocity, but the formation of polycrystalline YIG also starts to become more prevalent. The increase of the LSPE rate with the annealing temperature becomes apparent from the reduced time after which comparable lateral distances are reached (cp. Fig. 4.5). Here, the random nucleation could present an obstacle for the propagating LSPE front, which ideally would continue over the whole sample (cp. Fig. 4.1(j)). While some grains were observed via SEM, these did not hinder the propagation of the crystallisation front, nor the extraction of the crystallised distance. The longest laterally crystallised distance observed during this study was 2.2 µm, whereas later samples as the one seen in Fig. 4.3(b), yielded lateral growth of over 20 µm. However, for the latter, the elevated temperature and the long distance also led to a small decrease in crystal quality, as seen in the SEM image.

Figure 4.6 presents the lateral crystallisation velocities as a function of annealing temperature and the propagation direction. Each data point is derived from the fit in Fig. 4.5. The semi-logarithmic plot reveals a linear relationship between v_{lat} and T^{-1}, as expected from Eq. (4.1). This observation further corroborates the crystallisation of YIG via LSPE and mathematically describes the increase of v_{lat} with T from 21.5 nm/h at 600 °C to 173.1 nm/h at 650 °C observed in Fig. 4.5. All data points are fit simultaneously, as the activation energy is material characteristic and only the pre-factor is expected to differ along the directions [114–117, 131]. This linear fit yields an activation energy of $E_{\mathrm{A}} = 3.0 \pm 0.2$ eV for the LSPE of YIG.

For each crystal orientation, the pre-factor of the LSPE v_0 is now extracted by a linear fit and depicted in Fig. 4.6. With an E_{A} of 3.0 eV, these values are $v_0(\langle 100 \rangle) = 6.5 \times 10^{14}$ nm/s,

$v_0(\langle 110\rangle) = 6.5 \times 10^{14}$ nm/s and $v_0(\langle 112\rangle) = 6.9 \times 10^{14}$ nm/s.

Unlike previous findings for the crystallisation of bulk YIG, [142] the crystallisation velocity appears to be nearly independent of the crystal direction (cp. Fig. 4.6). This observation can be reconciled for the ⟨110⟩ and ⟨112⟩ directions, as their facets are reported to be the thermodynamically most stable while also displaying similar growth behaviour [142, 164, 165]. Their crystallisation velocities were also reported to be comparable with the ⟨112⟩ direction being slightly faster, which is also observed here [142]. No qualitative information could be found for the ⟨100⟩ direction, but the data also suggest a comparable behaviour to the ⟨110⟩ direction. Further, the largest difference in (vertical) crystallisation velocity was observed for the ⟨111⟩ direction, exhibiting a value roughly 10 times larger than along ⟨100⟩ [142, 164]. Unfortunately, no substrates were available where the ⟨111⟩ direction was in the film plane, therewith preventing to study the LSPE of YIG along this direction. While Fig. 4.6 does not suggest a significant dependency on the crystal direction, further studies including the lateral crystallisation along the ⟨111⟩ direction are required to resolve the orientation dependence of YIG.

The activation energy E_A and the respective pre-factors v_0 describing the LSPE of YIG are summarised in Tab. 4.1 and align well with those reported for the LSPE of other materials in the literature. When compared to model systems such as Si, Ge and $SrTiO_3$, YIG exhibits a higher E_A with v_0 values comparable to Si and Ge. Thus, the LSPE of YIG more closely resembles the LSPE behaviour of the prototypical elements Si and Ge than that of the oxide compound of $SrTiO_3$.

Furthermore, the E_A of 3.0 eV ± 0.2 eV extracted for the LSPE of YIG is consistent with studies of other epitaxial materials and the previous chapter. In section 3.5, the activation energy for YIG on GGG was extracted to be 3.98 eV, and higher on the other substrates of YAG and SiO_x (cp. Tab. 3.2). Further, for polycrystalline, bulk YIG obtained via oxide powder precursors a value of 5.08 eV was reported [158]. The higher E_A for heteroepitaxy

Table 4.1: Summary of activation energies E_A and prefactors v_0 for the LSPE of YIG in this chapter in comparison with the prototypical materials Si and Ge for epitaxial studies as well as the prototypical oxide compound of $SrTiO_3$.

Material	Ref	Orientation	E_A (eV)	v_0 (nm/ s)
YIG	this work	<100>	3.0 ± 0.2	6.5×10^{14}
YIG	this work	<110>	3.0 ± 0.2	6.5×10^{14}
YIG	this work	<112>	3.0 ± 0.2	6.9×10^{14}
Si	Csepregi[131]	<100>	2.3 ± 0.1	1.5×10^{13}
Si	Csepregi[131]	<110>	2.3 ± 0.1	6.4×10^{12}
Ge	Johnson[116]	<100>	2.15 ± 0.04	2.6×10^{16}
$SrTiO_3$	White[110]	<100>	0.77	5×10^5
$SrTiO_3$	Chen[133]	<100>	0.7	7.8×10^2

or polycrystalline YIG reflects the additional energy required due to the lattice mismatch or nucleation, which is not present in the lateral homoepitaxy here. Similarly, Chen et al. [133] find, that epitaxial $SrTiO_3$ exhibits an E_A roughly half of that obtained from nucleation and polycrystalline growth, reflecting the reduction observed here between (homo)epitaxial and polycrystalline YIG.

4.4 Summary: Lateral solid phase epitaxy of YIG

The LSPE of YIG was investigated and crystallographically described in this chapter. To that end, SiO_x mesas were defined onto lattice matched garnet substrates onto which amorphous YIG was deposited by room temperature magnetron sputtering. In a subsequent annealing step YIG initially crystallises from the garnet substrates and then proceeds to propagate laterally on top of the SiO_x mesa. The LSPE can be monitored via EBSD by annealing in a temperature range of 600 °C-650 °C, where nucleation is slow as discussed in the previous chapter. The respective lateral crystallisation velocities of YIG at these two boundary temperatures are 21.5 nm/h and 173.1 nm/h, highlighting the exponential temperature dependence. At 650 °C a LSPE could be observed which had propagated over 20 μm.

The analysis of the LSPE over a range of annealing temperatures and along different crystallographic orientations confirmed the expected exponential dependency on T described by Eq. (4.1). The dynamics of the LSPE of YIG are characterised by the variables summarised in Tab. 4.1. The activation energy was found to be in good agreement with the literature and the previous chapter, while the pre-factor appeared to be mostly independent on the crystal orientation along which the LSPE propagated. These insights provide a method of obtaining non-planar, micrometer-scale, single crystalline YIG on arbitrary mesa structures.

Further materials science based interest lies in the crystallographic direction dependence and if the LSPE velocity could be improved by doping, as it does for Si or Ge (cp. chapter 4.1). One possible dopant or substitution element would be Bi, as this simultaneously increases the optical activity, [67] which would also enable (or improve) magneto-optical experiments on the mesa structures.

With the LSPE approach for the fabrication of non-planar structures described in this chapter, two promising directions can be pursued: First, the LSPE paves the way for achieving free-standing, easily detachable single-crystalline YIG. By using SiO_x mesas, a selective etching using HF can be applied to remove the mesa, resulting in free-standing YIG. Further, after crystallising laterally, the single crystalline YIG could be detached, e.g. by focused ion-beam cutting, which would enable experiments that are otherwise constrained by the substrate [166–168]. Second, the LSPE provides a route to achieve non-planar YIG films for magnon-transport based experiments or futuristic spin-wave based computing interconnects [57, 58, 167, 169, 170].

Hence, with this chapter, one key goal towards non-planar spin transport is achieved. In the next part of the thesis, a platform enabling the investigation into non-planar geometries using magnetotransport experiments will be established.

PART II: MAGNETOTRANSPORT EXPERIMENTS

The non-planar YIG thin films - as established in the two previous chapters - can now act as a template for spintronic experiments. The second part of the thesis focuses on magnetotransport experiments. Magnetoresistance measurements are an indispensable tool in condensed matter physics and probe the electrical properties under the influence of a magnetic field. Magnetotransport experiments allow to infer information about the spin transport and its interactions, i.e., the spin polarisation of a current [21], the spin accumulation [171], the spin-transfer torque [42] or magnon mediated effects [51]. Hence, these type of experiments have become a staple of spintronic research and are envisioned for the non-planar YIG.

Performing transport experiments in the electrically insulating YIG is achieved by depositing a conducting metal on top, which is typically characterised by a large charge to spin current conversion. The latter can then interact with the adjacent magnetisation of the YIG. Therefore, the precise knowledge of the individual metal layer and its spintronic properties are essential. By additionally using orbital Hall active materials, characterised by a charge to orbital current interconversion, larger spin injections or spin-orbit torques are expected to manifest. The interface then crucially defines the resulting interaction of a spin or orbital current with the underlying magnetisation of a magnetically ordered layer. Thus, the interface between YIG/Pt is carefully optimised and the influence of the underlying YIG crystal structure statistically evaluated, as changes in the crystal structure naturally arise in the non-planar thin films.

In the next, introductory chapter, the basic concepts and parameters appearing in spintronics and orbitronics are reviewed and the connected magnetoresistances introduced. Chapter 6 then presents an in depth study of the intrinsic magnetoresistances occurring in Pt and Ti thin films. Chapter 7 follows up on the previous chapter by considering YIG/Pt bilayers. The spin transfer across the interface as seen in magnetotransport experiments is statistically analysed. A precise knowledge of the magnetotransport properties of Pt, intrinsic and in combination with YIG, are essential for future experiment in non-planar structures.

Chapter 5

FOUNDATIONS OF SPIN-ORBITRONICS AND MAGNETOTRANSPORT EXPERIMENTS

In this chapter, the fundamentals of spintronics and orbitronics are briefly introduced. Afterwards, the focus lies on magnetotransport experiments, which is the measuring technique used throughout the second part of the thesis. Here, the focus lies on the ordinary, the Hanle and the spin Hall magnetoresistance.

5.1 Spintronics and orbitronics

Spintronics describes the research field which aims to extend conventional electronics from using only the charge of an electron by additionally manipulating its spin [172, 173]. Here, the spin orbit coupling (SOC) is essential, as it links charge and spin degree of freedom. This coupling opens the possibility to exploit both degrees of freedom for spintronic devices [174–176] and correlates a conserved quantity (charge) with a non-conserved quantity (spin) [177]. For the last two decades, the field has been rapidly developing as captured in numerous review articles, e.g. Refs. [44, 173, 175, 177, 178]. Furthermore, spin transfer torque MRAMs have recently found their application in magnetic storage [25], while currently pursued concepts include spin-orbit torque magnetic random access memories (SOT-MRAM) or spin Hall nano-oscillators [26, 179–182].

For fundamental research, the spin Hall effect (SHE) and its inverse (ISHE) are of utmost importance, as they lead to a charge to spin current conversion and vice versa [33, 34, 177]. Both, the SHE and the ISHE, are commonly generated, detected and exploited in transport or optical experiments or in a combination of both [44, 177]. The SHE was first experimentally confirmed using optical methods in semiconductors [183] and the ISHE later directly observed in electronic measurements [184].

Figure 5.1(a) and (b) show a schematic of the SHE and the ISHE, respectively, arising in a material with SOC. An electrical current $\mathbf{J}_\mathrm{c}$ in such a material can give rise to a transverse, pure spin current $\mathbf{J}_\mathrm{s}$ which is polarised ($\mathbf{s}$) perpendicular to both charge and spin current (cp. Fig. 5.1(a)). Analogous, a pure spin current can generate a charge current with the same geometrical dependencies (cp. Fig. 5.1(b)). This interconversion is described by Eq. (5.1) [34, 43], where the spin Hall angle θ_s describes the efficiency:

$$\mathbf{J}_\mathrm{s} = \theta_\mathrm{s}\left(\frac{-\hbar}{2e}\right)\mathbf{J}_\mathrm{c} \times \mathbf{s} \tag{5.1}$$

The SHE arises due to extrinsic as well as intrinsic effects which are both extensively discussed in the literature. Initially, the SHE was theoretically predicted in 1971 [33] on the basis of (Mott) skew scattering [185]. The skew scattering mechanism describes the asymmetric deflection of electrons due to their spin and ascribed as the main mechanism in Ref. [183]. However, theoretical prediction [186, 187] and experiments in semiconductors [188, 189] suggested a SHE effect arising intrinsically from an internal spin-orbit force without the need of skew scattering. Therefore, extrinsic and intrinsic regimes are distinguished depending on the purity of a sample [45].

Experimentally, two material characteristic parameters are descriptive of the spin Hall properties of a material: The conversion efficiency of a charge to spin current is given by the spin Hall angle θ_s (cp. Eq. (5.1)) and the lifetime or propagation distance referred to as the spin diffusion length λ_s [190]. Out of all (stable) elements, Pt has become the prototypical material for generating spin currents [36]. This is due to the relatively large θ_s values of 1 to 10 % in Pt, which can be correlated to the resistivity of the Pt film [45, 61]. These spin Hall angles can be attributed the intrinsically large SHE predicted in Pt [41]. Similar to the SHE, λ_s is reported to vary between 1 to 10 nm in Pt [45, 61]. Therefore, Pt thin films of several nanometres are used in experiments.

The spin Hall effect was recently complemented by an orbital analogue: the orbital Hall effect (OrbHE) [191]. The phenomenological description closely resembles that of the SHE, with an orbital diffusion length λ_l and an orbital Hall angle θ_l, describing propagation and conversion efficiency, respectively. The complementing field aims to generate and manipulate orbital currents and is dubbed as orbitronics. While orbital currents were already discussed almost 20 years ago [192], the field of orbitronics only recently started to gain significant interest.

Go et al. [191] theoretically describe an intrinsic OrbHE stemming from orbital texture, which is induced due to the non-equilibrium generated from an applied electrical field. They show, that passing a charge current through a material induces a non-zero orbital angular momentum. Specifically, the OrbHE also arises without SOC and even when the orbital angular moment is completely quenched in equilibrium [191].

Figure 5.1(c) and (d) depict the OrbHE and its inverse (IOrbHE). Analogous to the SHE, a charge current generates a transverse orbital current and vice versa. Here, an orbital polarisation $\mathbf{l}$ is used to define the direction of the orbital angular moment. The OrbHE was experimentally confirmed in transport experiments on Mn thin films [55] and via optical methods in Ti and Cr [37, 56]. The experimental data confirms that the OrbHE

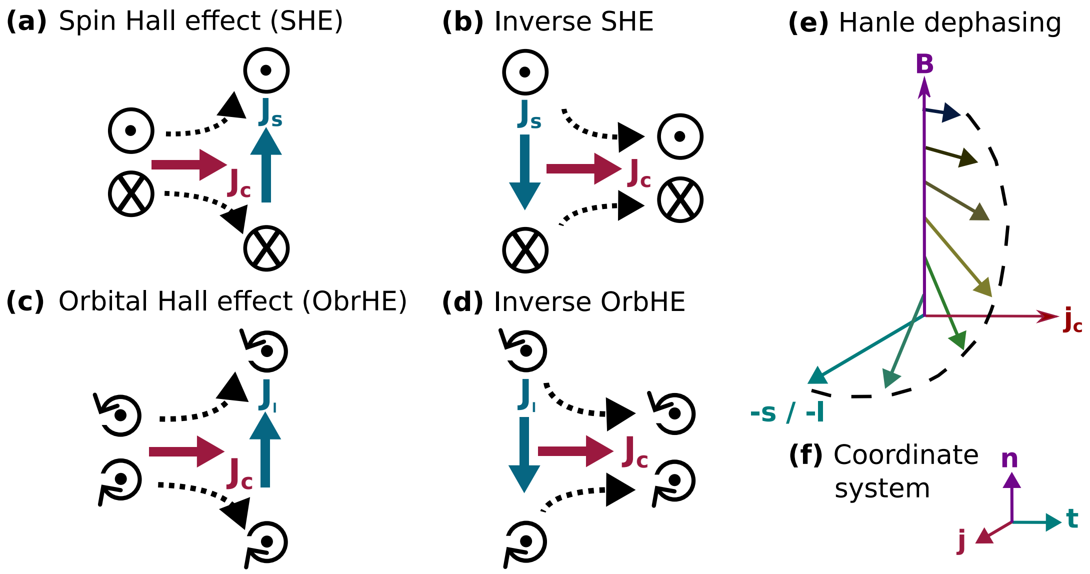

Figure 5.1: Schematic visualisation of (a) the spin Hall effect (SHE), (c) the orbital Hall effect (OrbHE) and their respective inverse effects (b) and (d). In materials with large spin orbit coupling, the SHE is more prevalent whereas in material with weak spin orbit coupling, the orbital Hall effect dominates. These effect cause a charge current to be partially converted to either a spin or orbital current, depending on the dominating mechanism in a material, resulting in a spin or orbital accumulation at the edges of a thin film. (e) In either of these materials, a magnetic field perpendicular to the spin / orbital accumulation causes a torque and by that a precession of the spin / orbital moment. This effect is known in optics as the Hanle dephasing and gives rise to the so called Hanle magnetoresistance (HMR). The occurrence of the HMR is a clear indication of a spin or orbital Hall active material. (f) depicts the coordinate system used throughout the thesis.

arises in various materials with weak SOC [36–38, 55, 56], as contrasted in Fig. [36]. In contrast, spintronics relies on a few selected heavy metals with large SOC [193].

This newly arising topic of orbitronics describes and utilises orbital currents, in a similar way to the effects known in spintronics. Orbital Hall active materials, like Ti, in combination with, e.g. Pt, could help to improve the efficiency of spintronic devices or pave the way for new concepts, as many OrbHE active material are readily available at low cost and therefore contemplated for application.

Probing the spin or orbital Hall properties of a material is achieved in various methods. Here, the focus lies within transport experiments. An extraction of typical spin or orbital Hall parameters without an adjacent magnetic material can be achieved via the Hanle magnetoresistance [171], as discussed in chapter 6. This setup ensures that the extracted properties are not altered by the presence of a magnetically ordered material [194]. In combination with a magnetically ordered material, a magnetisation dependent spin current flow occurs at the interface of, e.g. YIG/Pt. This so called spin Hall magnetoresistance is the content of chapter 7. The following section introduced the basic concepts of magnetotransport experiments.

5.2 Magnetotransport experiments

This section gives an introduction into magnetoresistances arising in spin or orbital Hall active materials, intrinsically and in combination with a magnetic layer below. The coordinate system used throughout the chapter is depicted in Fig. 5.1(f). Here, **j** denotes the direction along the current, **n** the surface normal direction of the sample and **t** the direction transverse to it. Throughout the thesis, longitudinal and transversal magnetoresistances (MR) are distinguished. The MR is generally defined via Eq. (5.2) [195].

$$MR = \frac{\rho(B) - \rho_0}{\rho_0} = \frac{\Delta\rho}{\rho_0} \tag{5.2}$$

Here, ρ is the resistivity, B the external magnetic field and ρ_0 the resistivity at 0 T. A longitudinal MR is extracted from the voltage drop V_L along **j**, whereas a transversal MR refers to the voltage drop V_T perpendicular to **j**, irrespective of the direction of **B**. The electrical contacts and Hall bar geometry of width w, thickness t and separation length of contacts l are detailed in Fig. 6.2(a) and are used to calculate the resistivity (cp. Eq. (5.3)):

$$\rho = \frac{U}{I}\frac{wt}{l} \tag{5.3}$$

5.2.1 Hanle magnetoresistance (HMR)

The Hanle magnetoresistance (HMR) arises from the joint action of the SHE and the ISHE and highlights the non-conserved nature of the spins. Initially described theoretically in 2007 [196] for spin accumulation, the HMR was experimentally confirmed in the heavy metals Pt and β-Ta in 2016 [171]. Starting from the SHE, a charge current is converted to a spin current, which is accompanied with a spin accumulation at the boundaries of the sample (cp. Fig. 5.1(a)). Due to the separation of spin species, a gradient in the (spin) chemical potential arises, which causes a backflow of spins. The ISHE acts upon these spins and causes a reconversion into a charge current (cp. Fig. 5.1(b)). The simultaneous action of SHE and ISHE describes the steady state of the system, in which the resistivity is unaffected.

An external magnetic field **B** can disrupt the steady state by interacting with the spin accumulation at the edges of the sample. The direction of the spin polarisation **s**, as described in Fig. 5.1(a)+(b), is now essential. If **B** and **s** include a finite angle, e.g. in the plane spanned by $\mathbf{J}_\mathrm{s}$ and $\mathbf{J}_\mathrm{c}$, a torque acts upon the spins. These start to precess around the magnetic field and, due to their diffusive nature, become dephased. This so called Hanle dephasing is depicted in Fig. 5.1(e). This phenomenon is named after Wilhelm Hanle, who described the influence of a magnetic field on the polarisation of light [197] in the 1920's. In the used coordinate system (cp. Fig. 5.1(f)), the relevant spin accumulation is along **t**, meaning that the HMR is expected to arise for $\mathbf{B}||\mathbf{j}$ and $\mathbf{B}||\mathbf{n}$.

Due to the precession and Hanle dephasing, the total spin accumulation is reduced in contrast to the steady state. A lower spin accumulation causes a smaller backflow, i.e. a smaller $\mathbf{J}_\mathrm{s}$ and therefore a reduced ISHE (cp. Fig. 5.1(b)). Experimentally, this can be observed as an increase in the resistance, as less charge current is generated in comparison to the steady state.

From magnetoresistance data, the spin Hall properties of Pt can be extracted, as the longitudinal HMR $\Delta\rho_\mathrm{L}/\rho_0$ is described via Eq. (5.4), initially derived in Ref. [171]:

$$\frac{\Delta\rho_\mathrm{L}}{\rho_0} = 2\theta_\mathrm{s}^2 \left[\frac{\lambda_\mathrm{s}}{t_\mathrm{Pt}} \tanh\left(\frac{t_\mathrm{Pt}}{2\lambda_\mathrm{s}}\right) - \Re \left[\frac{\Lambda}{t_\mathrm{Pt}} \tanh\left(\frac{t_\mathrm{Pt}}{2\Lambda}\right) \right] \right] \tag{5.4}$$

Here, θ_s and λ_s are the spin Hall angle and diffusion length, as defined previously, and t_Pt the Pt thickness. Next to these parameters, the diffusion coefficient D in the material significantly impacts the HMR and enters the equation via $\Lambda^{-1} = \sqrt{1/\lambda^2 + i/\lambda_\mathrm{m}^2}$ and $\lambda_\mathrm{m} = \sqrt{D\hbar/g\mu_B B}$, where $\hbar$ is the reduced Planck constant, g the gyromagnetic ratio and μ_B the Bohr magneton [171].

Next to the longitudinal MR, a transversal HMR can also arise [55, 171, 198]. This effect is measured as a voltage arising transverse to the current direction, i.e. where the ordinary Hall effect occurs. As depicted in Fig. 6.1(b), the transverse component is only arises for $\mathbf{B}||\mathbf{n}$. This observation can be understood from the dephasing discussed earlier (cp. Fig. 5.1(e)). Due to the precession, the spin polarisation now includes a component along the current direction, from which a current is generated via the ISHE. This current can then be detected via transverse contacts in the measurement. Due to the geometry of the experimental setup, the effect is only apparent for $\mathbf{B}||\mathbf{n}$.

The transverse HMR is described by Eq. (5.5),

$$\frac{\Delta\rho_\mathrm{T}}{\rho_0} = 2\theta_\mathrm{s}^2 \Im \left[\frac{\Lambda}{t_\mathrm{Pt}} \tanh\left(\frac{t_\mathrm{Pt}}{2\Lambda}\right) \right] \tag{5.5}$$

where $\Delta\rho_\mathrm{T}$ is the transverse resistivity arising from the Hanle effect. The remaining parameters are as introduced beforehand in Eq. (5.4) [171].

Figure 5.2 depict the typical curve shape of the longitudinal (a) and transversal (b) HMR. In theory, the HMR arising in longitudinal and transverse geometry should yield the same values for all three parameters θ_s, λ_s and D, which is experimentally not always observed [55, 171, 198].

Furthermore, the HMR strongly depends on the thickness of the Pt film, as evident from the mathematical description (cp. Eq (5.4) and Eq (5.5)). Since the spin diffusion length describes a mean length before the spin relaxes, an optimal thickness of the Pt exists. The dependency is visualised in Fig. 5.2(c), where a clear peak can be observed at t_Pt of 7.9 nm for the longitudinal and at 5.6 nm for the transversal HMR. Below and above, the HMR effect is smaller. For small magnetic fields, the maximum of the HMR is expected at $4.56\lambda_\mathrm{s}$ and $3.28\lambda_\mathrm{s}$ for the longitudinal and transversal HMR, respectively [171]. Large external fields cause a strong precession of the spins, which influences λ_m and hence, influences the position of the maximum. While the upper limit of the prefactor is 4.56 (or 3.28), the value becomes smaller under strong precession, i.e. the peak occurs earlier. Directly inferring λ_s from the maximum can therefore be erroneous. However, due to the scaling with B (cp. Fig. 5.2)(a) + (b), strong magnetic fields are often needed to

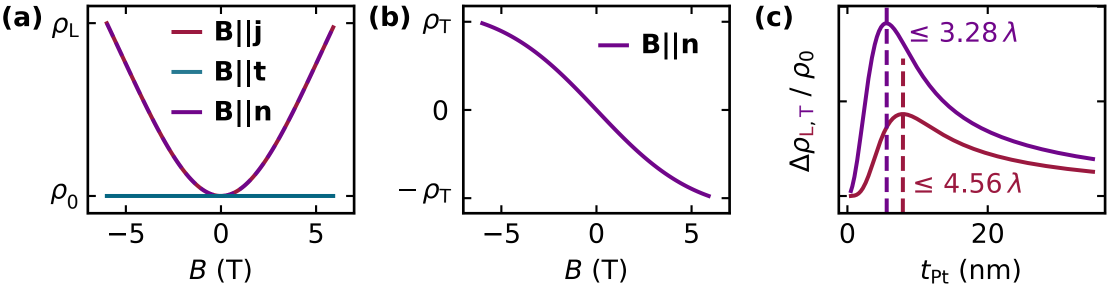

Figure 5.2: Visualisation of the HMR. (a) depicts the longitudinal and (b) the transversal HMR as a function of the external magnetic field for a fixed film thickness. (c) illustrates the both longitudinal and transversal HMR versus the thickness of the Pt film for a fixed external magnetic field of 6 T. A significant influence on the amplitude can be observed, with a distinct maximum at a characteristic thickness for both the longitudinal, as well as the transversal HMR. The maximum correlates to the diffusion length in the material.

resolve the effect.

The HMR has been dominantly investigated in spin Hall active materials like Pt and Ta [171]. Sala et al. [55] extended this spin Hanle picture to an orbital Hanle effect in Mn thin films. The description is analogue to the spin picture, where now an orbital accumulation arises at the sample boundaries, which can again interact with the external field, resulting in a Hanle effect and an HMR (cp. Fig. 5.1(e)). While the extracted θ_l and λ_l are attributed to the orbital Hall effect, the mathematical description of the HMR remains identical [55].

5.2.2 Ordinary magnetoresistance (OMR)

A second magnetoresistance can arise in thin metallic films solely due to the influence of a magnetic field. The longitudinal variant is the so called ordinary magnetoresistance (OMR), which arises in all metals and has been investigated thoroughly in the last century [199]. The OMR exhibits largely different values depending on the metal in question and is especially small in thin films, causing recent publications to commonly omit this MR. Nevertheless, the OMR was reported to occur parallel to spin current induced MR effects in Refs. [198, 200].

The transversal MR arising in analogy is the well known ordinary Hall effect (OHE). Here, a magnetic field causes a Lorenz force onto a moving charge carrier when their respective vectors enclose a finite angle. This force in turn causes a build up of electrons perpendicular to $\mathbf{j}$, which can be detected as a Hall voltage in transversal geometry (cp. Fig. 6.2). The dependency on the magnetic field is described by Eq. (5.6):

$$\rho_H = \frac{U_H t}{I} = R_H B = \frac{B}{ne} \tag{5.6}$$

Here, ρ_H is the Hall resistivity, R_H the Hall coefficient, n the charge carrier density and e the elementary charge.

Both the OHE and the OMR can be motivated using a simple free electron gas model

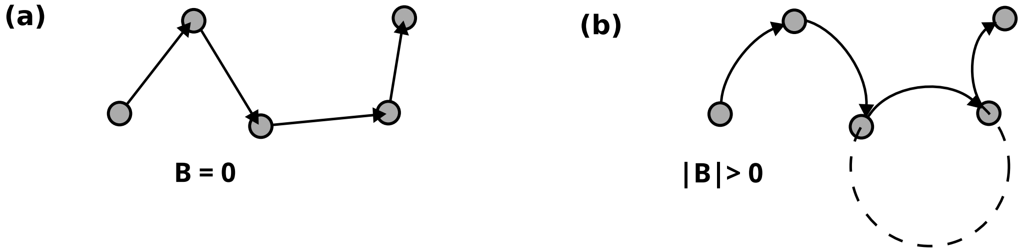

Figure 5.3: Schematic motivating the occurrence of the ordinary MR. The electrons drift motion is depicted in (a) without and in (b) under the influence of an external magnetic field. The effective mean free path is reduced to the magnetic field. A complete circular motion as sketched by the dotted line can only be observed in pure samples at low temperatures. Figure adapted from Ref. [195].

[195]. The main discussion will revolve around the lesser known OMR. When applying an electrical field, the electrons drift because of this external force and scatter along their path, which is schematically depicted in Fig. 5.3(a). To describe this behaviour, a mean free path l and time between scattering events τ is utilised. The electrical conductivity σ is derived as

$$\sigma = \frac{ne^2\tau}{m} = \frac{ne^2 l}{mv_\mathrm{F}} \tag{5.7}$$

with n and e as defined before, m being the mass and v_F the Fermi-velocity [195].

Under the influence of an uniform magnetic field B, the electrons are forced into a circular motion between the scattering events, as indicated by the dotted line in Fig. 5.3(b). Their motion is given by the cyclotron frequency $\omega_\mathrm{c} = eB/m$. The magnetic field can be interpreted as a reduction in mean free path resulting in a positive MR and be characterised by a mean angle turned between each collision ω_c. In combination with Eq. (5.7) the following Eq. (5.8) can be derived [199]:

$$\omega_\mathrm{c}\tau = \frac{B\sigma}{ne} \tag{5.8}$$

This equation already illustrates the most basic dependencies governing the OMR. The better the conductivity or the larger the external magnetic field, the larger the mean angle turned. A $\omega_\mathrm{c}\tau > 1$ is a good criterion under which the OMR is observed, as the magnetic field now considerably changes the conduction process [199].

A quick calculation for Pt suggests that no large OMR is expected. From the literature value of R_H of $24.4\,\mathrm{p\Omega\,m\,T^{-1}}$ [201], the charge carrier density of $2.56 \times 10^{29}\,\mathrm{m^{-3}}$ can be extracted, which in combination with the bulk resistivity ($\rho \approxeq 1/\sigma$) of $105\,\mathrm{n\Omega\,m}$ [202] yields a $\omega_\mathrm{c}\tau$ of 2.3×10^{-3} at 10 T. In comparison, Launay et al. [203] obtain a $\omega_\mathrm{c}\tau$ of 28 for pure Cu at 4.2 K for the same value of B, prompting them to observe a large MR of over 100 %. Here, the electrons are forced onto four full rotations, as depicted with the dotted line in Fig. 5.3(b) and influence of the magnetic field largely outweighs that of the scattering.

Equation 5.8 further allows to estimate on when to expect a large OMR. On the one hand, the larger the magnetic field, the stronger the influence. On the other hand, the better the conductivity the larger the mean angle turned. Therefore, ultra pure samples at low temperatures give rise to the highest OMR [199, 203]. The dependency on the conductivity further explains, why the OMR is commonly disregarded in Pt thin films (cp. Eq. (5.8)). Due to an increased influence of the surface [204, 205], among other defects, the resistivity of thin films is commonly 3-10 times higher than the bulk value [43, 171]. Furthermore, many spin dependent experiments are conducted at room temperature. The properties of Pt in the experimental setting cause a diminishing OMR response in typical spintronic experiments [171].

However, Eq. (5.8) cannot predict the scaling with the magnetic field, nor the amplitude. Furthermore, the free electron gas does not show an ordinary MR and cannot explain the experimental findings of a MR for $\mathbf{B}||\mathbf{j}$, which is in contrast to experimental findings [206]. To reconcile these issues in the simple free electron model, the electrons need to be considered in their crystal environment. To that end, the real Fermi surface and the effective mass has to be taken into account [199].

Depending on the Fermi surface and the type of charge carriers, the OMR can exhibit different dependencies on the magnetic field [207]. Most commonly observed is either a saturation with increasing B, i.e., $\Delta\rho_{\mathrm{L}}/\rho_0 \propto B^0$ or a quadratic increase, i.e., $\Delta\rho_{\mathrm{L}}/\rho_0 \propto B^2$. The equation phenomenologically describing the OMR $\frac{\Delta\rho_{\mathrm{L}}}{\rho_0}$ is the so called Kohler's rule, which is most commonly given in a quadratic form as in Eq. (5.9) [199]:

$$\frac{\Delta\rho_{\mathrm{L}}}{\rho_0} = A_{\mathrm{i}} \left(\frac{B_{\mathrm{i}}}{\rho_0} \right)^2 = F((\omega_c \tau)^2) \tag{5.9}$$

Here, A_{i} is a material dependent factor, B_{i} the external magnetic field with i describing the respective direction, **j**,**t**,**n** (cp. Fig. 6.2(a)). The scaling is in direct correlation to Eq. (5.8), corroborating the previously discussed dependencies.

However, experimentally many deviations from Kohler's rule are observed, with the exponent ranging from 0 to 2 [199, 200, 207, 208]. One reason is the complex interplay of field and current direction with respect to the crystal orientation and, by that, geometry of the Fermi surface. As in the following polycrystalline materials are investigated, Eq. (5.10) is applied.

$$\frac{\Delta\rho_{\mathrm{L}}}{\rho_0} = A_{\mathrm{i}} \left(\frac{B_{\mathrm{i}}}{\rho_0} \right)^n \tag{5.10}$$

Here, the exponent n can exhibit values of $n \in [0, 2]$ [199, 206–208], capturing all contributions. A similar approach was taken in Ref. [200].

Both, the OMR and the previously introduced HMR will be discussed as the occurring magnetoresistances in chapter 6.

5.2.3 Spin Hall magnetoresistance (SMR)

The spin Hall magnetoresistance (SMR) occurs in bilayers consisting of a magnetic layer (F) and a normal metal (NM) layer [42]. For the NM, heavy metals like Pt or Ta are commonly used, as they feature a large spin orbit coupling and, thus, a large spin Hall effect [41, 171]. Ferrimagnetic insulators like yttrium iron garnet (YIG) are the prototypical magnetic layers, as charge currents then only flows in the NM layer, which simplifies the analysis.

The basis for the SMR is the spin Hall effect (SHE) arising in a NM, as introduced in the previous section. Here, a charge current is converted into a spin current and a spin accumulation arises, now at the NM/F interface (see section 5.1, Eq. (5.1)). This adjacent magnetic layer can now disrupt the steady state of SHE and inverse SHE in the NM and give rise to the SMR.

The SMR is then modelled in terms of a magnetisation orientation (**M**) dependent spin transfer across the NM/F interface [42, 43, 209]. To control the direction of **M**, an external magnetic field is utilised. In YIG, several few mT usually suffice to saturate **M** in plane and roughly 100 mT out of plane (cp. chapter 3.3). For the SMR, small magnetic fields often suffice to observe and saturate the effect, in contrast to the HMR in chapter 6. If **M** encloses a finite angle to **s**, spin angular momentum can be transferred to the magnetic layer, as described by the spin transfer torque (STT) τ_{STT} in Eq. (5.11) [209].

$$\tau_{\mathrm{STT}} \propto \mathbf{M} \times (\mathbf{M} \times \mathbf{s}) \tag{5.11}$$

The maximal STT is reached for $\mathbf{M} \perp \mathbf{s}$ (cp. Eq. (5.11)). In a microscopic picture, a direction spin current flows across the surface, which effectively acts as a dissipation channel. Similar to the HMR, a decrease in spin accumulation and therefore, the ISHE, gives rise to an increase in resistivity ρ. As **s** is fixed due to the Hall bar geometry along **t** (cp. chapter 5.1), the projection of **M** onto this axis $\mathrm{m_t} = \mathbf{M}_{\mathrm{T}}/|\mathbf{M}|$ determines the SMR effect. Thus, in experiments the external magnetic field, and, by that, the magnetisation, is either swept [42] or rotated [43] with respect to the **t** direction.

In chapter 7, so called angle dependent magnetoresistance (ADMR) measurements will be performed. The fingerprint of the SMR obtained from ADMR experiments is presented in Fig. 5.4. The three rotation planes are perpendicular to either **n**, **j**, **t**, described by the angles α, β and γ and depicted in (a), (b) and (c), respectively. For $\mathbf{M} \| \mathbf{s}$ the effect vanishes while it is maximal for $\mathbf{M} \perp \mathbf{s}$. Hence, a modulation can be observed in Fig. 5.4(a) and (b), whereas the resistivity is always increased in (c). In a model system with a single domain and **M** always following **B**, the SMR can be written as [43]:

$$\mathrm{SMR} = \frac{\Delta\rho}{\rho_0} = \frac{\rho_1(1-m_{\mathrm{t}}^2)}{\rho_0} = \frac{\rho_1(1-\sin^2(\phi))}{\rho_0} = \frac{\rho_1(\cos^2(\phi))}{\rho_0} \tag{5.12}$$

Equation 5.12 follows the typical MR description (cp. Eq. (5.2)), with ρ_1 describing the amplitude of the SMR. Further, Eq. (5.12) incorporates the projection onto **t**, as explained above, where $\mathrm{m_t^2}$ can be expressed as $\sin^2(\phi)$, with $\phi \in \alpha, \beta$, using angular dependencies. It should be noted that for an in plane rotation using transversal contacts, the SMR also

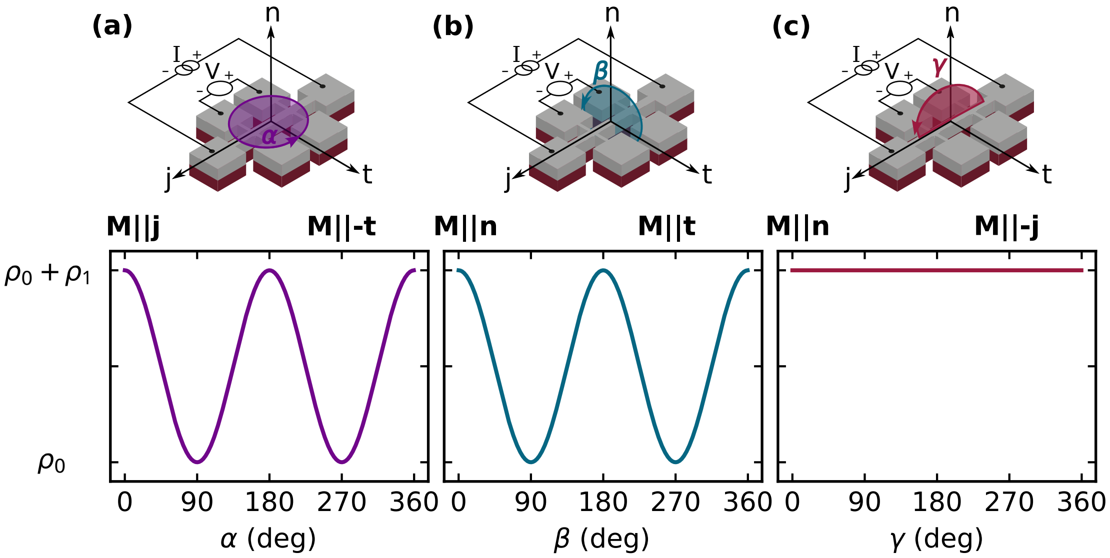

Figure 5.4: Angle dependent magnetoresistance (AMDR) signature of the SMR effect, as measured in longitudinal geometry. The coordinate system used throughout this section for the ADMR measurements is shown in the sketched Hall bars with for a rotation (a) in plane, (b) in the planes perpendicular to **j** and (c) **t**. The SMR can be observed as a $\cos^2(\phi)$ with $\phi \in \alpha, \beta$ in (a) and (b), where the resistivity ρ_0 is increased when $\mathbf{M} \perp \mathbf{s}$. Hence, in (c), the resistivity is always increased as **M** is always perpendicular to **s**.

arises, in theory yielding the same amplitude ρ_1 [43]. The SMR amplitude can then be expressed as Eq. (5.13) to characterise intrinsic parameters of the NM/F bilayer.

$$\frac{\rho_1}{\rho_0} = \frac{\theta_s^2 (2\lambda_s^2) \rho_0^{-1} G_r \tanh^2(\frac{t}{2\lambda_s})}{1 + 2\lambda_s \rho_0 G_r \coth(\frac{t}{\lambda_s})} \tag{5.13}$$

The microscopical description of the SMR is similar to the HMR, with only one parameter differing. This so called spin mixing conductance $G = G_r + iG_i$ characterises the spin transfer across the interface and is crucial for the SMR amplitude. The other parameters are the spin Hall angle θ_s and diffusion length λ_s of the NM (cp. chapter 5.1), its resistivity ρ_0 and thickness t.

The SMR was first described in YIG/Pt [42, 43] and has since then become an indispensable tool in spintronics research. Due to the large amount of experimental studies, the SMR is continuously refined [210–213]. The SMR will be the topic of chapter 7.

5.3 Experimental techniques

The substrates used in chapter 6 are MgO ($\mathbf{n}||\langle 100\rangle$, *CrysTec*), YAG ($Y_3Al_5O_{12}$, $\mathbf{n}||\langle 111\rangle$, *CrysTec*), thermally oxidized Si wafers (SiO_x, 1024 nm, amorphous, *Microchemicals*) and Sapphire (Al_2O_3, *CrysTec*). In chapter 7, commercially available YIG ($Y_3Fe_5O_{12}$, *Innovent*) substrates are used, with either $\mathbf{n}||\langle 111\rangle$ or $\langle 001\rangle$. Before the deposition, the utilised substrates were cleaned for 5 min in acetone and isopropylalcohol using an ultrasonic bath. The additional cleaning step for YIG is described in chapter 7.2.

All metal films presented in this chapter were deposited in the *AJA International* Orion sputtering chamber as described previously. The base pressure of the system was better than 1.5×10^{-7} mbar, with the deposition performed at room temperature using an Ar flow of 17 sccm, a process pressure of 2.6×10^{-3} mbar and radio frequency (rf) magnetron sputtering. Pt was deposited at 50 W resulting in a rate of $1.8\,\mathrm{nm\,min^{-1}}$, while Ti was sputtered with 100 W at $1.4\,\mathrm{nm\,min^{-1}}$. A $\mathrm{SiN_x}$ capping layer was sputtered reactively using a Si target, an Ar flow of 13 sccm, a N_2 flow of 4 sccm, at 100 W resulting in a rate of $1.0\,\mathrm{nm\,min^{-1}}$.

After the deposition, Hall bars are defined and patterned into the metal films (cp. Fig. 6.2(a)). To that end, optical lithography (Nanowriter Advanced, *Polos*) and subsequent Ar ion etching (Plasma Pro 80 RIE, *Oxford Instruments*) was performed, with the Hall bar dimensions being $l = 480\,\mu\mathrm{m}$ and $w = 50\,\mu\mathrm{m}$. Afterwards, the Hall bars were contacted using Al wedge bonding and characterised using a 3D vector magnet (*Oxford Instruments*), with a maximum B of 6 T.

X-ray diffraction experiments were conducted using Cu-K_α radiation in a Rigaku SmartLab. In this part, only symmetrical θ-2θ scans are presented.

Chapter 6

COMPETING MAGNETORESISTANCES IN SPUTTERED METAL THIN FILMS

One avenue in spintronic research deals with pure spin currents, which can be generated in several ways, e.g. via the spin Hall effect. Hence, the next chapter will focus on the prototypical material for generating spin currents: Pt. Here, the Hanle magnetoresistance proved to be a powerful tool for probing the intrinsic spintronic properties. In this chapter, the ordinary and Hanle magnetoresistance are found to occur simultaneously in Pt, with the electronic and structural properties determining the prevalent magnetoresistive effect. This discussion is then extended to Ti thin films, a material proposed to host a large orbital Hall effect. Orbital currents are an additional way of generating flow of pure angular momentum from a different intrinsic mechanism.

This chapter successfully shows that in all materials with a spin or orbital Hall effect the Hanle MR and the ordinary MR coexist and the purity and crystallinity of the metal film determines the dominating effect. Furthermore, the experimental results highlight a close relation between spintronics and orbitronics, despite their different microscopic origin.

This chapter is partly reproduced from S. Sailler et al. "Competing ordinary and Hanle magnetoresistance in Pt and Ti thin films", Phys. Rev. B ***111****, 104421 (2025) with the permission of APS Publishing. For this publication I deposited the Pt and Ti samples from Konstanz. Denise Reustlen performed the optical lithography of the Hall bar devices on these samples during her Bachelor thesis under my advisory. Giacomo Sala provided several samples, which were electrically characterised in Zurich and are used to compare the properties of the different thin films. I then electrically and structurally characterised all remaining films and evaluated the data. After scientific discussion with all co-authors, I illustrated all figures and wrote the first draft of the manuscript.*

6.1 Hanle magnetoresistance experiments in Pt thin films

Due to its intrinsically large charge to spin current interconversion [41], Pt has manifested itself as the prototypical material in spintronic research. The Hanle magnetoresistance (HMR) of spin Hall active materials has therefore also been dominantly researched in Pt [55, 171, 198, 214, 215] and probes the intrinsic spin Hall properties by as a dephasing of the spin accumulation (cp. section 5.2.1).

Figure 6.1 depicts the experimental observation of the HMR in 5 nm as detailed in Sala et al. [55]. Depicted in Fig. 6.1(a) is the longitudinal HMR as the change in resistivity $\Delta\rho_\mathrm{L}$ normalised by the resistivity of the Pt ρ_0 for field sweeps along **j**, **t**, **n**. As expected from HMR theory (cp. section 5.2.1), no MR can be observed for **B**||**t**, whereas a similar MR is be observed for **B** along the other two directions. Further, a transverse contribution in addition to the ordinary Hall effect arises for **B** along **n** (cp. Fig. 6.1(b)). A simultaneous fit to the data yields θ_s of 3.3 %, λ_s of 2 nm and D of 4.5 mm^2 s^{-1}, coherently describing the MR via Hanle theory [55].

However, despite seemingly identical experimental conditions in Refs. [55, 171, 198, 214, 215], the amplitude of the HMR and extracted parameters vary significantly. Several factors influencing the amplitude and the HMR parameters λ_s, θ_s and D are discussed. These include the resistivity of the Pt [45] and the substrate material [171, 198, 214].

More recently, the influence of the orbital Hall effect (OrbHE) to the properties of Pt is discussed [216, 217]. Pt is theoretically predicted to simultaneously host the SHE and the OrbHE [36]. If Pt would show both effects separately, contributions stemming from the orbital Hall effect and from orbital to spin conversion might arise in addition to the known spin Hall contribution [171]. Under these assumptions, two different peaks should arise in the thickness dependence (cp. Fig. 5.2(c)), corresponding to the spin λ_s and orbital λ_l

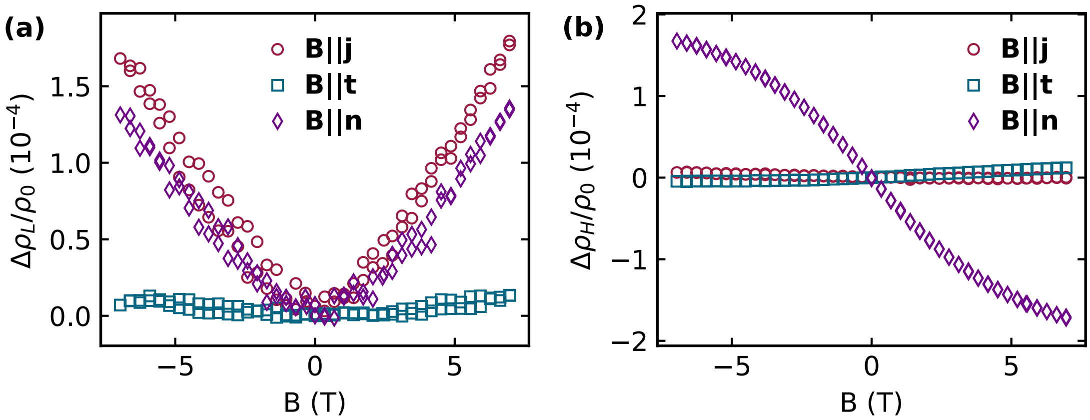

Figure 6.1: Observation of the Hanle magnetoresistance (HMR) in 5 nm Pt as detailed in Ref. [55]. (a) The longitudinal HMR arises for **B**||**j** or **n** as described by Eq. (5.4). (b) An additional transverse component can arise for **B**||**n** and is mathematically expressed by Eq. (5.5). The transverse HMR cannot be observed along other directions due to the experimental setup. *The data in this figure was obtained and provided by G. Sala.*

diffusion length.

However, despite the extensive use in spintronics, no unambiguous features stemming from the OrbHE in Pt have been reported so far [216, 217]. These results can be traced back to the large SOC in Pt. Due to the coupling, the OrbHE is converted into the SHE in these materials [191] and only one effective diffusion length is expected to arise [218]. Nonetheless, Pt is known to be able to absorb and convert orbital angular moment, which results in larger accumulations, torques and transport effects [38, 39]. Hence, the absolute amplitude of the HMR could be affected by the orbital Hall effect. Magnetoresistance experiments over a wide range of thicknesses could be a means to resolve the orbital contribution in Pt.

In the following, the magnetotransport properties of Pt thin films on isolating substrates will be thoroughly investigated. Here, signatures of the SHE are expected to manifest in the HMR and contributions of an OrbHE discussed. The results are then extended to light metal Ti, which is predicted to host a large OrbHE and a negligible SHE. In both cases, signatures of the spin or orbital Hall effect are found in samples without apparent (or with low) crystalline order and high resistivity, whereas crystalline, low resistivity samples do not show a measurable Hanle MR.

6.2 Competing ordinary and Hanle magnetoresistance in Pt thin films

This section details the transport results of Pt thin films of various thicknesses, from two different places of fabrication and on various substrates. If not explicitly specified, all Pt films discussed in this section were deposited in Konstanz. When comparing these films to other Pt samples they are thus referred to as ”Pt from Konstanz” (K_{Pt}). This Pt is thoroughly characterised in the next subsection and afterwards analysed following Hanle and ordinary MR theory. The dominant effect in Pt from Konstanz is the ordinary MR, while in seemingly identical samples, the Hanle MR dominates. As a comparison, Pt from Zurich is utilised. A typical film 5 nm thick film is depicted in Fig. 6.1, which is referred to as $Z_{Pt}(5)$ throughout the section. The material parameters influencing the prevalent magnetoresistance are evaluated and discussed throughout this section.

6.2.1 Structural and electrical characterisation of Pt thin films

After the deposition, each Pt film from Konstanz is electrically characterised. The coordinate system and convention was introduced in chapter 5 and is depicted again in Fig. 6.2(a). Transverse and longitudinal contacts are used to measure the respective voltage drop and extract the corresponding resistivity ρ as well as the MR, via the geometrical lengths known from section 5.3. Figure 6.2(b)-(d) depict the results for a 8 nm thick Pt film deposited on a MgO substrate. The measurements were performed at 300 K, with magnetic field sweeps measured along the current ($\mathbf{j}$), parallel to the surface normal ($\mathbf{n}$) and perpendicular to both ($\mathbf{t}$) for up to $\pm$ 6 T. The MR is then calculated as given by Eq. (5.2).

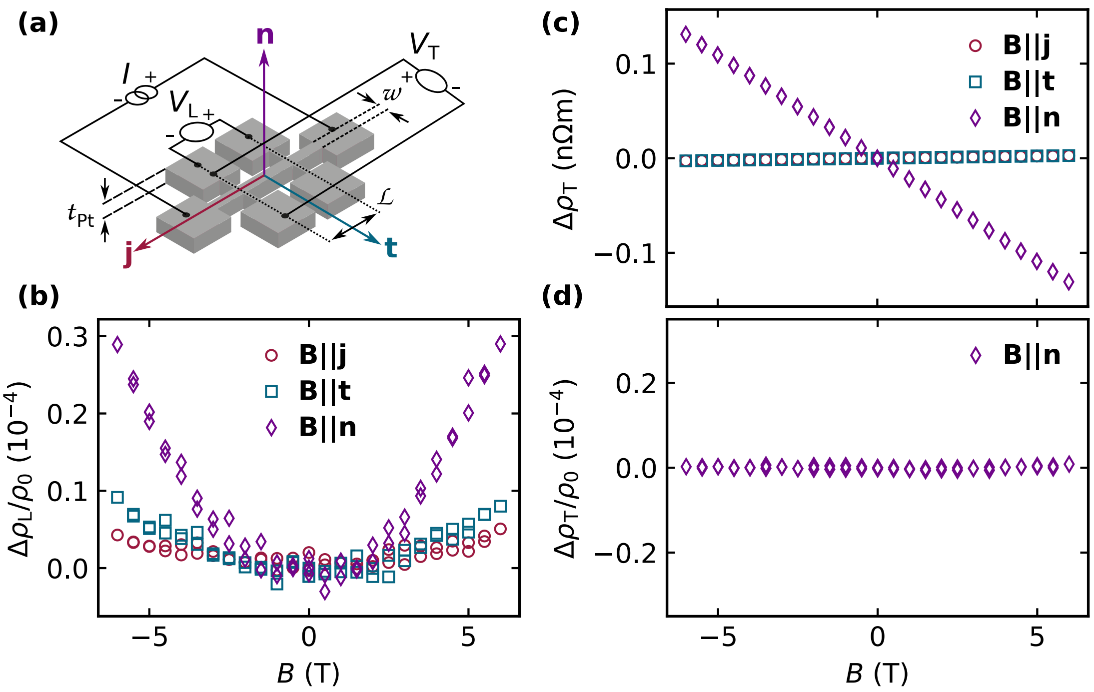

Figure 6.2: Electrical characterisation scheme for a 8 nm thick Pt film deposited on MgO. (a) Hall bar, with the dimensions defined by lithography (width w, length L and thickness t_{Pt}), as well as electrical contacts (longitudinal and transverse voltage drop V_{L} and V_{T} and source current I). The coordinate system is spanned by **j**,**t**,**n**. (b) Longitudinal and (c) transversal MR for an external magnetic field **B** applied along each coordinate axis. A parabolic increase can be observed in the data for the longitudinal MR, whereas the transversal MR only exhibits a linear slope for **B**||**n**. Possible constant longitudinal offsets in (c) were subtracted for visibility reasons. The linear slope in (c) can be attributed to the ordinary Hall effect (cp. Eq. (5.6)). After subtraction of a linear contribution, no residue is observed in (d). The observations in (b) and (d) are in contrast to the Pt films detailed in section 5.2.1, Fig. 6.1.

The longitudinal MR response is shown in Fig. 6.2(b), where a parabolic increase is observed for **B** along all three coordinate axis with the MR amplitude increasing from **j** over **t** to **n**. Contrary to the expectation from the Pt thin films presented in the introduction in Fig. 6.1(a) ($\mathrm{Z_{Pt}}(5)$), the curve shape and direction dependencies differ. Furthermore, the MR for Pt from Konstanz (Fig. 6.2(b)) is almost an order of magnitude smaller at the same B values in comparison to MR for Pt from Zurich (cp. Fig. 6.1(a)).

In Fig. 6.2(c) the corresponding transversal resistivity is depicted. Here, a possible offset, stemming from a longitudinal contribution to the signal, is subtracted for better readability. Only for **B**||**n**, a linear dependency on the magnetic field can be obtained. In the utilised geometry, this is expected and explained by the ordinary Hall effect, as given by Eq. (5.6). After applying a linear fit and subtracting it from (c), no residue can be observed, as shown in Fig. 6.2(d). A possible HMR contribution is expected to exhibit a non-linear dependency on B. Hence, the transversal MR in Fig. 6.2(c) also differs to the Pt from Zurich in Fig. 6.1(b), where a tanh like shape could be observed for **B**||**n**.

The Pt thin films deposited in Konstanz (Fig. 6.2(b)) exhibit a MR contrasting the expectation from section 5.2.1 and the recent literature (cp. Fig. 6.1). The data from Sala et al. [55] is coherently explained using HMR theory (see section 5.2.1), where longitudinal and transversal MR corroborate each other. The MR data obtained for Pt from Konstanz exhibits a parabolic scaling in Fig. 6.2(b), which hints towards the OMR (see section 5.2.2). This interpretation is supported by the absence of an $\tanh(B)$ type residue after subtraction of the OHE in Fig. 6.2(d), as the HMR should be observable in both longitudinal and transversal geometry. However, the absence of a residue in Fig. 6.2(d) does not allow for a definite conclusion, as the curve shape is determined by $\lambda_{\mathrm{s,1}}$ and D and can be linear within the detection limit [171]. Therefore, a contribution of the HMR to the longitudinal data cannot be ruled out and a unambiguous identification of the occurring MR will be conducted in the following.

6.2.2 Analysis of the occurring magnetoresistance following Hanle magnetoresistance theory

To identify the MR contributions observed in the Pt thin films from the previous section, both evaluations following Hanle and ordinary MR theory are conducted. Now, the Hanle MR is considered. To that end, multiple Pt thin films with thicknesses between 4 nm and 120 nm are measured as described in Fig. 6.2. This series allows for a thickness evaluation, which should shed light into a possible HMR contribution, as a characteristic peak is expected for a multiple of $\lambda_{\mathrm{s,1}}$ (see Fig. 5.2(c)). Both the longitudinal as well as the transversal resistivity is extracted and depicted in Fig. 6.3.

Figure 6.3(a) depicts the longitudinal MR $\Delta\rho_{\mathrm{L}}/\rho_0$ at 6 T, as a function of the film thickness for **B**||**j**, **t** and **n**. A non-trivial, non-monotonous thickness dependence can be observed along all field sweep directions. However, the thickness dependence exhibits the same features in all three field sweep directions. This observation contradicts the expectation from the HMR, where comparable amplitudes are expected for **B**||**j** and **n**, whereas no MR is expected for **B**||**t**. The thickness dependence supports the earlier findings that the MR cannot be explained via (spin) HMR theory alone.

In order to approximate the value of the HMR contribution and isolate it from the OMR, the scaling reported by Sagasta et al. [45] is utilised to calculate the expected spin diffusion length λ_{s} via Eq. (6.1),

$$\lambda_{\mathrm{s}} = C/\rho_0 \tag{6.1}$$

as well as the spin Hall angle θ_{s} via Eq. (6.2):

$$\theta_{\mathrm{s}} = \sigma_{\mathrm{s}}^{\mathrm{int}} \times \rho_0 \tag{6.2}$$

Here, C is a constant linear slope of $0.61 \times 10^{-15}\,\Omega\,\mathrm{m}^2$, $\sigma_{\mathrm{s}}^{\mathrm{int}}$ the intrinsic spin Hall conductivity of $1.6 \times 10^5\,\Omega^{-1}\,\mathrm{m}^{-1}$ and ρ_0 the resistivity at 0 T [45]. In order to gain a representative ρ_0, the mean value is calculated from the resistivity of the samples between 4 nm and 15 nm, as for these thicknesses, the HMR is typically observed [171, 198]. The

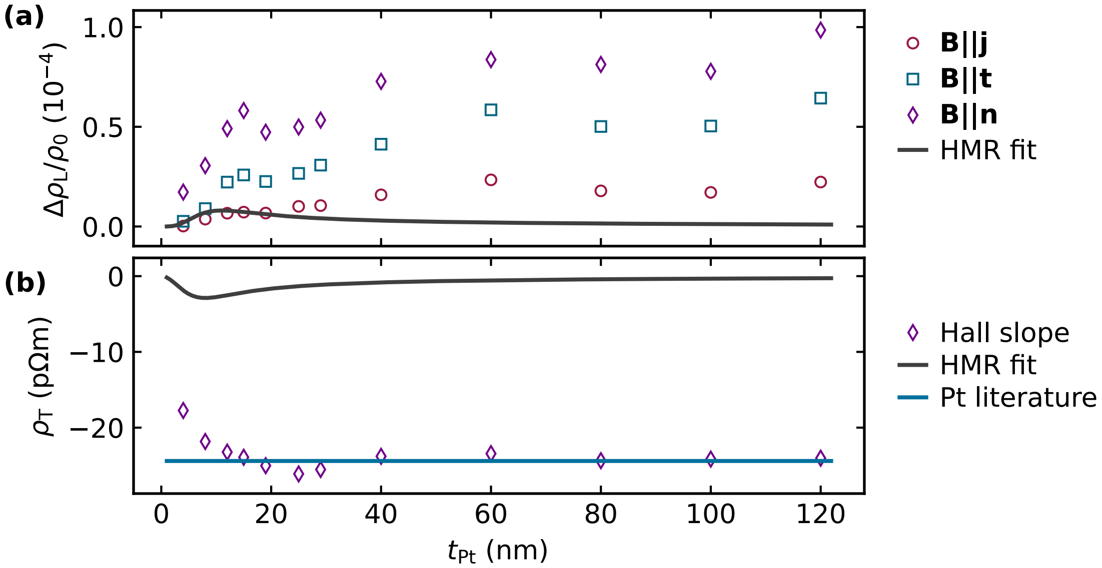

Figure 6.3: (a) Longitudinal MR $\Delta\rho_L/\rho_0$ as a function of Pt film thickness t_{Pt} for B-field sweeps along **j**, **t**, **n**. The MR is extracted according to Eq. (5.2) at 6 T. For **B** along all directions, the MR exhibits a non-trivial dependency on t_{Pt}. To analyse a HMR contribution, the expected longitudinal HMR (cp. Eq. (5.4)) is calculated using $\theta_s = 4\,\%$, $\lambda_s = 2.4\,\text{nm}$ (by following Eq. (6.2) and Eq 6.1, derived by Sagasta et al. [45]) and $D = 3.1 \times 10^{-5}\,\text{m}^2/\text{s}$ (extracted from a simple model detailed below in Fig. 6.11(b)) and plotted in the black curve. For **B**||**j**, these parameters reasonably capture the MR for Pt films with t_{Pt} below 20 nm, whereas thicker films show substantial deviation from the calculated HMR. Furthermore, from HMR theory, comparable amplitudes of the MR for **B**||**j** and **n** are expected, which is in contrast to the data. An additional MR contributing to **B**||**n** would be required to explain this. Additionally, no MR is expected for **B** along **t**, meaning that also here, a contribution in addition to the HMR is required. (b) Transversal resistivity ρ_T of Pt simultaneously measured for the samples depicted in (a). Each point corresponds to the linear slope at 1 T extracted from a fit to the data shown in Fig. 6.2(c) and is in good agreement with the bulk value of the ordinary Hall effect of Pt depicted in blue [201]. Using the same spin Hall parameters as in (a), the transverse HMR (cp. Eq. (5.5)) can be calculated and is given by the respective black curve. For t_{Pt} below 40 nm, a complex behaviour of ρ_T with the thickness is observed, which was previously reported for bilayers of YIG/Pt [219]. Above 40 nm, ρ_T can coherently be described via the ordinary Hall effect. This observation suggests that for these thicknesses, no further contribution to ρ_T from Hanle physics arises.

mean ρ_0 value is 249 nΩ m, which translates into a λ_s of 2.4 nm and a θ_s of 4 %. For the diffusion coefficient D, a value of $3.1 \times 10^{-5}\,\text{m}^2/\text{s}$ is used. This value is extracted from a simple model linking D to ρ_0 presented later in this chapter (see Fig. 6.11).

Using the extracted parameters, Eq. (5.4) can be modelled for a spin induced HMR, as visualised by the black line in Fig. 6.3(a). For Pt films with t_{Pt} below 20 nm, the calculated HMR is in reasonable agreement with the MR observed for **B**||**j**, however, above 20 nm, the calculated curve deviates from the data. After reaching a maximum, a decrease of the HMR amplitude towards higher t_{Pt} is expected, which is not seen within the data. Additionally, the calculation only captures the data for **B**||**j**, suggesting at least one further contribution in addition to the HMR stemming from spin Hall physics.

The transversal data acquired simultaneously should host a signature corresponding to the longitudinal data and is now discussed. To analyse the contribution, the transversal resistivity ρ_T is depicted in Fig. 6.3(b). Each point corresponds to the ordinary Hall resistivity at 1 T, obtained from the slope by a linear fit to the transversal data for $\mathbf{B}||\mathbf{n}$ (cp. Fig. 6.2(c)). The blue line represents the literature value of $-24.4\,\mathrm{p\Omega\,m\,T^{-1}}$ for Pt [201]. Next to the OHE, a contribution stemming from the HMR can arise in this geometry (cp. Eq. (5.5)). For t_Pt below 40 nm, the data points deviate from the bulk value and show a complex dependency on the thickness, a behaviour previously reported for yttrium iron garnet (YIG)/Pt bilayers in Ref. [219]. In contrast, all samples with $t_\mathrm{Pt} > 40\,\mathrm{nm}$ nicely fall onto the literature value of Pt.

Similarly to the above discussion on Fig. 6.3(a), the transversal (spin) HMR contribution can also be approximated to analyse a possible influence on ρ_T. To that end, the same spin Hall parameters are applied ($\rho_0 = 249\,\mathrm{n\Omega\,m}$, $\lambda_\mathrm{s} = 2.4\,\mathrm{nm}$, $\theta_\mathrm{s} = 4\,\%$ and $D = 3.1 \times 10^{-5}\,\mathrm{m^2/s}$) and the corresponding transverse HMR Eq. (5.5) depicted as the black curve in Fig. 6.3(b). Here, only a noticeable contribution to the OHE could be expected for t_Pt below 20 nm, where the data already exhibits a complex behaviour. Above 20 nm, the spin HMR negligibly influences the data and furthermore, the data is conclusively captured by the OHE.

Therefore, the transversal data corroborates the conclusion that no orbital HMR is present, while the spin HMR can neither be fully confirmed nor ruled out. If the orbital HMR with a different λ_l gave rise to the longitudinal MR in Fig. 6.3(a), the ρ_T value should deviate from the literature value of Pt as well, depicted as the solid blue line in Fig. 6.3(b). As this is not the case, a λ_l corresponding to the orbital Hall effect can be ruled out. For films below 20 nm, neither a subtraction nor addition of the transverse HMR (Eq. (5.5)) to the bulk ρ_T value fully captures the shape of the data. However, due to the complex behaviour, the spin HMR cannot be fully ruled out.

Combining the information from Fig. 6.3(a)+(b) allows to exclude the HMR as a major contribution to the observed MR. For t_Pt larger than 40 nm, ρ_T is described via the OHE (cp. Fig. 6.3(b)), suggesting that the longitudinal MR (Fig. 6.3(a)) for these thicknesses needs to arise from a different contribution. For lower thicknesses, the HMR cannot be ruled out completely. However, only the longitudinal MR for the first five samples for $\mathbf{B}||\mathbf{j}$ can be explained by HMR theory, while the complex behaviour of the transversal data does not unambiguously corroborate the HMR. Additionally, the MR for $\mathbf{B}||\mathbf{t}$ cannot be reconciled via the HMR and a different MR must arise (cp. section 5.2.1). Hence, the ordinary magnetoresistance (cp. section 5.2.2) is now considered.

6.2.3 Analysis of the occurring magnetoresistance following ordinary magnetoresistance theory

The same Pt data presented above in Fig. 6.2 is now analysed following OMR theory (see subsection 5.2.2). To that end, the longitudinal MR obtained at 6 T is plotted versus ρ_0^{-n} in Fig. 6.4(a), as a scaling of the MR with $\sigma = 1/\rho_0$ is expected from Eq. (5.8) and Eq. (5.10). Here, the MR is larger for samples with a lower resistivity. Therefore, the data

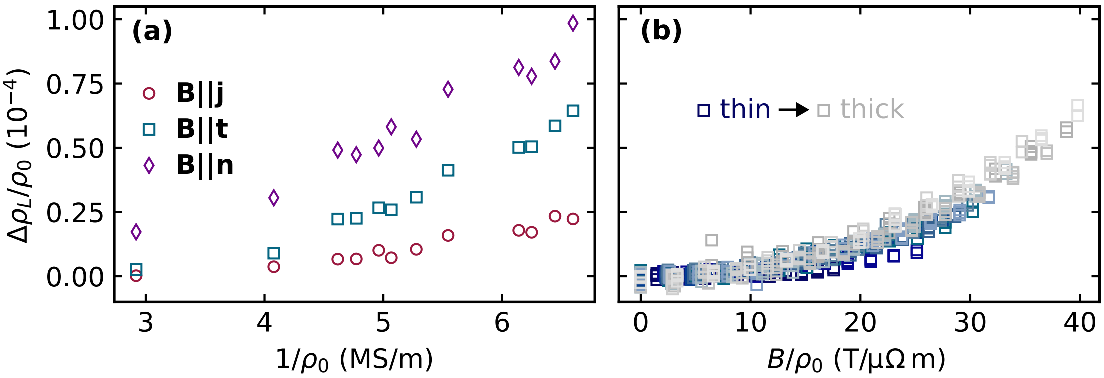

Figure 6.4: Longitudinal MR $\Delta\rho_{\mathrm{L}}/\rho_0$ as derived from Eq. (5.2) at 6 T as a function of (a) ρ_0^{-1} for **B** along all three coordinate directions and (b) B/ρ_0 for **B**||**t**. (a) highlights the scaling with the inverse resistivity, as previously suggested from the MR on different substrates (cp. Fig. 6.8). (b) depicts the data in a so called Kohler-plot. For the MR along **t**, no HMR is expected (cp. section 5.2.1), meaning an analysis via OMR theory following the dependency from Kohler's rule (cp. Eq. (5.10)) is justified (cp. section 5.2.2). A colour code from dark blue to gray is used to illustrate the respective thicknesses from 4 nm to 120 nm, respectively. Despite the varying thickness, the all samples depict a similar dependency on B/ρ_0.

corroborates the expected scaling from the OMR.

Figure 6.4(b) displays the so called Kohler-plot of the MR for **B**||**t** [208]. This direction is chosen, as no HMR is expected here (cp. section 5.2.1) and all contributions should stem from the OMR (cp. section 5.2.2). By plotting the longitudinal MR as a function of B/ρ_0, the dependency of Eq. (5.10) is immediately achieved. Furthermore, a comparison of different samples and at varying temperatures is possible, as changes in resistivity are considered this way [208]. The different thicknesses of the samples are given by the colour code gradually changing from dark blue (4 nm) to light gray (120 nm). Despite the differences in thickness, the scaling of the MR with B/ρ_0 is similar over all samples, which leads to the conclusion that the OMR is the main magnetoresistive effect for **B**||**t**.

In the following, the contributions to the MR for **B**||**j** and **n** are discussed. The MR along **n** cannot be conclusively understood as a combination of HMR (**B**||**j**) and OMR (**B**||**t**) for the first samples in Fig. 6.3, as their amplitudes do not add up to yield the observed MR (**B**||**n**). Additionally, for samples thicker than 20 nm, the HMR theory was not enough to describe the thickness dependence (cp. Fig. 6.3).

Therefore, each individual sweep for **B** along **j**, **t** and **n** was fit with Eq. (5.10), to determine if the OMR represents the dominant effect along all directions. Figure 6.5 presents the results of this analysis as a function of Pt thickness t_{Pt}. The resistivity of each sample is depicted in Fig. 6.5(a), where a thickness dependence can be observed, which is well known and commonly modelled using an extended Fuchs-Sondheimer model, as given by Eq. (6.3) [43, 204, 205].

$$\rho_{0,\mathrm{Pt}} = \rho_{\mathrm{inf}} \left(1 + \frac{3}{8(t_{\mathrm{Pt}} - h)} [l_{\mathrm{inf}}] (1 - p) \right) \tag{6.3}$$

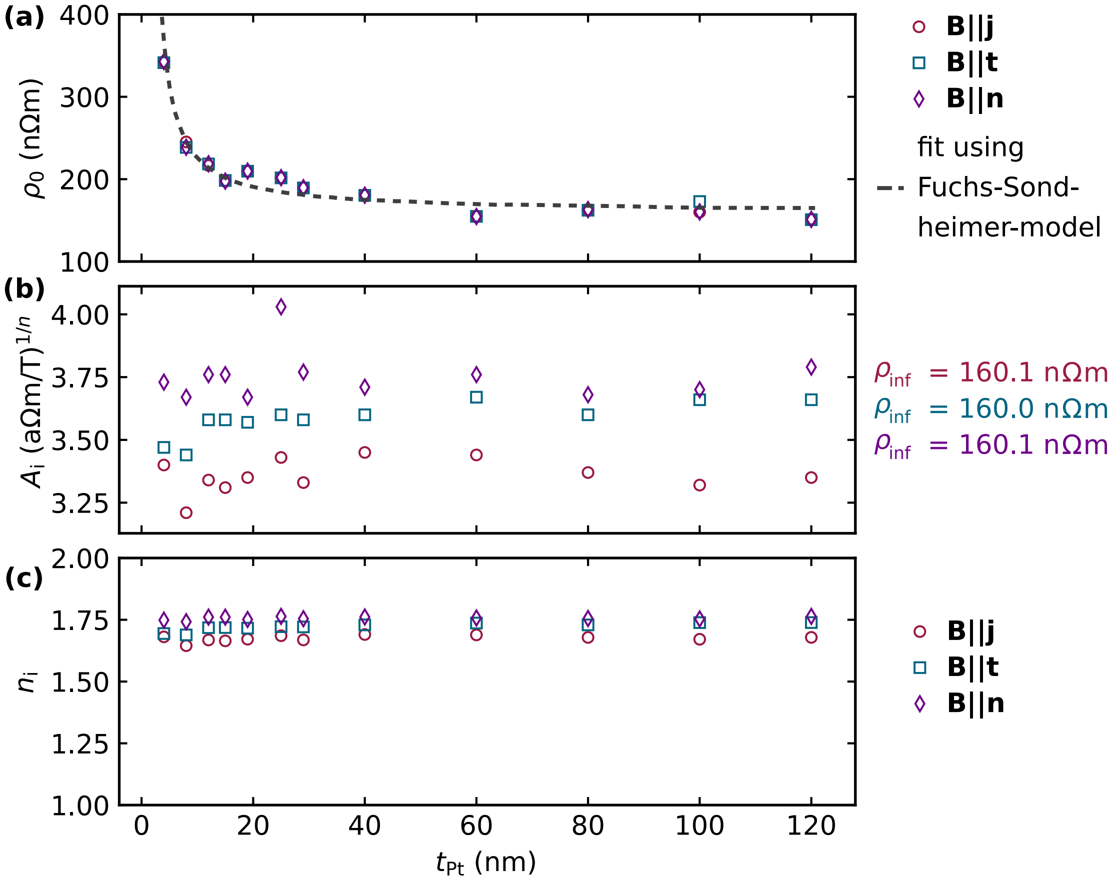

Figure 6.5: (a) Resistivity at 0 T ρ_0, (b) amplitude A_i as well as (c) exponent n_i of the respective Kohler fit versus the sample thickness. The resistivity for the bulk value is derived using an extended Fuchs-Sondheimer model [43, 204, 205]. The parameters obtained from fitting Eq. (5.10) to each individual sample along **j**, **t**, **n**, are almost identical for all samples and independent of the thickness. The mean values for A_i are 3.35, 3.58 and 3.75 (aΩm/T)$^{1/n}$ and 1.67, 1.72 and 1.76 for n along **j**, **t** and **n**, respectively.

Here, h is the surface roughness amplitude, p the scattering parameter at the surface, ρ_{inf} the resistivity and l_{inf} the mean free path for an infinitely thick film, respectively. For the fitting routine, $t_{\text{Pt}} > h$ is required and the diffusive limit of $p = 0$ is utilised, resulting in bulk resistivities ρ_{inf} of 160.1 nΩ m, 160.0 nΩ m and 160.1 nΩ m for Pt measured along **j**, **t** and **n**, respectively. The fit to the data is depicted with the dashed line in black in Fig. 6.5(a), nicely reproducing the behaviour of the resistivity.

Figure 6.5(b)+(c) depict the amplitude A_i and the exponent n_i as obtained from fitting Eq. (5.10) to the data. Both, A_i and n_i exhibit the lowest values for **B**||**j**, increase for **B**||**t** and show the largest values for **B**||**n**, with i describing the respective direction. However, the value only changes slightly across all samples, yielding mean amplitudes A_i of3.35 (aΩm/T)$^{1/n}$, 3.58 (aΩm/T)$^{1/n}$ and 3.75 (aΩm/T)$^{1/n}$ and exponents n_i of 1.67, 1.72

and 1.76 for **B** along **j**, **t**, **n**, respectively. The extracted exponents are in good agreement with a n_n value of 1.8 previously reported for Pt in Ref. [200]. Moreover, A_i and n_i only show a negligible dependence on t_Pt, indicating that the MR of all samples and along all directions is governed by the OMR.

Figure 6.5(b)+(c) showcase that the OMR amplitude and exponent vary for $\mathbf{B}||\mathbf{j}$, **t**, **n**, indicating a directional anisotropy of the OMR and, more importantly, a finite value for $\mathbf{B}||\mathbf{j}$. The latter seems unintuitive, as no OHE arises for this case. However, the occurrence of the OMR for $\mathbf{B}||\mathbf{j}$ was experimentally observed multiple times [199, 206] and can be reconciled by taking the current flow in the crystal into account, as detailed in section 5.2.2. As a result, defining a measured MR for $\mathbf{B}||\mathbf{t}$ as the OMR and subtracting it from simultaneously occurring effects, like the HMR along other directions, is insufficient for correctly identifying the individual contributions. This issue has been overlooked previously [198]. Additionally, the complex interplay of field and current direction with respect to the crystal orientation further complicates the analysis, meaning that amplitudes and exponents cannot be easily transferred. Only films without apparent structural order or those with current and field direction along highly symmetric crystal orientations are expected to yield similar values. This crystallographic direction dependence is further the cause of the anisotropy in A_i and n_i observed here (cp. Fig. 6.5(b)+(c)), as our films exhibit a $\langle 111 \rangle$ texture along **n** (cp. Fig. 6.8(d)). Even when assuming a coherent texture in plane, the respective crystallographic directions must differ from the out of plane direction.

Figures 6.4(a) and 6.5 demonstrate that the longitudinal MR $\Delta\rho_\mathrm{L}/\rho_0$ in Pt consistently scales with ρ_0^{-n} as described by Eq. (5.10) and not with the film thickness, as previously implied by Fig. 6.3. As ρ_0 differs between the samples, the resulting MR changes with it and thereby with the thickness. The fluctuations in ρ_0 (cp. Fig. 6.5(a)) artificially cause the thickness dependence previously discussed for $\mathbf{B}||\mathbf{j}$. Specifically, the reduced ρ_0 of the Pt films with t_Pt of 15 nm and 60 nm, in comparison to the surrounding samples, is the reason for a larger OMR resulting in the apparent peaks in Fig. 6.3. Additionally, the Pt films with the lowest resistivity (cp. Fig. 6.5(a)) are those that exhibit the largest MR observed in Pt on MgO (cp. Fig. 6.3), fully in line with OMR theory (cp. section 5.2.2). This observation further solidifies the conclusion that the here investigated Pt samples are dominated by the OMR.

The dependence of the HMR on ρ_0 is more complicated (cp. Eq. (5.4)), as indicated by Vélez et al. [171]. Here, they discuss different regimes, but extract no clear scaling. A more systematic approach is achieved by taking the established intrinsic scaling of $\lambda_\mathrm{s} \propto 1/\rho_0$ (cp. Eq. (6.1)) and $\theta_\mathrm{s} \propto \rho_0$ (cp. Eq. (6.2)) into account in combination with $D \propto 1/\rho_0$ derived later in Fig. 6.11(c). Taking these dependencies into account, results in a minimal influence of ρ_0 on the absolute HMR amplitude, with only the maximum value shifting to lower (higher) Pt thicknesses with an increase (decrease) of ρ_0, due to the changing λ_s (cp. Eq. (6.1) and Fig. 5.2). However, in order to explain the maximum observed in Fig. 6.3 at 60 nm, a λ_s of 13.1 nm would required. Using Eq. (6.1), this would require ρ_0 to be below the bulk resistivity of Pt [202]. Since no scaling on ρ_0 is expected for the HMR the previous analysis is further corroborated.

The different scaling is further highlighted in Fig. 6.6. In (a), the Kohler-plot for the

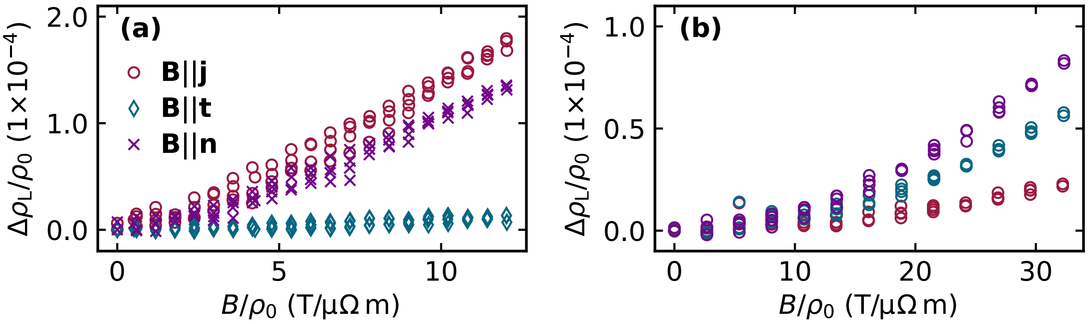

Figure 6.6: Kohler plot depicting a sample governed by (a) the HMR (same Pt film as in Fig. 6.1) and (b) the OMR (60 nm Pt on MgO).

Pt film from Zurich ($Z_{Pt}(5)$) showing a MR consistent with Hanle physics is depicted (cp. Fig. 6.1, while in (b) the low resistivity 60 nm Pt film on MgO is illustrated. One immediately notices the differences in the slopes, especially between the field sweep directions. Despite the similar MR amplitudes, the dependency on B/ρ_0, as well as the values reached on the B/ρ_0 axis, differ largely. As $B/\rho_0 \propto \omega_c\tau$ (cp. Eq. (5.8)), the scattering behaviour is different between the samples, validating the two different dominating MR effects. For the HMR, lower $\omega_c\tau$ seem to be favourable, whereas the opposite is true for the HMR. Furthermore, if the HMR was dominant in thin Pt films on MgO (as suggested by the calculated HMR in Fig. 6.3), a deviation from A_i and n_i in comparison to the thicker samples should be visible. The consistent values in Fig. 6.5(b)+(c) further suggest that even the thin Pt samples are fully dominated by the OMR.

Lastly, the temperature dependence of Pt on MgO for **B**||**n** is depicted in Fig. 6.7, which corroborates the previous findings. Here, Fig. 6.7(a) depicts the resistivity, which decreases as a function of temperature, in a typical manner for Pt [171, 214]. Figure 6.7(b) depicts the corresponding longitudinal MR versus the absolute temperature. In comparison with (a), a direct scaling between MR and resistivity can be observed, which is characteristic for the OMR, as detailed in section 5.2.2 (cp. Eq. (5.8)). The OMR was routinely investigated at low temperatures as the effect then becomes large [199]. In contrast, spin (orbital) current induced effects exhibit the opposite behaviour, as fewer spin (orbital) dependent scattering occurs, reducing, e.g. the MR amplitude with lower temperatures [55, 171, 214].

The thorough investigation and careful analysis of Pt from Konstanz on MgO leads to the conclusion that the OMR is the dominant magnetoresistive effect in these samples. The HMR contribution cannot fully be ruled out for the MR along **j** in these films, but is excluded as the dominant contribution. These results now raise the question, why the HMR is negligible for Pt from Konstanz, while a large HMR is observed on comparable samples (cp. Pt from Zurich Fig. 6.1 and Refs. [55, 171]). The differences in substrate and capping layer between the samples will be discussed in the next subsection.

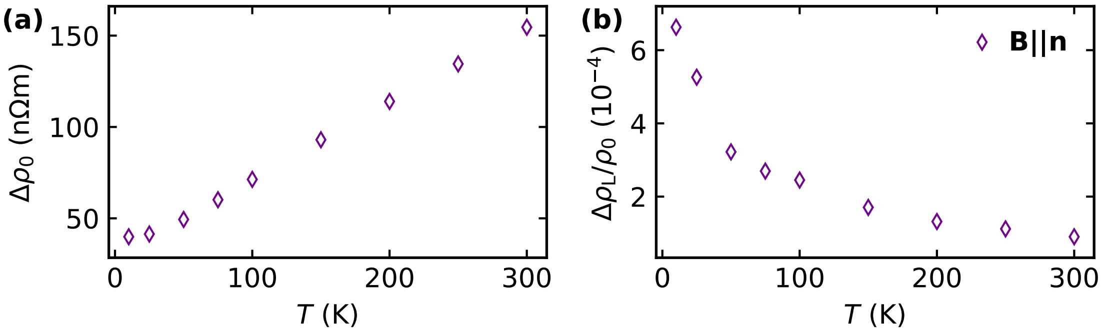

Figure 6.7: (a) Resistivity and (b) longitudinal MR at 6 T with **B** along **n** versus temperature for a typical sample. A decrease in resistivity is accompanied by an increase in MR amplitude towards lower temperatures. This linked behaviour highlights the scaling of the MR with ρ^{-n} and further corroborates the OMR to be the dominant effect. In comparison, for spin (orbital) current induced effects, like the HMR, a decreasing amplitude with decreasing temperature is most commonly observed [55, 171, 214].

6.2.4 Influence of substrate and capping layer on the resulting MR

Several differences between the Pt deposited in Konstanz are now discussed in comparison to Pt from Zurich [55] and other studies [198, 214]. This analysis aims to rule out influences which are not intrinsic to the Pt.

The Pt thickness of 8 nm of the sample from Konstanz (K_{Pt}) in Fig. 6.2 differs slightly to the 5 nm of $Z_{Pt}(5)$ in Fig. 6.1. While the thickness exhibits a large influence on the HMR, the maximum of the HMR for typical Pt parameters, i.e. θ_s, λ_s and D is expected near t_{Pt} of 8 nm (cp. Fig. 5.2). Further, the HMR amplitude falls off slower towards thicker films, ruling the Pt thickness out as a main reason for the differences in the MR response.

Further, different substrates are utilised throughout HMR studies of Pt, which is why the influence of the substrate is now specifically investigated. Both the HMR and the OMR are intrinsic to the Pt and, hence, should not depend on the substrate. However, a substrate is needed for thin films studies and an interface inevitable. Further, Li et al. [198] observe a large HMR due to a reduced diffusion coefficient D, which they attribute to the Al_2O_3 substrate. Other groups commonly use thermally oxidised Si wafers [171, 214, 218], where they find a MR in accordance with HMR theory. In contrast, the Pt films from Konstanz discussed in the previous subsections were deposited on MgO.

In order to analyse a possible influence of the substrate, 20 nm of Pt is deposited onto four different substrates during a single sputtering process. The substrates are MgO, YAG, Sapphire and SiO_x as introduced in section 5.3, allowing for a good comparison with the literature. The longitudinal MR of Pt on all four substrates is depicted in Fig. 6.8(a)-(c), with the field sweeps along **j**, **t**, **n** shown in (a),(b),(c), respectively. The MR response is comparable to the one in Fig. 6.2 and overall very similar on all substrates. The resistivity of the Pt film on MgO, YAG, Sapphire and SiO_x is 176 nΩ m, 180 nΩ m, 183 nΩ m and 220 nΩ m, respectively. The highest resistivity of Pt on SiO_x corresponds to a slightly reduced MR observed there in comparison to the other three substrates. This observation

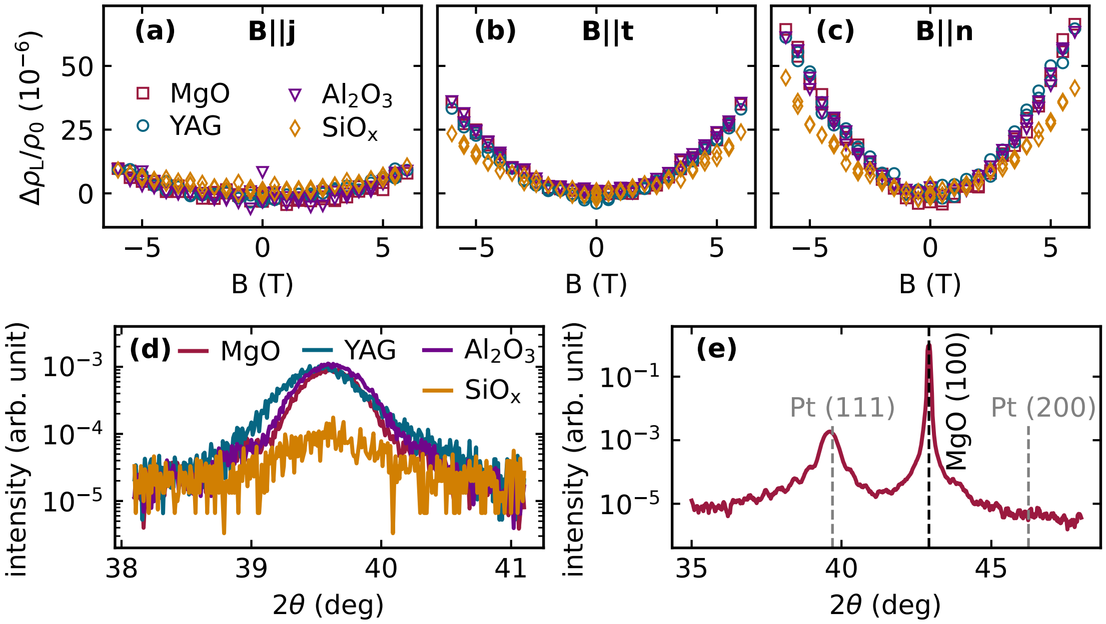

Figure 6.8: (a)-(c) Influence of the substrate on the longitudinal MR, as well as the crystalline quality probed by X-ray diffraction (XRD) in (d)+(e). Here, 20 nm of Pt are deposited onto YAG, MgO, Sapphire and SiO$_x$ (see section 5.3) during a single process and characterised at room temperature. Overall, the transport response of Pt is comparable on all substrates along all directions **j,t,n** in (a),(b),(c), respectively. A slightly higher resistivity of 220 nΩ m is obtained for Pt on SiO$_x$, which corresponds to a lower MR in comparison to Pt on the other three substrates (with 176 nΩ m, 180 nΩ m, 183 nΩ m on MgO, YAG and Sapphire, respectively). The resistivities correlate well to the intensity of the Pt ⟨111⟩ peak as obtained via XRD. After normalisation with the intensity of the substrate, a reduced signal is obtained for Pt on SiO$_x$, signalising a correlation between structural and electrical properties. However, a change in structural quality on the different substrates does not change the curve shape or field dependency of the observed MR, ruling the substrates out as a major contribution to the MR.

indicates a scaling with the resistivity, as suggested by OMR theory (cp. section 5.2.2).

In Fig. 6.8(d), the X-ray diffraction (XRD) data of each Pt film on each substrate is depicted. Here, a peak near 39.6 deg is evident, which corresponding to Pt ⟨111⟩ orientation. Figure 6.8(e) further depicts Pt on MgO over an extended scan range, where next to the Pt ⟨111⟩ peak also the Pt ⟨200⟩ is included. However, only the ⟨111⟩ peak is visible, which suggests a strongly textured Pt film. This out of plane texture is well known for Pt and expected for room temperature deposition processes [220].

The out of plane texture arises on all substrates in Fig. 6.8(d). Here, the Pt peak intensity on YAG, Sapphire and MgO is comparable. Further, on these substrates, Laue oscillations can be observed in the X-ray data, signalising a high crystalline quality. On the amorphous SiO$_x$, the intensity of the Pt peak is reduced in comparison to the other three. Therefore, Fig. 6.8 illustrates that the substrate can exhibit an influence on the Pt layer in the form of its crystal quality, which corresponds to a higher resistivity. The dependency on the crystallinity of the metal layer will be discussed again later in subsection 6.2.6. However,

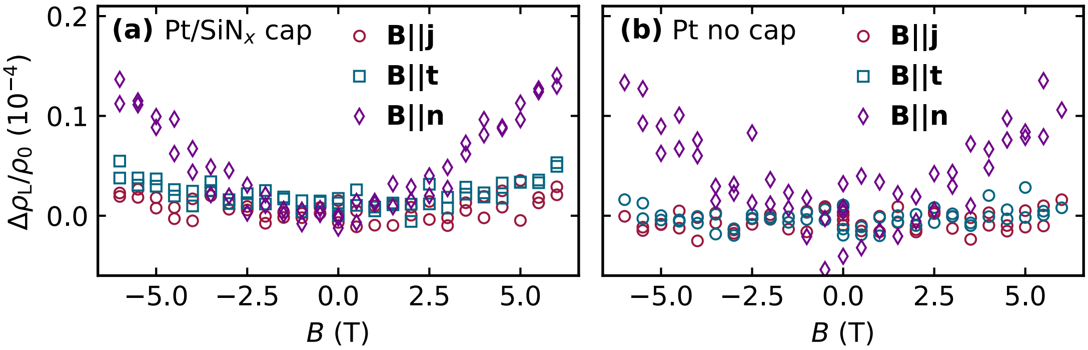

Figure 6.9: Longitudinal MR of Pt on SiO$_x$ for a (a) capped film and (b) an uncapped one. Both films have comparable thicknesses of 6 nm and 5 nm and resistivities of 398 nΩ m and 421 nΩ m, respectively. The transport response appears unchanged by an electrically insulating capping layer.

no significant influence on curve shape nor amplitude of the MR can be obtained by using a different substrate.

Lastly, a capping layer was utilised on Z$_{\mathrm{Pt}}$(5) by Sala et al. [55], which was not routinely done for the Pt films from Konstanz. Analogue to the substrate, no influence of the capping layer is expected. However, Pt is known to oxidise at the grain boundaries when not capped [221], which theoretically could influence the MR. To rule out an influence of the capping layer, two additional samples were deposited, as shown in Fig. 6.9. The 6 nm Pt thin film in Fig. 6.9(a) is capped and exhibits a resistivity of 398 nΩ m, while the 5 nm film in Fig. 6.9(b) is uncapped and shows a resistivity of 421 nΩ m. The transport response of both samples is very comparable to the previous ones in Fig. 6.2 and Fig. 6.8 and suggests that a continuous, electrically insulating capping layer does not significantly change the MR of the thin film.

The characterisation of Pt thin films indicates that the MR is reproducible and intrinsic to the metal layer. Neither a fully insulating SiN$_x$ capping layer (cp. Fig. 6.9) nor different substrates (cp. Fig. 6.8) changed the MR amplitude or the field dependencies in a significant manner. The resistivity and structural properties appear to influence the MR, but only in amplitude. The curve shape and field dependency for Pt from Konstanz are reproduced over many different films in Fig. 6.2, Fig. 6.8 and Fig. 6.9, and always appear to follow ordinary MR theory. The intrinsic properties causing the dominant MR will be discussed in the next section.

6.2.5 Prevalence of ordinary and Hanle magnetoresistance in Pt thin films

Despite Pt being the prototypical material in spintronics with a large spin Hall effect [222], no signs of an HMR, induced by spin or orbital accumulation, was observed in the previous section. The conditions under which the HMR contribution is expected to dominate is now determined and the missing HMR signal reconciled, where the discussion revolves around the resistivity ρ_0 and the diffusion coefficient D.

To that end, the resistivity of the Pt films is analysed in more detailed, since a different scaling in ρ_0 was extracted for the OMR and HMR and a strong influence on the dominant MR was suggested. A comparison with Pt films from the literature is summarized in Tab. 6.1 and reveals that the HMR was exclusively reported in films exhibiting higher resistivities than those measured in this study [55, 171, 214, 215]. For the clean, low resistivity Pt from Konstanz, only the OMR is observed, whereas in contrast for moderately dirty, high resistivity Pt ($\rho_0 > 500\,\mathrm{n\Omega\,m}$ [55, 171, 214, 215]) only the HMR is observed. For Pt films with a resistivity in between, both the HMR and OMR were reported to occur simultaneously [198]. From this observation, the naïve rule of thumb can be extracted, that Pt thin films with a ρ_0 of roughly five times the bulk resistivity of $\rho_{\mathrm{Pt}} = 105\,\mathrm{n\Omega\,m}$ [202] commonly exhibit a dominating HMR effect.

However, a scaling in resistivity alone cannot fully explain the observed behaviour, nor predict the dominant MR alone. This observation becomes evident from the ρ_0 of $341\,\mathrm{n\Omega\,m}$ for 4 nm Pt on MgO (cp. section 6.2.2) and the $421\,\mathrm{n\Omega\,m}$ for 5 nm Pt on $\mathrm{SiO_x}$ (cp. Fig. 6.9). Both films exhibit a MR consistent with OMR theory, whereas in this ρ_0 range, the HMR and OMR were reported to occur simultaneously (cp. Tab. 6.1) [198]. This observation indicates, that the resistivity alone cannot be the sole factor determining a dominant HMR (OMR). Considering the scaling of $\lambda_s \propto \rho_0^{-1}$ and $\theta_s \propto \rho_0$ as given by Eq. (6.1) and Eq. (6.2) [45], respectively, reveals that the diffusion coefficient D is the sole free parameter influencing the HMR in Eq. (5.4) and Eq. (5.5) and additionally the only variable where no definite scaling with ρ (σ) was reported.

Before discussing the influence of the diffusion coefficient D, it should be pointed out that the Pt from Konstanz is spin Hall active and spin current induced effects can be observed. When measuring the spin Hall magnetoresistance (SMR) [42, 209] on a bilayer consisting of YIG and 4 nm Pt, a large SMR of 3.5×10^{-4} can be measured. This SMR value is comparable to literature [43] and reproduced multiple times in the following chapter 7.1. A spin Hall inactive Pt can therefore be excluded. As both θ_s and λ_s appear in the microscopic description of the HMR (cp. section 5.2.1) and the SMR (cp. section 5.2.3), the diffusion coefficient D is the only differing parameter between the two magnetoresistances. Hence, D must exert a significant influence on the HMR amplitude and vary between the Pt from different groups.

A differing D value for the Pt from Konstanz can be motivated by the following calcu-

Table 6.1: Comparison of different studies on the HMR in Pt thin films. Depending on the resistivity of the Pt at zero field, either the OMR or the HMR dominate, with a range where both effects are observable.

Ref	ρ_0 ($\mathrm{n\Omega\,m}$)	MR
this work	151-341	OMR
Li [198]	200-500	OMR + HMR
Wu [214]	505	HMR
Sala [55]	580	HMR
Vélez [171]	631-1059	HMR
Maruyama [215]	500 - 7000	HMR

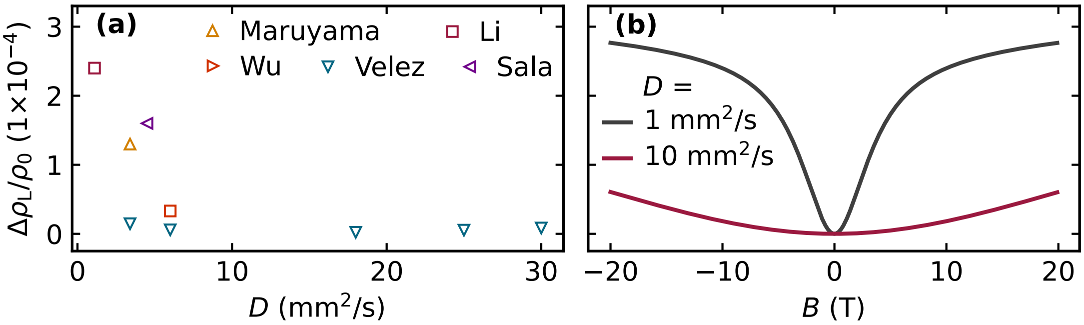

Figure 6.10: Influence of the diffusion coefficient D on the longitudinal HMR. (a) HMR at 6 T reported by different groups (cp. Tab. 6.1) versus D, where the HMR is larger in samples with a low D. (b) HMR calculated exemplarily with θ_s of 2.3 % and λ_s of 2 nm for a small (large) D resulting in a strong (weak) interaction with B. For large B values in combination with a slow diffusion (i.e. large τ_s) the HMR saturates as seen for a small D, fully corroborating the literature of (a).

lation for the 4 nm Pt thin film with ρ_0 of 341 nΩ m. By assuming a Pt specific D [214] of 3.4×10^{-6} m^2/s extracted for Pt in [171] allows for an approximation of the HMR. To that end, the theoretical λ_s of 1.8 nm (cp. Eq. (6.1)), as well as θ_s of 5.5 % (cp. Eq. (6.2)) are calculated. At 6 T, these parameters would result in a longitudinal HMR of 1.6×10^{-4} in contrast to the 2.6×10^{-6} observed for $\mathbf{B}\|\mathbf{j}$ in Fig. 6.2. This deviation clearly indicates that D strongly influences the HMR amplitude and that its value can differ between films.

Figure 6.10(a) depicts the longitudinal HMR at 6 T for thin Pt films (<7 nm) from the literature (cp. Tab. 6.1) versus D. All data is extracted for Pt films with t_{Pt} between 2-7 nm at room temperature, with the exception of the data from Vélez et al. [171], which was measured at 100 K. The data highlights the largely differing values of D in Pt thin films and the strong influence on the amplitude. Generally, a lower D is accompanied by a larger HMR.

The influence of D on the HMR is given by $\lambda_m = \sqrt{D\hbar/g\mu_B B}$ [171], which directly influences the amplitude of Eq. (5.4) and Eq. (5.5) through the $\mathfrak{R}$ and $\mathfrak{I}$ part, respectively. The diffusion coefficient exhibits the inverse effect as the magnetic field B, meaning an increase in D is met with a decrease in HMR amplitude. Via Eq. (6.4) [55, 198]

$$\tau_s = \lambda_s^2/D \tag{6.4}$$

the diffusion coefficient D and spin relaxation time τ_s are connected. τ_s is commonly used to describe the interaction of the spin accumulation with B [196]. Hence, for a constant λ_s, a large (small) D suggests a small (large) τ_s, which manifests in a weak (strong) interaction with B, as depicted in Fig. 6.10(b). Material systems with τ_s values above roughly 1 ps then exhibit a large HMR effect accompanied with a characteristic saturation towards large B values in the longitudinal (cp. Fig. 6.10(b)) and a strong tanh(B) dependency in the transversal MR data (cp. Fig. 6.1(b)) [198].

The HMR and the respectively extracted parameters are further analysed in Fig. 6.11

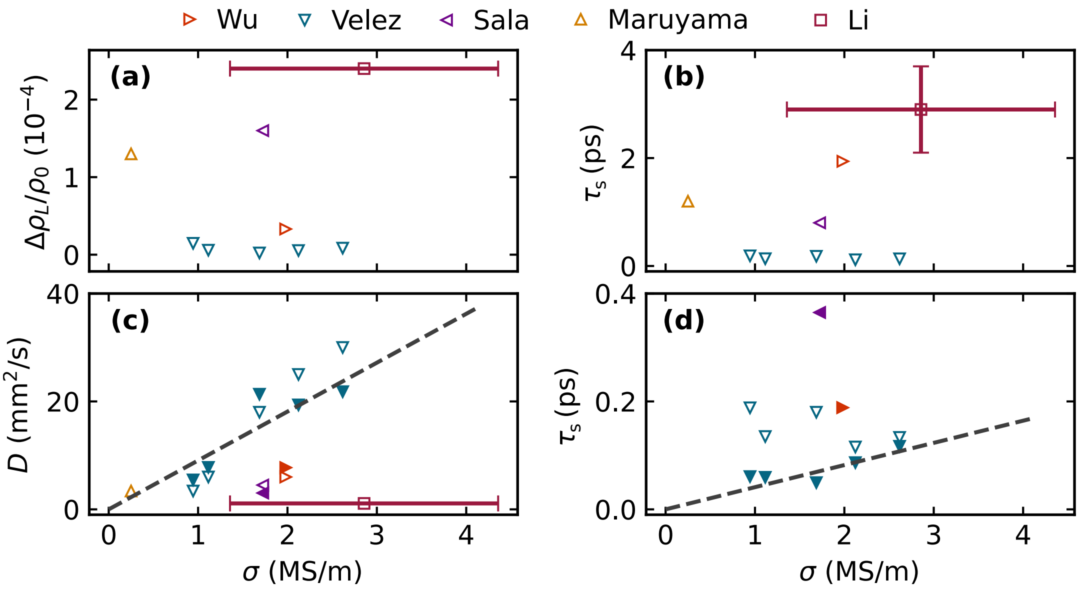

Figure 6.11: Literature comparison of the typical HMR parameters as a function of conductivity σ for reports from Tab. 6.1. (a) Longitudinal HMR at 6 T, (b) spin relaxation time $\tau_s = \lambda_s^2/D$, (c) diffusion coefficient D and (d) τ_s again on a smaller scale as in (b). To reconcile the different behaviour in HMR amplitude, not only the resistivity but also D (or τ_s) need to be considered. For both, a scaling with σ is expected since $\tau_s = \lambda_s^2/D$ and $\lambda_s \propto \sigma$ [45, 223]. From Eq. (5.7) a linear scaling of $\tau_s \propto \sigma$ is assumed, which then leads to $D \propto \sigma$. This linear behaviour is checked for the data in (c) and (d). Here, open symbols represent the values as detailed in the paper. However, due to different assumptions in the paper, a comparison is challenging. To that end, D and τ_s are calculated by taking the established scaling from Eq. (6.1) and Eq. (6.2) into account, which leaves D as the only free fit parameter of Eq. (5.4). The so extracted D and $\tau_s = \lambda_s^2/D$ are depicted by the full symbols and a linear fit is applied to the recalculated data from Vélez et al. [171]. The slope in (c) yields $9.06 \times 10^{-12}\,\Omega\text{m}^3\text{s}^{-1}$, which was used to calculate D for the HMR shown in Fig. 6.3(a) and (b). The linear behaviour in (c) and (d) highlights a scaling in σ, which can consistently explain the HMR parameters from one group. However, to reconcile the differences in extracted parameters for the HMR between groups, an additional contribution to the HMR besides $\sigma(\rho)$ is required.

to investigate the interplay of D with the resistivity ρ_0. The values are extracted from the same works as in Tab. 6.1 and Fig. 6.10. By taking the previously described dependencies into account, i.e., $\lambda_s \propto \sigma$ (cp. Eq. (6.1)) [45, 223], $\tau_s = \lambda_s^2/D$ (cp. Eq. (6.4)) in combination with the Drude-model $\sigma \propto \tau_s$ (cp. Eq. (5.7)), a proportionality of $D \propto \sigma$ and $\tau_s \propto \sigma$ is expected. Hence, all parameters are depicted as a function of conductivity $\sigma \approxeq 1/\rho_0$. Fig. 6.11(a) illustrates the HMR amplitude at 6 T, (b) the spin relaxation time τ_s, (c) the diffusion coefficient D and (d) a detailed section of (b). No direct scaling of the HMR with the resistivity can be observed in Fig. 6.11(a). This observation is reconciled by inserting all dependencies in Eq. 5.4. Then only a shift in the maximum towards different thickness is evident, which corroborates Fig. 6.11(a) and the earlier discussion that the HMR does not depend on ρ_0 (cp. section 6.2.3).

No obvious dependency of D or τ_s on σ can be observed throughout Fig. 6.11(b)-(d) between the groups, indicating that a simultaneous description is challenging and a scaling of D beyond the resistivity needs to be considered. In Fig. 6.11(c)+(d), open symbols are used for values directly extracted from the paper (cp. Tab. 6.1). However, depending on the reference, different assumptions were made, i.e., either θ_s [171], λ_s [55] or D[214] are fixed during the fitting routine. To account for these differences, λ_s and θ_s are recalculated via Eq. (6.1) and Eq. 6.2, respectively and then utilised to fit the HMR with D as the only free parameter. The so extracted values for D and τ_s are given by the filled symbols in Fig. 6.11(c)+(d). Despite the recalculation, no clear trend can be observed between different publications, implying that an additional contribution to D exists.

However, the HMR extracted from multiple samples by Vélez et al. [171] obtained after recalculation depicts a scaling in σ and is further evaluated in the following. Here, a linear fit is applied to the data given by the full symbols of D over σ in Fig. 6.11(c) with no y-axis offset being utilised. The fits result in a slope of $9.06 \times 10^{-12}\,\Omega\mathrm{m}^3\mathrm{s}^{-1}$ for D/σ as illustrated by the dashed line in Fig. 6.11(c). By using the slope known from Eq. (6.1) of $C = \lambda_s/\sigma$ of $0.61 \times 10^{-15}\,\Omega\,\mathrm{m}^2$ [45], a slope of $4.1 \times 10^{-20}\,\Omega\mathrm{ms}$ is obtained, which is depicted in Fig. 6.11(d). These results indicate that all Pt films from one group (Vélez et al. [171]) exhibit a linear scaling of both τ_s and D in σ, in addition to the scaling in σ applied via Eq. (6.1) and Eq. (6.2), suggesting a consistent description of their HMR with σ.

In contrast, D and τ_s for the remaining groups do not fall onto the linear extracted scaling in σ (cp. Fig. 6.11(c)-(d)), at times differing by orders of magnitude, highlighting an additional contribution to D. Several possible influences are discussed in the following.

A contribution to D from thickness or roughness differences between the films can be excluded. Variations here would only lead to a different ρ_0 (or σ) and could also not explain the large deviations in D nor the amplitude of the HMR. To fully exclude the thickness and roughness as a parameter, the ρ_{inf} value extracted from the Fuchs-Sondheimer model [43, 204, 205] in Eq. (6.3) should be compared. However, this data is only available for the Pt from Konstanz and further represents a scaling in ρ. Therefore, another contribution to D must be considered, which is not directly included in the resistivity.

A similar argument as before can be made for the interface, as indicated by the findings in section 6.2.4. Neither different substrates (cp. Fig. 6.8) nor capping layers (cp. Fig. 6.9) exhibited a significant effect. This observation can be reconciled by the fact that the HMR is governed by the (back) diffusion, i.e. the ISHE in Fig. 5.1(b). Even if a larger spin accumulation arises due to the emergence of a Rashba-Edelstein effect stemming from the interface [35], the relevant parameter for the HMR, D, is unaffected by this. Hence, the mechanism needs to be intrinsic to the Pt as well.

Further, a direct dependency from the deposition technique itself is unlikely. Sputtering was utilised here and in Refs. [55, 171, 214] as the deposition technique, yet the resulting films exhibit largely values in amplitude, D and τ_s (cp. Fig. 6.11(a)-(c)). Further, across all, the same substrates were utilised, corroborating the previous point.

Another influence could stem from the orbital Hall effect (OrbHE) in Pt [36], which could be contributing to the large HMR amplitude reported in Refs. [55, 198]. In Pt, only one effective λ is expected to arise [191, 218] due to the large spin orbit coupling in Pt, meaning a contribution to the HMR could not be resolved independently. However, as the back diffusion is not obviously affected by an additional contribution, the HMR might still not be observed and OrbHE alone cannot be the only contribution to D. Furthermore, the (inverse) OrbHE cannot be differentiated from the (I)SHE within the experimental setup.

While impurities from the deposition chamber or the target material can impact D, they are challenging to analyse. The deposition chamber can be excluded as a source of impurities for Pt from Konstanz, as many different users frequently used the system and no significant changes were observed for Pt over time. The purity of Pt itself is challenging to analyse. First of all, multiple targets are not economic and could not be tested. Second, impurities in the percent or permille range of nanometre thick Pt films are tough to quantify. Hence, the influence on this parameter cannot be fully resolved. Ref. [224] report surface states, which effectively trap the electrons resulting in a low D (high τ_s), which could stem from impurities or interaction at the interface.

It should be noted that magnetic substrates exhibit a large influence on the MR. In Refs. [171, 214], the HMR observed on YIG[1] is much larger than the respective HMR on SiO_x or Pyrex. Furthermore, Pt on amorphous YIG [225] exhibits a large MR despite no long range magnetic order in the YIG layer. While the MR is attributed to the spin Hall MR in Ref. [225], a large contribution from the HMR is feasible, stemming from a trapping of electrons, due to an interaction with local magnetic moments in the amorphous YIG. This interpretation is corroborated by the field dependency of the MR. However, this interplay can neither explain the differences in HMR amplitude observed in Fig. 6.11 nor the unresolvable HMR in the Pt from Konstanz, unless magnetic impurities were present in the Pt film or the substrates in Refs. [55, 198].

All aforementioned influences and parameters can theoretically impact the resulting MR, but are hard to quantify. In the following, an apparent influence of crystalline order is described and analysed.

6.2.6 Influence of crystallinity on the dominating MR

In the following, an influence of the crystallinity of the Pt thin films is proposed to be a contribution to D, as it differs between the Pt films in the literature [55, 171, 198] and further is quantifiable in contrast to, e.g. the purity. While deposition technique and (diamagnetic) substrates might not directly influence the HMR, both can impact the crystalline quality of Pt. High temperature deposition can lead to single crystalline Pt on the right substrate [220], while the influence of the substrates was already seen in Fig. 6.8. However, on all substrates Pt grew with a $\langle 111 \rangle$ texture, signalising that this change was narrow. A change in crystalline quality or crystallinity, i.e. amorphous vs polycrystalline vs single crystalline, should influence D, as both the diffusing species as well as the host material are known to influence the resulting D value at one given temperature [156].

To allow for the best possible comparison of crystallinity and MR, two sputtered Pt films with t_{Pt} of 5 nm are compared on SiO_x substrates. Hence, the sample from Konstanz $K_{Pt}(5)$ introduced earlier in Fig. 6.9(b) is compared to $Z_{Pt}(5)$, the sample from Zurich used throughout the section from Fig. 6.1. The structural and electrical characterisation

---

[1] Here, the HMR is detected as an MR increasing with B on top of the spin Hall MR contribution.

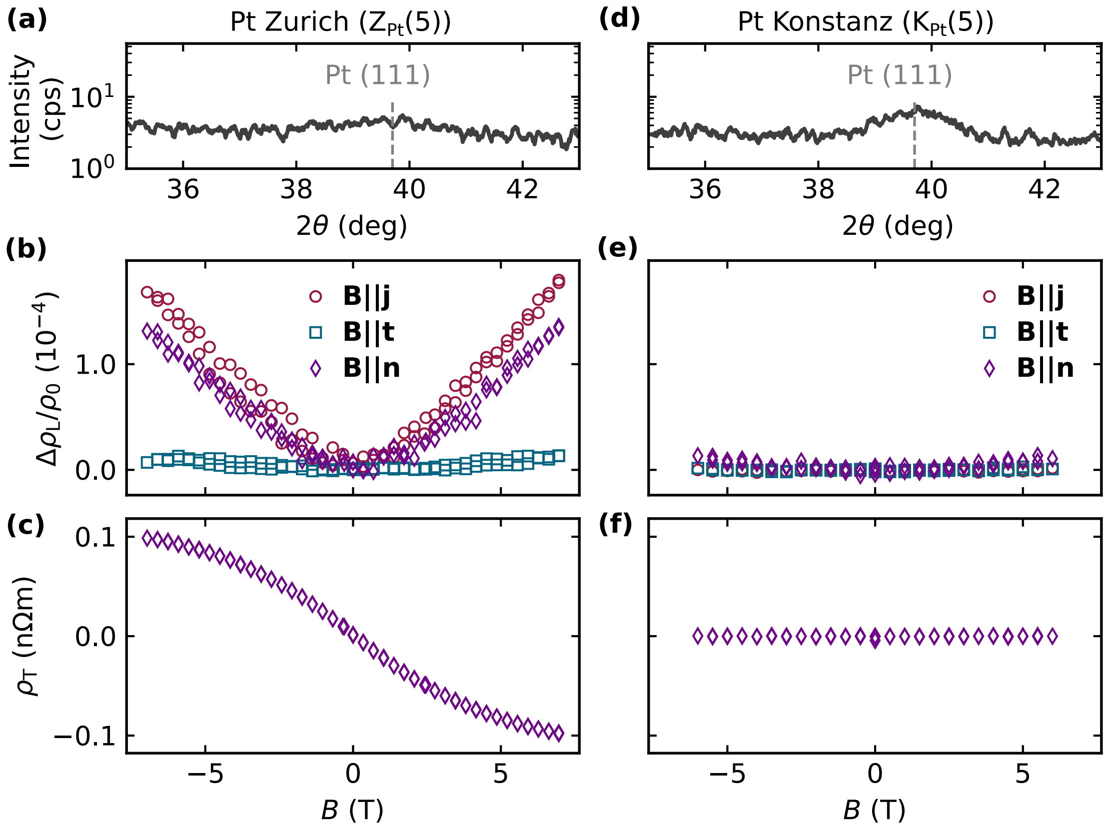

Figure 6.12: Characterisation and comparison of Pt from Zurich (left column, sample $Z_{Pt}(5)$, same as in Fig. 6.1 and Pt from Konstanz (right column, sample $K_{Pt}(5)$, same as in Fig. 6.9(b). Both samples consist of 5 nm Pt on SiO_2, for better comparability. In (a) the intensity obtained via X-ray diffraction (XRD) in symmetrical a $\theta - 2\theta$ scan is depicted. (b) illustrates the longitudinal MR and (c) the transversal resistivity after subtracting the linear ordinary Hall contribution (cp. Fig. 6.2) of $Z_{Pt}(5)$ along the relevant direction for the HMR, $\mathbf{B}\|\mathbf{n}$. (d)-(f) same for sample $K_{Pt}(5)$. A pronounced ⟨111⟩ peak can be observed in (b) in contrast to a small increase in intensity for (a). A correlation between crystallinity and HMR is plausible, where the less crystalline Pt ($Z_{Pt}(5)$) depicts an MR consistently described by Hanle theory [55], while the highly crystalline Pt (($K_{Pt}(5)$)) exhibits the ordinary MR. The difference in crystallinity will be discussed again for Ti in the following section 6.3.1.

was performed on two nominally identical samples samples where no lithography was performed.

The crystallinity is probed via X-ray diffraction (XRD) in symmetrical $\theta - 2\theta$ scans and shown in Fig. 6.12(a) and (b), for $Z_{Pt}(5)$ and $K_{Pt}(5)$, respectively. A pronounced Pt ⟨111⟩ peak can be observed for $K_{Pt}(5)$ in comparison to the significantly lower intensity exhibited by $Z_{Pt}(5)$. For Fig. 6.12(a) it is arguable if any relevant structural order formed. The Pt from Konstanz in Fig. 6.12(b) in any case exhibits more crystalline order, comparable to the earlier findings for 20 nm Pt in Fig. 6.8. Additionally, high crystalline quality Pt was obtained on crystalline substrates, exhibiting Laue oscillations on the ⟨111⟩ peak.

The transport properties of the two films were already discussed in great detail and are summarised with Fig. 6.12(b)-(f). $K_{Pt}(5)$ exhibits a ρ_0 of 421 nΩ m in comparison to the 580 nΩ m of sample $Z_{Pt}(5)$. Despite being nominally identical, the magnetotransport response significantly differs. Figure 6.12(b) and (c) depict the longitudinal HMR and the transverse resistivity (after subtracting the ordinary Hall contribution from ρ_T) for $Z_{Pt}(5)$ (same as Fig. 6.1). As discussed previously, the longitudinal and transversal data corroborate each other and the MR of $Z_{Pt}(5)$ is consistently explained in the Hanle picture [55]. In contrast, Fig. 6.12(e) and (f) depict the same for $K_{Pt}(5)$, where an amplitude of the longitudinal MR for $\mathbf{B}||\mathbf{j}$ lower than 1×10^{-6} at 6 T is extracted (for a better visualisation of the MR refer to Fig. 6.9(b)). The curve shape and amplitude of $\Delta\rho_L/\rho_0$ as well as the missing $\tanh(B)$ contribution in ρ_T are consistent with the findings in section 6.2.3 and show also in $K_{Pt}(5)$ the dominating MR is the OMR.

Despite $K_{Pt}(5)$ and $Z_{Pt}(5)$ being nominally identical and exhibiting only slightly different resistivity values, the dominating MR as well as the order of magnitude of the effect vary substantially (cp. Fig. 6.12). Since the Pt from Konstanz can be consistently understood via OMR theory and no HMR is observed, an influence of crystallinity and crystal quality is proposed, where a high crystallinity corresponds to a high diffusion coefficient. This proposition is corroborated by the theoretically expected D value for Pt from Konstanz of $3.1 \times 10^{-5}\,\mathrm{m^2/s}$. When observing the HMR, lower values of D in the order of $1 \times 10^{-6}\,\mathrm{m^2/s}$ to $6 \times 10^{-6}\,\mathrm{m^2/s}$ are commonly reported in the literature [55, 171, 198], which correspond to a larger HMR (cp. Fig. 6.10). Further, as the D for the Pt from Konstanz of $3.1 \times 10^{-5}\,\mathrm{m^2/s}$ was extracted from the ρ_0 scaling in Fig. 6.11(c), it only represents a lower limit. The exact value must be even higher, since the HMR could not be resolved. The observation is consistent with the previously described findings and with HMR theory (cp. Fig. 6.10).

The dependency on crystal quality is corroborated by a comparison with the available literature. For example, Vélez et al. [171] report barely any intensity for Pt and Sala et al. [55] investigate Mn films with no apparent structural order. Both observe an (orbital) HMR effect. Li et al. [198] report a highly crystalline Pt in which they observe both the HMR and the OMR. Their XRD data, however, is obtained for a 40 nm Pt film, which makes a direct comparison challenging. The simultaneous observation of ordinary and Hanle MR can be reconciled by attributing the OMR to the low resistivity and high crystalline quality of their Pt, whereas (magnetic) impurities would be needed to explain the resulting HMR and the extraordinary large τ_s values (cp. Fig. 6.11(b)). An attempt to reproduce the large HMR and τ_s solely due to the substrate was unsuccessful (cp. Fig. 6.8), which shows that impurities could be the subject of further study.

In conclusion, both the OMR and (spin) HMR arise in Pt layers, where the resistivity can be used as a rule of thumb, but alone is not enough to predict the dominating MR. A ρ_0 of roughly 5 times the bulk resistivity of Pt is commonly reported to lead to a dominating HMR. However, the crystallinity appears to exhibit an influence on the diffusion, which in turn can lead to low HMR values. Hence, even high resistivity films might not show the HMR. In contrast, the OMR becomes more prevalent the lower the resistivity. Here, the crystalline quality has a direct influence on ρ_0 and thereby on the MR. The OMR effect is small in Pt and can be further reduced by investigating high resistivity films.

The next section follows up on the influence of crystallinity and the interplay of ordinary and Hanle MR, where these characteristics are investigated and extended to the orbital Hall active material Ti.

6.3 Competing ordinary and Hanle magnetoresistance in Ti thin films

Orbitronics has become of major interest in recent years in recent years due to the large amount of materials expected to host an orbital Hall effect [36], which could be a means to improve, e.g. the spin-orbit torque efficiency [38]. In particular, the orbital Hall effect was experimentally observed in Ti [37] using optical methods (cp. section 5.1). However, no transport experiments were reported for Ti up to now. In order to characterise Ti regarding a possible orbital HMR, samples from Zurich and Konstanz are investigated, which are both sputtered on $\mathrm{SiO_x}$ substrates to ensure comparability, where $\mathrm{Z_{Ti}}(26)$ describes the sample from Zurich with $t_{\mathrm{Ti}} = 26\,\mathrm{nm}$ and $\mathrm{K_{Ti}}(30)$ a sample from Konstanz with $t_{\mathrm{Ti}} = 30\,\mathrm{nm}$.

6.3.1 Structural and electrical characterisation of Ti thin films

The electrical and structural properties are characterised as in the previous section (cp. section 6.2.1) and are detailed in Fig. 6.13, where the left (right) column represents the data from Zurich (Konstanz). In the XRD data (cp. Fig. 6.13(a)+(d)), a strong peak is observed for $\mathrm{Z_{Ti}}(26)$ near the Ti ⟨002⟩ peak position, which is the highest intensity peak for bcc-Ti, suggesting a (poly)crystalline film. In stark contrast, no crystalline order is observed for $\mathrm{K_{Ti}}(30)$ over the full scan range, signalising a completely amorphous film. Despite the similar thicknesses, strong differences in crystallinity are observed between the two films. The structural data can again be correlated to the electrical characterisation in Fig. 6.13(b)+(c) and (e)+(f), which corroborates the crystallinity as a key parameter influencing the dominant MR.

Figure 6.13(b)+(c) depict the longitudinal MR and the transversal resistivity of $\mathrm{Z_{Ti}}(26)$, respectively. This sample exhibits a resistivity of $1.31\,\mu\Omega\,\mathrm{m}$ and a $\Delta\rho_{\mathrm{L}}/\rho_0$ of roughly 1.5×10^{-5} at 6 T with a parabolic increase along all three sweep directions (cp. Fig. 6.12(b)), hinting at the OMR. The OMR is further supported by the absence of a residue in ρ_{T} stemming from an HMR contribution after subtraction of the ordinary Hall effect (cp. Fig. 6.12(c)). Due to the similarity to the previously discussed Pt films in Fig. 6.12(b)+(c), the transport response of the crystalline Ti film is therefore attributed to the OMR.

In contrast, Fig. 6.13(e)+(f) depicts $\Delta\rho_{\mathrm{L}}/\rho_0$ and ρ_{T} of $\mathrm{K_{Ti}}(30)$. This sample exhibits a resistivity of $2.49\,\mu\Omega\,\mathrm{m}$ and a large longitudinal MR of 1.4×10^{-4} for $\mathbf{B}$ along $\mathbf{j}$ and $\mathbf{n}$. This MR is almost 10 times larger than the value obtained for $\mathrm{Z_{Ti}}(26)$ in (b) and the data begins to saturate towards high B values, suggesting a dominant HMR effect. Additionally, the MR for $\mathbf{B}||\mathbf{t}$ is comparably small, signalising a negligible OMR contribution. Furthermore, the strong $\tanh(B)$ residue corroborates the interpretation via HMR theory. Due to the

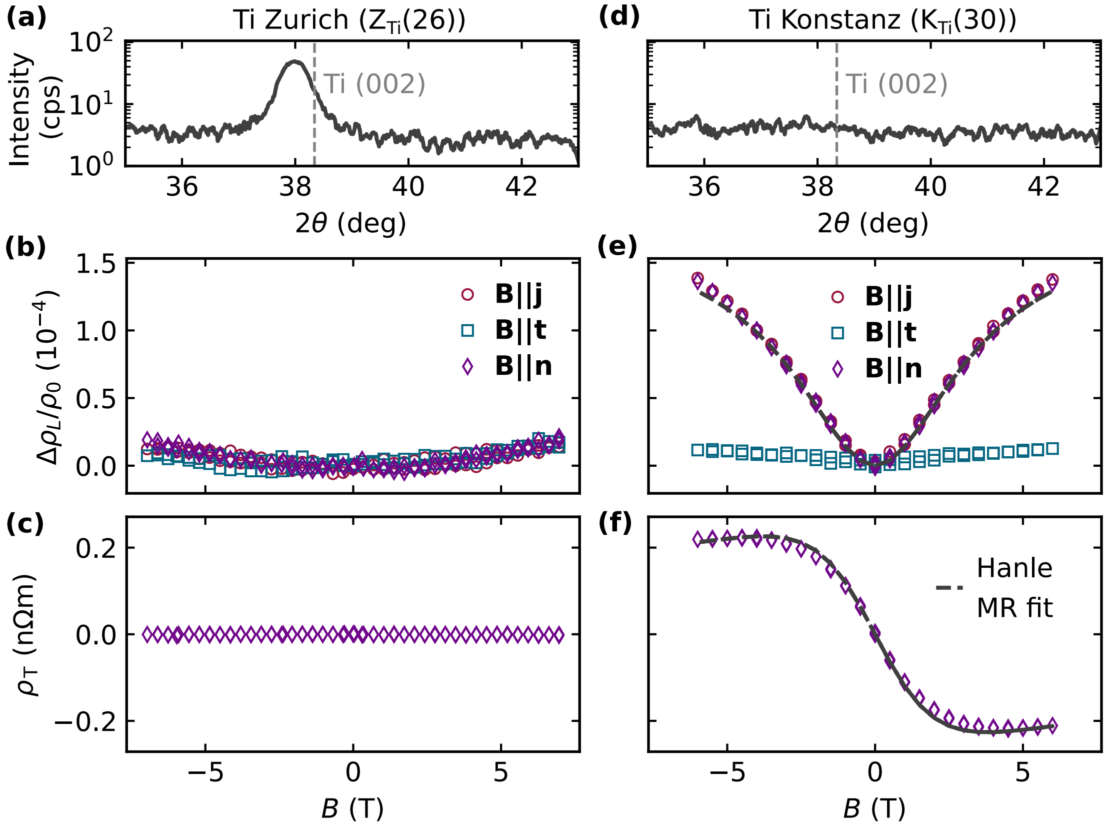

Figure 6.13: Characterisation and comparison of Ti from Zurich (left column, sample $Z_{\mathrm{Ti}}(26)$ and Pt from Konstanz (right column, sample $K_{\mathrm{Ti}}(30)$). (a)+(d) The XRD analysis shows significant differences in crystallinity, where $Z_{\mathrm{Ti}}(26)$ exhibits a strong peak near the ⟨002⟩ position of Ti, whereas no structural order can be observed on $K_{\mathrm{Ti}}(30)$. (b)+(e) Longitudinal MR for **B**|**j**,**t**,**n**. In (b), the MR of $Z_{\mathrm{Ti}}(26)$ exhibits a small amplitude along all directions with a parabolic increase in B, similar to the OMR discussed for Pt (cp. Fig. 6.12). In contrast $K_{\mathrm{Ti}}(30)$ in (e) shows a large MR which saturates towards larger B values with a field dependency as expected for the HMR. The longitudinal data is corroborated by the transverse resistivity in (c)+(f), where no residue below the ordinary Hall signal can be found for $Z_{\mathrm{Ti}}(26)$, in contrast to the tanh(B) shaped signal observed in $K_{\mathrm{Ti}}(30)$. Further, the longitudinal and transversal data of $K_{\mathrm{Ti}}(30)$ corroborate each other, as highlighted by the simultaneous fit in (e)+(f) depicted in black (see main text for parameters), suggesting an MR consistent with HMR theory. Similar to Pt, the crystalline sample exhibits a MR according to OMR theory, whereas the amorphous Ti can be understood via HMR theory. This observation confirms the first observation of the HMR in Ti and furthermore corroborates the scaling with crystallinity, as suggested by Fig. 6.12.

large orbital Hall and insignificant spin Hall effect theoretically expected [36], the MR response of $K_{\mathrm{Ti}}(30)$ is ascribed to the orbital HMR.

It should be noted that the samples additionally differ in their ordinary Hall effect, as visible in Fig. 6.14. Here, ρ_{T} is shown as measured, where only along **B**||**n** a signal is obtained. A negative slope is obtained for the crystalline $Z_{\mathrm{Ti}}(26)$ in Fig. 6.14, whereas a positive slope with a roughly 10 times larger amplitude is observed for the amorphous

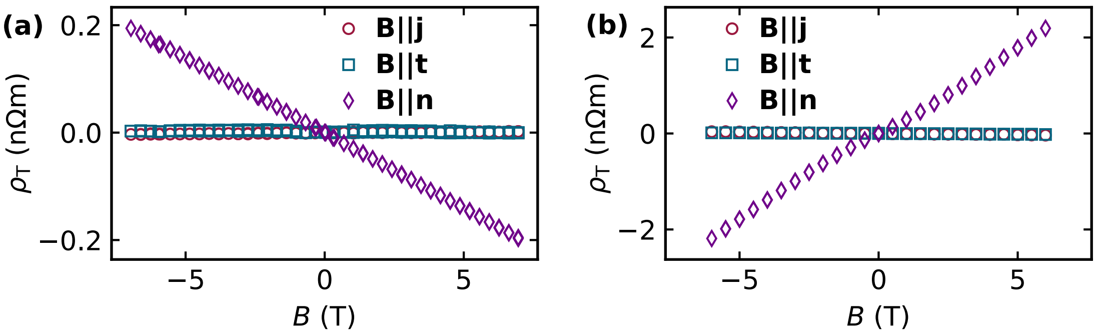

Figure 6.14: Transversal resistivity ρ_T as measured for (a) $Z_{Ti}(26)$ and (b) $K_{Ti}(30)$. The standard geometry introduced in Fig. 6.2(a) is utilised for both samples. Nonetheless, two contrasting slopes are obtained, where $Z_{Ti}(26)$ exhibits a negative slope with a smaller amplitude in comparison to the positive slope of $K_{Ti}(30)$. Hall coefficients of different size and sign have previously been reported for Ti and traced back to temperature, impurities and crystalline texture [226]. Hence, the differences in ρ_T between (a) and (b) are attributed to the structural differences observed in Fig. 6.13(a)+(d). Additionally, a non-linear contribution is observed for $K_{Ti}(30)$, which further influences the amplitude. In contrast, no non-linear residue is found for ρ_T of $Z_{Ti}(26)$, as previously depicted for both samples after subtraction in Fig. 6.13(c)+(f).

$K_{Ti}(30)$ in Fig. 6.14(b). Variations in the Hall slope and its sign are known for Ti and have previously been attributed to temperature, impurities and crystallographic texture [226]. The temperature can be excluded as a factor, as both samples were characterised at 300 K. However, their crystalline properties differ significantly, as depicted by Fig. 6.13(a)+(d). Therefore, the contrasting ρ_T response is mainly attributed to the structural differences. Additionally, a non-linear contribution is superimposed on the ordinary Hall effect in $K_{Ti}(30)$, whereas no residue remains for $Z_{Ti}(26)$ (cp. Fig. 6.13(c)+(f)), further influencing the amplitude. In section 6.3.2 impurities are further discussed, which are also thought to influence ρ_T here.

To quantify the orbital Hall effect of $K_{Ti}(30)$, a simultaneous fit of the HMR to the data is conducted, as seen in black in Fig. 6.13(e)+(f). To that end $\Delta\rho_L/\rho_0$ (cp. Fig. 6.13(e)) is fit with Eq. (5.4) and $\Delta\rho_T/\rho_0$ (cp. Fig. 6.13(f)) with Eq. (5.5), yielding a set of orbital Hall parameters θ_l of 2.3 %, λ_l of 7.0 nm and D of 1.8×10^{-5} m^2/s, which are descriptive of both fits. The obtained parameters are in reasonable agreement compared to other materials probed via the HMR [55, 198]. However, the extracted λ_l of 7.0 nm is well above the typical λ_s values reported for Pt of 1-2 nm [45, 171], but below the 50 to 60 nm estimated in Choi et al. [37] for Ti. It should be noted that depending on the starting parameters, multiple combinations of D, λ_l and θ_l allow the fit to converge, as two data sets are fit with three free parameters. In order to avoid this ambiguity, one value is commonly set as fixed during the fitting routine (see discussion of Fig. 6.11 and Refs. [55, 171, 198]). Another possibility is the evaluation of the thickness dependence, where a distinct maximum arises (cp. section 5.2.1). However, even as a function of thickness, an unambiguous determination of $\lambda_{s,l}$ is challenging as discussed in the next section. This circumstance is further complicated as even in one sample different values for λ_l were observed in Ti [227]. Using fixed minimal (maximal) λ_l values of 2 nm (60 nm), allows to determine an upper (lower) boundary of 4.3 % (1.5 %), which translates into an orbital Hall conductivity $\sigma_{\mathrm{OH}} = (\hbar/e)\theta_l/\rho_{\mathrm{Ti}}$ of 17 403 $(\hbar/e)(\Omega\mathrm{m})^{-1}$ (5957 $(\hbar/e)(\Omega\mathrm{m})^{-1}$). The σ_{OH} is in good agreement with experimental results [37] but well below the theoretical prediction [36].

The Ti characterisation signals that the amorphous Ti (sample $\mathrm{K}_{\mathrm{Ti}}(30)$) exhibits a transport response in accordance with Hanle MR theory, whereas the crystalline Ti (sample $\mathrm{Z}_{\mathrm{Ti}}(26)$) is dominated by the ordinary MR. Furthermore, in comparison to the bulk resistivity of Ti $\rho_{0,\mathrm{Ti}}$ of 450 nΩ m, the HMR is observed in $\mathrm{K}_{\mathrm{Ti}}(30)$ with 2.49 µΩ m, and the OMR in $\mathrm{Z}_{\mathrm{Ti}}(26)$ with 1.31 µΩ m, which follows the trend proposed for Pt, where the HMR is observed at $5 \times \rho_{\mathrm{bulk}}$. These observations suggest a similar scaling in resistivity and crystallinity in the orbital Hall material of Ti in comparison to the well established spin Hall material of Pt described in subsection 6.2.6. Before reconciling and summarising the observations in Pt and Ti, complementary data for the orbital HMR of Ti in $\mathrm{K}_{\mathrm{Ti}}(30)$ and the challenging extraction of λ_l will be discussed in the next chapter.

6.3.2 Thickness and temperature dependence of the Hanle MR in Ti

Section 6.3.1 detailed the first observation of the orbital HMR in Ti. To corroborate the HMR, its dependence on thickness and temperature were extracted and are discussed in this section. The temperature dependence can be used to support the occurring MR (cp. subsection 6.2.3). Hence, the evolution of the transport characteristics of sample $\mathrm{K}_{\mathrm{Ti}}(30)$ are illustrated in Fig. 6.15. In contrast to Pt (cp. Fig. 6.7, neither the HMR, the Hall slope nor the resistivity significantly change with the sample temperature (cp. Fig. 6.15(a),(b),(c), respectively). The obtainable residual resistivity ratio (RRR), i.e., $\rho_{300\mathrm{K}}/\rho_{50\mathrm{K}}$ [2], is calculated. For Ti, this yields a value of $\mathrm{RRR}_{\mathrm{Ti}} = 1.02$, indicating a negligible change in ρ_0 and, therefore, a very disordered sample. In contrast, the $\mathrm{RRR}_{\mathrm{Pt}}$ is roughly 4 and corroborated by the linear decrease of ρ_0 from 300 K to 50 K in Fig. 6.7. Hence, the scattering is initially dominated by phonons and impurities only become relevant for low temperatures, signalising more order in the Pt. Similarly, the Hall slope extracted in Fig. 6.15(b) only changes narrowly with temperature.

The large disorder extracted for $\mathrm{K}_{\mathrm{Ti}}(30)$ from the temperature dependence of ρ_0 in Fig. 6.7(c) is in good agreement with the structural data and corroborates the observed HMR. A large number of defects can be correlated to the amorphous appearance of $\mathrm{K}_{\mathrm{Ti}}(30)$ in the XRD (cp. Fig. 6.13(d)). For both the OMR and the HMR, the resistivity dependence was discussed in the respective chapter. However, as the changes in ρ_0 are insignificant, the MR also is not subject to change (cp. Fig. 6.15(a)). Due to the obtained structural disorder, the OMR can be excluded, corroborated by a small $\omega_c\tau$ of 0.0016 at 10 T, approximated by the Hall slope and ρ_0 via Eq. (5.8). The disorder instead correlates to many scattering events, which again translates into more spin or orbital dependent scattering, as captured by Eq. (6.2). While the temperature dependence is unexpected, the HMR can be understood

---

[2] Usually, the RRR is calculated as the ratio from room temperature to 0 K [195]. However, for Ti, only the data down to 50 K was available. Thus $\rho_{300\mathrm{K}}/\rho_{50\mathrm{K}}$ is used for the comparison of both, Pt and Ti.

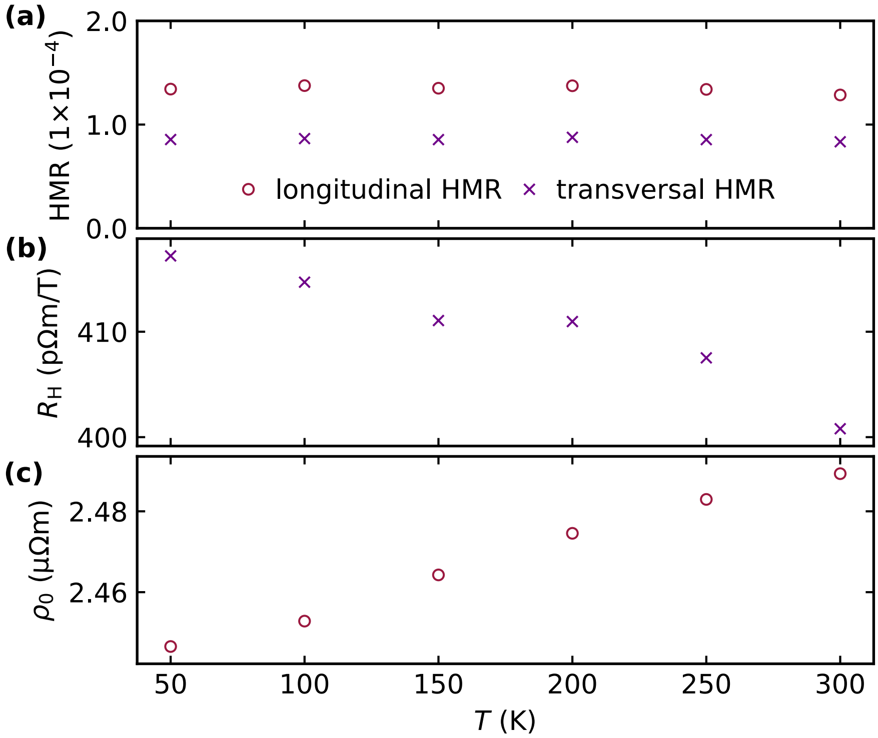

Figure 6.15: Temperature dependence of (a) longitudinal and transversal HMR, (b) Hall constant R_H and (c) resistivity of Ti ($K_{Ti}(30)$). The HMR does not seem to change with temperature, which can be understood by a nearly constant resistivity in (c). The temperature dependence corroborates the structural disorder of the sample and rules out a dominant OMR contribution.

due to many scattering events corroborated by the highly disordered sample.

To further discuss the MR in Ti, the thickness dependency is now presented and discussed, as it is commonly applied to extract λ_l from the characteristic peak (cp. section 5.2.1). Figure 6.16(a) depicts the thickness dependence extracted from multiple samples of the longitudinal and transversal MR (ρ_L/ρ_0 and ρ_T/ρ_0). The data points are extracted as the mean value for $\mathbf{B}||\mathbf{n}$ at $\pm$ 6 T, with the error extracted as the deviation of the mean value. Similar to other studies [55, 198], the largest HMR is observed at the same thickness for both the longitudinal and transverse resistivity. This is in contrast to theory [171], where the longitudinal and transverse HMR reach the respective maximum at different thicknesses.

In Fig. 6.16(b), the resistivity of each individual sample at 0 T is depicted. Samples below 10 nm were too high in resistivity to yield a measurable MR, while samples grown with Ti thicknesses above 45 nm started to become crystalline, exhibiting a peak in the XRD measurements at a similar 2θ value as seen in Fig. 6.13(a) for $Z_{Ti}(26)$. For these thicker samples, the MR response was inhomogeneous over multiple devices on the same sample, with many showing different amplitudes and curve shapes, while generally a

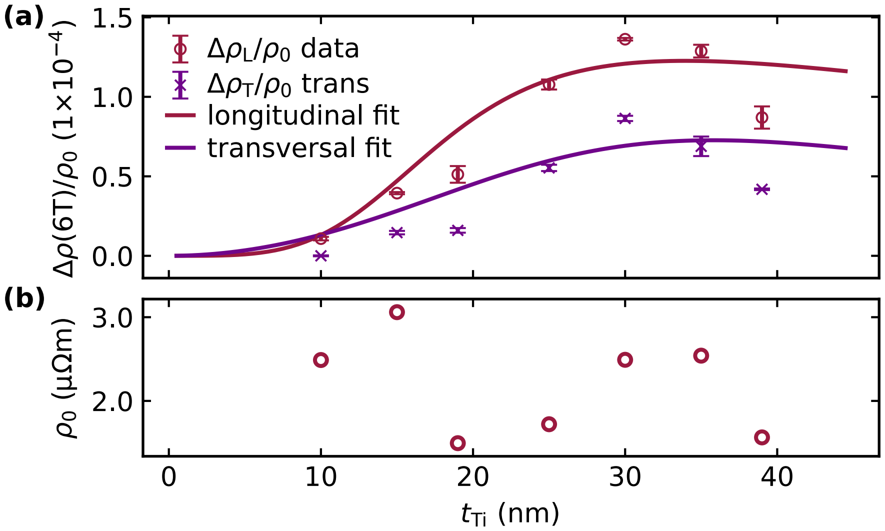

Figure 6.16: (a) Thickness dependence of the HMR in Ti for the longitudinal data (coloured red) and transversal (purple). A maximum is observed at 30 nm for both data points. The solid lines are the fits of Eq. (5.4) and Eq. (5.5) to the respective data points. (b) Resistivity of the individual samples. The difference in resistivity is expected to influence the HMR amplitudes in (a), causing deviations from sample to sample.

strong MR for $\mathbf{B}||\mathbf{t}$ arose. Due to the difficulty in entangling the different contributions, these samples are not included. However, the occurrence of further MR contributions upon observing crystalline order again stress that the structural properties sensitively influence the resulting MR.

Fitting the thickness dependence of the MR, as described by Eq. (5.4) and Eq. (5.5), of the remaining samples results in the behaviour depicted by the solid lines in Fig. 6.16(a). A simultaneous fit of both data sets did not converge, which is why for each direction the respective equation, Eq. (5.4) and Eq. (5.5) are fit to the data. The resulting parameters are summarised in Tab. 6.2. Here, a good agreement of the longitudinal (transversal) data of the orbital Hall angle $\theta_l = 1.5\,\%$ ($1.45\,\%$) and the diffusion length in Ti $\lambda_l = 19\,\mathrm{nm}$ ($25\,\mathrm{nm}$) can be found. The diffusion coefficient D, however differs by one order of magnitude to achieve a good fit to the data. A similar behaviour was also found in Mn [55], with the reason remaining unclear.

The values extracted for λ_l from the thickness dependence differ to those of the simultaneous fit in Eq. (6.13)(h)+(j), as summarised by Tab. 6.2. The evaluation is complicated by several reasons, as the thickness series of Ti is far from ideal. First of all, thicker samples would help in obtaining a clearer thickness dependence and help with a simultaneous fit. However, as the samples become crystalline, additional contributions cannot be ruled out and the MR cannot be conclusively attributed to the HMR. Furthermore, the changes in resistivity seen in Fig. 6.16(b) are expected to influence θ_l, λ_l and D of the samples, when assuming a similar scaling with the resistivity in Ti, as described for Pt in section 6.2. The reduced MR of the lower resistive samples with t_{Ti} of 19 nm and 39 nm appear to

Table 6.2: Extracted parameters by fitting Eq. (5.4) and Eq. (5.5) to the thickness dependence of the longitudinal and transversal data. Additionally, the values extracted from the simultaneous fit detailed in Fig. 6.13(e)+(f) are added as HMR(B). The asterisk marks the fixed parameter during the fitting.

extracted via	θ_l(%)	λ_l (nm)	D (m^2/s)
longitudinal	1.50	19	3.7×10^{-5}
transversal	1.45	25	1.3×10^{-4}
HMR($\mathbf{B}$)	4.3	2*	1.6×10^{-6}
HMR($\mathbf{B}$)	2.3	7	1.8×10^{-5}
HMR($\mathbf{B}$)	1.5	60*	5.4×10^{-5}

corroborate this scaling.However, the large variations in ρ_0 strongly impact the thickness dependency of the HMR.

Additionally, it should be pointed out again that extracting an unambiguous λ_l from the thickness dependence is only possible when $\lambda_m^2 \propto \frac{D}{B}$ is small compared to $\lambda_{s,l}$ (see section 5.2.1). As this is not the case here, the maximum of the HMR in the thicknesses dependence no longer lies at $4.56\lambda_l$ ($3.28\lambda_l$) for the longitudinal (transversal) HMR, as described in section 5.2.1. Instead, only a lower limit of λ_l can be estimated from the maximum at 30 nm, as the largest prefactor reachable is $4.56\lambda_l$. For the Ti series in Fig. 6.16(a) this correlation translates into a minimal λ_l of 6.6 nm, with larger values being possible as listed in Tab. 6.2. The dependence of λ_l on the peak position further shows that a λ_l of 2 nm cannot be plausible for Ti. While parameters can be found, which describe the field dependence in Fig. 6.13, these parameters fail to capture the thickness dependence in Fig. 6.16(a). Lastly, Ref. [227] recently showed that λ_l can differ by up to a factor 3 at different interfaces in the same sampl. This observation could impede the evaluation further, as the HMR probes the dephasing of a spin or orbital accumulation at both film edges, which would result in an superimposed signal. Two different dependencies would imply twice the number of fit parameters, which adds upon the already high complexity of the HMR description (cp. section 5.2.1).

The above mentioned reasons make the unambiguous determination of the diffusion length in Ti difficult and explain the challenges inherent to fitting the thickness dependence. However, a reasonable range can be extracted by field and thickness dependence, which describe the orbital Hall parameters of Ti, as summarised in Tab. 6.2.

6.4 On the occurrence of the ordinary and the Hanle MR in metal thin films

This final section summarises and compares the findings for Pt and Ti thin films on the prevalence of OMR and HMR. The resistivity is a good indicator for the expected MR, where the HMR is dominantly observed at $5\times\rho_{\text{bulk}}$. However, deviations from this rule of thumb are observable in Fig. 6.11 and Fig. 6.16.

Other parameters next to ρ_0 need to be considered, of which external factors like the deposition technique the respective parameters can be excluded. Throughout the chapter, all samples were fabricated by sputter deposition, where some process details differ, yet the resulting MR was unaffected by these differences. Neither the capping layer nor the substrate impact the resulting MR significantly, as discussed for Pt in subsection 6.2.4 and 6.2.5. This observation is further validated by Tab. 6.3, where the sputtering details for the Ti films are added. Neither type of sputtering, power nor rate of deposition appears to be a major influence on the resulting MR (cp. Tab. 6.3) and no changes in deposition were sufficient to change the dominating MR. Further, the MR is not linked to a device and the cause of the difference in transport response needs to be intrinsic to the metal layer.

To reconcile the quantitative differences in dominant MR and its amplitude, the contribution of the diffusion coefficient D is essential next to ρ_0. The analysis of Fig. 6.11 concluded that D is influenced by ρ_0, as captured by the Drude model describing the bulk electronic properties. However, an influence not directly included in ρ_0 is required and introduced over via structural properties, namely the crystallinity. Both Pt (cp. section 6.2.6) and Ti (cp. section 6.3.1), suggest that D becomes larger with increasing crystallinity of the metal layer. Crystalline order exhibits a crucial role in the theoretical framework of the orbital Hall effect (OrbHE) [191, 228]. Intriguingly, the sizeable orbital HMR in Ti (cp. Fig. 6.13(e)+(f)) emerges despite the lack of structural order in the sample. This interpretation suggests that the arising orbital accumulation is conserved without defined structural order, which could be associated to a reduced orbital quenching stemming from the the crystal field [229].

Assuming that the orbital diffusion and spin diffusion resemble each other, an analogue scaling as in Pt of $\rho_0 \propto \theta_{s,l}$ and $\propto 1/\lambda_{s,l}$ is expected for Ti. A lower θ_l is thus accompanied with a larger λ_l. In combination with a fast diffusion in the crystalline samples, the quantitative differences in the transport response could be reconciled. While in the crystalline Ti films, a robust orbital accumulation is theoretically expected [37, 191], the interaction with B is negligible due to the fast diffusion (cp. Fig. 6.10). The scaling explains the vanishing HMR contribution in the crystalline samples (cp. Fig. 6.12 and Fig. 6.13).

A large intrinsic spin or orbital Hall effect in, e.g. Pt [41] or Ti [36], does not automatically result in an occurring HMR. Therefore, it is essential to consider the crystallinity of the film, as the structural properties impact the scattering within. In turn, this dependency implies that the scattering mechanism in the thin film significantly influences the resulting properties, which is corroborated by the theoretical discourse on the relevance of lattice defects impacting the OrbHE [228, 230].

Thus, in all metals with a spin or orbital Hall conductivity the HMR and OMR are proposed to coexist. Observing only one MR does not exclude the other in the same material, while the dominant contribution to the overall MR is highly sensitive on specific parameters. In clean, crystalline metal films, characterised by a low resistivity, high structural order with few impurities and a high diffusion coefficient, the OMR likely prevails. In contrast, the HMR dominates amorphous, moderately dirty thin films, characterised by a high resistivity, the absence of structural order combined with more impurities and a low diffusion coefficient. This scaling appears to exist in both spin and orbital Hall active materials, displaying that the fields are intrinsically connected.

The experimental distinction between both HMR and OMR can be challenging. A longitudinal MR with comparable values for **B** along **j** and **n** in combination with a notably smaller MR for **B**||**t** is a strong indicator for the Hanle MR. The $\Delta\rho_L/\rho_0$ for the OMR can exhibit a complex field dependency with respect to crystal and current direction. However, the MR along **j** is typically reduced in comparison to the MR perpendicular to **j** [231]. Further, when the OMR is evaluated in a Kohler plot, matching prefactors A_i and exponents n_i along the sweep directions are expected over multiple samples and temperatures [208]. To eliminate the crystal dependency, the measurements should ideally be performed along highly symmetric crystallographic directions or in amorphous films. Lastly, the OMR exhibits a characteristic scaling with B/ρ^n, which is often quadratic, i.e. ρ_0^{-2}, whereas the HMR is in first order independent on ρ_0, but instead can be identified over its characteristic thickness dependence (cp. Fig. 5.2). Due to the difference in scaling with the resistivity, another way of validating the MR is over its temperature dependence. As the OMR scales with ρ^{-n}, its amplitude typically increases with decreasing temperature (cp. Fig. 6.7), whereas MR effects from spin or orbital Hall physics commonly exhibit smaller amplitudes towards lower temperatures [55, 171, 214].

The transversal resistivity should then be evaluated in order to corroborate the longitudinal MR. Obtaining a linear slope in ρ_T points towards the ordinary Hall effect (OHE) complementing the OMR. Additionally observing a $\tanh(B)$ type signal on top of the OHE can support an HMR contribution. However, a linear transversal HMR contribution can arise in thin films with a large D value, which is then hard to differentiate from the OHE. On the other hand, a non-linear OHE can also stem from multi-band transport. Finding spin (orbital) Hall parameters which satisfy both the longitudinal (Eq. (5.4)) and transversal HMR (Eq. (5.5)) is, therefore, a strong sign of a consistent MR response within one sample. In addition, a characteristic thickness dependence in both longitudinal and transversal geometry, as described by HMR theory (cp. Fig. 5.2), is then a robust indication of the HMR.

Table 6.3: Summary of the deposition parameters used for sputtering of the different metal thin films on SiO_x substrates (RF=radio frequency, DC=direct current). No clear trend stemming from the deposition can be derived.

Sample	Type	Power (W)	T_{depo} (K)	rate (nm/min)	Capping	MR
$K_{Pt}(5)$	RF	50 W	300 K	1.8	-	OMR
$K_{Pt}(6)$	RF	50 W	300 K	1.8	SiN (7)	OMR
$K_{Ti}(30)$	RF	100 W	300 K	1.3	-	HMR
$Z_{Pt}(5)$	DC	4 W	300 K	2.0	SiN (8)	HMR
$Z_{Ti}(26)$	DC	11 W	300 K	1.2	SiN (8)	OMR

6.5 Summary: Competing ordinary and Hanle MR in metal thin films

This chapter detailed the structural and transport properties of the prototypical materials for spin- and orbitronics: Pt and Ti. Initially, various sputter deposited Pt films with thicknesses of 4 nm to 120 nm are investigated by following HMR and OMR theory. A complex dependence of the MR on the film thickness is obtained, which cannot be consistently explained by an HMR stemming from either a spin or orbital Hall effect. Instead, careful analysis concludes that the observed MR in Pt on MgO arises from the OMR, which is in contrast to previous reports of Pt thin films [55, 171, 198, 214]. The OMR is anisotropic with respect to the external magnetic field, which highlights a characteristic that needs to be carefully considered in MR studies.

After establishing the dominant MR in these thin films, different Pt and Ti films were analysed. In Pt, the HMR is prevalent in samples with a resistivity roughly five times the bulk value or above, but the resistivity alone is not enough to predict the dominant MR. Further, a comparison with various reports on the HMR reveal that discrepancies in extracted parameters cannot be resolved within a simple Drude model. This observation implies that the mechanism governing the diffusion and dephasing of a spin (orbital) accumulation are not yet fully understood. In Ti, a large orbital HMR is obtained in samples characterised by low structural order and large amounts of defects. The relationship between crystallinity of the sample and dominating MR in Ti qualitatively resembles that of Pt, despite the different intrinsic mechanisms causing the spin and orbital Hall effect. This correlation implies that the HMR is predominantly observed in thin films exhibiting a high resistivity and no structural order, which implies a scattering dominated transport and slow diffusion.

From this comparison, the coexistence of the HMR and OMR in metal thin films exhibiting a spin or orbital Hall conductivity is proposed. The dominant MR is determined by the resistivity and the diffusion coefficient of the specific thin film, which in turn depends on the crystallinity and purity of the sample. In clean, crystalline materials the OMR dominates, whereas moderately dirty samples with a high resistivity and without apparent structural order promote the occurrence of the HMR. In order to differentiate between the coexisting magnetoresistive effects in metal thin films without magnetic order, distinct characteristics are highlighted and can be used as a guideline to correctly identify the MR and possible spin (orbital) Hall contributions.

The results of the chapter reveal a generic scaling with resistivity and crystallinity in spintronics and orbitronics, connecting both subfields. This correlation is especially intriguing as it arises in materials with strong as well as weak spin orbit coupling, which per se is unintuitive and could be subject to further studies. Additionally, this dependency of crystallinity on D could impact studies using the magneto-optical Kerr effect, as similarly, spin (orbital) accumulations become more difficult to probe in samples characterised by a high D. From a materials science perspective this correlation between the resistivity and the crystalline quality opens up new paths to optimise the spin (orbital) Hall parameters of a material by optimising films towards lower structural quality or by introducing impurities in a controlled manner.

With this chapter, the intrinsic properties of Pt have been thoroughly investigated. Pt is the second required ingredient for non-planar spintronic devices based on the structures from part 1. In the next chapter, planar YIG and Pt thin films (from Konstanz) will be combined and characterised as a preparation for the non-planar experiments. In these bilayers another magnetoresistive effect arises, the so called spin Hall magnetoresistance (SMR). The results of this chapter allow to approximate the contributions of the OMR and the HMR in the metal layer and to quantitatively set them in relation to the SMR.

Chapter 7

STATISTICAL STUDY OF THE SPIN HALL MAGNETORESISTANCE

This chapter focuses on fundamental magnetotransport experiments in planar YIG/Pt heterostructures and represents the next important step towards spin transport experiments in non-planar YIG structures. In these bilayers, the transfer of spin momentum across the YIG/Pt interface is crucial. Therefore, a well-defined interface is required, which can be challenging to obtain when utilising commercial YIG samples. Similarly, the non-planar YIG described in part I is obtained by ex-situ annealing, causing the surface to become contaminated during the process. To work around this issue, at first the surface treatment is optimised to yield a reproducibly good YIG/Pt interface, under which a robust spin Hall magnetoresistance (SMR) arises. The SMR serves as a measure for the efficiency of spin transfer into the YIG. Insights into its variations across a sample contain pivotal information for non-planar experiments, as relevant changes in the transport response can be evaluated and differentiated from spurious statistical deviations from the mean value.

Therefore, the SMR is systematically studied over numerous samples in hundreds of devices. A narrowly distributed SMR with a standard deviation of roughly 10 % of the mean value is obtained. Afterwards, the Pt Hall bars are rotated with respect to the crystal orientation of the YIG film and the differences are evaluated. In YIG($\mathbf{n}\|\langle 001\rangle$) samples, a previously undiscovered crystal dependency of the SMR can be observed via this statistical approach. The orientation dependence is then modelled in terms of a crystal orientation dependent magnon occupation, which influences the magnetisation and hence, the SMR.

For this chapter, I deposited the Pt films, optimised the surface treatment for a reproducibly good interface and wrote the first draft for a manuscript (in preparation) [1]. Denise Reustlen and Richard Schlitz built the automated measuring setup. Denise Reustlen further performed the lithography and the measurements during her Master's thesis, which I advised. All measurements *in section 7.3 were conducted by Davina Schmidt during her student internship. The scientific discussion and interpretation of the data was conducted together with all co-authors.*

7.1 Spin Hall magnetoresistance

After the initial discovery in YIG/Pt [42, 43] and theoretical description [209], the SMR has been extensively studied in many systems. Next to the prototypical bilayer of YIG/Pt, the SMR has been investigated in all types of magnetically ordered materials like ferromagnets [232], ferrimagnetic insulators [43], canted ferrimagnets [233], antiferromagnets [234–236], the newly found class of altermagnets [2] and paramagnets [237]. Further, more complex ferrimagntic structures like spinal oxides [200] or spin spiral-multiferroics have been probed [238, 239] where the SMR proved to be a powerful tool to investigate the surface magnetisation or spin states in chiral magnets.

However, some aspects of the SMR remain under discussion, including the amplitude and the different contributions to it. Notably, the amplitude of the SMR can differ by orders of magnitude, especially between different bilayer combinations [2, 43, 236]. Moreover, even in the prototypical material combination of YIG/Pt, the SMR effect varies significantly in the literature [43, 240, 241]. These differences can be traced back to multiple parameters determining the amplitude, e.g. the spin Hall properties of Pt [45], the thickness of Pt [43] and the interface [241–243] (cp. Eq. (5.13)).

Out of the mentioned parameters, the Pt thickness, crystalline orientation and resistivity can be controlled well via the deposition process [220]. The crystalline structure of the underlying magnetically ordered material depends on the fabrication technique, but is also generally well defined. However, even if both layers are well controlled, the interface quality between them can differ significantly. Depending on the processing, the YIG/Pt interface is either obtained in an in-situ [43] or ex-situ process [243]. The largest SMR in YIG/Pt was observed for an in-situ interface [43]. While an in-situ interface is preferred, the fabrication is not always feasible. For ex-situ deposition processes, the surface treatment significantly impacts the SMR, as the effect size sensitively depends on the quality of the interface [241–244]. Therefore, differing SMR values between samples needs to be carefully evaluated.

Next to the interface quality, magnetic frustration [241] and magnonic effects can additionally affect the amplitude of the SMR [52, 245]. From non-local experiments, the magnonic contribution can be approximated to several 10 %, but an exact determination in the local SMR is challenging [51, 246].

Furthermore, the crystal orientation of both the metal layer and the magnetic layer are reported to influence the SMR. For Pt, large differences in the spin Hall angle, spin diffusion length or spin torque efficiencies have been reported as a function of the underlying crystal [247–251]. Though, in some cases, e.g. for epitaxial Pt, contradictory results exist regarding the anisotropy or isotropy of the crystalline orientation dependency [194, 252]. One possible explanation is an interaction with the underlying magnetic layer, which influences the Pt at the interface and, therefore, its properties.

The magnetic layer is also reported to exhibit a dependency on the crystalline direction in, e.g. the ferrimagnetic spinel oxide $CoFe_2O_4$ [222] or the altermagnetic $Ba_2CoGe_2O_7$ (BCGO). Here, crystal orientation dependent spin mixing conductances and magnonic contributions are discussed. In YIG/Pt bilayers, no systematic studies of the underlying YIG crystal orientation were conducted. A study on YIG/Pt by Wu et al. [253] report different SMR amplitudes, which they also attribute to a crystalline dependency of the spin mixing conductance G (cp. section 5.2.3). However, the effect is extracted from three different samples. Due to the strong influence of the interface on the SMR, an unambiguous extraction of parameters is challenging and no statistical errors are given, meaning that these results need to be viewed with caution. Further, a crystalline dependency complicates the disentangling of the individual effects, especially in epitaxial systems. Similar to the magnonic contributions, the differences in amplitude stemming from the crystalline orientation are usually of the size of several 10 %.

Despite the large differences in amplitude, the amount of parameters and effects described previously, the SMR amplitude is commonly extracted from a single Hall bar. This value is then taken as representative for the respective material combination. This assumption can be misleading, given the large impact of the interface on the SMR amplitude. Furthermore, not much is known about the reproducibility and the statistical deviations over a single sample. In order to discuss changes in the SMR between multiple samples and effects in the order of several % contributing to the amplitude, a statistical study is required.

This chapter describes the first statistical analysis of various YIG/Pt bilayers. To that end, commercially available YIG substrates are used, which means that the Pt is deposited in an ex-situ process. To that end, Refs. [242, 243] describe an optimal YIG surface treatment, to which some adjustments were made, as detailed in section 7.2. The functioning pre-cleaning process is then confirmed by a quantitative analysis of the SMR in YIG/Pt. Here, the statistical distribution of the SMR is evaluated for 225 nominally identical Hall bars (cp. section 7.3). Afterwards, Pt Hall bars rotated with respect to the YIG crystal orientation are investigated (see section 7.4). The statistical approach enables a clear differentiation between occurring effects and statistical differences, especially when the effect size is of several percent.

7.2 Optimisation of the interface quality

Firstly, the interface optimisation process will be detailed under which a robust, reproducible and large SMR value can be observed. Prior to this optimisation, the SMR value was found to vary from 1×10^{-5} to 5×10^{-4} between samples and, at times, even on the same sample between different devices [254]. Such variations would impede any statistical analysis and comparison between samples.

In the literature, two different surface treatment processes are described. Pütter et al. [243] achieve the best ex-situ SMR value after cleaning the surface with piranha acid (H_2SO_4:H_2O_2). Jungfleisch et al. [242] further test different surface cleaning procedures using typical process gases Ar and O_2. The exact parameters are, however, not disclosed.

In order to replicate the different surface treatment options, several samples are prepared, as summarised in Tab. 7.1. All samples were initially cleaned in acetone and isopropyl alcohol for 5 min to remove any residues from the packaging. Samples S1 to S5 were then additionally etched using piranha acid for 45 s, which dominantly removes carbon contaminations from the atmosphere and also etches non crystalline YIG. After the etching the samples are stored in purified water until being dry blown and loaded into the sputtering system.

For samples S5 and S9, no further surface treatment was conducted before the Pt deposition. The deposition parameters are disclosed in chapter 5.3, with a standard process yielding 5.5 nm Pt. In contrast, samples S1 and S2 were annealed for 30 min in the sputtering chamber before the deposition, at 200 °C and 150 °C, respectively. This heating aims to remove any desorbed water at the surface. Samples S3 and S7 were simultaneously physically etched using Ar ions in the sputtering chamber and S4 and S8 using a 1:1 mixture of Ar and O_2 at elevated pressures of 26×10^{-3} mbar. Afterwards, Pt was deposited onto theses samples as described before. S6 was stored in DI water for two weeks in order to investigate if this delay has any deteriorating influence. Following the delay, sample S6 was then processed identically as S1.

For a quick analysis of the samples' electrical properties, a four point measurement of the whole film is conducted in a Halbach magnet array. To that end, four probes are placed

Table 7.1: Summary of surface treatment parameters before Pt deposition for samples S1 to S10. The surface treatment follows a temporal order from left to right. Initially, all samples were cleaned in an ultrasonic bath for 5 min in acetone and isopropyl alcohol (IPA), which is therefore not mentioned in the table. The Ar etching step before the piranha dip was introduced with the re-usage of samples S5, S7 and S8. Sample S6 was kept in DI water for two weeks before the sputtering proces. The last surface treatment was conducted in the sputtering chamber. The resulting SMR effect was approximated via a wafer prober by contacting the four corners of the rectangular sample.

sample	Ar etch	piranha	sputter chamber	SMR ≈
S1	-	45 s	200 °C, 30 min	3.6×10^{-4}
S2	-	45 s	150 °C, 30 min	0.6×10^{-4}
S3	-	45 s	Ar (26 µbar)	0.4×10^{-4}
S4	-	45 s	Ar:O_2 1:1 (26 µbar)	0.3×10^{-4}
S5	-	45 s	-	0.3×10^{-4}
S6	-	45 s	200 °C, 30 min*	0.3×10^{-4}
S7	-	-	Ar (26 µbar)	0.4×10^{-4}
S8	-	-	Ar:O_2 1:1 (26 µbar)	0.2×10^{-4}
S9	-	-	Aceton + IPA	0.2×10^{-4}
S5v2	-	45 s	200 °C, 30 min	7×10^{-4}
S7v2	3 min	45s	200 °C, 30 min	17×10^{-4}
S8v2	3 min	45s	200 °C, 30 min	12×10^{-4}
S10	3 min	45s	200 °C, 30 min	20×10^{-4}

at the corners of the rectangular sample and the magnet rotated in plane (cp. Fig. 5.4). This way, a quick examination of the resistivity and the SMR can be performed without requiring lithography. However, as the current path is not clearly defined, the SMR is slightly exaggerated in comparison to the obtained values via the defined Hall bars in the following sections. This overestimation is also partly due to the simultaneously occurring transversal SMR effect. Nonetheless, the SMR values obtained clearly separate good from bad interfaces.

The largest SMR out of all samples S1 to S9 is obtained for sample S1, which exhibits a value comparable to other ex-situ YIG/Pt samples [243]. All other samples show SMR values below 1×10^{-4}. The heating treatment at 200 °C appears to be crucial in order to obtain a large SMR amplitude. The temperature of 150 °C should in theory suffice to desorb all water. However, as the thermocouple is below the sample holder in the sputtering system, the temperatures at the sample itself did not reach above 100 °C. Sample S6 was utilised to test the reproducibility of the surface treatment of S1. However, the sample was stored in DI water in two weeks and the large amplitudes could not be reproduced here.

In an attempt to check if samples could be reused, S5, S7 and S8 were processed again. In the case of S5, the backside was simply used, following the processing of S1. Samples S7 and S8 were instead etched using the RIE Plasma Pro80 (cp. section 5.3). This way, the Pt was physically removed from the YIG layer using Ar ions. Additionally, the YIG film below was further etched for roughly 3 min, in order to make sure no residues from the Pt and previous processing were left. After etching, the samples were treated identically to S1, differing only in the Ar etch step mentioned before. These three samples are now dubbed S5v2, S7v2 and S8v2 (cp. Tab. 7.1) to indicate the recycling.

After the second Pt deposition and electrical characterisation, these samples now exhibit larger SMR values than their first versions. Interestingly, the SMR is also larger than for sample S1. This effect is especially notable for S7v2 and S8v2, which only differ in the processing prior to the piranha. Hence, a positive influence of the physical etching in combination with the chemical etching on the interface quality appears evident. To validate this effect, a fresh sample (S10) is prepared. Here, the Ar step is conducted before the Piranha dip following the sample preparations of S7v2 and S8v2. Again, a large SMR value is measured on this device (cp. Tab. 7.1). Therefore, all samples prepared after S10, are prepared identically to S7v2, S8v2 and S10 and exhibit a reproducible SMR of roughly 1 to 2×10^{-3} (not shown here).

The influence of the Ar pre-etch is not fully understood but could be attributed to several interactions. Foremost, the physical etching step helps to remove any residues on the surface. Since piranha predominantly etches organic residues, the Ar^+ ions might help in removing other, e.g. inorganic residues. Due to the Ar^+ bombardment, the first YIG layers also become amorphous [244] and are chemically etched afterwards, resulting in a fresh surface, which imitates an in-situ interface. A clean interface with a defined crystal structure is achieved, which then also exhibits comparable SMR values [43]. A direct influence of the Ar^+ surface treatment is also discussed in the literature, where an increase in the real part of the spin mixing conductance G_r of 1.3 [241] to 5 times [255] compared to the untreated value was reported. Here, the binding energy [255] and changes in the crystal structure at the interface [244] or the magnetic ordering [241] are discussed. However, in these publications the Ar treatment is usually performed after the piranha dip, suggesting that the dominating contribution for samples S7v2 to S10 is the clean surface.

Further, Qui et al. [244] report the formation of an amorphous layer and a smaller ISHE across the interface due to the Ar bombardment. The small SMR observed in samples S3-S8 could be attributed to such an amorphous layer, as these samples were cleaned in-situ using a plasma after the piranha etch. However, the detailed influence of the Ar treatment is not further investigated here, but its importance and the correct sequence becomes evident from the order of magnitude larger SMR values in samples S7v2 and below (Tab. 7.1).

Therefore, all samples prepared afterwards (S11-S14) were processed like sample S10 and checked using the probe station before patterning. The established pre-cleaning process is now confirmed over a 30 mm^2 sample using a statistical analysis approach.

7.3 Statistical investigation of the spin Hall magnetoresistance in 225 devices

In this section, the first systematic statistical study of the spin Hall magnetoresistance (SMR) is conducted. To that end, 225 Hall bars are defined into the Pt via optical lithography onto the GGG/YIG/Pt sample S8v2 (cp. Tab. 7.1). The crystallographic directions utilised throughout this chapter always refer to the single crystalline YIG/GGG, as the crystal orientations are well defined. The Pt again exhibits an out of plane texture along $\langle 111 \rangle$, as presented in chapter 6 (cp. Fig. 6.8) and polycrystalline grains in the plane.

The crystallographic directions of the YIG layer are therefore taken into account in the following and can be identified as depicted in Fig. 7.1(a). In this section, the current is always applied along $[1\bar{1}0] \| \mathbf{j}$, while the magnetic field is rotated in the sample plane spanned by $[1\bar{1}0]$ and $[11\bar{2}]$. Figure 7.1(b) depicts a microscopic image of the patterned device with a grid of 1-18 describing the rows and A-Y the columns. For maximum coverage of the YIG surface, the devices are shifted, meaning devices from, e.g. column A (B) appear every other row in uneven (even) rows. This layout allows for a fully covered sample with 225 individual devices (cp. Fig. 7.1(b)).

The electrical characterisation is conducted in a custom build probe station. In this section, the four probes were placed manually in a four point measuring scheme, as depicted in Fig. 7.1(a). A Halbach array provides a magnetic field of 70 mT, which is rotated from 0 deg to 360 deg and back. The longitudinal voltage drop is measured, allowing for the evaluation of the SMR.

To estimate the systematic error of the measuring scheme, several devices were measured 10 times in a row. The results of one devices (9I) is depicted in Fig. 7.1(c). Over these devices, the resistivity and MR amplitude exhibit very similar values. Fitting the 10 data sets with Eq. (5.12) yields a resistivity of 269 nΩ m, which is also in good agreement with the Pt obtained in the previous chapter 6. The simultaneously extracted SMR value

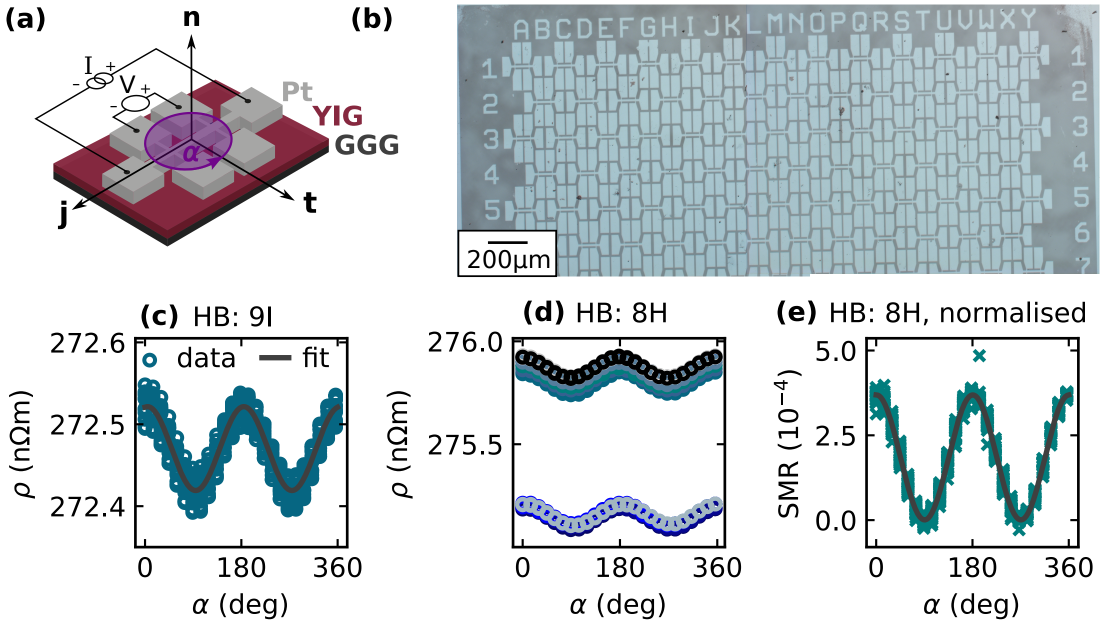

Figure 7.1: (a) Hall bar on top of the YIG samples with the in plane rotation angle α, as defined in Fig. 5.4(a). The current is always applied along $\mathbf{j}\|[1\bar{1}0]$ with respect to the crystallographic directions of the underlying YIG/GGG. (b) Microscopic images depicting the upper part of the sample. The devices are shifted with respect to each other for maximum coverage of the sample, resulting in 225 devices patterned onto the 5x6 mm^2 wafer. (c)-(d) depict two device measured 10 times in a row to account for the repeatability of the measurement, with the SMR being 4.0×10^{-4} and 3.8×10^{-4}, respectively. (e) shows the results for device H8, which was contacted anew before each of the 15 total measurements. (f) illustrates the same data as in (e) after normalisation with ρ_0, which accounts to small deviations in temperature and contacting. The SMR amplitude is 3.8×10^{-4} and its error from the simultaneous fit (purple) 0.4 %.

is 4.0×10^{-4} and the obtained fit is given by the solid dark gray line in Fig. 7.1(c). The error in SMR amplitude is extracted as 3.1 % for device 9I, whereas the error in resistivity is five orders of magnitude smaller than the value itself. For the other devices, comparable resistivities, SMR values and errors are extracted (not shown). This analysis highlights that a single measurement yields representative values.

Furthermore, the contacting process was tested with device 8H, as depicted in in Fig. 7.1(d) and (e). For each measurement, the probes were lifted from the pads and contacted again, to simulate the measuring process across the whole sample. Here, deviations in the resistivity between measurements can be observed (cp. Fig. 7.1(d)). These likely stem from deviations in room temperature and the contacting. However, when normalising with ρ_0, the SMR is very comparable over all data sets (cp. Fig. 7.1(e)). This is corroborated by the fit to all data sets depicted in dark gray, which yields a SMR value of 3.8×10^{-4} and a very narrow error in the extracted amplitude of 0.4 %, highlighting the reproducibility of the contacting.

The repeated measurements suggest that the setup yields reproducible data with a

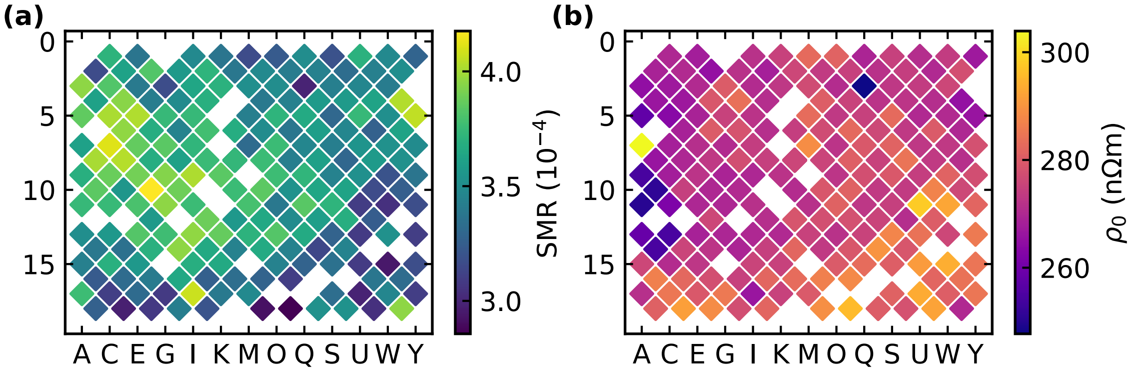

Figure 7.2: Statistical analysis of the SMR from 225 devices patterned on sample S8v2. The measurement of each device is evaluated and fitted as introduced in Fig. 5.4(a) and Fig. 7.1(c)-(e), and plotted in a heat-map, where each diamond corresponds to a Hall bar and its row and column index (cp. Fig. 7.1(b)). (a) depicts the SMR value and (b) the resistivity as given by the colour code of each individual device. Areas which remain white correspond to broken or shorted device from which no reasonable parameters could be extracted. A good reproducibility of the SMR over the sample can be observed. However, towards the left of each heat-map in (a) [(b)] an accumulation of large SMR [low resistivity] values can be observed.

small error and is suited for the statistical analysis. However, the data also implies that changes of a few percent can stem from the measurement or the devices. With a few individual devices analysed and the systematic error of the setup discussed, now all 225 devices are considered.

Figure 7.2 depicts the extracted values of SMR (a) and resistivity (b) presented in a heat-map covering all devices. Each diamond corresponds to a Hall bar presented in Fig. 7.1(b). The individual SMR value and resistivity is encoded in the respective colour map. White spaces signalise broken or shorted devices which correspondingly do not appear in the evaluation. In total, 16 faulty devices exist, which is roughly 10 % of the total devices, signalising a reasonable yield. Additionally, seven outliers were excluded, which optically appeared intact but exhibited strong deviations in resistivity or SMR value. This preprocessing of the data ensures that the heat-maps and histograms are not dominated by a single device.

The heat-maps depict robust transport properties over the whole YIG/Pt sample. This observation signalises that the position on the wafer exhibits no significant influence on the SMR or ρ and in turn implies that extracting the SMR from a single device can be representative for the specific normal metal / magnetic layer combination. Further, the data suggests that no obvious systematic errors are introduced via deposition, lithography and etching.

However, a trend of ρ and SMR can nevertheless be observed in the colour over the heat map (cp. Figure 7.2(a)+(b)). A slightly brighter area, corresponding to a larger SMR value can be observed towards the left (rows 3-10 and columns A-I), which can be correlated to a lower resistivity, appearing darker for the same devices. This correlation is supported by Fig. 7.3(a), where the SMR versus the resistivity is depicted, which nicely

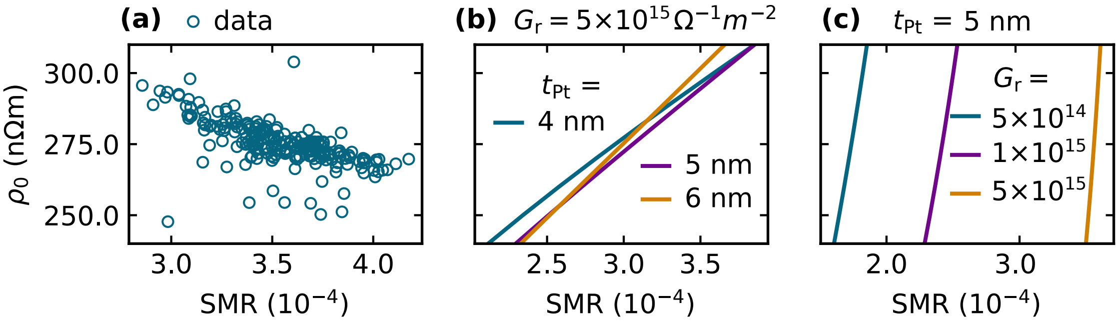

Figure 7.3: (a) Evaluation of the resistivity versus the SMR of each device depicted in Fig. 7.2. The trend of a larger SMR with a lower resistivity is supported by this illustration. (b)-(c) Theoretical expectation for the SMR from Eq. (5.13) as a function of resistivity ρ, thickness t_{Pt} and the real part of the spin mixing conductance G_r. In (b) a G_r of $1 \times 10^{15}\,\Omega^{-1}\,\mathrm{m}^{-2}$ is utilised and the thickness varied. For θ_s and λ_s, the intrinsic scaling of the Pt [45] is taken into account as introduced in chapter 6.2.2. In (c), t_{Pt}, θ_s and λ_s are kept constant and only G_r (in $\Omega^{-1}\,\mathrm{m}^{-2}$) is varied. A slight influence of ρ_0 on the SMR is evident, which is largely outweighed by G_r. From these naïve calculations, the opposite trend to (a) would be expected for the ρ versus the SMR.

captures the mentioned behaviour.

Since ρ_0 is one of the parameters describing the SMR in Eq. (5.13), a dependency on ρ is feasible. However, from the naïve expectation, the opposite trend would arise (cp. Fig. 7.3(b)). For this estimation, G_r is assumed to be $1 \times 10^{15}\,\Omega^{-1}\,\mathrm{m}^{-2}$, which roughly reproduces the amplitude of Fig. 7.3(a). Next, the scaling introduced by Sagasta et al. [45] (cp. previous chapter, section 6.2.2, Eqs. 6.1+ 6.2) is used to calculate θ_s and λ_s, leaving the thickness as the last parameter. Exemplarily the expected dependency of the SMR on ρ of a 4, 5 or 6 nm thick Pt is depicted in blue, purple and amber (cp. Fig. 7.3(b)). The calculated behaviour exhibits the opposite trend for all three thicknesses, suggesting further, that the behaviour cannot be reconciled from thickness fluctuations.

However, even when calculating one characteristic θ_s and λ_s for the Pt from the bulk resistivity (cp. Fuchs-Sondheimer theory [204, 205], section 6.2.3), the SMR would still increase with a higher resistivity for a constant G_r and t_{Pt} (see Fig. 7.3(c)). This way the intrinsic θ_s and λ_s arise from the bulk properties Pt and a change in ρ_0, stemming from thickness fluctuations and surface roughness, would not contribute a change in the properties. Nevertheless, the trend in Fig. 7.3(c) exhibits the opposite dependency as in the data. Thus, only variations in the interface, i.e. G_r, can explain the scaling observed in Fig. 7.3(a). A better interface corresponds to a larger SMR, as seen in Fig. 7.3(c). One possible explanation is that a smooth surface is accompanied by a sharp interface, and, therefore, exhibits a large G_r [244], as well as a low resistivity, as described by the Fuchs-Sondheimer model (cp. Eq. (6.3)). A correlation of ρ_0 with G_r might overshadow the dependencies of Fig. 7.3(b). However, the trend could not be reproduced in subsequent samples and sections, after the setup was optimised and automated. Therefore, this interaction is not further discussed.

To further discuss the statistical analysis, the SMR and resistivity are presented in

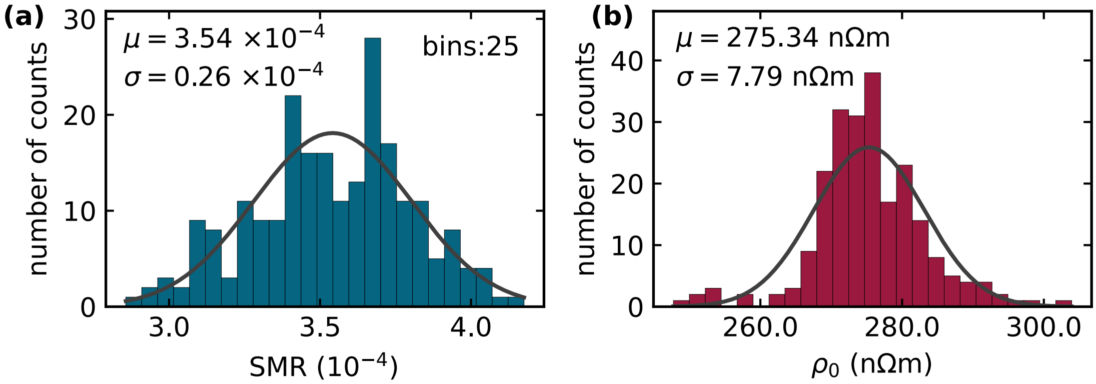

Figure 7.4: Illustration of all previously discussed devices with their (a) SMR and (b) resistivity values in a histogram. Here, 25 bins were utilised, where the SMR values (a) exhibit a slightly broader spread than the resistivity (b). By analysing the data using a Gaussian distribution, the mean value μ and standard deviation σ can be extracted, as given in the respective histogram. After adjusting the amplitude, the Gaussian distribution using μ and σ can be added, as given by the dark gray curves. The Gaussian distribution appears to capture the data reasonably well.

histograms, see Fig. 7.4. This illustration captures the statistical distribution and allows for more precise statements about the spread of the respective parameter (SMR or ρ). When analysing both parameters in the context of a Gaussian distribution, the mean value μ and the standard deviation σ can be extracted from the data. By normalising the amplitude, the Gaussian distribution can be visualised in the histogram, which is given by Eq. (7.1).

$$f(x) = \frac{1}{\sqrt{2\pi\sigma^2}}\exp\left(-\frac{1}{2}\left[\frac{x-\mu}{\sigma}\right]^2\right) \tag{7.1}$$

Here, the distribution of a measured parameter x (i.e. the SMR or ρ) is described by $f(x)$ with μ and σ corresponding to mean value and standard deviation, as introduced above. The Gaussian distributions in dark gray capture the two histograms reasonably well, which suggests that the data is Gaussian distributed and the values representative.

The SMR in Fig. 7.4(a) exhibits a comparably broad distribution in comparison to the resistivity in Fig. 7.4(b). This observation is corroborated by the standard deviations σ_{SMR} and σ_ρ of 0.26×10^{-4} and $7.79\,\mathrm{n\Omega\,m}$ from the mean values μ_{SMR} and μ_ρ of 3.54×10^{-4} and $275\,\mathrm{n\Omega\,m}$. In turn the coefficient of variation σ/μ for the SMR is 7 % and 3 % for ρ, which confirms the slightly broader distribution in Fig. 7.4(a) compared to (b). However, in both cases, the spread is narrow, corroborating the robust value over the whole sample.

Additionally, the SMR amplitude of $3.54 \times 10^{-4} \pm 0.26 \times 10^{-4}$ is in good agreement with the literature. Similar SMR values of roughly 3×10^{-4} were obtained in ex-situ YIG/Pt interfaces, also using piranha acid [243]. In comparison to the 1×10^{-3} of an in-situ interface [43] the SMR is smaller, but larger than 5×10^{-5} for samples without prior surface treatment [241]. This leads to the conclusion that the sample exhibits a representative SMR value. Additionally, the standard deviation of this representative SMR value over a large sample is now established. The SMR now can be discussed under the extracted coefficient of variation σ/μ of 7 %.

In comparison to the statistical error from a single device measured multiple times (see Fig. 7.1(c)-(e)), the values for the standard deviation obtained in Fig. 7.4 are larger. This suggests that slight variations in the final device geometry and the individual interface further add onto this error.

In conclusion, the statistical distribution of the SMR was investigated in 225 devices on a single sample in combination with the corresponding resistivity. A narrow, Gaussian distributed SMR and resistivity was found, with the standard deviation being smaller than 10 % of the mean value. The mean SMR value μ_{SMR} of 3.54×10^{-4} is robust over the whole sample and in good agreement with the literature, suggesting that σ_{SMR} of 0.26×10^{-4} is representative for the SMR. Therefore, an extracted value of the SMR is descriptive for this combination within the here presented statistical error. The results highlight, that changes in the range of several percent attributed, e.g. to the crystal structure, need to be carefully considered. Using the statistical approach, the influence of the underlying crystal structure of YIG will be analysed in the following.

7.4 Pt Hall bars rotated with respect to the YIG crystal direction

With the statistical distribution of the SMR evaluated, Pt Hall bars rotated with respect to the underlying YIG single crystal are considered in the following. This is because in the non-planar geometries, the Pt strips can be defined with respect to different YIG crystal orientations. Further, the crystalline direction changes inevitably in the non-planar structure, suggesting that a crystalline dependency should be carefully considered. Recently, a strong dependency of the SMR amplitude was reported in bilayers of the altermagnetic candidate material $Ba_2CoGe_2O_7$ (BCGO)/Pt [2]. The amplitude of the SMR changes up to 100 % depending on the orientation of the Hall bar with respect to the crystal orientation. This difference cannot be reconciled via the interface, the resistivity or statistical variations of the SMR over a sample. The Hall bars in BCGO/Pt were defined on a single sample, ruling the interface quality between samples out as an influence. Further the resistivity exhibited no trend on the SMR [2], which is why the effect is attributed to the crystal structure of the BCGO. Therefore, in the following, the influence of the crystal orientation on the SMR in YIG/Pt is investigated using the statical approach.

7.4.1 Pt Hall bars rotated in the plane spanned by YIG $[1\bar{1}0]$ and $[11\bar{2}]$

To investigate the influence of the underlying YIG, its crystal orientation is used to define the coordinate system. This definition is depicted for a Hall bar in Fig. 7.5 (a), where the $\langle 111 \rangle$ orientation is aligned along the surface normal and the two in plane directions are $\langle 11\bar{2} \rangle$ and $\langle \bar{1}10 \rangle$.

In order to separate between the rotation of the external magnetic field **B** and the rotation of the Hall bars, a second angle φ is defined. α describes the rotation of the external magnetic as before, while φ describes the angle between the current direction **j** of

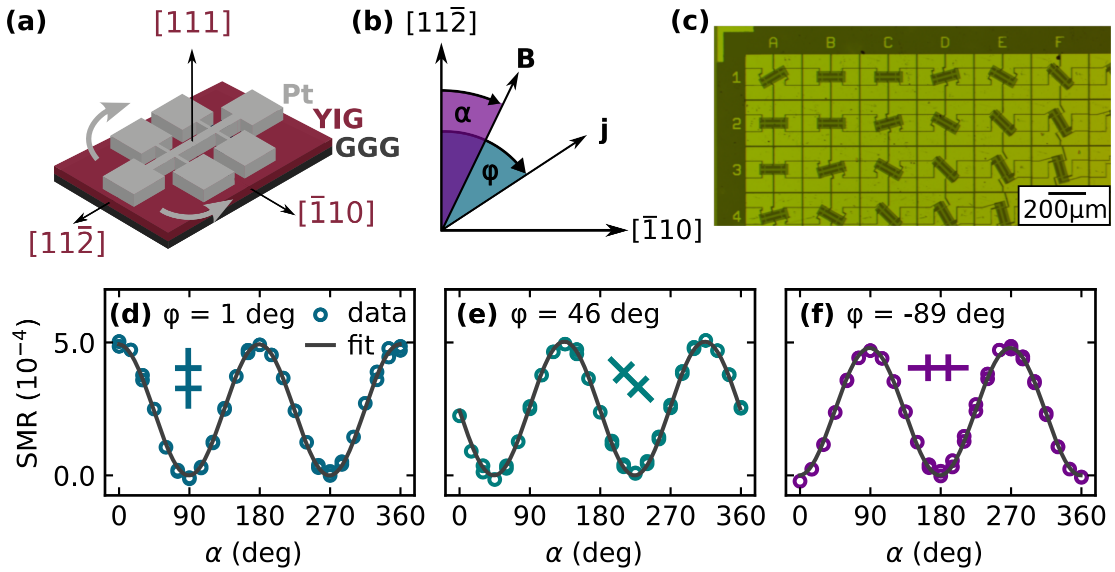

Figure 7.5: Concept of rotated Hall bars. (a) depicts the GGG/YIG wafer with well defined crystal orientations, which are used to define the coordinate system. The Pt Hall bars are rotated with respect to the YIG crystal. (b) coordinate system and definition of the angle φ, describing the rotation of the Hall bars. (c) micrograph of the patterned sample. (d)-(f) measured SMR for three typical devices of sample S12. Due to the rotation of the Hall bars, the SMR is shifted by φ with respect to the static crystal orientation and magnetic field rotation α. The extracted angle φ of the corresponding Hall bars are given by the inset.

the Hall bar with respect to the crystal orientation of the YIG (cp. Fig. 7.5(b)). An image of the patterned sample is depicted in Fig. 7.5(c), clearly illustrating the rotation.

As the YIG crystal orientations are fixed and the magnetic field is rotated from the same starting point, the orientation of the Hall bar becomes evident in the transport response. The SMR extracted for three rotated Hall bars is depicted in Fig. 7.5(d)-(f). Here, the SMR amplitude is comparable for the three devices, while enclosing different φ values. To account for this a $\cos^2(\alpha + \varphi)$ dependency is fit to the data, where φ now represents the rotation of the Hall bar, as depicted by the insets.

The results of the whole probed area are presented in Fig. 7.6, where each device corresponds to a position on the sample. Overall, a robust SMR is observed over the probed area (cp. Fig. 7.6(a)). The mean resistivity is larger than in the previous sample, but its value consistent across the sample itself (cp. Fig. 7.6(b)). The extracted angle φ acts as a control and follows the layout from Fig. 7.5(c). Due to the π periodicity of the $\cos^2(\alpha)$, the 90 deg and -90 deg devices cannot be distinguished by the fit, which can be seen in the transition from black to yellow. However, the ambiguity is no issue, as the crystallographic orientations of the cubic YIG are also π periodic, meaning that φ is always correctly attributed to the YIG crystal orientation.

No systematic change in the SMR is observable over the sample. This observation suggests that the SMR amplitude in the $\langle 110 \rangle$ - $\langle 112 \rangle$ plane is unaffected by the YIG crystal

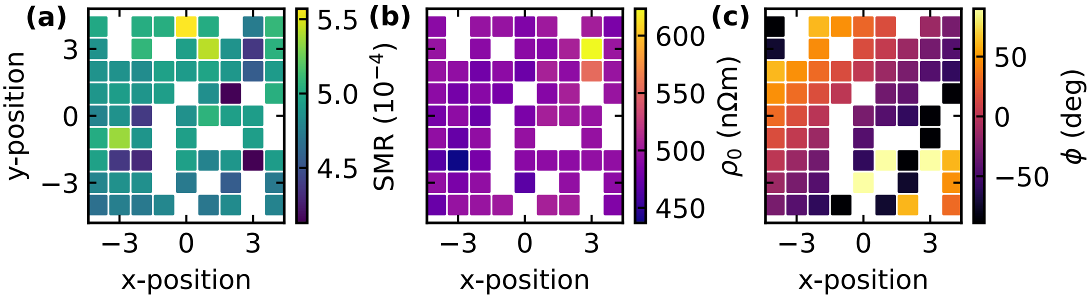

Figure 7.6: Evaluation of the rotated Hall bars of sample S12 as given by the heat map. The x and y position correspond to the device on the sample (cp. Fig. 7.5(c)). (a) depicts the SMR, (b) the resistivity and (c) the angle of rotation φ of all measured Hall bars. White spaces correspond to defect devices or large outliers. No systematic change in SMR can be observed and no correlation to ρ or φ is evident.

structure below. An influence of the YIG crystal orientation would be visible as a systematic change over the diagonals, which is not the case. Further, no scaling with ρ is observed in this sample when comparing the two heat maps (cp. Fig. 7.6(a)+(b)). The result is also consistent with the literature [194, 256], where no change in amplitude was detected in a magnetic layer with $\mathbf{n} || \langle 111 \rangle$.

To support the results from Fig. 7.6 two more samples were investigated and their histograms and φ dependence evaluated. All three samples are summarised in Fig. 7.7. The left column depicts the histogram of the SMR distribution and a fit according to Eq. (7.1), while the right column shows the corresponding dependence on the rotation angle φ. In all cases, the SMR histogram can be described via a Gaussian distribution, with slight differences in mean value and standard deviation. Sample S11 was utilised to adjust the wafer prober and the raw signal was worse in comparison to all other samples. While the mean value μ is comparable to section 7.3, the large standard deviation σ is not representative. In contrast, the other two samples show a large mean SMR and a relative error below 5 % of the mean, making them ideal to investigate a possible crystal orientation dependence.

Figure 7.7(d)-(f) now depict the SMR versus φ, corroborating the previous results from Fig. 7.6. Here, the heat maps visually imply that the SMR is independent on the crystal orientation for YIG with $\mathbf{n} || \langle 111 \rangle$. This result is confirmed by the randomly scattered SMR over φ in the right column. Here, the mean SMR value from the corresponding histogram is depicted as a solid line and the 1σ interval given by the dashed ones. Within this interval, no systematic change of the SMR as a function of the rotation is discernible.

It should be noted that the resistivity was evaluated identically (not shown here). Similarly, no dependence on φ could be extracted and the histogram was in first order Gaussian distributed. An influence of ρ on the SMR is therefore excluded for this subsection.

The samples with $\mathbf{n} || \langle 111 \rangle$ investigated up to now are summarised in Tab. 7.2. The mean value, its standard deviation and the resistivity are listed and the individual sample name given. As the SMR does not depend on φ, sample S8v2 from the previous section 7.3

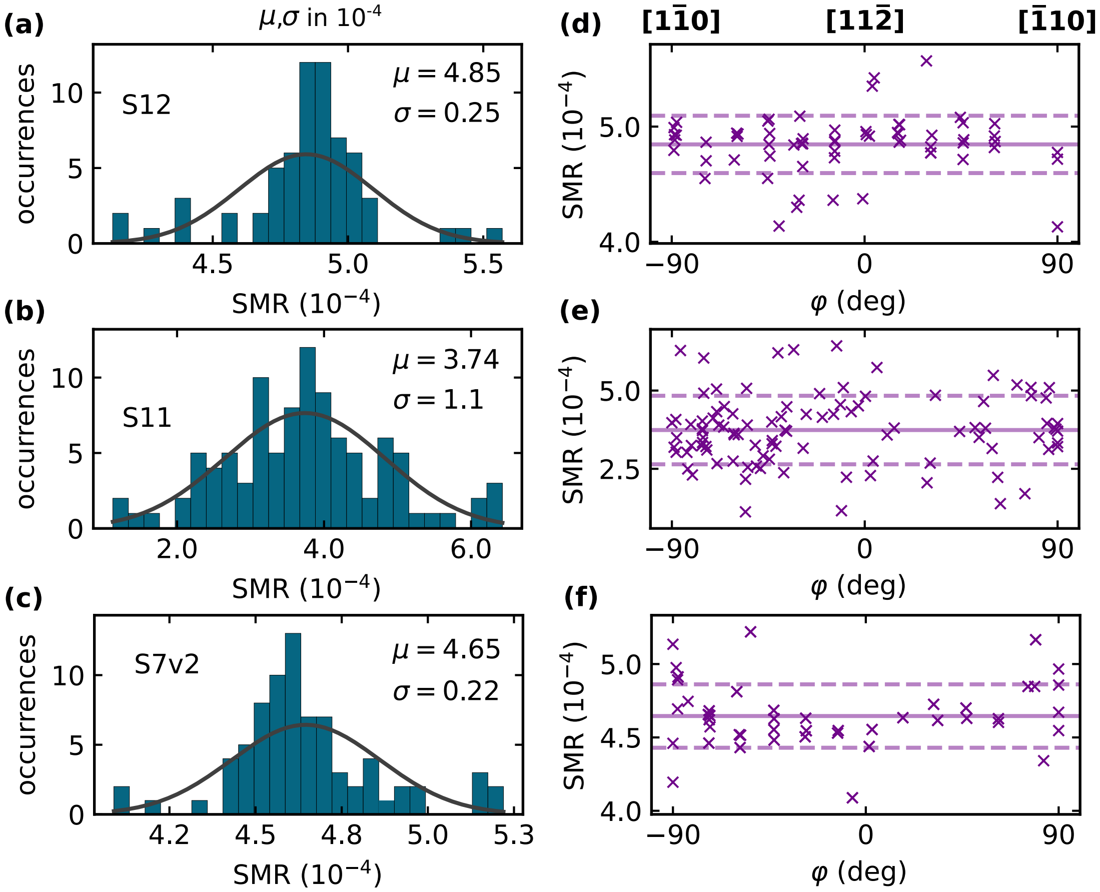

Figure 7.7: (a)-(c) Histograms of the SMR for the three samples measured in the $[1\bar{1}0]$-$[11\bar{2}]$ plane and (d)-(f) the SMR versus the angle of rotation φ. The solid line represents the mean and the dashed lines the 1σ interval. Within the data and this interval, no influence of the underlying crystal is apparent.

is also added.

Table 7.2 highlights a consistent SMR value over the sample with a narrow standard distribution. The resistivity of the individual samples vary, which might stem from thickness deviations or the processing itself. However, the resistivity values are comparable to the literature [43]. Further, the SMR amplitude is only slightly affected by ρ, as discussed with Fig. 7.3, which is evident by the mean values of roughly 3 to 5×10^{-4} (cp. Tab. 7.2). With the exception of sample S10, which showed a spread in acquired data points, the standard deviation is roughly multiple samples.

In conclusion, the SMR in YIG($\langle 111 \rangle$)/Pt bilayers can be reproduced within a relative uncertainty of 10 %. Within this uncertainty, no systematic influence between the crystal orientations $\langle 110 \rangle$ and $\langle 112 \rangle$ can be extracted. In order to extend this study to other directions, YIG substrates with $\mathbf{n} \| \langle 001 \rangle$ are discussed in the next section.

7.4.2 Pt Hall bars rotated in the plane spanned by YIG [100] and [010]

In addition to the previous samples, YIG/Pt bilayers with n||[001] are now considered. These samples allow for the investigation of ⟨100⟩ directions in comparison to ⟨110⟩. Within this plane, a strong anisotropy of the SMR was reported in epitaxial Co/Pt [248] and larger anisotropies are expected in YIG [256].

The processing is identical to the samples of the previous subsection. After the surface cleaning procedure from section 7.2, 5.5 nm Pt are deposited on the YIG films and Hall bars patterned with respect to the crystal orientation, as sketched in Fig. 7.5(a). The YIG crystal orientation is again used to define the coordinate system, which now rotates from $[1\bar{1}0]$ to [110], as depicted in Fig. 7.8(a). The evaluation of the SMR is analogue to Fig. 7.5(d)-(f) and the results are directly discussed.

Figure 7.8(a) depicts the evaluated heat maps of the transport response of a YIG(⟨001⟩) /Pt bilayer, referred to as S13. The extracted angle φ in Fig. 7.8(b) nicely resembles the arrangement on the sample, acting as a proof for the fit. Further, the SMR and resistivity exhibit robust amplitudes of roughly 4.4×10^{-4} and 411 nΩ m, see Fig. 7.8(c)+(d) respectively, making the sample comparable to previous ones. Additionally, the absolute change in both SMR and ρ is small, indicating a narrow distribution and a well suited sample for the investigation of a dependence on φ.

By comparing the three heat maps in Figure 7.8(b)-(d), a trend can be observed between the angle φ and the SMR. Along the diagonals, a similar colour is apparent, suggesting that the SMR exhibits a similar value for a given angle φ. However, darker and lighter diagonals are evident, meaning that the SMR varies with φ. This trend cannot be observed within the colour code of the resistivity (cp. Fig. 7.8(d)). .

To corroborate a crystallographic influence, the histogram of the SMR as well as the dependence on φ are now analysed. Figure 7.9(a) depicts the histogram of the SMR obtained from S13. Here, two peaks are apparent, one at roughly 4.34×10^{-4} and a second at 4.46×10^{-4}. Due to the additional modulation with φ, a Gaussian distribution does not suffice and a bimodal distribution consisting of two Gaussian distributions is utilised, effectively convoluting two delta functions with a Gaussian. The curve is obtained by initially fitting the minima and maxima in Fig. 7.9(b) and then the bimodal distribution

Table 7.2: Summary of the investigated samples with the YIG ⟨111⟩ crystal orientation along the surface normal direction **n**. The mean value μ_{SMR}, its standard deviation σ_{SMR}, as well as the mean resistivity μ_ρ of the investigated samples is listed.

sample	orientation	μ_{SMR}	σ_{SMR}	μ_ρ (nΩm)
S8v2	**n** || ⟨111⟩	3.45×10^{-4}	0.26×10^{-4}	275
S7v2	**n** || ⟨111⟩	4.65×10^{-4}	0.22×10^{-4}	313
S11	**n** || ⟨111⟩	3.74×10^{-4}	1.1×10^{-4}	407
S12	**n** || ⟨111⟩	4.85×10^{-4}	0.25×10^{-4}	493

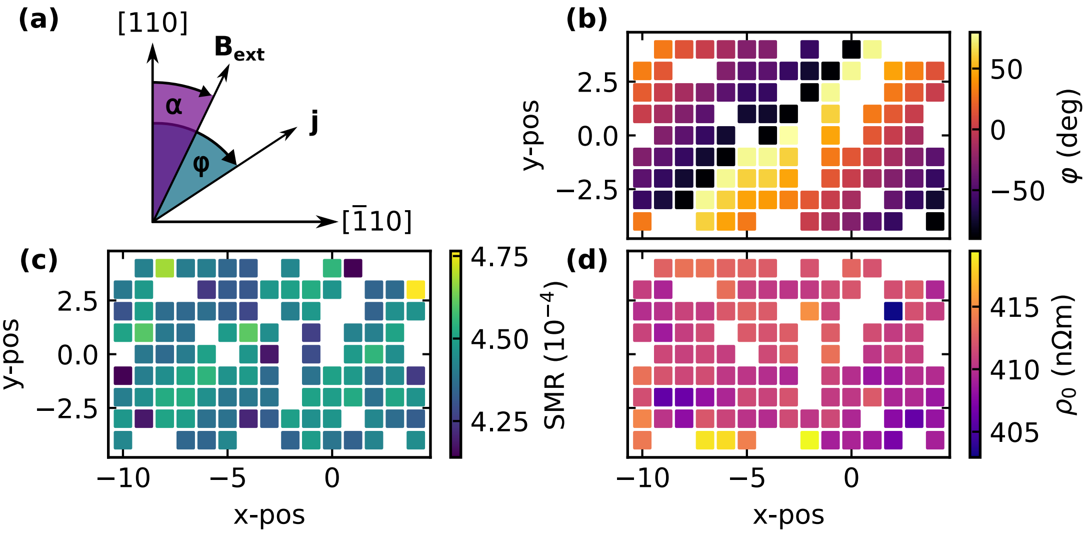

Figure 7.8: Evaluation of 117 rotated Hall bars on a YIG($\langle 001\rangle$)/Pt bilayer (sample S13). The concept of the rotated Hall bars is identical to Fig. 7.5, with the exception of the underlying YIG crystal orientation. (a) depicts the coordinate system for samples with $\mathbf{n}\|\langle 001\rangle$ and the rotation angle φ of the individual Hall bars. (b)-(d) depict the results in the form of the heat maps for S13. In (b), φ imitates the layout, confirming the analysis. The SMR in (c) exhibits a robust value over the sample. Along the diagonals, a trend can be observed, suggesting a robust value for a given φ, but a change with φ. This correlation cannot be found within the resistivity (d), implying an influence of the underlying YIG crystal orientation on the SMR.

using a single standard deviation. This σ exhibits an exceptionally low value of 0.043×10^{-4}. The two mean values μ_L and μ_R then describe the positions of the two SMR levels.

The modulation with the underlying crystal structure is supported by Fig. 7.9(b), depicting the SMR as a function of φ. Here, the fourfold symmetry becomes apparent from the data. Hall bars aligned with a $\langle 110\rangle$ direction, i.e. at −90 deg, 0 deg, 90 deg, exhibit larger SMR values in comparison to those along a $\langle 100\rangle$ direction at −45 deg and 45 deg. The two mean values from Fig. 7.9(a) are depicted as the solid lines, capturing the two levels of the SMR. The fourfold symmetry can be understood from the cubic symmetry of the YIG crystal.

To rule out an influence of the resistivity, its histogram and variation with φ are also illustrated in Fig. 7.9(b)+(e). The resistivity exhibits a very good agreement with a Gaussian distribution, as illustrated by the fit with a mean value of 411 nΩ m and its standard deviation of 2.33 nΩ m. In contrast to the SMR, no double peak can be observed. Further, no systematic change of ρ with φ is evident from Fig. 7.9(e) within the 1σ interval. Therefore, ρ is excluded as a parameter influencing the SMR modulation in Fig. 7.9(a).

To further corroborate the modulation of the SMR with φ, a second sample S14 was fabricated and evaluated. Similarly to the previous sample, the resistivity is Gaussian distributed with μ_ρ of 344 nΩ m and σ_ρ of 3.8 nΩ m. Additionally, no influence on the SMR was apparent, which is why the ρ is not shown here.

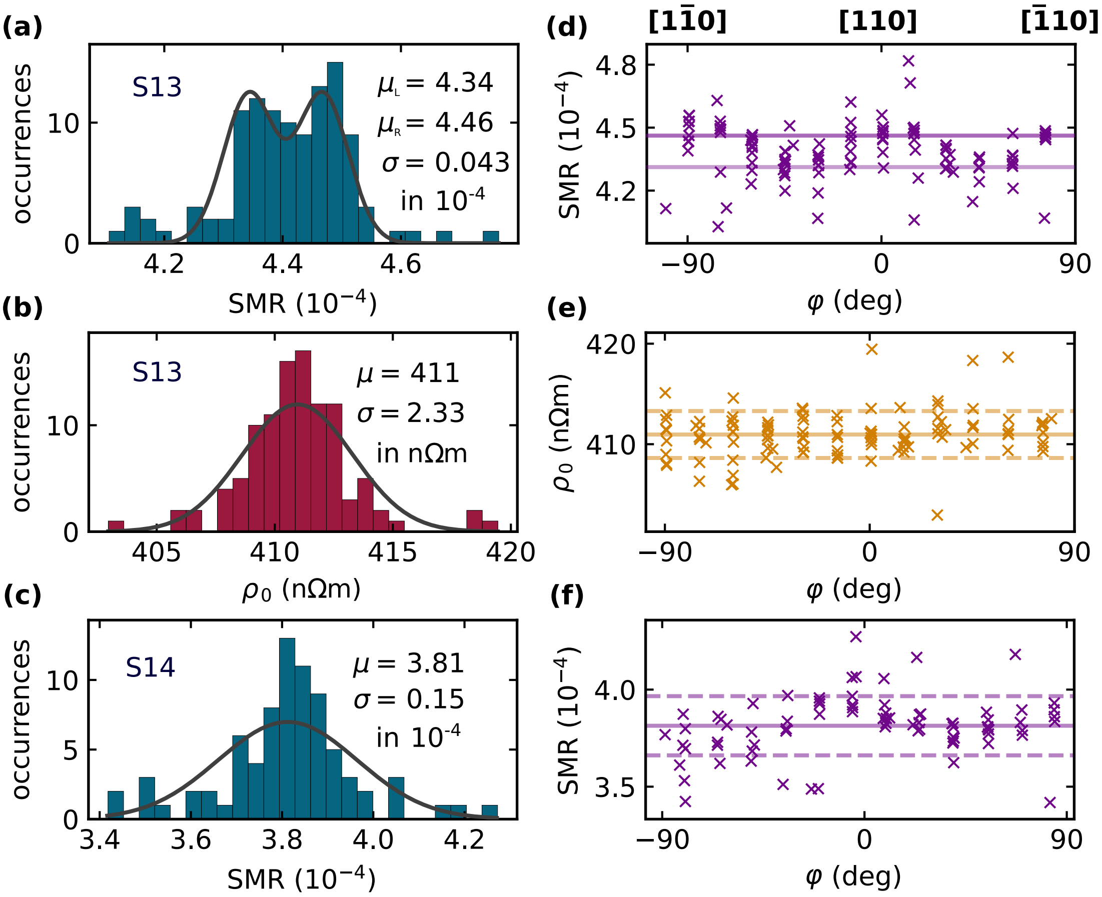

Figure 7.9: (a)+(c) Histograms of the SMR for the two samples measured in the [100]-[010] plane. (d)+(f) respective SMR versus the angle of the rotation φ. (b)+(e) depict the corresponding resistivity distribution of sample S14 from (a)+(d). Here, a modulation of the SMR with the underlying YIG crystal can be observed. Along the $\langle 110 \rangle$ orientations of YIG the SMR is larger than along a $\langle 100 \rangle$ direction. (b) and (e) underline that the effect is not artificially stemming from the resistivity. Hence, in (a), a bimodal distribution with two mean values and one standard deviation is used for the fit. The two levels are given with the lines in (b). The standard deviation is not depicted for visibility (c) and (f) depict a sample reproducing the effect. Here, fewer devices were probed and the modulation is less prevalent for negatively rotated Hall bars.

Figure 7.9(c)+(f) depicts the SMR as a histogram and as a function of φ, respectively. In the histogram, the double peak feature is not as apparent as in Fig. 7.9(a), and the data is coherently described in one Gaussian distribution. For this sample, the standard deviation is much larger than the amplitude of the modulation, meaning that the two Gaussians overlap and result in a single peak. The increased standard deviation becomes apparent, e.g in Fig. 7.9(f), where one notices that the data for negative φ values varies significantly more than for positive angle. While fewer Hall bars were measured in this sample, the reduced quality of the modulation is not clear and has to be investigated further.

However, the $\cos(4\varphi)$ modulation observed in Fig. 7.9(d) can be reproduced. Near 0 deg and 90 deg, the SMR is larger than at −45 deg and 45 deg, imitating the dependency from S13 (cp. Fig. 7.9(d)) and following the YIG orientations of $\langle 110 \rangle$. The dependence of the SMR on the underlying YIG($\langle 001 \rangle$) crystal structure is thereby confirmed.

The observation of a $\cos(4\varphi)$ dependency has not been previously reported in SMR experiments and underlying influences are now discussed. Out of possible factors, the Pt can be ruled out, as the modulation only appears along specific YIG orientations. No modulation was apparent in section 7.3, where nominally identical Pt films were used, but on a different substrate. Further, the Pt films were confirmed to be textured out of plane but polycrystalline in plane, regardless of the substrate (cp. Fig. 6.8).

In short, the SMR in YIG($\langle 001 \rangle$)/Pt bilayers was statistically investigated. A robust mean value with a narrow standard deviation of 1 % gave rise to a modulation with respect to the underlying YIG crystal structure. Hence, the influence is attributed to the underlying YIG crystal structured and modelled in the following.

7.4.3 Semi-quantitative model for the SMR modulation with the underlying YIG crystal orientation

The only parameter contributing to the SMR not intrinsic to the Pt is the spin mixing conductance G (cp. in Eq. (5.13)). G characterises the spin current transport across the interface of the magnetic and normal layer [257]. Relevant for its size are the contributing magnetic moments [211, 258], which implies a characteristic G for each pairing. This correlation suggests that changes in the magnetisation are reflected in G and, therefore, in the SMR.

A change in magnetisation occurs in magnetically ordered materials, e.g with temperature or under the influence of an external magnetic field [259]. These changes can be attributed to the magnon occupation in YIG. Magnons are the quasiparticle of the spin structure and describe its excitation and, therefore, follow the Bose-Einstein statistics:

$$n(E) = \frac{1}{\exp(E/(k_B T)) - 1} \tag{7.2}$$

Here, $n(E)$ is the expected number of magnons at a given energy E, k_B the Boltzmann constant and T the absolute temperature. The occupation then depends on the density of states of the material in question. For YIG, the magnon spectrum is very complex [74, 260], due to the large number of atoms in the unit cell (cp. Fig. 2.1). In order to approximate the effect, a parabolic dispersion relation $\omega(k) \propto k^2$ is assumed, which is accurate for small parts of the Brillouin zone [74] and, therefore, serves as a good first approximation. For a fully quantitative model all bands and exact dispersion relations would have to be taken into account. The corresponding density of state (DOS) $g(E)$ in 3D can be expressed as [261]

$$g(E) = \frac{1}{4\pi^2} \left(\frac{1}{A}\right)^{\frac{3}{2}} \sqrt{E - \Delta} \tag{7.3}$$

where A is the spin wave stiffness and Δ the magnon energy gap. A is commonly given as [261]

$$A = \frac{\hbar\omega}{k^2} = \frac{J_\mathrm{A} S a^2}{\hbar} \tag{7.4}$$

where J_A is the exchange integral, $\hbar$ is the reduced Planck constant, S is the spin angular momentum, and a the lattice parameter. Typical values for A are, e.g. 281 meV$\mathrm{\AA}^2$ for Fe, which corresponds to $4.5 \times 10^{-40}\,\mathrm{Jm}^2$ [261]. The spin wave stiffness was modelled for YIG in Ref. [73], where values between 2 and $6 \times 10^{-40}\,\mathrm{Jm}^2$ are extracted, agreeing well with the previously mentioned order of magnitude.

A more recent report finds an exchange stiffness D of $5.2 \times 10^{-17}\,\mathrm{Tm}^2$ or exchange constant K of $3.76 \times 10^{-12}\,\mathrm{J/m}$ [262]. Here, a similar A can be found by reconciling the units using the gyromagnetic ratio γ, $\hbar$, $S = 5/2$ and $D = 2K/M_\mathrm{s}$,

$$A = \frac{\hbar\omega}{k^2} = \hbar\gamma D = \frac{2\hbar\gamma K}{M_\mathrm{s}} = \frac{2K\hbar\gamma a^3}{8g\mu_\mathrm{B} S} = \frac{Ka^3}{10} \tag{7.5}$$

which yields the same dependency for A as described in Ref. [73]. With a of 1.2376 nm and K of $3.76 \times 10^{-12}\,\mathrm{J/m}$, a spin wave stiffness A of $7.12 \times 10^{-40}\,\mathrm{Jm}^2$ is extracted, which also nicely falls into the correct order of magnitude. [1] Therefore, all extracted spin wave stiffnesses are suited and the three different A values reported in Ref. [73] are used in the following evaluation (cp. Fig. 7.11), as the largest value is similar to the one from Ref. [262].

With the distribution (Eq. (7.2)) and all parameters of the density of states (Eq. (7.3)) at hand, the magnon population N_magn can be calculated by solving the following integral:

$$N_\mathrm{magn} = \frac{1}{4\pi^2}\left(\frac{1}{A}\right)^{\frac{3}{2}} \int_\Delta^\infty \frac{\sqrt{E-\Delta}}{\exp(E/(k_B T)) - 1}\, dE \tag{7.6}$$

Here, all parameters are as before. It should be noted that the numerical integration was conducted from Δ (lower bound) to 10 eV (upper bound), due to a divergence in the numerical integration. However, the extracted magnon number was unaffected by an upper limit larger than 1 eV, suggesting a correctly calculated magnon occupation.

Figure 7.10 illustrates the previously described concepts. In Fig. 7.10(a), the Bose-Einstein distribution (Eq. (7.2)) is given in dark gray and the DOS (Eq. (7.3)) for two different Δ values is depicted, where a larger gap correlates to a shift on the energy axis to the right. Calculating the product of Eq. (7.3) and Eq. (7.2) results in the solid curve depicted in Fig. 7.10(c). The magnon population N_magn (Eq. (7.6)) correlates to the area under the curve, i.e. the value of the integral in Eq. (7.6) (shaded in Fig. 7.10(c)). As each magnon reduces the saturation magnetisation M_0 by $\hbar\gamma$, resulting in a reduced magnetisation M_red:

---

[1] It should be noted that D and K yield slightly different results due to the extraction and recalculation at room temperature. For a direct comparison with Ref. [73], K is utilised here.

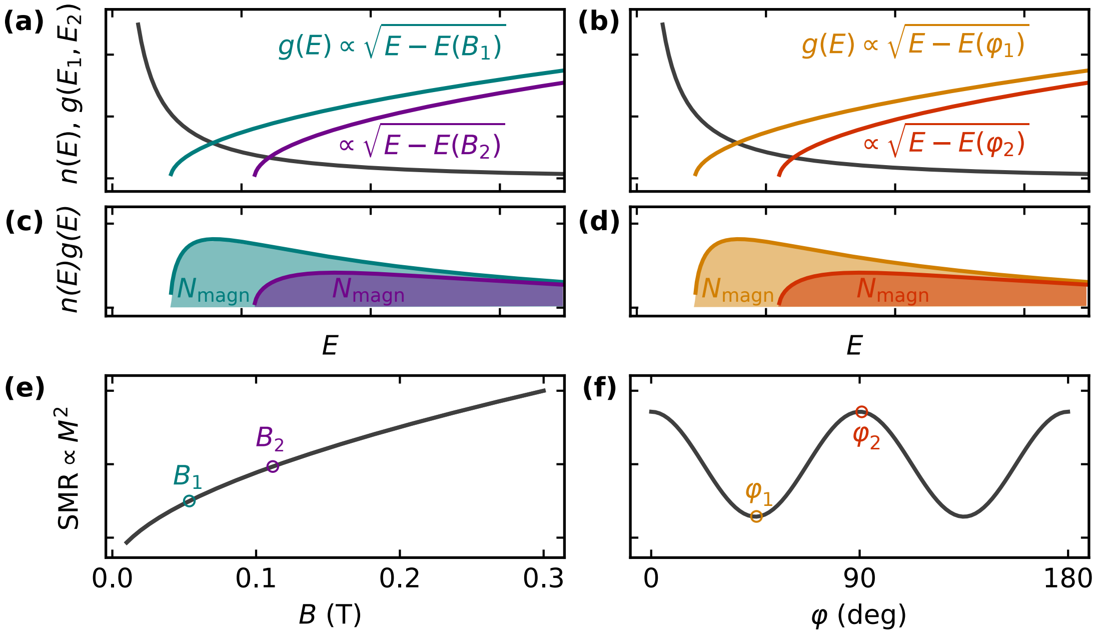

Figure 7.10: Theoretical expectations for the SMR amplitude. (a) and (b) illustrate the Bose-Einstein distribution $n(E)$ (Eq. (7.2)) and the density of states $g(E)$ (Eq. (7.3)). In (a), the gap is caused by an external magnetic field B, whereas in (b), the gap is caused by the underlying crystal structure due to a crystal anisotropy. In YIG, a four fold symmetry as described by rotation angle φ is expected for $\mathbf{n}\|\langle 001\rangle$. (c) and (d) depict the product of $n(E) \times g(E)$. The shaded area under the graph represents the integral, i.e. the number of magnons resulting from the different gaps. (c) and (d) depict the expected behaviour of the SMR, when taking a scaling with M^2 into account. The different fields B_1 and B_2 or crystal orientations φ_1 (45 deg) and φ_2 (90 deg) are depicted within the expected SMR scaling.

$$M_{\text{red}} = M_0 - \hbar\gamma N_{\text{magn}} \tag{7.7}$$

Depending on Δ, the value of M changes, which can be probed via the SMR, due to its scaling with $\propto M^2$ [43, 211, 245]. From Eq. (5.12),

$$\text{SMR} \propto m_t^2 = (M_{\text{red}}/M_0)^2 \times \cos^2(\phi) \tag{7.8}$$

is derived. Hence, even at a fixed field, i.e. a constant $\phi \in \alpha, \beta$ (cp. Fig. 5.4), the SMR changes.

The expected behaviour of the SMR as a function of the external magnetic field B is depicted in Fig. 7.10(e). A larger magnetic field B_2 corresponds to a larger (Zeeman) gap, resulting in a lower magnon occupation and, hence, a larger magnetisation. The curve shape of the SMR as a function of B is thereby non-linear, due to the exponentially increased occupation for lower energies (cp. Eq. (7.2) and Fig. 7.10(a) $n(E)$).

A similar argument can now be made for crystal anisotropies causing a magnon gap. For YIG (cp. Fig. 2.1), a cubic anisotropy is expected from the crystal structure, when considering the plane spanned by ⟨100⟩-⟨010⟩. This anisotropy is then the cause of the modulation with the rotation angle φ observed in Fig. 7.9. Now, the cubic anisotropy causes two energetically distinct levels, which are represented by φ_1 along ⟨100⟩ and φ_2 along ⟨110⟩ (cp. Fig. 7.10(d)). The two different gaps from the anisotropy now similarly result in different magnon occupations and therewith, different M_{red} values. The difference of $M_{\mathrm{red},110}$ and $M_{\mathrm{red},100}$ is then measured in the SMR, which manifests as a modulation with respect to the underlying crystal structure. For a cubic anisotropy, a $\cos(4\varphi)$ shaped modulation is then obtained in the SMR, as depicted in Fig. 7.10(d).

In order to quantitatively describe the data, a description of the gap Δ is required. Here, the energy of the collective excitation of the magnetic system, as described by ferromagnetic resonance (FMR, cp. chapter 3.3, are utilised [263, 264]. These can be obtained from a free energy density calculation and analytically solved for certain directions. For a cubic lattice and an in plane magnetisation, the energy of the gap $\Delta = \hbar\omega = hf$ can be extracted along ⟨110⟩ as [264]:

$$\Delta = \hbar\gamma\sqrt{\left(B_{\mathrm{ext}} + \mu_0 M_{\mathrm{s}} - \frac{2K_{\mathrm{u}}}{M_s} + \frac{2K_{\mathrm{c},1}}{M_{\mathrm{s}}}\right) \times \left(B - \frac{2K_{\mathrm{c},1}}{M_{\mathrm{s}}}\right)} \tag{7.9}$$

and along ⟨100⟩ as [264]:

$$\Delta = \hbar\gamma\sqrt{\left(B_{\mathrm{ext}} + \mu_0 M_{\mathrm{s}} - \frac{2K_{\mathrm{u}}}{M_s} + \frac{2K_{\mathrm{c},1}}{M_{\mathrm{s}}}\right) \times \left(B + \frac{2K_{\mathrm{c},1}}{M_{\mathrm{s}}}\right)} \tag{7.10}$$

Here, μ_0 is the vacuum permittivity, $K_{\mathrm{c},1}$ the first cubic anisotropy constant, K_{u} the uniaxial anisotropy and B the external magnetic field. For the calculation of the gap Δ in YIG, a $K_{\mathrm{c},1}$ of $-610\,\mathrm{J/m^3}$ and K_{u} of $0\,\mathrm{J/m^3}$ are employed. Lastly, both equations include a Zeeman contribution via B_{ext} and hence capture both dependencies visualised in Fig. 7.10(a) and (b).

By inserting Eq. (7.9) or Eq. (7.10) into Eq. (7.6), a full description of the system via a $\Delta(B, \varphi)$ is achieved. Here, the angle of rotation φ is modelled via $K_{\mathrm{c},1}$ for 0 deg with Eq. (7.9) and for 45 deg with Eq. (7.10). At low external fields, the cubic anisotropy strongly affects the value of $\Delta(B, K_{\mathrm{c},1})$, as evident by the calculated gaps at 40 mT, $\Delta(B = 0.04\,\mathrm{T}, \varphi = 0\,\mathrm{deg})$ of 1.17×10^{-5} eV and $\Delta(B = 0.04\,\mathrm{T}, \varphi = 45\,\mathrm{deg})$ of 0.94×10^{-5} eV, respectively - a difference of roughly 20 % between the two φ values. Towards higher fields, the Zeeman term dominates and the difference becomes negligible, as evident from $\Delta(B = 4\,\mathrm{T}, \varphi = 0\,\mathrm{deg})$ of 47.3×10^{-5} eV and $\Delta(B = 4\,\mathrm{T}, \varphi = 45\,\mathrm{deg})$ of 47.2×10^{-5} eV, i.e. 0.2 % change in gap between the crystal orientations. The extracted gaps are further in good agreement with literature values for YIG [265].

The presented model now predicts two aspects: First, a dependency of the SMR on B should be evident, which should be non-linear towards lower magnetic fields (cp. Fig. 7.10(c)). Secondly, the anisotropy in the crystal orientation dependent SMR should also scale with B and is expected to be more prevalent towards smaller B values.

In order to test the expectation, a Hall bar from sample S14 is bonded and measured

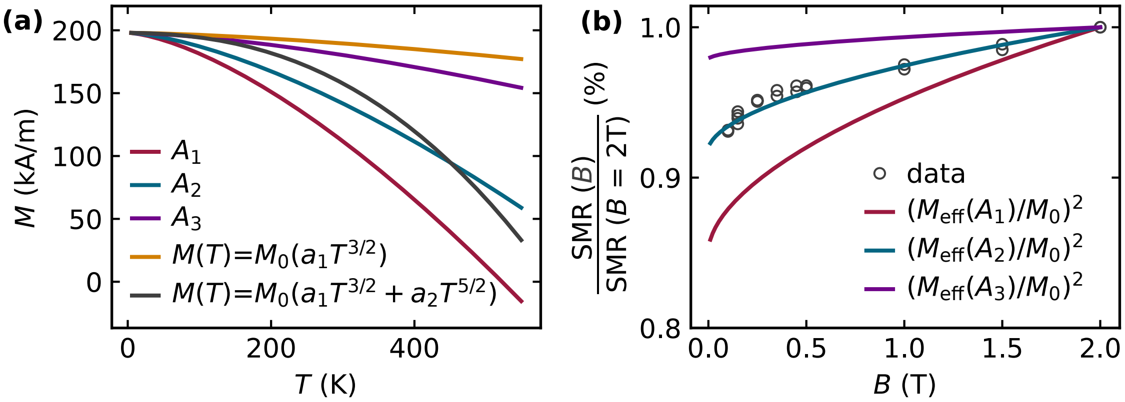

Figure 7.11: (a) Different $M(T)$ curves as modelled via Eq. (7.6) with the spin waves stiffnesses A_1 to A_3 from Ref. [73]. Here, A_2 captures the room temperature magnetisation the best. Additionally, the $M(T)$ for YIG from Ref. [266] is depicted, highlighting the shortcomings of the $T^{3/2}$ law from Eq. (7.6). (b) Room temperature SMR measurements on S14 at different magnetic fields of identically oriented Hall bars. At each B value, a rotation is measured and the SMR amplitude extracted. Lastly, all values are normalised to the SMR at 2 T. The expected curve shape calculated via Eqs. 7.6, 7.10 and 7.7 with A_1, A_2 and A_3 from (a) are the depicted in the respective $(M_{\mathrm{red}}/M_0)^2$ curve. A_2 nicely captures the data, whereas A_1 and A_3 overestimate (underestimate) the data.

in the cryostat at room temperature. Here, the magnetic field can be swept at controlled conditions. The results are depicted in Fig. 7.11(b). Here, the SMR is normalised to the maximum value at 2 T, where the largest SMR is observed. The change in SMR amplitude becomes steeper towards lower B values, confirming the expectation.

To model the B field dependence, the spin waves stiffnesses needs to correctly capture the change in magnetisation of YIG. Modelling this is challenging, as the $M(T) \propto T^{3/2}$ law described by Eq. (7.6) is only valid for low temperatures in YIG. Hence, often higher order correction terms are introduced to capture the behaviour [266]. Figure 7.11(a) depicts the $M(T)$ curves calculated using Eq. (7.6) and Eq. (7.7) for the three spin wave stiffnesses A_1, A_2 and A_3 from Ref. [73] of $2.24 \times 10^{-40}\,\mathrm{Jm}^2$, $2.98 \times 10^{-40}\,\mathrm{Jm}^2$ and $6.46 \times 10^{-40}\,\mathrm{Jm}^2$. Additionally, the $M(T)$, as extracted by ferromagnetic resonance in Ref. [266], is depicted in dark gray and yellow. The yellow curve highlights the short comings of the $T^{3/2}$ law and that higher order terms are required to correctly model the $M(T)$ of YIG.

Nonetheless, using A_2 results in a magnetisation of YIG of $141\,\mathrm{kA\,m^{-1}}$ at room temperatures, which almost exactly resembles the literature value of bulk YIG (cp. section 2.1). While A_1 overestimates the magnonic contributions, A_3 largely underestimates them. Therefore, for the room temperature measurements, A_2 is expected to correctly estimate the change in magnetisation, which is corroborated by the modelled curves Fig. 7.11(b). Here, M_0 of $198\,\mathrm{kA\,m^{-1}}$ is reduced by a number of magnons (cp. Eq. (7.7)), which depends on the temperature (cp. Eq. (7.6)) as well as the value of the external field (Eq. (7.9)). The calculated change $\left(\frac{M_{\mathrm{eff}}}{M_0}\right)^2 = \left(\frac{M_0 - M_{\mathrm{red}}}{M_0}\right)^2$ obtained for the three A values is given by the solid lines. Similar to Fig. 7.11(a), A_2 nicely captures the behaviour of the data, while

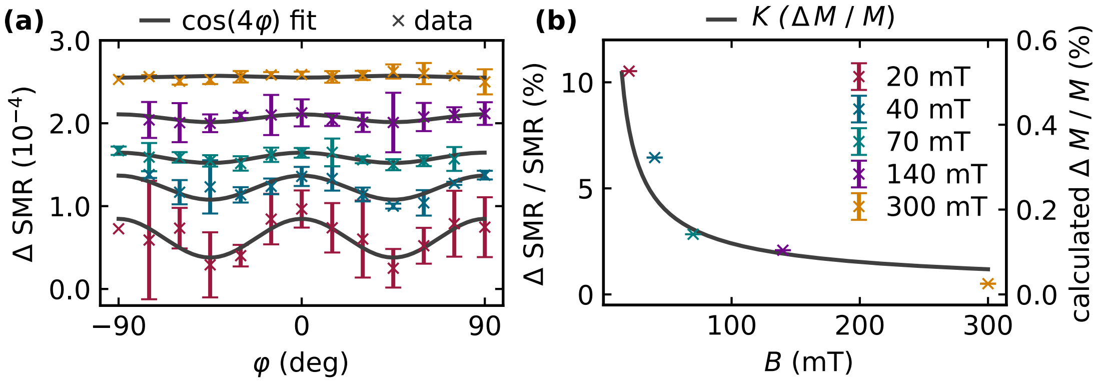

Figure 7.12: Evolution of the modulation in S13 (YIG($\langle 001\rangle$)/Pt). For each rotation angle φ the value of the SMR is averaged and depicted in (a). Due to the fourfold symmetry in the rotation plane, a $\cos(4\varphi)$ function is fit to the data to extract the amplitude. The amplitude of the modulation normalised by the SMR value is depicted in (b). Here, an increase in amplitude can be observed towards lower magnetic fields, whereas the modulation cannot be resolved for larger fields. The dependency can be quantitively understood via the difference in magnon occupation and magnetisation depending on $\Delta(B, \varphi)$.

A_1 (A_3) overestimates (underestimates) the SMR(B) dependency.

Note that the qualitative curve shape in Fig. 7.11(b) can be excellently reproduced by plotting $(M_{\mathrm{red}}/M_0)^2$ (cp. Eq. (7.7)) for any of the A values, if an additional scaling factor is included. When basing the calculation on the spin wave stiffness A_2 of $2.99 \times 10^{-40}\,\mathrm{Jm}^2$, which correctly reproduces the room temperature magnetisation in Fig. 7.11(a), the amplitude of the SMR(B) is immediately correctly captured without the need of a scaling factor. Thus, despite the tremendous simplification, the derived theory can quantitatively explain the experimental observations.

Now, the crystallographic dependency is touched upon again. If the modulation of the SMR stems from the magnonic contribution (cp. Fig. 7.10(d)), the difference between the crystal directions should increase with smaller external magnetic fields, as effectively the difference of the SMR(B) curves (see Fig. 7.10(c)) of the underlying crystal structure is measured. Therefore, several Halbach arrays were built and the device measured at external magnetic fields of 20 mT to 300 mT. For each array, a statistical measurement series was conducted and the results evaluated as before (cp. Fig. 7.9). Here, each angle φ is binned and the median and its standard deviation calculated.

Figure 7.12(a) shows the results of the field dependent statistical evaluations. The magnetic fields increase from 20 mT for the bottom curve (red) to 300 mT at the top (yellow). The mean SMR is subtracted and the curves are shifted with respect to each other for better visualisation. The largest differences between φ of 0 deg ($\parallel\langle 110\rangle$) and 45 deg ($\parallel\langle 100\rangle$) is observed at the lowest field. The earlier discussion yielded $\Delta(B, \langle 110\rangle) > \Delta(B, \langle 100\rangle)$, where the influence of $K_{c,1}$ was evident towards low external magnetic fields. Further the gaps result in $M_{110} > M_{100}$, which coherently captures the data. Hence, the variation in φ is also attributed to different magnon populations based on the underlying crystal structure, i.e. the differing gap due to the cubic anisotropy.

A $\cos(4\varphi)$ is fit to the data in order to extract the amplitude. This amplitude, normalised by the SMR value is then plotted as a function of B in Fig. 7.12(b). [2] In dark gray, the theoretical expectation is illustrated, using A_2 for the calculation of the difference in M_{red} (cp. Eq. (7.7)) between the $\langle 110 \rangle$ and $\langle 100 \rangle$ direction. The curve shape of the calculation resembles the data points well, implying a coherent explanation of the results in this chapter stemming from changing magnon occupations.

However, to obtain a good agreement with the data, a correction factor of 20 had to be applied. Figure 7.12(b) depicts the experimentally extracted change in SMR between the crystal directions in the left ordinate axis, whereas the predicted change is given at the right ordinate axis. The theoretical prediction strongly underestimates the effect. This disparity can partially be attributed to the complex magnon spectrum of YIG, which deviates from the quadratic dispersion relation [74, 260]. Hence, the $\sqrt{E}$ approximation does not capture all magnon modes, in particular at low energies where the Bose-Einstein distribution has the largest occupations, as evident from the $M(T)$ contributions in Fig. 7.11(a). Further, dipolar interactions are not included, which heavily influence the magnon occupation at low energies [267]. Hence, the magnon occupation and the change in magnetisation is underestimated by the present theory. Lastly, the non-local magnon mediated magnetoresistance Refs. [51, 52] also contributes to the amplitude and is not factored in. While the data cannot be fully reconciled using the naïve $g(E) \propto \sqrt{E}$ assumption, the curve shapes are in good agreement with the data, which supports the interpretation.

These results confirm the dependency of the SMR on the underlying crystal structure and present the first conclusive observation of this effect in a single YIG/Pt bilayer. However, a modulation could only be observed in specific directions. No changes in the SMR are expected if the free energy density of the probed plane is identical, or if the differences are to narrow to be resolved. Considering that the plane perpendicular to $\langle 111 \rangle$ is one where the magnon gap does not change [194, 263], the absence of an SMR modulation for this crystal cut (cp. subsection 7.4.1) is expected.

It is important to emphasize that the observed scaling of the magnetoresistance with M^2, as well as the presented magnon framework, extends beyond the experimental results. Firstly, the statistical approach enabled access to the occupation statistics of the dynamic excitations of the magnetisation using transport experiments. As the basis of the modulation lies within the magnetisation, a similar dependency on M^2 is also expected for other magnetoresistances, which depend on M^2, like the anisotropic magnetoresistance (AMR) [268]. Additionally, in the non-local analogue of the SMR [51, 52], the described anisotropies are expected to be even more prominent and potentially enhanced by a crystal orientation dependent damping [256]. Therefore, when considering the non-planar geometries, the direction of the Pt strip with respect to the crystal structure needs to be carefully chosen and a possibly stronger influence of the crystal orientation on the magnon propagation studied. The results and the model presented in this section, therefore, have implications over a broad spectrum of magnetoresistances.

However, when coming back to the crystal orientation dependent changes in the

---

[2] The fit function is $A\cos(4\varphi)$+C, where C captures the offset, i.e. the mean SMR. As for x = $\cos(4\varphi)$, x $\in$ [-1,1], 2A/c is plotted in Fig. 7.12(b) to capture the full amplitude.

SMR in BCGO/Pt from the first section [2], the effect in YIG/Pt is small in comparison. Furthermore, the data and modulation of the SMR in Ref. [2] is measured at 2 T and 2 K. At this temperature and field, magnonic contributions are mostly suppressed and the modulation is likely of a different origin in comparison to the one here. This conclusion suggests that several factors can lead to a crystalline dependency of the SMR.

7.5 Summary: Statistical evaluation of the spin Hall magnetoresistance

In summary, multiple samples of YIG/Pt bilayers were statistically investigated. To that end, numerous devices were patterned onto each sample and measured using a custom built wafer prober. In a first sample with 225 devices, a robust SMR value was obtained over a 5×6 mm^2 sample. The mean value μ_{SMR} is 3.45×10^{-4} and the corresponding standard deviation σ_{SMR} 0.26×10^{-4}. A $\sigma_{\mathrm{SMR}}/\mu_{\mathrm{SMR}}$ ratio of less than 10 % can be derived, which is reproduced over multiple samples. This statistical study confirms a narrowly distributed and reproducible SMR over the complete sample. However, differences in the SMR value in the order of 10 % need to be carefully discussed in the future.

Afterwards, the Hall bars were rotated with respect to the underlying crystal structure of YIG($\mathbf{n}||\langle 001\rangle$) and YIG($\mathbf{n}||\langle 111\rangle$). When rotating Hall bars in the plane perpendicular to $\langle 111\rangle$, no dependence of the SMR on the rotation angle φ could be resolved within the statistical variations. However, in the plane along $\langle 100\rangle$ and $\langle 110\rangle$, a modulation with the crystal orientation arises. The resistivity and the Pt are ruled out as possible factors influencing the modulation, whereas an exceptionally low σ_{SMR} ratio of 0.04×10^{-4} enabled the detection of the effect.

The modulation can be understood via different magnon occupations and corresponding magnetisations, as a change in M is reflected in the SMR. To model this effect, the magnon occupation was calculated by taking a field and crystal dependent gap into account. This gap is based upon the collective excitation of the magnetic system as described by the ferromagnetic resonance. The predicted curve shape is in excellent agreement with the data and fully corroborates the model.

The measured results have wide ranging implications, as dynamic excitations of the magnetisation were probed using DC transport experiments. Hence, the extracted dependency on M^2 and the scaling with field and anisotropy are expected in all material combinations giving rise to an SMR. More importantly, the results are expected to be transferred to other magnetoresistances which sensitively depend on M^2, like the AMR. Further, in the non-local variant of the SMR [51, 52], the crystal dependent anisotropies should be even more pronounced. Hence, when conducting transport experiments in non-planar YIG/Pt geometries, the consequences of this chapter need to be carefully considered.

Chapter 8

SUMMARY AND CONCLUSIONS

The goal of this thesis was to provide a platform for non-planar spintronic experiments, using the prototypical materials of the field: YIG and Pt. Non-planar YIG structures pave the way for magnon-transport based research or futuristic spin-wave based computing interconnects [57, 58, 167, 169, 170]. One way of investigating non-planar structures are magnetotransport experiments, using Pt as a means to induce spin currents. This thesis covered both aspects separately: the successful sample fabrication of non-planar YIG and magnetotransport experiments in Pt, Ti and YIG/Pt bilayers. The established sample preparation routine and transport results lay the foundation for spintronic research experiments in non-planar geometries.

Part I focused on the sample growth and crystallisation. In order to obtain non-planar, single crystalline YIG structures via room temperature sputtering and subsequent annealing several requirements need to be fulfilled. First of all, for the non planar geometry, a temperature stable template [69] in combination with a lattice matched substrate is required. In addition, profound knowledge of the crystallisation behaviour of YIG on the mentioned stack is crucial. Therefore, chapter 2 introduced the basic concept of YIG, sputter deposition and crystallisation. Then, in chapter 3, a thorough structural and magnetic characterisation of the sputtered YIG was performed. The obtained data corroborates that a process yielding high quality YIG films has been established in Konstanz.

With these results at hand, an extensive time and temperature series was conducted in chapter 3, granting insights into the crystallisation dynamics of YIG. On a non-lattice matched substrate, like SiO_x, nucleation is always required in order to form crystalline YIG. In contrast, on lattice matched GGG substrates, YIG crystallises in a coherent solid phase epitaxy picture. On YAG, which exhibits a large lattice mismatch to YIG, a more complex crystallisation behaviour is found. Thus chapter 3 presents a full description of the crystallisation process of amorphous YIG on lattice matched (GGG, YAG) and non-lattice matched SiO_x substrates. The crystallisation parameters extracted allow for an approximation of crystallisation velocities and to determine the temperature window where crystalline YIG films can be obtained.

The different crystallisation windows of lattice matched and non-lattice matched substrates can now be exploited, as detailed in chapter 4. The non-lattice matched SiO_x is utilised as a temperature stable, artificial mesa structure, which partially covers a lattice matched substrate, like GGG. Onto the GGG/SiO_x stack, an amorphous YIG layer is subsequently sputtered. By annealing in the correct temperature window, YIG first crystallises vertically from the GGG and then laterally over the mesa. This process is called lateral solid phase epitaxy, which was thoroughly described in the chapter. The results present the dynamics of the lateral solid phase epitaxy in YIG for the first time and further demonstrate the successful fabrication of non-planar, single crystalline YIG on top of an artificial mesa.

This new sample preparation route opens up a simple method for obtaining YIG in non-planar geometries in addition to the previously reported methods in Ref. [69, 90]. Investigating such structures can be envisioned by measuring the time resolved magneto optical Kerr effect on top of the step or conducting magnetotransport experiments on and across the step [51, 52]. To enable such transport experiments, a fundamental investigation into typical injector materials was conducted and the interface between YIG/Pt optimised and afterwards statistically characterised.

In part II of the thesis, Pt, Ti and YIG/Pt bilayers were investigated using magnetotransport experiments, paving the way for future experiments. Chapter 6 describes the intrinsic magnetoresistances in the two prototypical materials for spin- and orbitronics: Pt and Ti. In contrast to the expectation, a dominant ordinary magnetoresistance (OMR) contribution is found in Pt samples deposited in Konstanz. This OMR is dominant in low resistivity samples exhibiting clear crystalline order. In Ti, a large orbital Hanle magnetoresistance (HMR) is observed for the first time in samples characterised by low structural order and large amounts of defects. The relationship between crystallinity of the sample and dominating MR in Ti qualitatively resembles that of Pt, despite the different intrinsic mechanisms causing the spin and orbital Hall effect. Therefore, the results highlight a close connection of the subfields of spintronics and orbitronics. With chapter 6 a broader understanding of the intrinsic magnetoresistances in Pt and Ti is achieved. The chapter highlights, that while the HMR is a great tool for semi-directly detecting the spin or orbital Hall effect, it is only dominant in structurally disordered, high resistive samples. In contrast, the coexisting OMR can become dominant in low resistivity, high purity samples and overshadow the HMR. Lastly, clear guidelines in differentiating the two magnetoresistances are given at the end of chapter 6.

Combining spin and orbital Hall active materials provides a means to increase the exerted torque on the magnetic layer [32] or the injection and detection of magnons [39]. The exact knowledge of the intrinsic parameters allows for further optimisation of effect sizes. Further, the contributions of the OMR and HMR in addition to the spin Hall magnetoresistance (SMR) in bilayers of YIG/Pt can be approximated and incorporated in the analysis. The SMR in turn characterises the angular momentum transfer from YIG into Pt and, therefore, comprises the last important step for non-planar transport experiments. The distribution and reproducibility of the SMR as well as its dependency on the interface and underlying crystal structure are pivotal information, as changes in the transport response due to the non-planar sample geometry can therewith be correctly identified.

Hence, chapter 7 focuses on establishing the statistical distribution of the SMR in planar structures. To that end numerous samples were probed, each consisting of hundreds of Hall bar devices. The results clearly indicate how to obtain the best possible ex-situ YIG/Pt interfaces. Further, the SMR amplitude is extracted to be robust over a single sample with a standard deviation of roughly 10 % of the mean. Between samples the absolute value can vary much stronger than the individual standard deviation. Future experiments reporting SMR changes on the order of several 10 %, such as those attributed to the crystal orientation [248–250, 253], need to be interpreted with caution and take the statistical distribution into account. With the statistical approach, a crystallographic dependence of the SMR could be resolved. For the YIG orientations ⟨100⟩ and ⟨110⟩ in the plane, a modulation of the SMR is found, which mimics the symmetry of the YIG crystal. The modulation is then modelled via different magnon occupations and corresponding magnetisations, as a function of field and crystal orientation. The measured results have wide ranging implications, providing access to the occupation statistics of the dynamic excitations of the magnetisation in transport measurements. In turn, a similar influence is also expected in other magnetoresistive effects which are sensitive to changes in M^2. Furthermore, this crystalline dependency is expected to be more prominent in the non-local magnetoresistance [51, 52], which could be a tool to probe the non-planar YIG from the first part of the thesis. Hence, the non-local magnetoresistance should be investigated and the crystalline orientation of YIG in the non-local devices carefully considered.

Overall, the goal of this thesis was to elevate YIG research to the next dimension, which has been achieved. The newly established method of fabricating non-planar YIG provides a means of studying non-planar geometries. When envisioning magnetotransport experiments in these structures, the way has been paved from the insights gained into the intrinsic effects in spin and orbital Hall active materials as well as the statistical distribution in bilayers.

List of Publications

[1] S. Sailler, D. Reustlen, D. Schmidt, M. Lammel, R. Schlitz, and S. T. B. Goennenwein, in preparation (2025).

[2] M. Leiviskä, R. Firouzmandi, K.-H. Ahn, P. Kubaščik, Z. Soban, S. P. Bommanaboyena, C. Müller, D. Kriegner, S. Sailler, M. Lammel, K. K. Bestha, L. Šmejkal, J. Zelezny, A. U. B. Wolter, M. Scheufele, J. Fischer, M. Opel, S. Geprägs, M. Althammer, B. Büchner, T. Jungwirth, L. Nádvorník, S. T. B. Goennenwein, V. Kocsis, and H. Reichlová, Physical Review Materials **9**, 084403 (2025).

[3] A. Badura, W. H. Campos, V. K. Bharadwaj, I. Kounta, L. Michez, M. Petit, J. Rial, M. Leiviskä, V. Baltz, F. Krizek, D. Kriegner, J. Zemen, S. Telkamp, S. Sailler, M. Lammel, R. J. Ubiergo, A. B. Hellenes, R. González-Hernández, J. Sinova, T. Jungwirth, S. T. B. Goennenwein, L. Šmejkal, and H. Reichlova, Nature Communications **16**, 7111 (2025).

[4] S. Sailler, G. Sala, D. Reustlen, R. Schlitz, M.-G. Kang, P. Gambardella, S. T. B. Goennenwein, and M. Lammel, Physical Review B **111**, 104421 (2025).

[5] S. Sailler, R. Bueno Villoro, S. Bayesteh, H. Schlörb, M. O. Cichocka, K. Nielsch, S. Zhang, and N. Pérez, Materials Today Physics **46**, 101477 (2024).

[6] S. Sailler, G. Skobjin, H. Schlörb, B. Boehm, O. Hellwig, A. Thomas, S. T. B. Goennenwein, and M. Lammel, Physical Review Materials **8**, 043402 (2024).

[7] S. Sailler, D. Pohl, H. Schlörb, B. Rellinghaus, A. Thomas, S. T. B. Goennenwein, and M. Lammel, Physical Review Materials **8**, L020402 (2024).

[8] S. Bayesteh, S. Sailler, H. Schlörb, R. He, G. Schierning, K. Nielsch, and N. Pérez, Materials Today Physics **24**, 100669 (2022).

BIBLIOGRAPHY

[9] S. L. Moskowitz, *Advanced Materials Innovation: Managing Global Technology in the 21st century* (John Wiley & Sons, Hoboken, New Jersey, 2016), pp. 3–16.

[10] E. Mollick, IEEE Annals of the History of Computing **28**, 62–75 (2006).

[11] A. Samal, S. L. Tripathi, and S. K. Mohapatra, Transactions on Electrical and Electronic Materials **21**, 443–455 (2020).

[12] S. M. Rossnagel, IBM Journal of Research and Development **43**, 163–179 (1999).

[13] R. W. Johnson, A. Hultqvist, and S. F. Bent, Materials Today **17**, 236–246 (2014).

[14] B. A. Joyce, Reports on Progress in Physics **48**, 1637–1697 (1985).

[15] P. R. Gray, P. J. Hurst, S. H. Lewis, and R. G. Meyer, *Analysis and Design of Analog Integrated Circuits* (John Wiley & Sons, Hoboken, New Jersey, 2024), pp. 127–131.

[16] V. Bakshi, ed., *EUV Lithography* (SPIE Press, Bellingham, Washington, 2009), pp. 1–46.

[17] D. Mamaluy and X. Gao, Applied Physics Letters **106**, 193503 (2015).

[18] A. P. Jacob, R. Xie, M. G. Sung, L. Liebmann, R. T. P. Lee, and B. Taylor, International Journal of High Speed Electronics and Systems **26**, 1740001 (2017).

[19] A. W. Topol, D. C. L. Tulipe, L. Shi, D. J. Frank, K. Bernstein, S. E. Steen, A. Kumar, G. U. Singco, A. M. Young, K. W. Guarini, and M. Ieong, IBM Journal of Research and Development **50**, 491–506 (2006).

[20] B. Dieny, I. L. Prejbeanu, K. Garello, P. Gambardella, P. Freitas, R. Lehndorff, W. Raberg, U. Ebels, S. O. Demokritov, J. Akerman, A. Deac, P. Pirro, C. Adelmann, A. Anane, A. V. Chumak, A. Hirohata, S. Mangin, S. O. Valenzuela, M. C. Onbaşlı, M. d'Aquino, G. Prenat, G. Finocchio, L. Lopez-Diaz, R. Chantrell, O. Chubykalo-Fesenko, and P. Bortolotti, Nature Electronics **3**, 446–459 (2020).

[21] A. Fert, Reviews of Modern Physics **80**, 1517–1530 (2008).

[22] B. Bhushan, Microsystem Technologies **29**, 1529–1546 (2023).

[23] D. A. Thompson and J. S. Best, IBM Journal of Research and Development **44**, 311–322 (2000).

[24] M. Kryder and C. S. Kim, IEEE Transactions on Magnetics **45**, 3406–3413 (2009).

[25] D. C. Worledge and G. Hu, Nature Reviews Electrical Engineering **1**, 730–747 (2024).

[26] I. M. Miron, K. Garello, G. Gaudin, P.-J. Zermatten, M. V. Costache, S. Auffret, S. Bandiera, B. Rodmacq, A. Schuhl, and P. Gambardella, Nature (London) **476**, 189–193 (2011).

[27] L. Liu, C.-F. Pai, Y. Li, H. W. Tseng, D. C. Ralph, and R. A. Buhrman, Science **336**, 555–558 (2012).

[28] B. Dieny, Journal of Magnetism and Magnetic Materials **136**, 335–359 (1994).

[29] L. Berger, Physical Review B **54**, 9353–9358 (1996).

[30] C. Chappert, A. Fert, and F. N. Van Dau, Nature Materials **6**, 813–823 (2007).

[31] S. S. P. Parkin, C. Kaiser, A. Panchula, P. M. Rice, B. Hughes, M. Samant, and S.-H. Yang, Nature Materials **3**, 862–867 (2004).

[32] Q. Shao, P. Li, L. Liu, H. Yang, S. Fukami, A. Razavi, H. Wu, K. Wang, F. Freimuth, Y. Mokrousov, M. D. Stiles, S. Emori, A. Hoffmann, J. Akerman, K. Roy, J.-P. Wang, S.-H. Yang, K. Garello, and W. Zhang, IEEE Transactions on Magnetics **57**, 1–39 (2021).

[33] M. Dyakonov and V. Perel, Physics Letters A **35**, 459–460 (1971).

[34] J. E. Hirsch, Physical Review Letters **83**, 1834–1837 (1999).

[35] A. Manchon, H. C. Koo, J. Nitta, S. M. Frolov, and R. A. Duine, Nature Materials **14**, 871–882 (2015).

[36] L. Salemi and P. M. Oppeneer, Physical Review Materials **6**, 095001 (2022).

[37] Y.-G. Choi, D. Jo, K.-H. Ko, D. Go, K.-H. Kim, H. G. Park, C. Kim, B.-C. Min, G.-M. Choi, and H.-W. Lee, Nature (London) **619**, 52–56 (2023).

[38] S. Ding, A. Ross, D. Go, L. Baldrati, Z. Ren, F. Freimuth, S. Becker, F. Kammerbauer, J. Yang, G. Jakob, Y. Mokrousov, and M. Kläui, Physical Review Letters **125**, 177201 (2020).

[39] J. A. Mendoza-Rodarte, M. Cosset-Chéneau, B. J. van Wees, and M. H. D. Guimarães, Physical Review Letters **132**, 226704 (2024).

[40] D. Jo, D. Go, G.-M. Choi, and H.-W. Lee, npj Spintronics **2**, 19 (2024).

[41] G. Y. Guo, S. Murakami, T.-W. Chen, and N. Nagaosa, Physical Review Letters **100**, 096401 (2008).

[42] H. Nakayama, M. Althammer, Y.-T. Chen, K. Uchida, Y. Kajiwara, D. Kikuchi, T. Ohtani, S. Geprägs, M. Opel, S. Takahashi, R. Gross, G. E. W. Bauer, S. T. B. Goennenwein, and E. Saitoh, Physical Review Letters **110**, 206601 (2013).

[43]M. Althammer, S. Meyer, H. Nakayama, M. Schreier, S. Altmannshofer, M. Weiler, H. Huebl, S. Geprägs, M. Opel, R. Gross, D. Meier, C. Klewe, T. Kuschel, J.-M. Schmalhorst, G. Reiss, L. Shen, A. Gupta, Y.-T. Chen, G. E. W. Bauer, E. Saitoh, and S. T. B. Goennenwein, Physical Review B **87**, 224401 (2013).

[44]A. Hoffmann, IEEE Transactions on Magnetics **49**, 5172–5193 (2013).

[45]E. Sagasta, Y. Omori, M. Isasa, M. Gradhand, L. E. Hueso, Y. Niimi, Y. Otani, and F. Casanova, Physical Review B **94**, 060412 (2016).

[46]O. I. Gorbatov, G. Johansson, A. Jakobsson, S. Mankovsky, H. Ebert, I. Di Marco, J. Minár, and C. Etz, Physical Review B **104**, 174401 (2021).

[47]Y. Kajiwara, K. Harii, S. Takahashi, J. Ohe, K. Uchida, M. Mizuguchi, H. Umezawa, H. Kawai, K. Ando, K. Takanashi, S. Maekawa, and E. Saitoh, Nature (London) **464**, 262–266 (2010).

[48]H. Chang, P. Li, W. Zhang, T. Liu, A. Hoffmann, L. Deng, and M. Wu, IEEE Magnetics Letters **5**, 1–4 (2014).

[49]C. Hauser, T. Richter, N. Homonnay, C. Eisenschmidt, M. Qaid, H. Deniz, D. Hesse, M. Sawicki, S. Ebbinghaus, and G. Schmidt, Scientific Reports **6**, 20827 (2016).

[50]C. Dubs, O. Surzhenko, R. Thomas, J. Osten, T. Schneider, K. Lenz, J. Grenzer, R. Hübner, and E. Wendler, Physical Review Materials **4**, 024416 (2020).

[51]L. J. Cornelissen, J. Liu, R. A. Duine, J. B. Youssef, and B. J. van Wees, Nature Physics **11**, 1022–1026 (2015).

[52]S. T. B. Goennenwein, R. Schlitz, M. Pernpeintner, K. Ganzhorn, M. Althammer, R. Gross, and H. Huebl, Applied Physics Letters **107**, 172405 (2015).

[53]C. Liu, J. Chen, T. Liu, F. Heimbach, H. Yu, Y. Xiao, J. Hu, M. Liu, H. Chang, T. Stueckler, S. Tu, Y. Zhang, Y. Zhang, P. Gao, Z. Liao, D. Yu, K. Xia, N. Lei, W. Zhao, and M. Wu, Nature Communications **9**, 738 (2018).

[54]J. F. Dillon, Physical Review **105**, 759–760 (1957).

[55]G. Sala, H. Wang, W. Legrand, and P. Gambardella, Physical Review Letters **131**, 156703 (2023).

[56]I. Lyalin, S. Alikhah, M. Berritta, P. M. Oppeneer, and R. K. Kawakami, Physical Review Letters **131**, 156702 (2023).

[57]A. V. Chumak, V. I. Vasyuchka, A. A. Serga, and B. Hillebrands, Nature Physics **11**, 453–461 (2015).

[58] A. V. Chumak, P. Kabos, M. Wu, C. Abert, C. Adelmann, A. O. Adeyeye, J. Åkerman, F. G. Aliev, A. Anane, A. Awad, C. H. Back, A. Barman, G. E. W. Bauer, M. Becherer, E. N. Beginin, V. A. S. V. Bittencourt, Y. M. Blanter, P. Bortolotti, I. Boventer, D. A. Bozhko, S. A. Bunyaev, J. J. Carmiggelt, R. R. Cheenikundil, F. Ciubotaru, S. Cotofana, G. Csaba, O. V. Dobrovolskiy, C. Dubs, M. Elyasi, K. G. Fripp, H. Fulara, I. A. Golovchanskiy, C. Gonzalez-Ballestero, P. Graczyk, D. Grundler, P. Gruszecki, G. Gubbiotti, K. Guslienko, A. Haldar, S. Hamdioui, R. Hertel, B. Hillebrands, T. Hioki, A. Houshang, C.-M. Hu, H. Huebl, M. Huth, E. Iacocca, M. B. Jungfleisch, G. N. Kakazei, A. Khitun, R. Khymyn, T. Kikkawa, M. Klaui, O. Klein, J. W. Klos, S. Knauer, S. Koraltan, M. Kostylev, M. Krawczyk, I. N. Krivorotov, V. V. Kruglyak, D. Lachance-Quirion, S. Ladak, R. Lebrun, Y. Li, M. Lindner, R. Macedo, S. Mayr, G. A. Melkov, S. Mieszczak, Y. Nakamura, H. T. Nembach, A. A. Nikitin, S. A. Nikitov, V. Novosad, J. A. Otalora, Y. Otani, A. Papp, B. Pigeau, P. Pirro, W. Porod, F. Porrati, H. Qin, B. Rana, T. Reimann, F. Riente, O. Romero-Isart, A. Ross, A. V. Sadovnikov, A. R. Safin, E. Saitoh, G. Schmidt, H. Schultheiss, K. Schultheiss, A. A. Serga, S. Sharma, J. M. Shaw, D. Suess, O. Surzhenko, K. Szulc, T. Taniguchi, M. Urbanek, K. Usami, A. B. Ustinov, T. Van Der Sar, S. Van Dijken, V. I. Vasyuchka, R. Verba, S. V. Kusminskiy, Q. Wang, M. Weides, M. Weiler, S. Wintz, S. P. Wolski, and X. Zhang, IEEE Transactions on Magnetics **58**, 1–72 (2022).

[59] R. Streubel, P. Fischer, F. Kronast, V. P. Kravchuk, D. D. Sheka, Y. Gaididei, O. G. Schmidt, and D. Makarov, Journal of Physics D: Applied Physics **49**, 363001 (2016).

[60] A. Fernández-Pacheco, R. Streubel, O. Fruchart, R. Hertel, P. Fischer, and R. P. Cowburn, Nature Communications **8**, 15756 (2017).

[61] M. Isasa, E. Villamor, L. E. Hueso, M. Gradhand, and F. Casanova, Physical Review B **91**, 024402 (2015).

[62] Y. Krockenberger, H. Matsui, T. Hasegawa, M. Kawasaki, and Y. Tokura, Applied Physics Letters **93**, 092505 (2008).

[63] M. Albrecht, G. Hu, I. L. Guhr, T. C. Ulbrich, J. Boneberg, P. Leiderer, and G. Schatz, Nature Materials **4**, 203–206 (2005).

[64] P. Hansen, P. Röschmann, and W. Tolksdorf, Journal of Applied Physics **45**, 2728–2732 (1974).

[65] P. W. Jang and J. Y. Kim, IEEE Transactions on Magnetics **37**, 2438–2440 (2001).

[66] P. Jang, S. Yamamoto, and H. Kuniki, Physica Status Solidi (a) **201**, 1851–1854 (2004).

[67] T. Boudiar, B. Payet-Gervy, M.-F. Blanc-Mignon, J.-J. Rousseau, M. Le Berre, and H. Joisten, Journal of Magnetism and Magnetic Materials **284**, 77–85 (2004).

[68] P. Trempler, R. Dreyer, P. Geyer, C. Hauser, G. Woltersdorf, and G. Schmidt, Applied Physics Letters **117**, 232401 (2020).

[69] M. Lammel, *Advancing 3D Spintronics: Atomic Layer Deposition of Platinum and Yttrium Iron Garnet Thin Films*, Dissertation (Technische Universität Dresden, Dresden, 2021).

[70] S. Geller and M. Gilleo, Journal of Physics and Chemistry of Solids **3**, 30–36 (1957).

[71] S. C. Abrahams and S. Geller, Acta Crystallographica **11**, 437–441 (1958).

[72] M. Shone, Circuits, Systems and Signal Processing **4**, 89–103 (1985).

[73] E. E. Anderson, Physical Review **134**, A1581–A1585 (1964).

[74] V. Cherepanov, I. Kolokolov, and V. L'vov, Physics Reports **229**, 81–144 (1993).

[75] H. L. Wang, C. H. Du, Y. Pu, R. Adur, P. C. Hammel, and F. Y. Yang, Physical Review B **88**, 100406 (2013).

[76] H. Sakimura, T. Tashiro, and K. Ando, Nature Communications **5**, 5730 (2014).

[77] N. Beaulieu, N. Kervarec, N. Thiery, O. Klein, V. Naletov, H. Hurdequint, G. De Loubens, J. B. Youssef, and N. Vukadinovic, IEEE Magnetics Letters **9**, 1–5 (2018).

[78] M. Lammel, D. Scheffler, D. Pohl, P. Swekis, S. Reitzig, S. Piontek, H. Reichlova, R. Schlitz, K. Geishendorf, L. Siegl, B. Rellinghaus, L. M. Eng, K. Nielsch, S. T. B. Goennenwein, and A. Thomas, Physical Review Materials **6**, 044411 (2022).

[79] G. B. Stringfellow, Reports on Progress in Physics **45**, 469–525 (1982).

[80] P. G. Evans, Y. Chen, J. A. Tilka, S. E. Babcock, and T. F. Kuech, Current Opinion in Solid State and Materials Science **22**, 229–242 (2018).

[81] R. Gross and A. Marx, *Festkörperphysik* (De Gruyter, Berlin, Boston, 2014), pp. 143–165.

[82] M. Yeadon and J. M. Gibson, *Molecular Beam Epitaxy, Semiconductors*, edited by R. A. Meyers (Academic Press, New York, 2003), pp. 113–121.

[83] V. G. Dubrovskii, *Nucleation Theory and Growth of Nanostructures* (Springer, Berlin, Heidelberg, 2014), pp. 18–24.

[84] P. Görnert, R. Hergt, E. Sinn, M. Wendt, B. Keszei, and J. Vandlik, Journal of Crystal Growth **87**, 331–337 (1988).

[85] J. Čermák, A. Abrahám, T. Fabián, P. Kaboš, and P. Hyben, Journal of Magnetism and Magnetic Materials **83**, 427–429 (1990).

[86] A. R. Will-Cole, J. L. Hart, V. Lauter, A. Grutter, C. Dubs, M. Lindner, T. Reimann, N. R. Valdez, C. J. Pearce, T. C. Monson, J. J. Cha, D. Heiman, and N. X. Sun, Physical Review Materials **7**, 054411 (2023).

[87] A. Heinrich, S. Leitenmeier, T. Körner, R. Lux, M. Herbort, and B. Stritzker, Journal of the Magnetics Society of Japan **30**, 584–587 (2006).

[88] M. Haidar, M. Ranjbar, M. Balinsky, R. K. Dumas, S. Khartsev, and J. Åkerman, Journal of Applied Physics **117**, 17D119 (2015).

[89] C. Hauser, C. Eisenschmidt, T. Richter, A. Müller, H. Deniz, and G. Schmidt, Journal of Applied Physics **122**, 083908 (2017).

[90] F. Heyroth, C. Hauser, P. Trempler, P. Geyer, F. Syrowatka, R. Dreyer, S. G. Ebbinghaus, G. Woltersdorf, and G. Schmidt, Physical Review Applied **12**, 054031 (2019).

[91] G. Gurjar, V. Sharma, S. Patnaik, and B. K. Kuanr, Materials Research Express **8**, 066401 (2021).

[92] O. d'Allivy Kelly, A. Anane, R. Bernard, J. Ben Youssef, C. Hahn, A. H. Molpeceres, C. Carrétéro, E. Jacquet, C. Deranlot, P. Bortolotti, R. Lebourgeois, J.-C. Mage, G. De Loubens, O. Klein, V. Cros, and A. Fert, Applied Physics Letters **103**, 082408 (2013).

[93] M.-B. Park and N.-H. Cho, Journal of Magnetism and Magnetic Materials **231**, 253–264 (2001).

[94] S. Yamamoto, H. Kuniki, H. Kurisu, M. Matsuura, and P. Jang, Physica Status Solidi (a) **201**, 1810–1814 (2004).

[95] Y.-M. Kang, S.-H. Wee, S.-I. Baik, S.-G. Min, S.-C. Yu, S.-H. Moon, Y.-W. Kim, and S.-I. Yoo, Journal of Applied Physics **97**, 10A319 (2005).

[96] A. D. Block, P. Dulal, B. J. H. Stadler, and N. C. A. Seaton, IEEE Photonics J. **6**, 1–8 (2014).

[97] T. Liu, H. Chang, V. Vlaminck, Y. Sun, M. Kabatek, A. Hoffmann, L. Deng, and M. Wu, Journal of Applied Physics **115**, 17A501 (2014).

[98] J. Lustikova, Y. Shiomi, Z. Qiu, T. Kikkawa, R. Iguchi, K. Uchida, and E. Saitoh, Journal of Applied Physics **116**, 153902 (2014).

[99] M. B. Jungfleisch, W. Zhang, W. Jiang, H. Chang, J. Sklenar, S. M. Wu, J. E. Pearson, A. Bhattacharya, J. B. Ketterson, M. Wu, and A. Hoffmann, Journal of Applied Physics **117**, 17D128 (2015).

[100] Y. Zhang, J. Xie, L. Deng, and L. Bi, IEEE Transactions on Magnetics **51**, 1–4 (2015).

[101] S. Li, W. Zhang, J. Ding, J. E. Pearson, V. Novosad, and A. Hoffmann, Nanoscale **8**, 388–394 (2016).

[102] J. F. K. Cooper, C. J. Kinane, S. Langridge, M. Ali, B. J. Hickey, T. Niizeki, K. Uchida, E. Saitoh, H. Ambaye, and A. Glavic, Physical Review B **96**, 104404 (2017).

[103] J. Lian, Y. Chen, Z. Liu, M. Zhu, G. Wang, W. Zhang, and X. Dong, Ceramics International **43**, 7477–7481 (2017).

[104] A. Talalaevskij, M. Decker, J. Stigloher, A. Mitra, H. S. Körner, O. Cespedes, C. H. Back, and B. J. Hickey, Physical Review B **95**, 064409 (2017).

[105] N. Zhu, H. Chang, A. Franson, T. Liu, X. Zhang, E. Johnston-Halperin, M. Wu, and H. X. Tang, Applied Physics Letters **110**, 252401 (2017).

[106] J. Ding, C. Liu, Y. Zhang, U. Erugu, Z. Quan, R. Yu, E. McCollum, S. Mo, S. Yang, H. Ding, X. Xu, J. Tang, X. Yang, and M. Wu, Physical Review Applied **14**, 014017 (2020).

[107] J. Ding, T. Liu, H. Chang, and M. Wu, IEEE Magnetics Letters **11**, 1–5 (2020).

[108] J.-H. Seol, J.-H. An, G.-W. Park, T. Nguyen Thi, D. Duong Viet, B.-G. Park, P. C. Van, and J.-R. Jeong, Thin Solid Films **774**, 139846 (2023).

[109] P. Cao Van, T. T. Nguyen, V. D. Duong, M. H. Nguyen, J.-H. Seol, G.-W. Park, G.-H. Kim, D.-H. Kim, and J.-R. Jeong, Current Applied Physics **42**, 80–85 (2022).

[110] C. White, L. Boatner, P. Sklad, C. McHargue, J. Rankin, G. Farlow, and M. Aziz, Nuclear Instruments and Methods in Physics Research Section B: Beam Interactions with Materials and Atoms **32**, 11–22 (1988).

[111] B. C. Johnson, J. C. McCallum, and M. J. Aziz, *Solid-Phase Epitaxy*, edited by T. F. Kuech (Elsevier, Amsterdam, 2015), pp. 317–363.

[112] B. Hoefflinger, *ITRS: The International Technology Roadmap for Semiconductors* (Springer, Berlin, Heidelberg, 2011), pp. 161–174.

[113] L. Csepregi, J. W. Mayer, and T. W. Sigmon, Applied Physics Letters **29**, 92–93 (1976).

[114] L. Csepregi, R. Küllen, J. Mayer, and T. Sigmon, Solid State Communications **21**, 1019–1021 (1977).

[115] J. S. Williams, Nuclear Instruments and Methods in Physics Research **209-210**, 219–228 (1983).

[116] B. C. Johnson, P. Gortmaker, and J. C. McCallum, Physical Review B **77**, 214109 (2008).

[117] A. Claverie, S. Koffel, N. Cherkashin, G. Benassayag, and P. Scheiblin, Thin Solid Films **518**, 2307–2313 (2010).

[118] K. T. Ho, I. Suni, and M.-A. Nicolet, Journal of Applied Physics **56**, 1207–1212 (1984).

[119] G.-Q. Lu, E. Nygren, and M. J. Aziz, Journal of Applied Physics **70**, 5323–5345 (1991).

[120] H. Ishiwara, H. Yamamoto, S. Furukawa, M. Tamura, and T. Tokuyama, Applied Physics Letters **43**, 1028–1030 (1983).

[121] H. Ishiwara, M. Tanaka, and S. Furukawa, Applied Physics Letters **49**, 1363–1365 (1986).

[122] G. K. Celler and S. Cristoloveanu, Journal of Applied Physics **93**, 4955–4978 (2003).

[123] K. Kusukawa, M. Moniwa, M. Ohkura, and E. Takeda, Applied Physics Letters **56**, 560–562 (1990).

[124] D. Scheffler, *Magnetron Sputtering of Magnetic Thin Film Materials for Spintronics*, Dissertation (Technische Universität Dresden, Dresden, 2024).

[125] S. Gates-Rector and T. Blanton, Powder Diffraction (PDF: 00-013-0493) **34**, 352–360 (2019).

[126] S. Gates-Rector and T. Blanton, Powder Diffraction (PDF: 00-033-0040) **34**, 352–360 (2019).

[127] S. Gates-Rector and T. Blanton, Powder Diffraction (PDF: 00-043-0507) **34**, 352–360 (2019).

[128] L. Spieß, ed., *Moderne Röntgenbeugung: Röntgendiffraktometrie für Materialwissenschaftler, Physiker und Chemiker* (Vieweg + Teubner, Wiesbaden, 2009).

[129] E. Chason and T. M. Mayer, Critical Reviews in Solid State and Materials Sciences **22**, 1–67 (1997).

[130] W. Legrand, Y. Kemna, S. Schären, H. Wang, D. Petrosyan, L. Holder, R. Schlitz, M. H. Aguirre, M. Lammel, and P. Gambardella, Advanced Functional Materials, 2503644 (2025).

[131] L. Csepregi, J. Mayer, and T. Sigmon, Physics Letters A **54**, 157–158 (1975).

[132] M. Roumie, B. A. Samad, M. Tabbal, M. Abi-Akl, M.-F. Blanc-Mignon, and B. Nsouli, Materials Chemistry and Physics **124**, 188–191 (2010).

[133] Y. Chen, M. H. Yusuf, Y. Guan, R. Jacobson, M. G. Lagally, S. E. Babcock, T. F. Kuech, and P. G. Evans, ACS Applied Materials & Interfaces **9**, 41034–41042 (2017).

[134] H. Bai, X. Z. Zhan, G. Li, J. Su, Z. Z. Zhu, Y. Zhang, T. Zhu, and J. W. Cai, Applied Physics Letters **115**, 182401 (2019).

[135] A. Mitra, O. Cespedes, Q. Ramasse, M. Ali, S. Marmion, M. Ward, R. M. D. Brydson, C. J. Kinane, J. F. K. Cooper, S. Langridge, and B. J. Hickey, Scientific Reports **7**, 11774 (2017).

[136] C. L. Jermain, S. V. Aradhya, N. D. Reynolds, R. A. Buhrman, J. T. Brangham, M. R. Page, P. C. Hammel, F. Y. Yang, and D. C. Ralph, Physical Review B **95**, 174411 (2017).

[137] M. Lammel, K. Geishendorf, M. A. Choffel, D. M. Hamann, D. C. Johnson, K. Nielsch, and A. Thomas, Applied Physics Letters **117**, 213106 (2020).

[138] M. Renninger, Zeitschrift für Physik **106**, 141–176 (1937).

[139] S. Gates-Rector and T. Blanton, Powder Diffraction (PDF: 00-005-0565) **34**, 352–360 (2019).

[140] D. Dingley, Journal of Microscopy **213**, 214–224 (2004).

[141] J. W. Nielsen and E. F. Dearborn, Journal of Physics and Chemistry of Solids **5**, 202–207 (1958).

[142] W. Tolksdorf and I. Bartels, Journal of Crystal Growth **54**, 417–424 (1981).

[143] P. Bennema, E. A. Giess, and J. E. Weidenborner, Journal of Crystal Growth **62**, 41–60 (1983).

[144] H. P. Klug and L. E. Alexander, *X-Ray Diffraction Procedures: for Polycrystalline and Amorphous Materials* (Wiley, New York, 1976), pp. 493–494.

[145] Y. M. Mos, A. C. Vermeulen, C. J. N. Buisman, and J. Weijma, Geomicrobiology Journal **35**, 511–517 (2018).

[146] G. Schmidt, C. Hauser, P. Trempler, M. Paleschke, and E. T. Papaioannou, Physica Status Solidi (b) **257** (2020).

[147] H. Zheng, J. Zhou, J. Deng, P. Zheng, L. Zheng, M. Han, Y. Yang, L. Deng, and H. Qin, Materials Letters **123**, 181–183 (2014).

[148] Y. Rao, D. Zhang, H. Zhang, L. Jin, Q. Yang, Z. Zhong, M. Li, C. Hong, and B. Ma, Journal of Physics D: Applied Physics **51**, 435001 (2018).

[149] K. Kasahara, S. Sueda, and T. Manago, AIP Advances **12**, 015204 (2022).

[150] A. Krysztofik, S. Özoğlu, R. D. McMichael, and E. Coy, Scientific Reports **11**, 14011 (2021).

[151] A. M. Miller, M. Lemon, M. A. Choffel, S. R. Rich, F. Harvel, and D. C. Johnson, Zeitschrift für Naturforschung B **77**, 313–322 (2022).

[152]M. Avrami, The Journal of Chemical Physics **7**, 1103–1112 (1939).

[153]M. Avrami, The Journal of Chemical Physics **8**, 212–224 (1940).

[154]M. Avrami, The Journal of Chemical Physics **9**, 177–184 (1941).

[155]K. Shirzad and C. Viney, Journal of The Royal Society Interface **20**, 20230242 (2023).

[156]W. D. Callister, *Materials Science and Engineering: An Introduction* (John Wiley & Sons, New York, 2007).

[157]H. Wang, C. Du, P. C. Hammel, and F. Yang, Physical Review B **89**, 134404 (2014).

[158]W. F. F. Wan Ali, M. Othman, M. F. Ain, N. S. Abdullah, and Z. A. Ahmad, Journal of the American Ceramic Society **99**, 315–323 (2016).

[159]B. R. Johnson and W. M. Kriven, Journal of Materials Research **16**, 1795–1805 (2001).

[160]Y. P. Khanna and T. J. Taylor, Polymer Engineering and Science **28**, 1042–1045 (1988).

[161]J.-S. Lee and S.-K. Joo, Japanese Journal of Applied Physics **39**, 6343–6347 (2000).

[162]K. Taira, Y. Hirose, S. Nakao, N. Yamada, T. Kogure, T. Shibata, T. Sasaki, and T. Hasegawa, ACS Nano **8**, 6145–6150 (2014).

[163]Y. Chen, J. A. Tilka, Y. Ahn, J. Park, A. Pateras, T. Zhou, D. E. Savage, I. McNulty, M. V. Holt, D. M. Paskiewicz, D. D. Fong, T. F. Kuech, and P. G. Evans, The Journal of Physical Chemistry C **123**, 7447–7456 (2019).

[164]W. V. Erk, H. J. G. J. V. Hoek-Martens, and G. Bartels, Journal of Crystal Growth **48**, 621–634 (1980).

[165]E. Beregi, E. Sterk, F. Tanos, E. Hartmann, and J. Lábár, Journal of Crystal Growth **65**, 562–567 (1983).

[166]S. Kosen, A. F. Van Loo, D. A. Bozhko, L. Mihalceanu, and A. D. Karenowska, APL Materials **7**, 101120 (2019).

[167]A. Barman, G. Gubbiotti, S. Ladak, A. O. Adeyeye, M. Krawczyk, J. Gräfe, C. Adelmann, S. Cotofana, A. Naeemi, V. I. Vasyuchka, B. Hillebrands, S. A. Nikitov, H. Yu, D. Grundler, A. V. Sadovnikov, A. A. Grachev, S. E. Sheshukova, J.-Y. Duquesne, M. Marangolo, G. Csaba, W. Porod, V. E. Demidov, S. Urazhdin, S. O. Demokritov, E. Albisetti, D. Petti, R. Bertacco, H. Schultheiss, V. V. Kruglyak, V. D. Poimanov, S. Sahoo, J. Sinha, H. Yang, M. Münzenberg, T. Moriyama, S. Mizukami, P. Landeros, R. A. Gallardo, G. Carlotti, J.-V. Kim, R. L. Stamps, R. E. Camley, B. Rana, Y. Otani, W. Yu, T. Yu, G. E. W. Bauer, C. Back, G. S. Uhrig, O. V. Dobrovolskiy, B. Budinska, H. Qin, S. Van Dijken, A. V. Chumak, A. Khitun, D. E. Nikonov, I. A. Young, B. W. Zingsem, and M. Winklhofer, Journal of Physics: Condensed Matter **33**, 413001 (2021).

[168]S. Guo, B. McCullian, P. Chris Hammel, and F. Yang, Journal of Magnetism and Magnetic Materials **562**, 169795 (2022).

[169]V. K. Sakharov, E. N. Beginin, Y. V. Khivintsev, A. V. Sadovnikov, A. I. Stognij, Y. A. Filimonov, and S. A. Nikitov, Applied Physics Letters **117**, 022403 (2020).

[170] M. M. Salazar-Cardona, L. Körber, H. Schultheiss, K. Lenz, A. Thomas, K. Nielsch, A. Kákay, and J. A. Otálora, Applied Physics Letters **118**, 262411 (2021).

[171] S. Vélez, V. N. Golovach, A. Bedoya-Pinto, M. Isasa, E. Sagasta, M. Abadia, C. Rogero, L. E. Hueso, F. S. Bergeret, and F. Casanova, Physical Review Letters **116**, 016603 (2016).

[172] S. A. Wolf, D. D. Awschalom, R. A. Buhrman, J. M. Daughton, S. Von Molnár, M. L. Roukes, A. Y. Chtchelkanova, and D. M. Treger, Science **294**, 1488–1495 (2001).

[173] I. Žutić, J. Fabian, and S. Das Sarma, Reviews of Modern Physics **76**, 323–410 (2004).

[174] T. Kuschel and G. Reiss, Nature Nanotechnology **10**, 22–24 (2015).

[175] A. Manchon, J. Železný, I. M. Miron, T. Jungwirth, J. Sinova, A. Thiaville, K. Garello, and P. Gambardella, Reviews of Modern Physics **91**, 035004 (2019).

[176] V. Krizakova, M. Perumkunnil, S. Couet, P. Gambardella, and K. Garello, Journal of Magnetism and Magnetic Materials **562**, 169692 (2022).

[177] J. Sinova, S. O. Valenzuela, J. Wunderlich, C. H. Back, and T. Jungwirth, Reviews of Modern Physics **87**, 1213–1260 (2015).

[178] T. Jungwirth, J. Wunderlich, and K. Olejník, Nature Materials **11**, 382–390 (2012).

[179] R. H. Liu, W. L. Lim, and S. Urazhdin, Physical Review Letters **110**, 147601 (2013).

[180] W. Zhao and G. Prenat, eds., *Spintronics-based computing* (Springer International Publishing, 2015), pp. 145–157.

[181] T. Chen, R. K. Dumas, A. Eklund, P. K. Muduli, A. Houshang, A. A. Awad, P. Durrenfeld, B. G. Malm, A. Rusu, and J. Åkerman, Proceedings of the IEEE **104**, 1919–1945 (2016).

[182] X. Han, X. Wang, C. Wan, G. Yu, and X. Lv, Applied Physics Letters **118**, 120502 (2021).

[183] Y. K. Kato, R. C. Myers, A. C. Gossard, and D. D. Awschalom, Science **306**, 1910–1913 (2004).

[184] S. O. Valenzuela and M. Tinkham, Nature (London) **442**, 176–179 (2006).

[185] N. F. Mott, Proceedings of the Royal Society of London Series A **124**, 425–442 (1929).

[186] S. Murakami, N. Nagaosa, and S.-C. Zhang, Science **301**, 1348–1351 (2003).

[187] J. Sinova, D. Culcer, Q. Niu, N. A. Sinitsyn, T. Jungwirth, and A. H. MacDonald, Physical Review Letters **92**, 126603 (2004).

[188] J. Wunderlich, B. Kaestner, J. Sinova, and T. Jungwirth, Physical Review Letters **94**, 047204 (2005).

[189] C. Brüne, A. Roth, E. G. Novik, M. König, H. Buhmann, E. M. Hankiewicz, W. Hanke, J. Sinova, and L. W. Molenkamp, Nature Physics **6**, 448–454 (2010).

[190] J. Bass and W. P. Pratt, Journal of Physics: Condensed Matter **19**, 183201 (2007).

[191] D. Go, D. Jo, C. Kim, and H.-W. Lee, Physical Review Letters **121**, 086602 (2018).

[192] B. A. Bernevig, T. L. Hughes, and S.-C. Zhang, Physical Review Letters **95**, 066601 (2005).

[193]T. Tanaka, H. Kontani, M. Naito, T. Naito, D. S. Hirashima, K. Yamada, and J. Inoue, Physical Review B **77**, 165117 (2008).

[194]A. Gudín, A. Anadón, I. Arnay, R. Guerrero, J. Camarero, S. Petit-Watelot, P. Perna, and J.-C. Rojas-Sánchez, Physical Review Materials **7**, 124412 (2023).

[195]R. Gross and A. Marx, *Festkörperphysik* (De Gruyter, Berlin, Boston, 2014), pp. 259–312.

[196]M. I. Dyakonov, Physical Review Letters **99**, 126601 (2007).

[197]W. Hanle, Zeitschrift für Physik **30**, 93–105 (1924).

[198]J. Li, A. H. Comstock, D. Sun, and X. Xu, Physical Review B **106**, 184420 (2022).

[199]A. B. Pippard, *Magnetoresistance in metals*, Cambridge Studies in Low Temperature Physics (Cambridge University Press, Cambridge (England), New York, 1989).

[200]M. Isasa, S. Vélez, E. Sagasta, A. Bedoya-Pinto, N. Dix, F. Sánchez, L. E. Hueso, J. Fontcuberta, and F. Casanova, Physical Review Applied **6**, 034007 (2016).

[201]P. Gehlhoff, E. Justi, and M. Kohler, Zeitschrift für Naturforschung A **5**, 16–18 (1950).

[202]J. Rumble, ed., *CRC Handbook of Chemistry and Physics* (CRC Press, Boca Raton, 2022).

[203]J. De Launay, R. Dolecek, and R. Webber, Journal of Physics and Chemistry of Solids **11**, 37–42 (1959).

[204]K. Fuchs, Mathematical Proceedings of the Cambridge Philosophical Society **34**, 100–108 (1938).

[205]E. Sondheimer, Advances in Physics **1**, 1–42 (1952).

[206]P. Vašek, K. Míšek, and P. Svoboda, Czechoslovak Journal of Physics **25**, 794–805 (1975).

[207]E. Fawcett, Advances in Physics **13**, 139–191 (1964).

[208]M. Kohler, Annalen der Physik **424**, 211–218 (1938).

[209]Y.-T. Chen, S. Takahashi, H. Nakayama, M. Althammer, S. T. B. Goennenwein, E. Saitoh, and G. E. W. Bauer, Physical Review B **87**, 144411 (2013).

[210]Y.-T. Chen, S. Takahashi, H. Nakayama, M. Althammer, S. T. B. Goennenwein, E. Saitoh, and G. E. W. Bauer, Journal of Physics: Condensed Matter **28**, 103004 (2016).

[211]X.-P. Zhang, F. S. Bergeret, and V. N. Golovach, Nano Letters **19**, 6330–6337 (2019).

[212]T. Kato, Y. Ohnuma, and M. Matsuo, Physical Review B **102**, 094437 (2020).

[213]D. A. Reiss, T. Kampfrath, and P. W. Brouwer, Physical Review B **104**, 024415 (2021).

[214]H. Wu, X. Zhang, C. H. Wan, B. S. Tao, L. Huang, W. J. Kong, and X. F. Han, Physical Review B **94**, 174407 (2016).

[215]Y. Maruyama, R. Ohshima, E. Shigematsu, Y. Ando, and M. Shiraishi, Applied Physics Express **16**, 023004 (2023).

[216]S. Kumar and S. Kumar, Nature Communications **14**, 8185 (2023).

[217]H. Moriya, M. Taniguchi, D. Jo, D. Go, N. Soya, H. Hayashi, Y. Mokrousov, H.-W. Lee, and K. Ando, Nano Letters **24**, 6459–6464 (2024).

[218]G. Sala and P. Gambardella, Physical Review Research **4**, 033037 (2022).

[219]S. Meyer, R. Schlitz, S. Geprägs, M. Opel, H. Huebl, R. Gross, and S. T. B. Goennenwein, Applied Physics Letters **106**, 132402 (2015).

[220]J. Narayan, P. Tiwari, K. Jagannadham, and O. W. Holland, Applied Physics Letters **64**, 2093–2095 (1994).

[221]T. Huber, A. Opitz, and J. Fleig, Solid State Ionics **273**, 8–12 (2015).

[222]M. Isasa, A. Bedoya-Pinto, S. Vélez, F. Golmar, F. Sánchez, L. E. Hueso, J. Fontcuberta, and F. Casanova, Applied Physics Letters **105**, 142402 (2014).

[223]Y. Liu, Z. Yuan, R. J. H. Wesselink, A. A. Starikov, M. van Schilfgaarde, and P. J. Kelly, Physical Review B **91**, 220405 (2015).

[224]R. Rouzegar, M. A. Wahada, A. L. Chekhov, W. Hoppe, G. Bierhance, J. Jechumtál, L. Nádvorník, M. Wolf, T. S. Seifert, S. S. P. Parkin, G. Woltersdorf, P. W. Brouwer, and T. Kampfrath, Nano Letters **24**, 7852–7860 (2024).

[225]M. Lammel, R. Schlitz, K. Geishendorf, D. Makarov, T. Kosub, S. Fabretti, H. Reichlova, R. Huebner, K. Nielsch, A. Thomas, and S. T. B. Goennenwein, Applied Physics Letters **114**, 252402 (2019).

[226]L. Roesch and R. H. Willens, Journal of Applied Physics **34**, 2159–2162 (1963).

[227]J. C. Idrobo, J. Rusz, G. Datt, D. Jo, S. Alikhah, D. Muradas, U. Noumbe, M. V. Kamalakar, and P. M. Oppeneer, *Direct observation of nanometer-scale orbital angular momentum accumulation*, 2024.

[228]P. Tang and G. E. W. Bauer, Physical Review Letters **133**, 186302 (2024).

[229]L. Liao, F. Xue, L. Han, J. Kim, R. Zhang, L. Li, J. Liu, X. Kou, C. Song, F. Pan, and Y. Otani, Physical Review B **105**, 104434 (2022).

[230]H. Liu and D. Culcer, Physical Review Letters **132**, 186302 (2024).

[231]J. Nickel, *Magnetoresistance Overview* (Hewlett-Packard Laboratories, Technical Publications Department, Palo Alto, 1995).

[232]J. Kim, P. Sheng, S. Takahashi, S. Mitani, and M. Hayashi, Physical Review Letters **116**, 097201 (2016).

[233]K. Ganzhorn, J. Barker, R. Schlitz, B. A. Piot, K. Ollefs, F. Guillou, F. Wilhelm, A. Rogalev, M. Opel, M. Althammer, S. Geprägs, H. Huebl, R. Gross, G. E. W. Bauer, and S. T. B. Goennenwein, Physical Review B **94**, 094401 (2016).

[234]Z. Ding, B. L. Chen, J. H. Liang, J. Zhu, J. X. Li, and Y. Z. Wu, Physical Review B **90**, 134424 (2014).

[235]J. Fischer, O. Gomonay, R. Schlitz, K. Ganzhorn, N. Vlietstra, M. Althammer, H. Huebl, M. Opel, R. Gross, S. T. B. Goennenwein, and S. Geprägs, Physical Review B **97**, 014417 (2018).

[236]J. Fischer, M. Althammer, N. Vlietstra, H. Huebl, S. T. Goennenwein, R. Gross, S. Geprägs, and M. Opel, Physical Review Applied **13**, 014019 (2020).

[237] K. Oyanagi, J. M. Gomez-Perez, X.-P. Zhang, T. Kikkawa, Y. Chen, E. Sagasta, A. Chuvilin, L. E. Hueso, V. N. Golovach, F. S. Bergeret, F. Casanova, and E. Saitoh, Physical Review B **104**, 134428 (2021).

[238] A. Aqeel, N. Vlietstra, J. A. Heuver, G. E. W. Bauer, B. Noheda, B. J. van Wees, and T. T. M. Palstra, Physical Review B **92**, 224410 (2015).

[239] A. Aqeel, N. Vlietstra, A. Roy, M. Mostovoy, B. J. Van Wees, and T. T. M. Palstra, Physical Review B **94**, 134418 (2016).

[240] S. R. Marmion, M. Ali, M. McLaren, D. A. Williams, and B. J. Hickey, Physical Review B **89**, 220404 (2014).

[241] S. Vélez, A. Bedoya-Pinto, W. Yan, L. E. Hueso, and F. Casanova, Physical Review B **94**, 174405 (2016).

[242] M. B. Jungfleisch, V. Lauer, R. Neb, A. V. Chumak, and B. Hillebrands, Applied Physics Letters **103**, 022411 (2013).

[243] S. Pütter, S. Geprägs, R. Schlitz, M. Althammer, A. Erb, R. Gross, and S. T. B. Goennenwein, Applied Physics Letters **110**, 012403 (2017).

[244] Z. Qiu, K. Ando, K. Uchida, Y. Kajiwara, R. Takahashi, H. Nakayama, T. An, Y. Fujikawa, and E. Saitoh, Applied Physics Letters **103**, 092404 (2013).

[245] P. Noël, R. Schlitz, E. Karadža, C.-H. Lambert, L. Nessi, F. Binda, and P. Gambardella, Physical Review Letters **134**, 146701 (2025).

[246] R. Lebrun, A. Ross, S. A. Bender, A. Qaiumzadeh, L. Baldrati, J. Cramer, A. Brataas, R. A. Duine, and M. Kläui, Nature **561**, 222–225 (2018).

[247] S. Keller, L. Mihalceanu, M. R. Schweizer, P. Lang, B. Heinz, M. Geilen, T. Brächer, P. Pirro, T. Meyer, A. Conca, D. Karfaridis, G. Vourlias, T. Kehagias, B. Hillebrands, and E. T. Papaioannou, New Journal of Physics **20**, 053002 (2018).

[248] R. Thompson, J. Ryu, Y. Du, S. Karube, M. Kohda, and J. Nitta, Physical Review B **101**, 214415 (2020).

[249] R. Thompson, J. Ryu, G. Choi, S. Karube, M. Kohda, J. Nitta, and B.-G. Park, Physical Review Applied **15**, 014055 (2021).

[250] Y. Xiao, H. Wang, and E. E. Fullerton, Frontiers in Physics **9**, 791736 (2022).

[251] T. Ikebuchi, Y. Shiota, T. Ono, K. Nakamura, and T. Moriyama, Applied Physics Letters **120**, 072406 (2022).

[252] Q. Bai, J. Mao, J. Yun, Y. Zhai, M. Chang, X. Zhang, J. Zhang, Y. Zuo, and L. Xi, Applied Physics Letters **118**, 132403 (2021).

[253] Y. Wu, Z. Xu, J. Chen, X. Xu, J. Miao, and Y. Jiang, Applied Physics A **127**, 419 (2021).

[254] A. Rachoutis, *Non local spin transport experiments*, MA thesis (University of Konstanz, Konstanz, 2024).

[255] C. Burrowes, B. Heinrich, B. Kardasz, E. A. Montoya, E. Girt, Y. Sun, Y.-Y. Song, and M. Wu, Applied Physics Letters **100**, 092403 (2012).

[256] Z. Zhao, L. Zhang, Y. Chen, Z. Zhong, X. Tang, Y. Zhang, H. Zhang, and L. Jin, Applied Physics Letters **124**, 052405 (2024).

[257] A. Brataas, Y. V. Nazarov, and G. E. W. Bauer, Physical Review Letters **84**, 2481–2484 (2000).

[258] A. B. Cahaya, A. O. Leon, and G. E. W. Bauer, Physical Review B **96**, 144434 (2017).

[259] S. Blundell, *Magnetism in Condensed Matter*, Oxford Master Series in Condensed Matter Physics (Oxford University Press, Oxford, New York, 2001), pp. 85–92.

[260] A. J. Princep, R. A. Ewings, S. Ward, S. Tóth, C. Dubs, D. Prabhakaran, and A. T. Boothroyd, npj Quantum Materials **2**, 63 (2017).

[261] R. Gross and A. Marx, *Festkörperphysik* (De Gruyter, Berlin, Boston, 2014), pp. 751–763.

[262] S. Klingler, V. Amin, S. Geprägs, K. Ganzhorn, H. Maier-Flaig, M. Althammer, H. Huebl, R. Gross, R. D. McMichael, M. D. Stiles, S. T. B. Goennenwein, and M. Weiler, Physical Review Letters **120**, 12720 (2018).

[263] A. Jalali-Roudsar, V. Denysenkov, and S. Khartsev, Journal of Magnetism and Magnetic Materials **288**, 15–21 (2005).

[264] A. Brandlmaier, *Magnetische Anisotropie in dünnen Schichten aus Magnetit*, Diplomarbeit (TU München, München, 2006).

[265] S. S.-L. Zhang and S. Zhang, Physical Review Letters **109**, 096603 (2012).

[266] I. H. Solt, Journal of Applied Physics **33**, 1189–1191 (1962).

[267] B. A. Kalinikos and A. N. Slavin, Journal of Physics C: Solid State Physics **19**, 7013–7033 (1986).

[268] T. McGuire and R. Potter, IEEE Transactions on Magnetics **11**, 1018–1038 (1975).

ACKNOWLEDGMENTS

I want to express my sincere gratitude to everyone who supported, advised and (or) encouraged me during the course of this thesis. My thanks go out to everyone who gave scientific or practical advice, who taught me something new, who welcomed me to Konstanz during the start of my PhD, who proofread any part of the thesis, who trusted in me or who contributed to this thesis in one way or another. I hope that everyone who doesn't find themselves on the following, most likely incomplete list, will forgive me. Here, I particularly want to thank:

- *Dr. Michaela Lammel* for being an incredible supervisor and person. For your enthusiasm for samples and deposition. For giving me all the scientific freedom I wanted and just letting me experiment and figure things out myself - but always being there to help if something didn't work. For always having an open door and ear. For always being the first to cross check and proof read everything, so it looked good before it even reached STBG. For taking care of ordering samples, buying new deposition chambers and all the stuff no one really wants to do - without all the foundations you laid, the thesis would not have been possible. I am looking forward to growing many more samples together in all the new instruments you just brought to Konstanz. Lastly, I just want to say thanks for the great three and a half years working together at the university and all the free time spend together outside the university.
- *Prof. Dr. Sebastian T. B. Goennenwein* for being the supervisor of the supervisors and for always coming from a higher flight altitude. For allowing me to independently pursue the projects and for having such faith in me with all the students, instruments and projects. For teaching me what is important for someone who hasn't stared at the data for months and for always finding a way to phrase things better.
- *Prof. Dr. Lukas Schmidt-Mende* for agreeing to review this thesis despite the short notice and little pre-warning.

- *PD. Dr. Andy Thomas* for winning me for this project, for providing guidance and insights at the start of the PhD. For providing an amazing evaluation software and a clean colour code. I apologise for the A4 format and the British English, even though I think the latter is superior.
- *Dr. Heike Schlörb* for initially bringing me in contact with Andy and for laying the foundation of my scientific path.
- *Dr. Matthias Hagner* for keeping the nano.lab running. For knowing seemingly everything about the instruments and fixing them. For not being annoyed when I stopped for the fifth time at your door to quickly ask something. For all the good times and discussion late at night. It made being at P8 feel like home.
- *Denise Reustlen* for being my first Bachelor student and for repeatedly coming back, first as a HiWi and then for the Master's thesis! For basically taking care of everything sample related after the deposition. For your impressive will to keep going and to measure everything. The complete second part of this thesis is thanks to you. For continuing the project step by step and for all the amazing time together in the lab - I hope we continue to work on many projects in the future together.
- *Gregor Skobjin* for laying the foundations of the crystallisation dynamics as my first student, for being the go to chemist in the group and for continuing with the sputtering. I really enjoyed working together.
- *Dr. Richard Schlitz* for his immense knowledge in magnonics, for his persistent way of telling everyone that "everything is clear" and for explaining all the "easy" physics to me. For also always helping me with the matr1x software, for being an encyclopedia in coding and for setting up all the dipsticks and GUI's. For all discussions during bouldering, biking, coffee breaks or at the Pampanin - I really enjoyed it and learned a lot in the short time.
- *Dr. Giacomo Sala* for providing a bunch of samples and data for the discussion revolving around the occurring magnetoresistances. For all the discussion about the correct diffusion coefficient and for confirming that Python is superior to Origin.
- *Prof. Dr. Pietro Gambardella* & *Dr. Min-Gu Kang* for teaching me to keep asking questions, for always wanting to understand every aspect and data point and for suggesting the ordinary magnetoresistance as a dominant contribution in our Pt films. The discussion opened the path for a consistent explanation and taught me a lot.
- *Prof. Dr. Olav Hellwig* & *Dr. Benny Böhm* for initially helping me with the Rigaku XRD in Konstanz and for providing insightful tips in the structural characterisation.
- *Dr. Darius Pohl* for the uncomplicated cooperation and for the efficient and quick TEM study of the lateral YIG mesa.

- *To all students who worked with me during my PhD: Rony Werner, Denise Reustlen, Gregor Skobjin, Anna Schwarz, Robin Swoboda, Davina Schmidt, Thorben Bielewski and Akis Rachoutis*. Thank you for all the work you did. I really enjoyed working together and learned a lot doing so. I hope you also learned something from me.
- *Ilona Wimmer* for introducing me to the Konstanz way of life, for being the best office partner at the start of my PhD, for your love of the Fäaschtbänkler and all the festivities in Konstanz. For making my start in Konstanz and the PhD memorable.
- *Franz Herbst* for all the discussion around magnons and statistics towards the end of the PhD. For deriving two pages of equations and then telling me that my initial assumption was actually pretty alright.
- *Marvin Weiss* for the noise time together, for helping me grasp the basics of waves and fluctuations better and for reminding me that I should not neglect my free time.
- *Nadine Nabben* for being down to earth, for the "witzig oder nicht witzig" Box and for always rating my jokes as funny!
- *Luise Holder* for being the first person I knew in Konstanz from the Dresden times. For making the start in Konstanz so much easier.
- Everyone in the best office of P852 and the whole *AG Goennenwein*, especially those not mentioned previously. For the great atmosphere and for enduring my flat out amazing wordplays.
- *Sebastian Großenbach* for being a great friend and colleague on P8, for all the quick discussions about the cryostats and all the free time spend together! I hope we continue to go on many "relaxed" hikes together in the future.
- *Roman Hartmann*, for his deep knowledge in structural characterisation, be it the AFM, the XRD or the EBSD. For suggesting to give EBSD a shot.
- *Jürgen Maier & Ralf Sieber* for the continuos supply of liquid Helium for the CHAOS and the SQUID. For making many of the measurements in this thesis possible and for the constructive help when the CHAOS was causing trouble again.
- *Dr. Christiane Runge-Froböse* for managing all the finances and the office stuff - for organising a contract and for bringing order into the ordering list.
- *The cleaning staff, the facility management and the workshop of the university of Konstanz* for keeping the place running and making new experiments possible.
- My great friends from the Dresden times in no particular order (except Valentina ;)): *Valentina, Matthias, Justin, Flo, Doro, Melina, Julia, Francesca and Jacob*. For keeping in touch, spending part of their holidays with me, inviting me to WG parties or simply visiting me in Konstanz - all despite the long distance. I draw a lot of strength from your friendships!

- The *Eis-Pampanin* for the spaghetti ice and for being a great meeting place. For always being there at the end of a bike trip.

- The *Känguru* for confirming my 50/50 suspicion and for clarifying that everything is either funny or not funny. This knowledge makes life so much easier.

- *Viola* "*Bro*"*-lein* for voting for me during the WG casting and for including me in her circle of friends. Rumour has it that you played an essential role in shaping my life in Konstanz.

- *Katrin Zoller* for always remaining positive and insisting everything will work out. For enduring my moods and lifting me up - I tell you way to rarely: I really appreciate all the little and big gestures. For always being the go to "non-physicist" and for almost being an expert now. For being so enthusiastic for outdoor holidays and for being spontaneous about it. I am looking forward to the future with you.

- Lastly, *my family*: First and foremost, *my parents Artur and Birgit* for their unwavering support, all I have learned from them and for always having my back. My sister *Andrea* for showing me a different way to happiness. My godfather *Markus* for his consistent support throughout my whole life, his interest in my projects and everything he made possible.